

A Theoretical Study of the Atomic and Electronic  
Structures of Three Prospective Atomic Scale Wire  
Systems

Stephen Andrew Shevlin  
University College London  
PhD Thesis

February 2001

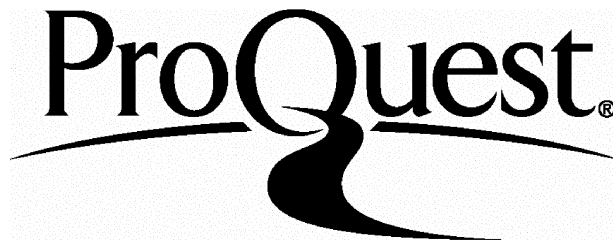
ProQuest Number: U643743

All rights reserved

INFORMATION TO ALL USERS

The quality of this reproduction is dependent upon the quality of the copy submitted.

In the unlikely event that the author did not send a complete manuscript and there are missing pages, these will be noted. Also, if material had to be removed, a note will indicate the deletion.



ProQuest U643743

Published by ProQuest LLC(2016). Copyright of the Dissertation is held by the Author.

All rights reserved.

This work is protected against unauthorized copying under Title 17, United States Code.  
Microform Edition © ProQuest LLC.

ProQuest LLC  
789 East Eisenhower Parkway  
P.O. Box 1346  
Ann Arbor, MI 48106-1346

## Abstract

The structural and electronic properties of several candidate atomic scale wires are analysed. Three candidates are studied: the trans-polyacetylene molecule, the silicon line on the (001) face of cubic silicon carbide (the  $(n \times 2)$  series of reconstructions) and the indium chain on the (111) face of silicon carbide (the  $(4 \times 1)$  reconstruction). We use the polyacetylene molecule as a test-bed for the techniques that we use to calculate transport properties in an empirically based tight-binding Hamiltonian (the SSH Hamiltonian). We calculate the transport properties of wires that show evidence of a strong coupling of the electronic degrees of freedom to the phonon degrees of freedom (Peierls distorted wires).

The structure of the  $(n \times 2)$  series of silicon lines (composed of the  $(3 \times 2)$  reconstruction which forms the line and the  $c(4 \times 2)$  reconstruction which forms the surface the line resides on) are modelled in a supercell geometry using ab initio plane-wave calculations in the Local-Density-Approximation and an ab initio Density Functional Theory based tight-binding technique. We found that the thermodynamically favoured model for the  $(3 \times 2)$  reconstruction was the Two-Adlayer-Asymmetric-Dimer Model (with 1ML of Si adatoms) and the favoured model for the  $c(4 \times 2)$  reconstruction is the Additional-Dimer-Row-Model (with 0.5ML of Si adatoms). In the tight-binding approximation the line was found to undergo a Peierls-like transition and holes are observed to form polaron-like defects. The transport properties of the line are also calculated.

Finally we find which of the two models of the Si(111)- $(4 \times 1)$ -In reconstruction is thermodynamically favoured in a supercell geometry. We use ab initio plane wave techniques in the Local-Density-Approximation, and calculate and compare the electronic structure of the two models with respect to the characteristic energies for electron dispersion along and across the chain structures. We also consider the effects of electronic structure on the in-plane transport properties of the indium lines.

## Preface

This thesis is an account of the work that was performed by the author from the period October 1997 to February 2001 under the supervision of Dr. A. J. Fisher and Dr. A. H. Harker. It has not been previously submitted to this or any other university. Parts of this thesis have been published or are in press, these papers are listed below.

1. *Modelling of the  $\beta$ -SiC(001) (3 $\times$ 2) surface reconstruction*, S. A. Shevlin and A. J. Fisher, App. Surf. Sci. **162-163**, 94 (2000)
2. *Modelling the c(4 $\times$ 2) reconstruction of  $\beta$ -SiC(001)*, S. A. Shevlin and A. J. Fisher, Phys. Rev. B **62**, 6904 (2000)
3. *The series of (n $\times$ 2) Si-rich reconstructions of  $\beta$ -SiC(001): a prospective atomic wire?*, S. A. Shevlin, A. J. Fisher and E. Hernández, Phys. Rev. B. **63**, 195306, (2001)
4. *Coherent electron-phonon coupling and polaron-like transport in molecular wires*, H. Ness, S.A. Shevlin and A.J. Fisher, Phys. Rev. B. **63**, 125422, (2001)

# Contents

<b>1</b>	<b>Introduction: The nanoscale: Basic physics and devices</b>	<b>11</b>
1.1	An Introduction to the nanoworld . . . . .	11
1.1.1	Motivation: Why are people interested in this? . . . . .	11
1.1.2	Important length scales . . . . .	13
1.2	Devices that can be manufactured at the nanoscale . . . . .	17
1.3	Candidate atomic scale wires . . . . .	24
1.4	Theoretical concepts . . . . .	28
1.5	Concluding remarks . . . . .	34
<b>2</b>	<b>Theory</b>	<b>35</b>
2.1	Modelling systems: Density Functional Theory . . . . .	35
2.1.1	Introduction . . . . .	35
2.1.2	The validity of the LDA . . . . .	38
2.1.3	Varieties of DFT method . . . . .	39
2.1.4	The PAW method: Wavefunctions . . . . .	43
2.1.5	The PAW method: Operators and energies . . . . .	45
2.2	Modelling systems: Tight-Binding . . . . .	48
2.3	Transport in atomic scale wires: An overview . . . . .	53
2.3.1	Introduction . . . . .	53
2.3.2	Where does resistance come from? . . . . .	56
2.3.3	Measurement issues . . . . .	59
2.3.4	Calculating the transmission probability . . . . .	61
2.3.5	Size effects . . . . .	64
2.4	Calculating the conductivity . . . . .	65

<b>3</b>	<b>The Polyacetylene molecule: An ideal testbed for studies of atomic scale wires</b>	<b>73</b>
3.1	Background Information	74
3.2	The Su-Schrieffer-Heeger (SSH) Hamiltonian	76
3.3	Calculating phonon modes, which ones are important?	81
3.4	Calculation of electron-phonon coupling	87
3.5	Transport properties: A brief discussion	89
3.6	Conclusion	91
<b>4</b>	<b>Silicon carbide: Ab initio studies of the <math>(3\times 2)</math> and <math>c(4\times 2)</math> surfaces</b>	<b>92</b>
4.1	Review of silicon carbide	93
4.1.1	Background information on silicon carbide	93
4.1.2	The $(n\times 2)$ series of reconstructions (silicon atomic lines): Physical characteristics and method of formation	96
4.1.3	Models of the $(3\times 2)$ reconstruction and relevant experimental evidence	99
4.1.4	Models of the $c(4\times 2)$ reconstruction and relevant experimental evidence	105
4.2	Ab initio simulations of the $(3\times 2)$ reconstruction	108
4.2.1	General points	108
4.2.2	Simulations of the ADRM model: Physical properties	112
4.2.3	Simulations of the DDRM model: Physical properties	113
4.2.4	Simulations of the TAADM model: Physical properties	114
4.2.5	Simulations of the ADRM model: Electronic properties	115
4.2.6	Simulations of the DDRM model: Electronic properties	117
4.2.7	Simulations of the TAADM model: Electronic properties	120
4.2.8	Thermodynamic results: Which $(3\times 2)$ model is favoured?	122
4.3	Ab initio simulations of the $c(4\times 2)$ reconstruction	125
4.3.1	Simulations of the AUDD model: Physical properties	125
4.3.2	Simulations of the MRAD model: Physical properties	125
4.3.3	Simulations of the AUDD model: Electronic properties	125
4.3.4	Simulations of the MRAD model: Electronic properties	127
4.3.5	Thermodynamic results: Which $c(4\times 2)$ model is favoured?	129

4.4	Conclusions . . . . .	129
<b>5</b>	<b>Silicon carbide: Tight-binding analysis of the structure of the (n×2) series of reconstructions</b>	<b>133</b>
5.1	Tight-binding: Formalism . . . . .	134
5.1.1	Tight-binding: Parameterisation . . . . .	134
5.1.2	Tight-binding: Tests . . . . .	135
5.1.3	Tight-binding: Correspondence with DFT results . . . . .	136
5.2	Structural properties of the (n×2) series . . . . .	138
5.2.1	Variation of line structure with n . . . . .	139
5.2.2	Thermodynamic results . . . . .	141
5.3	Electronic properties of the (n×2) series . . . . .	141
5.3.1	Variation of bandgap and HOMO state with n . . . . .	141
5.3.2	Density matrix analysis . . . . .	144
5.3.3	Proposed mechanism of structural transition for the metastable reconstruction . . . . .	148
5.4	Discussion on the ground-state and metastable structures . . . . .	149
5.5	Larger unit cells: (7×4) unit cell . . . . .	150
5.5.1	Structural properties of the (7×4) unit cell . . . . .	150
5.5.2	Electronic properties of the (7×4) unit cell . . . . .	152
5.5.3	Density matrix analysis . . . . .	153
5.6	Conclusions . . . . .	155
<b>6</b>	<b>Transport properties of the silicon lines</b>	<b>158</b>
6.1	Effects of charge injection into system . . . . .	159
6.1.1	Structural effects of charge injection: Polaron formation . . . . .	159
6.1.2	Effect of polaron formation on electronic structure . . . . .	162
6.2	Which phonon modes couple strongly to the polaron? . . . . .	165
6.2.1	Calculation of phonon modes: Formalism and tests . . . . .	165
6.2.2	Huang-Rhys factor analysis . . . . .	167
6.3	Electron-phonon coupling . . . . .	171
6.4	Transport properties . . . . .	173
6.5	Conclusions . . . . .	176

<b>7</b>	<b>Ab initio study of the In atomic chain on the (111) face of silicon</b>	<b>178</b>
7.1	Background information . . . . .	179
7.1.1	The Si(4×1)-In reconstruction . . . . .	179
7.1.2	Models . . . . .	182
7.2	PAW simulations: Tests . . . . .	186
7.2.1	Projector test: Lattice parameters of Si and InAs . . . . .	186
7.2.2	Simulation of the $(\sqrt{3} \times \sqrt{3})$ Si(111)-In reconstruction . . . . .	188
7.3	Ab initio simulations of the (4×1) unit cell: General points . . . . .	190
7.4	Simulation of the Bunk model . . . . .	191
7.4.1	Physical structure . . . . .	191
7.4.2	Electronic structure . . . . .	192
7.5	Simulation of the Saranin model . . . . .	195
7.5.1	Physical structure . . . . .	195
7.5.2	Electronic structure . . . . .	196
7.6	Thermodynamic results: Which model is favoured? . . . . .	198
7.7	Conclusions . . . . .	201
<b>8</b>	<b>Conclusions and suggestions for further work</b>	<b>203</b>
8.1	The polyacetylene molecule . . . . .	203
8.1.1	Conclusions . . . . .	203
8.1.2	Suggestions for further work . . . . .	204
8.2	The silicon lines on silicon carbide . . . . .	206
8.2.1	Conclusions . . . . .	206
8.2.2	Suggestions for further work . . . . .	208
8.3	Indium atomic chains on silicon . . . . .	211
8.3.1	Conclusions . . . . .	211
8.3.2	Suggestions for further work . . . . .	212
8.4	Final remarks . . . . .	214
<b>A</b>	<b>Binding energy in the tight-binding bond form</b>	<b>216</b>
<b>B</b>	<b>Validity of approximations used in calculation of transport?</b>	<b>218</b>
<b>C</b>	<b>The Car-Parrinello algorithm</b>	<b>223</b>

# List of Tables

- 4.1 Summary of the ability of different models to match experiments. + indicates agreement with the experiment, - indicates disagreement with experiment and  $\circ$  indicates ambivalent agreement with experiment.  
104
- 4.2 Summary of the ability of different models to match experiments and theory considerations. + indicates agreement with the experiment, - indicates disagreement with experiment and  $\circ$  indicates ambivalent agreement with experiment.  
107
- 4.3 Equilibrium bond lengths for the addimers and buckling of addimers (magnitude) in our total energy calculations and length of dimers in the terminating or surface layer. All distances are in Å. See Figures 4.6-4.9 for information on the nomenclature.  
113
- 4.4 'Dispersion' of HOMO state along  $[\bar{1}10]$  ( $\Gamma - J'$ ) and  $[110]$  ( $\Gamma - J$ ) directions, for various models. Also shown are values found in the literature. All values are in eV.  
115
- 4.5 Equilibrium bond lengths for the addimers and dimers in the terminating or surface layer and amount of buckling (magnitude) found in our total energy calculations. All distances are in Å. See Figures 4.10 and 4.11 for more.  
125

- 5.1 Structure of the various (3×2) models as found in our tight-binding scheme and how they compare to DFT simulations. See Figures 4.6-4.9 for the meaning of labels.  $\Delta z$  refers to the buckle of an addimer. All distances are in Å.  
137
- 5.2 The addimer structure of our two structures of the (7×2) unit cell; the ground-state (GS) and metastable state (MS). We also show the buckling of the addimers. See Figure 5.3 for the definition of  $a_1 - a_5$ .  
141
- 5.3 The variation of electronic structure with  $n$  for the ground-state system. We show the dispersion of the HOMO state along the  $\times n$  and  $\times 2$  directions and the range of band gap. All units are in eV.  
142
- 5.4 The variation of electronic structure with  $n$  for the metastable state system. We show the dispersion of the HOMO state along the  $\times n$  and  $\times 2$  directions and the range of band gap. All units are in eV.  
143
- 5.5 Dispersion of the LUMO state for the metastable structure in eV.  
143
- 5.6 Dispersion of the LUMO state for the ground-state structure in eV.  
144
- 5.7 Dispersion for the HOMO (and LUMO in brackets) states for the “metastable” structures before and after dimerisation along the  $\times 7$  and  $\times 4$  directions and the range of the HOMO-LUMO gap in eV. We present results for the flat addimer (top pair) and buckled addimer structures (bottom pair).  
153
- 6.1 Significant Huang-Rhys factors for hole polaron system. Phonon modes are arranged in increasing frequency (there are 144 phonon modes in total).168
- 6.2 Significant Huang-Rhys factors for electron polaron system. Phonon modes are arranged in increasing frequency (there are 144 phonon modes in total).169

7.1	Summary of the ability of different models to match experiments. + indicate agreement with the experiment, - indicates disagreement with experiment and ◦ indicates ambivalent agreement with experiment. . . . .	186
7.2	Equilibrium bond lengths for the indium and silicon addimers. All distances are in Å. See Figure 7.4 for nomenclature. . . . .	191

## Acknowledgements

This thesis is the distillation of over three years of work as a PhD student at the Condensed Matter and Materials Physics group in the Department of Physics at University College London. Quite obviously, for these three years I was not a solitary figure who concentrated on his work to the exclusion of everything else (disregarding appearances to the contrary). Therefore it is my great pleasure to acknowledge everyone who has contributed something to the gestation of this thesis, either providing scientific help or personal help (also known as “buying me a pint”).

Firstly I should like to thank my doctoral supervisors, **Andrew Fisher** and **Tony Harker**. Both of them have performed above and beyond the call of duty, always willing and able to discuss work when they could, providing able advice and encouragement when I needed it, supporting the route I have taken to write this thesis and always making me understand the physics of what I am doing. Secondly I should like to thank **Hervé Ness** for his willingness to answer my questions on the physics of transport at the atomic scale and for the interesting and fruitful discussions we have had. Thirdly I should like to thank **Eddie Hernández** for letting me play with his TROCADERO code and then letting me (for want of a better word) butcher it to obtain some of my results. The Engineering and Physical Sciences Research Council is also thanked for providing me with the funds to pursue my PhD.

Other people have contributed to the scientific work presented in this thesis, in particular I would like to thank **Gerárd Dujardin** and coworkers for the discussions on the  $(3 \times 2)$  surface of silicon carbide and the use of STM images presented in this thesis. From the CMMP group I would like to thank **David Bowler** for advice on the simulation on various aspects of the silicon lines, **Marshall Stoneham** for advice and discussions on various aspects of solid state physics, **Lev Kantorovich** for always been willing and able to answer my questions on any aspect of physics I was interested in, **Alex Shluger** for always forcing me to consider the full implications of what I am doing, **John Harding** for advice on the thermodynamical calculations that have been performed and **Werner Hofer** for running several tests that I have asked him to do.

My housemates over the past few years have contributed significantly towards making this thesis the document it is by making the person who wrote the thing the person he is. **Adam Foster** shall always be remembered for his interesting tea combinations and his gentle wit regarding my grooming (\*I\* do not have to suffer the wrath of Finnish barbers), **Jonathan Wasse** has always amused me with his skillful food preparations and his support for his football team (you can always defect to the \*real\* Blues, Birmingham City). **Hanna Vehkamäki** for always amusing me with your observations of UCL and the UK (a CD of my music shall be on the way soon, alternatively you can provide the sound effects yourself), **Klaas Stephan** for always been an agreeable chap and **Rosa Schwandt** for been another person who is trying to finish a thesis off and look for a job at the same time.

The CMMP group has not just been a place where one can work efficiently, it has also been an enjoyable environment in which to work. There are far too many people to thank but a few people who deserve to be singled out include **Andy Gormanly** who

is one of the original “Gang of Seven” and has always been up for a laugh, a wander and a drink. **Louise Dash** is another one who was often up for a drink, or an amusing comment (pity about the taste in music though. . .). **Francisco López** has always been available for a quick chat and has often given useful advice (and nice wine and a few good CD’s). **Andrew Steer** has always been up for letting me misuse his computer for non-academic work (and for always making the coffee). **Peter Sushko** (and **Shu Hayama** and **Andy Kerridge** and **Daniel Ucko**) are thanked for putting up with various meaningless comments that I have uttered from time to time in order to get away from the grind of work. **Andreas Markmann** is thanked for letting me borrow various CD’s of his from time to time. And the group secretary **Denise Ottley** is thanked for providing sterling support over the last three years.

I have lived a life outside UCL as well, and my life has been impacted by the many people who have (in one sense or another) kept me on the path. **Rick** has always kept me amused and entertained (did you actually read that paper?). **Ian** for coming down to London as well as preparing some very nice meals (let’s not buy quite as much food and wine, eh?). **Matthew** and **Margaret** for keeping in touch and offering me lifts (when will the stag night and reception take place?). **Suzanne** and **Lee** for the good laughs, and **Jim** for the sage advice (and how is Oz?). **Richy** and **Liz** and **Paul** for the films in London, the drinks and the deathmatch games. The crews of **umstb5** and the **WEF** for the distractions. The **Ambleside** lot for the task of legend. **Rob**, **Grae**, **Rowls**, **Jam**, **George**, **Elaine** and **Kev** for the nights out in sunny exotic Tamworth (oh, and Torquay). And the mighty **Birmingham City** for being a constant throughout the three years (constantly in the First Division that is).

Finally I would like to acknowledge my family, for the love and support that I have received from them. There have been times that I have been a bear, much thanks to you all for putting up with me, and for the emails and phone calls that have let me know what is going on. This thesis is a testament to you as much as it is to me.

# Chapter 1

## Introduction: The nanoscale: Basic physics and devices

### 1.1 An Introduction to the nanoworld

#### 1.1.1 Motivation: Why are people interested in this?

On writing a diary:

“I do not intend to publish it; I am merely going to record the facts for the information of God”.

“Don’t you think God knows the facts?”

“Yes, He knows the facts, but he does not know *this version of the facts.*”

*Leo Szilard* in conversation with *Hans Bethe*.

In the world of the late nineties/early noughts, it is becoming increasingly obvious to the layman that electronic devices are becoming smaller and smaller. The logical endpoint of this trend of miniaturisation is the development, fabrication, and use of electronic devices that function on the atomic scale, that is at a length scale of the order of or less than a nanometre ( $10^{-9}$  of a metre).

Current manufacturing and fabrication processes (at an industrial scale) have still not reached this length scale. But, we can estimate when these processes will reach this level, and start manufacturing individual elements (wires, transistors and capacitors) at the

atomic scale. In 1965 Gordon Moore of Intel made an analysis of the variation of device size with time, and found that there was an exponential decrease in device size (or respectively an exponential increase in device performance for a fixed size) with a doubling time of two years (this has since changed to a doubling time of eighteen months). This means that we can predict that by, approximately, the year 2017 electronic devices will be fabricated at the atomic scale [1]. It is thus extremely important from a technological viewpoint to understand how electronic devices will perform at the atomic scale. It is also important to devise new types of devices that can function at an economical price at this length scale. The current CMOS technologies cannot be scaled all the way down to the atomic scale for two reasons: firstly that at a critical thickness of semiconductor film electrons can tunnel through the film thus destroying device functionality, and secondly even if it were possible to work around this limitation the cost of constructing a fabrication plant to manufacture these devices with the desired purity from defects would be prohibitively expensive, on the order of the Gross Domestic Product of a large country (see the SIA roadmap for more information [1]).

The behaviour of devices which can function at the atomic scale was first discussed about forty years ago, by the physicist Richard Feynman, in his seminal lecture “There’s Plenty of Room at the Bottom” [2]. In this seminar he mentions the capability of electron beam lithography to etch material at the atomic scale [3], the possibilities of writing and manipulating information at the molecular level (we ourselves are living proof that this is possible, as DNA and mRNA molecules store and manipulate information respectively [4]), the possibility of creating atomic scale computers [5] and the possibility that we can engineer the properties of materials by altering their structure at the atomic scale [6, 7, 8].

One other possibility that Feynman mentioned was that at this length scale, the properties of devices can be radically different from devices at larger length scales. There can be several reasons for this. Firstly, that at the atomic length scale, the atomic structure of the device is of critical importance. Defects in the device can dominate device performance, which means that the manufacture of these atomic scale devices must be to a very high tolerance (of course, devices could be designed that use these defects to their advantage, but one would still have to make certain that one had the correct number and type of defects one required). The electrons may couple to other

physical phenomena, for instance to a magnetic field (the Aharonov-Bohm effect) [9], or to phonons (lattice vibrations) [10, 11, 12, 13, 14, 15, 16, 17, 18, 19, 20, 21, 22] or electron-electron interactions may be important [23].

Finally, if one were performing logic operations, in theory it is possible to utilize entanglement at this length scale to massively increase the efficiency of certain computations [24]. It should be obvious therefore that not only is there a pressing technological need to understand the physics of device performance at the atomic scale, but also that the physics of device performance at the atomic scale are intrinsically interesting.

At this length scale quantum mechanical effects can affect the performance of the device. For instance, due to tunnelling of an electron through an atomic scale interconnect, the effective resistance of the interconnect could be less than one would expect from purely classical arguments [25]. On the atomic scale, we cannot treat electrons by the semi-classical approximation, but instead we have to treat electrons as discrete entities. This means that we cannot treat the electronic structure within the confines of band theory, but rather that we must explicitly include quantized states [25]. Finally, depending on the length scale of the device the electronic properties can alter (see next section for more information). These effects mean that there exists a scientific reason for studying atomic scale devices in addition to the technological imperative that has already been stated.

### 1.1.2 Important length scales

As we shrink our device from our everyday 1m to the atomic length scale of  $10^{-10}$ m, the properties of the electrons that are present in the device can change. One can define a variety of different length scales that can lead to different quantum phenomena, such as the De Broglie wavelength, the mean free path and the phase-relaxation length [26]. Note that for all of the examples in this section we are talking about 2D electrons, as the origin of this classification scheme lies in discussions of thin semiconductor films.

We can write the Fermi wavelength as  $\lambda_f = 2\pi/k_f = \sqrt{2\pi/n_s}$ , where  $n_s$  is the electron density of the material. For an electron density of  $5 \times 10^{11} \text{cm}^{-2}$ , the Fermi wavelength is about 35 nm. The current at low temperatures is mainly carried by electrons near the Fermi energy, and thus the Fermi wavelength is the relevant length scale. Electrons with different energies (or longer wavelengths) do not contribute to the conductance of

an atomic scale interconnect.

Electrons moving through a perfect crystal behave as though they are moving through a perfect vacuum but with a different mass (the effective mass) [25, 23, 27, 28, 29]. Any resistance to the electron motion is due to imperfections in the lattice, i.e., intrinsic defects or thermal phonons. This resistance causes the momentum of the electron to change in a random way. The momentum relaxation time  $\tau_m$  is related to the collision time  $\tau_c$  by

$$\frac{1}{\tau_m} \rightarrow \frac{1}{\tau_c} \alpha_m \quad (1.1)$$

where  $\alpha_m$  (which can vary from 0 to 1) denotes the effectiveness of a single collision in destroying the original momentum. The mean free path  $L_m$ , the length travelled before the electron has lost the momentum it originally possessed, is the product of the momentum relaxation time and the Fermi velocity,  $L_m = v_f \tau_m$ . The Fermi velocity is given by

$$v_f = \frac{\hbar k_f}{m} = \frac{\hbar}{m} \sqrt{2\pi n_s} \quad (1.2)$$

which is  $3 \times 10^7 \text{ cms}^{-1}$  if  $n_s = 5 \times 10^{11} \text{ cm}^{-2}$ . If we assume that the mean relaxation time is 100 ps then this gives us a  $L_m$  equal to 30  $\mu\text{m}$ . Electrons that travel through a device without scattering are often called *ballistic* electrons. If a device is smaller than the mean free path, then the electrical conductance of the device displays stepwise behaviour where the conductance is quantized in unit of  $e^2/\hbar$  [30].

To calculate the phase-relaxation length we can make use of an analogy with the mean free path. We can write the phase-relaxation time as

$$\frac{1}{\tau_\phi} \rightarrow \frac{1}{\tau_c} \alpha_\phi \quad (1.3)$$

where  $\alpha_\phi$  represents the effectiveness of a collision in destroying phase. However, we need to think about the destruction of phase, as this is a complicated problem, and

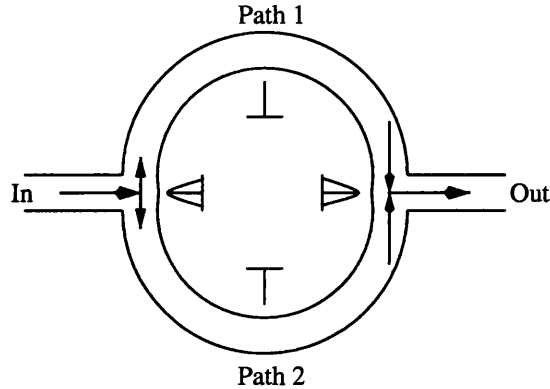


Figure 1.1: Interference patterns around a mesoscopic ring in a zero magnetic field.

requires a lot of attention. Consider a mesoscopic ring into which electrons are injected. In zero magnetic field the beam of electrons will split and interfere constructively at the recombination point (see Figure 1.1). If we now apply a magnetic field perpendicular to the ring, we will interfere with the phase of the electrons. We can change the interference from constructive to destructive, and back again [9] (see Figure 1.2).

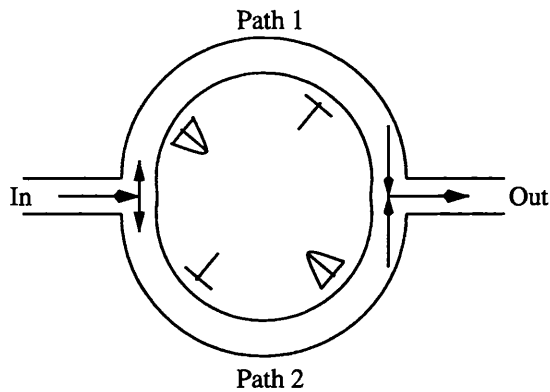


Figure 1.2: Interference patterns around a mesoscopic ring in a non-zero magnetic field.

Consider that we add *static* impurities to the ring in a random fashion. The two arms of the ring are no longer identical. In zero magnetic field the interference at the recombination point will no longer be constructive. However, if we now apply a magnetic field to the ring, we can once again recover the constructive/destructive interference. We can thus conclude that for *static* impurities, the phase-destructive time tends to  $\tau_\phi \rightarrow \infty$ , that is that  $\alpha_\phi \rightarrow \infty$ . This means that the electronic states in the ring are well defined.

To destroy phase, we require the presence of dynamic scatterers like phonons or electron-electron interactions [31], which mix states. As the phase interference is now not stationary, there is no stationary interference pattern and consequently the phase is

destroyed (as the constructive and destructive interference time-averages to zero). We can also destroy phase if the static impurities have an internal degree of freedom, because if an electron changes the internal state of an impurity as it travels along one of the two rings, then we can measure its path, thus *destroying any quantum mechanical properties of the electron, such as interference, or phase* [32].

So what is the associated phase-relaxation time  $\tau_\phi$ ? It is not necessarily equal to the collision time  $\tau_c$ . For instance, if we consider the mesoscopic ring above, long wavelength phonons would affect both arms of the ring equally, and thus would not be effective in destroying phase. For a phonon with energy  $\hbar\omega$ , the mean squared energy spread of an electron after a time  $\tau_\phi$  is the product of the square of the energy change per collision and the number of collisions [33] (assuming uncorrelated random energy transfer)

$$(\Delta E)^2 = (\hbar\omega)^2(\tau_\phi/\tau_c). \quad (1.4)$$

The phase relaxation time  $\tau_\phi$  is defined as the time at which the mean squared spread in the phase is of order one, i.e.,

$$\Delta\phi \sim (\Delta E)\tau_\phi/\hbar \sim 1 \rightarrow \tau_\phi = (\tau_c/\omega^2)^{\frac{1}{3}} \quad (1.5)$$

As we are interested in high mobility semiconductors and metals, we can thus define the phase-relaxation length to be the product of the phase-relaxation time with the Fermi velocity

$$L_\phi = v_f\tau_\phi. \quad (1.6)$$

If the size of the device is less than the phase-relaxation length, then transport through the device can be described as coherent.

If electrons are confined to length scales of the order of nanometres, then the electrons can possess low dimensional behaviour, or as we will use from now on *quasi*-low dimensional behaviour (as in our four dimensional spacetime no material can be one-

dimensional). This means that if we consider the full 3D Schrödinger equation and the potentials that act on the electrons, an electron is considered to possess quasi-low dimensional behaviour if in one or more dimensions the potential is a): extremely large thus confining the electrons in that direction and b): the separation of potential barriers in this direction is less than all three characteristic length scales. If condition b): is not fulfilled then the electrons are only semi-classically trapped by the potential barrier and the one-electron states are not quantized, instead forming a continuum of states (see the next section for more information).

Electrons can be confined in the interface between two separate semiconductors, and can be regarded as quasi-two-dimensional. The electrons that are strongly confined in an atomic wire can be regarded as quasi-one-dimensional, and may possess properties different from the Fermi liquid model, such as the electrons acting as a Luttinger liquid [23]. And if electrons are confined to a quantum dot (or “artificial atom”), then they can be treated as quasi-zero-dimensional.

There are many devices that one can build at the atomic scale [34]. However, the MOSFET (Metal-Oxide Semiconductor Field Effect Transistor), which is the most common type of transistor used in the electronics industry, cannot be scaled down to the atomic length scale without major modifications. As the MOSFET reaches the atomic length scale, the high electric fields due to a bias field can cause ‘avalanche breakdown’ which can damage the MOSFET by causing the silicon oxide film which forms the dielectric to fall apart, heat disruption becomes a problem and the above mentioned defect problem becomes an issue. Therefore industry has to look for alternative electronic devices. These can be divided into two broad classes [35], the solid-state quantum-effect/single electron devices, and molecular electronic devices. These device operations depend on quantum mechanical effects.

## 1.2 Devices that can be manufactured at the nanoscale

The solid-state quantum-effect/single electron devices all share one thing in common, they all possess a small ‘island’ of some metallic or semiconducting material in which electrons can be confined. This island has a role similar to that of a channel in a FET. These devices can in turn be divided into two broad classes

1. *Resonant Tunnelling Devices.* Island confines electrons with one or two classical degrees of freedom [36].
2. *Single-Electron-Transistors.* Island confines electrons with three classical degrees of freedom [37].

These devices can also be manufactured from components such as quantum dots which are islands which confine electrons with zero classical degrees of freedom, although quantum dots can also be used as the components of many different types of devices.

The type of device formed depends on the size, shape and composition of the island that is present in the device. The smallest dimension of the island that is formed ranges from 5 to 100 nm, and the island can either be formed from a material different from the rest of the device, or be defined by an electric field generated from a series of electrodes.

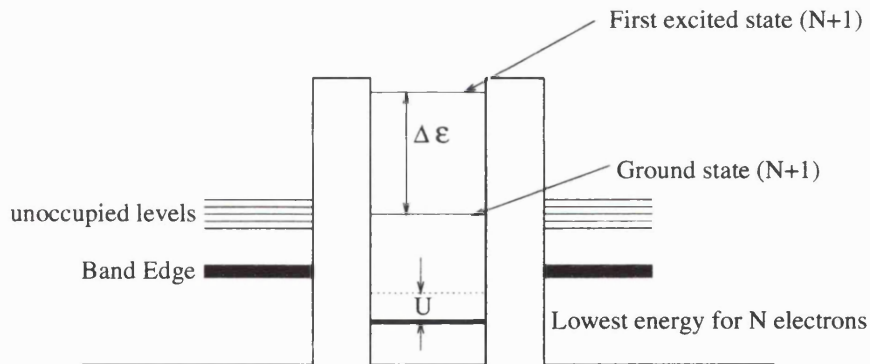


Figure 1.3: Quantization of states in a narrow potential well.

Whatever the case, there exists a potential barrier between the island and the material that surrounds the island (for the following discussion we will be assuming a purely one dimensional case, see Figure 1.3). Any electrons that are trapped on the island exhibit two quantum mechanical effects, firstly that the states the electron can inhabit are quantized and differ from one another by an energy  $\Delta\epsilon$ , and secondly that if the extent of the barriers confining the electrons is small enough, then the electrons can tunnel through the barrier, either to tunnel into the island or to tunnel off the island.

These quantum effects influence the transport properties of the device. When a voltage is applied across the device, this induces the electrons in the source to attempt to move across the barrier into the island. The only way an electron can travel to the island is to tunnel through the barrier, but only if there is an empty state available at the

same energy (or at most one phonon energy away) in the island (as the Pauli principle prevents two electrons from occupying the same state).

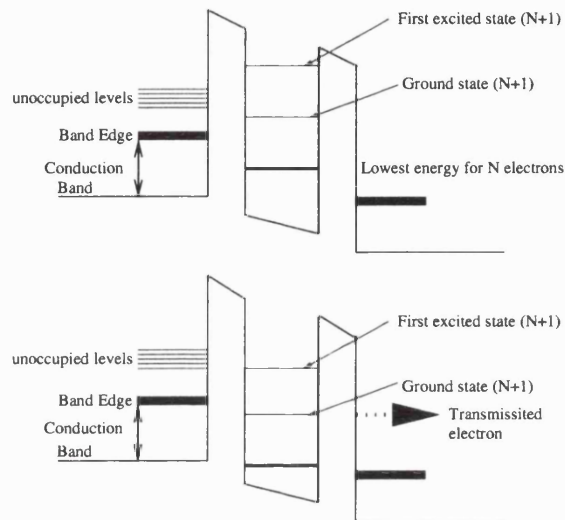


Figure 1.4: Change in height of a barrier under the influence of an electric field.

We will use Resonant Tunnelling Devices (RTDs) to illustrate the operation of various solid-state devices. Under the influence of a bias, the energy of the states in the island can be changed. As we increase the bias, the energy of all the states in the island is lowered (see Figure 1.4). When the bias potential is sufficient to lower the energy of an unoccupied state inside the well to below the valence band, then we can say that the device is in resonance or on, as it is now possible for source electrons to tunnel through the device. As there are many unoccupied states inside the island, then the RTD can have multiple on/off states, depending on the bias voltage (that is as the voltage changes, source electrons can access multiple unoccupied states as they are brought down to the conduction band). This means that as we vary the bias, the conductivity changes, but because of the discrete energy levels the conductivity can only change in *discrete* steps. This notion that the conductivity of an atomic scale object depends on the number of states that an electron can access is an important one, and will be discussed later in this thesis.

Let us now generalise our arguments for electrons travelling through an atomic scale device, by considering the three dimensionality of the device and the Coulomb force. For a three dimensional island, with different dimensions along each axis  $x$ ,  $y$ , and  $z$ , an electron's energy is quantized separately in each direction (but only if the Schrödinger

equation is separable), i.e.,  $\Delta\epsilon_x$ ,  $\Delta\epsilon_y$  and  $\Delta\epsilon_z$ . These  $\Delta\epsilon$  are calculated for an isolated electron. If we consider  $N$  electrons in the island, then the energy for the  $(N+1)$  electron to enter the island has to overcome the Coulomb potential of the  $N$  electrons in the island  $U$ . Therefore for an electron to tunnel through the barrier into an island it has to possess an energy of  $\Delta\epsilon_{x,y,z}$  plus  $U$ . The magnitude of  $U$  and  $\Delta\epsilon$  are sensitive to the size and shape of the island.  $\Delta\epsilon$  is inversely proportional to the square of the size of the island (generally, it is the shortest dimension of the island that affects the quantization the strongest).  $U$  varies as the inverse of the size of the island (the longest dimension most strongly affects  $U$ ). Thus we can engineer our island to either minimise, maximise, or some combination of the two,  $\Delta\epsilon_{x,y,z}$  and/or  $U$ . This is why there exist two categories of solid-state devices.

Using these arguments, we see that the conductivity of an RTD (which usually has one ‘short’ and two ‘long’ wire-like directions) is solely determined by  $\Delta\epsilon$ . The conductivity of a Quantum Dot (which has three ‘short’ dimensions) is determined by both  $\Delta\epsilon$  and  $U$ . Single-Electron Transistors (SETs) possess a metal island which contains  $\sim 10^6$  mobile electrons. Although the size of a SET is often approximately the same as a QD, the length scales depend on the materials used.  $\Delta\epsilon$  is small for SET’s, while  $U$  is large. Thus the conductivity of an SET is determined by  $U$  alone. This limit is called ‘Coulomb blockade’, as at low voltages electrons cannot tunnel into the island.

Although these devices have been fabricated in the laboratory, there are several disadvantages that may render them unfit for use in industry. They are

1. For multistate confinement devices, there is a residual current when the device is off-resonant. We could thus confuse on and off states.
2. Switching in RTD’s can be very sensitive to fluctuations in voltage [38].
3. An exponential sensitivity of tunnelling current on the width of the potential barriers. Devices would have to be fabricated to extremely high standards.

Devices made from individual molecules could offer solutions to these problems, especially the fabrication problem. It is exceptionally difficult to fabricate solid-state structures at the nanoscale by the billion. However it is exceptionally easy to fabricate individual molecules by the billion [39]. (Note: We define molecular electronics to mean electronics involving covalently bonded molecular structures electrically isolated from a

substrate).

There are at least four broad classes of molecular electronic switching devices that are found in the literature.

1. *Electric-field controlled molecular electronic switching devices*: Molecular version of quantum-effect devices [40].
2. *Electromechanical molecular electronic devices*: These employ electrically or mechanically applied forces to change the conformation or to move a switch atom or molecule [41, 42, 43, 44].
3. *Photoactive/photochromic molecular switching devices*: Use light to change the electron conformation, or shape to switch a current [45].
4. *Electrochemical mechanical devices*: Uses electrochemical reactions to change conformation or electron configuration to switch a current [46].

The first two categories of molecular electronic devices can be laid down on a solid substrate and so are applicable to atomic scale computers. The latter two types of device are not applicable, as they either cannot be packed in a dense network (photoactive devices would have to exist in volumes of length  $\sim 500$  nm), or would require wet chemistry (the electrochemical devices would need to be placed in a solvent).

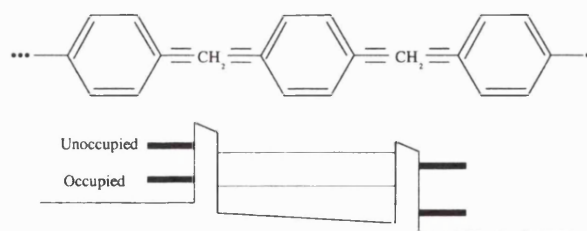


Figure 1.5: quantum well embedded in a molecule with top of valence band and bottom of conduction band shown. The  $\text{CH}_2$  groups represent the potential barriers, and the benzene groups in the middle represent the quantum well.

It may be possible to use molecular structures for quantum confinement, as proposed above (the QD's detailed above). One could either embed metal nanoclusters in a supermolecular framework, as such QD's could be uniformly fabricated and then assembled in a very regular structure. Alternatively a quantum well could be embedded in a molecule, one which functions as a molecular wire (see below). This device would function as a two lead RTD (see Figure 1.5).

Unlike the quantum effect molecular devices, we cannot make an easy comparison between transistors and electromechanical molecular devices. It has already been shown that it is possible to make a switch consisting of only a few molecules. One can use an STM tip to press down on a  $C_{60}$  molecule (or buckyball) on a substrate [44, 47, 48]. The force imparted by the STM causes the buckyball to deform. This changes the conductivity properties to change, forcing the buckyball to shift from on-resonance to off-resonance. Off-resonant buckyballs suffer a reduction of 50% in current, thus leading to identifiable on/off states. However, it would be extremely impractical to use an STM tip to operate a switch in an industrial product. Another proposal for a molecular transistor is the deposition of a molecular wire on a substrate that has been structured at the atomic scale to act as a series of gates [49]. Some rectifying properties have been found. However this idea is at the moment entirely theoretical.

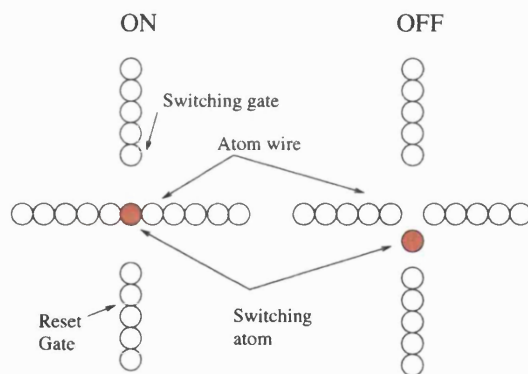


Figure 1.6: Schematic of an atomic relay (obtained from Goldhaber *et al*, Proc. IEEE **85**, 521, (1997)).

Several theoretical schemes have been proposed to make molecular-scale switches that do not rely on the presence of a STM. Wada [42] proposed a scheme known as the atomic relay (see Figure 1.6). A mobile atom that is not firmly attached to the substrate is present in the junction between four terminals. When the switch is 'on', the mobile atom lies between two terminals, allowing a current to flow between the two terminals. When the switch is turned 'off', an electric field that passes through the other two terminals forces the atom to move to one side, thus breaking the connection. Unfortunately, this switch would require a low operating temperature, as it would be quite easy to evaporate mobile atoms off the substrate, for instance by electro-migration induced by the electric field.

Rather than using the movement of a single atom as a switch, Goldhaber *et al* [35] suggested that a molecule with a rotational group can act as a switch (see Figure 1.7). When an electric field is applied to the molecule, the switching group would rotate. When the switch is 'on', the functional group that exists in the gap between the two terminals has a high conductivity, but when the switch is turned 'off' the switching group is rotated away from the terminals, and a replacement group with a lower conductivity takes its place.

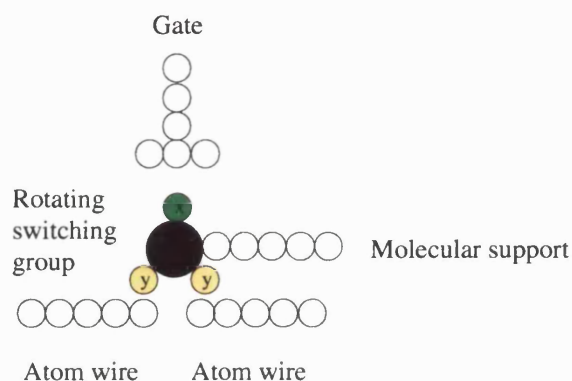


Figure 1.7: An example of a molecular switch.

We have mentioned the need for nanoscale devices, the physics of these devices and the various designs that currently exist for these devices. However, for any of these devices to work we require a method to transmit a net current into and out of these devices. The obvious solution would seem to be a set of atomic scale interconnects or *wires*. However it is an open question whether these wires and/or devices need even be fabricated. There have been theoretical studies that have outlined the possibility that one can structure a material at the atomic scale so that any switches and wires can be activated or deactivated by manipulating the dynamical properties of the system as a whole [50, 51, 52, 53]. These studies use the atomic scale (subnanometre) structuring of the material so that when the initial one-electron states of the system are acted upon by some outside driving system (such as a laser), they are driven into final stationary 'attractor' states in such a way that a net current has been driven through the material and/or the electrical properties of the material have changed in a measurable way analogous to a set of switches being thrown. However these studies have (so far) been completely hypothetical.

Another approach that has been suggested is the quantum cellular automata (QCA) approach. There are two basic approaches, the SET approach [54] and the magnetic

approach [55], in which we have a series of quantum dots which can flip sign (either adding or subtracting electrons, or changing the sign of the internal magnetic field) under the influence of an input electric or magnetic field. The SET approach has (at the moment) limited applications as the operating temperature is in the range of a few millikelvins. The magnetic approach operates at room temperature. However we are interested in electronic transport at a useful operating temperature. Therefore we wish to concentrate on the seemingly more concrete applications of atomic scale wires. What are our options?

### 1.3 Candidate atomic scale wires

There are several different designs for prospective atomic scale wires. These vary from using molecules, to fabrication using an STM or AFM tip.

1. *Molecular wires*: These are wires which are formed from molecules. Examples of such wires would include trans-polyacetylene [18, 20, 21, 22, 56, 57, 58, 59], p-phenylene sulfides [60], fused rigid porphyrin-oligomers [61], the alkanethiols [62], phthalocyanines [63], the thiophene polyenes [13, 64] and fullerene nanotubes of carbon [65, 66, 67] and silicon [68].
2. *Atomic Nanobridges*: These are formed by either an STM tip crashing into the surface and then withdrawing [69, 70], or by electron-beam irradiation [71]. A short-lived atomic bridge is formed, through which current can flow. However stress effects tend to destroy these bridges.
3. *Dangling Bond Wires*: These are formed by using an STM to desorb hydrogen from a silicon surface [72, 73, 74]. The resulting line of dangling bonds are metallic and can act as wires [75, 76, 77].
4. *Zeolitic Chains*: These chains are formed by using the cavities of zeolites to construct atomic scale chains of metals [78, 79], or to construct interlinking chains of polymers [80].
5. *Self Assembled Lines*: These lines are formed from the inherent surface properties of the substrate. A material is either deposited on the substrate and self-assembles, such as indium on silicon(111) [81, 82, 83, 84, 85, 86, 87, 88, 89, 90, 91, 92, 93,

94, 95], gallium on silicon [96] or gold on silicon(111) [97, 98, 99, 100, 101, 102]. Alternatively, these structures can be formed by desorbing excess material from a substrate, such as bismuth from silicon(001) [103, 104] or silicon from silicon carbide(001) [105, 106, 107, 108, 109]. Note: The indium and silicon lines can be formed by either absorption or desorbtion.

As one can see from the above discussion of length scales, one has to be careful about the nomenclature one uses to describe devices. For example, a nanowire, a quantum wire and an atomic wire can all mean different things. A nanowire is a wire that has an extent of the order of nanometres (in the literature this can mean anything from one nanometre to several thousand nanometres). A quantum wire is a wire in which the electrons display quantum behaviour. Quantum wires can (depending on the material and the temperature) be several micrometres in extent. An atomic wire is a wire that has an extent of the order of the atomic length scale, i.e. several Å's. These atomic wires are necessarily quantum wires, at any accessible temperature.

Molecular wires are characterised by a sequence of extended repeating structures, or monomers. The monomers are linked together by  $\pi$  orbitals. These  $\pi$  orbitals conjugate with each other to form a single large  $\pi$  orbital which is delocalised throughout the molecule. It is this delocalised  $\pi$  orbital that permits electrons to tunnel through the molecule for a range of electron energy. We can make an analogy with carbon nanotubes, although in this case the analysis is complicated by the consideration that a nanotube can have multiple walls and it is possible to have a series of nanotubes, with each nanotube surrounded by a larger nanotube (like a Russian Matreski doll). Interactions between the various nanotubes cause the nanotube to undergo a transition from a metallic to a semiconducting or insulating phase, and depending on the way a single-walled nanotube is 'wrapped up' a single walled nanotube is either metallic or semiconducting [110, 111, 112].

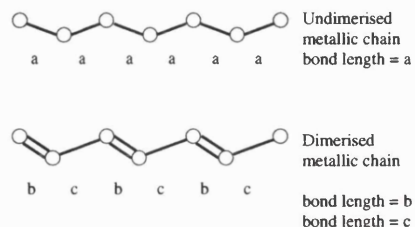


Figure 1.8: Dimerisation of a molecule.

Some molecules (such as trans-polyacetylene) can undergo a structural transition such that a structure where C-C bond lengths are all even transforms to a case where there are two separate C-C bond lengths, a long one and a short one [18, 59] (see Figure 1.8). This *dimerisation* is intimately related to the trans-polyacetylene molecule acting as a one-dimensional metal. Although we will not detail the mechanism for such a transition until the next section, we will define a *dimerisation parameter* that represents the magnitude of this alternation in bond length

$$d_j = (-1)^j (b_{j,j+1} - b_{j,j-1}) \quad (1.7)$$

where  $b_{j,j+1}$  is the length of the bond between atoms  $j$  and  $j + 1$ . This parameter is far more useful than it would appear, as it enables one to analyze the effect of defects in an atomic wire in a simple and understandable manner, as a dimerised atomic wire that contains no defects has a completely flat dimerisation curve, and the presence of defects perturbs this flat dimerisation curve.

A dangling bond (DB) wire is fabricated by STM desorption of hydrogen on the hydrogen-terminated surface of silicon, in a Ultra-High-Vacuum system (UHV) (see Figure 1.9). This means that these systems are not usable in practical atomic-scale devices, but they can serve as a useful testbed for interesting physical phenomena (such as the effects of inelastic coupling, see next section). As the hydrogen-silicon bonds are broken by current injection [72] and/or field effect [74] (although probably the former), the hydrogen atoms evaporate into the vacuum, leaving empty bonds behind. If we depassivate a line either parallel or perpendicular to the  $(2 \times 1)$  reconstruction of Si(100), the empty bonds that are left are able to overlap. The properties of the specific DB wire depend on the direction the DB wire runs in, and whether the wire is formed from a row of single DB's or a row of pairs of DB's. However, in all cases the DB wires initially (before reconstruction occurs) have a finite density of states at the band gap, while the surrounding hydrogen-terminated surface has a wide band gap [75]. This suggests that the DB wire is conductive, and that any electrons that are injected into the DB wire will be well confined.

This is an important point that must be considered in any study of atomic scale wires, the isolation of the atomic wire from the substrate. For the case of a molecular wire

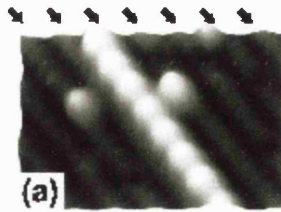


Figure 1.9: A dangling bond wire (image taken from Hitosugi *et al*, Phys. Rev. Lett. **82**, 4034, (1999)).

deposited on a substrate, it depends on the type of force that is holding the molecule to the substrate. If the molecule is physisorbed (that is there are only weak Van der Waals type forces holding the molecule in place) then any electrons that are injected into the molecule will be electronically isolated from the substrate. This is due to the long residence time of an electron in the bond due to the small bonding energy, as found from  $\Delta E \Delta t \sim \hbar$ . Assuming that forming a Van der Waals bond costs 0.01 eV, an electron resides in the molecule for  $\sim 10^{-14}$ s. However, if the molecule is chemisorbed to the substrate, that is that it is held in place by chemical bonding, then the confinement of any electrons that are injected into the wire is far from assured. Using the same estimation approach as before, and assuming that forming a chemical bond costs 1 eV, then a typical residence time for an electron in the molecule would be of order  $\sim 10^{-16}$ s, two orders of magnitude smaller than the physisorbed case. This also seems to be a potential problem for self-assembled wires, which are often strongly bonded to the surface and can be stable at room temperature. One has to look at the charge distribution of states that are close to the Fermi level and are strongly associated with the wire to see whether they are constrained to the wire or are free to disperse into the bulk.

We have discussed in general terms how at the nanoscale the behaviour of electrons can differ from ordinary experience and how we can fabricate devices that can function at the atomic scale. We have discussed prospective atomic scale wires that could feed current in and out of these devices (atomic scale electronics). We now need to consider in more detail what theoretical concepts are useful to study the conductivity of atomic scale wires and what methods we can use to simulate prospective atomic scale wires.

## 1.4 Theoretical concepts

At the atomic scale, the properties of materials can differ from their bulk properties. For instance, it has been reported that a one atomic layer thick film of gold on the titanium(110) surface is not metallic but a semiconductor. Another example is a Peierls distortion [113], an effect which can change the electronic structure of one-dimensional structures and so is of obvious relevance to atomic scale wires [18, 59, 95].

Let us start off by considering a linear chain of atoms, all equally spaced apart by a distance  $a$ . This means that all multiples of  $a$  are lattice vectors, and that the unit cell in reciprocal space is

$$-\frac{\pi}{a} \leq k \leq \frac{\pi}{a} \quad (1.8)$$

and that the energy as a function of  $k$  would be a smooth cosine function if a simple tight-binding model is appropriate (see Figure 1.10).

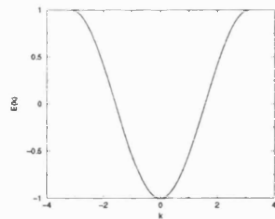


Figure 1.10: Plot of energy as a function of wavevector for a regular undimerised atomic chain.

Now suppose that we displace an atom slightly, with the pattern of each displacement repeating every  $r$ th atom (i.e., every  $i$ th atom out of  $r$  atoms is moved slightly in the same direction). The translational symmetry of the linear chain is immediately reduced, and that instead of having a unit cell containing one atom and having a lattice vector of  $a$ , each unit cell now contains  $r$  atoms and has a lattice vector of  $ra$ . The cell in reciprocal space is now

$$-\frac{\pi}{ra} \leq k \leq \frac{\pi}{ra} \quad (1.9)$$

The effect of such a perturbation is to change the function  $E(k)$ . For the specific case of

$r=2$  this has the effect of causing vertical breaks to occur at the Fermi surface, caused by the coupling between the filled and empty states. This separates any two eigenvalues at the Fermi surface which are close to each other (see Figure 1.11). If the pair of states at the Fermi level are partially occupied in the ideal case (a metal), then following any distortion one of the states will be displaced downwards in energy and will become occupied and the state which is displaced upwards in energy will become unoccupied. The metal will become a semiconductor.

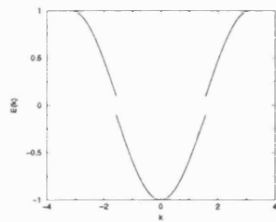


Figure 1.11: Plot of energy as a function of wavevector for a dimerised semimetallic chain.

It follows that for a one-dimensional metal with a partly filled band a regular chain structure will never become stable, as it is always possible to find a distortion with a suitable value of  $r$  for which a band gap will open up at or near the edge of the Fermi distribution. To maximise the gain of energy, and hence the distortion,  $r$  has to be small number, unless there are other metallic bands or strong correlation effects. Neglecting these factors the favourable case is that in which the Fermi distribution ends at  $k = \pi/2a$ . This means that there is one electron per atom, including spin. This means that  $r = 2$ , and that there is a regular bond alternation, or dimerisation, which is observed to occur in (for example) polyacetylene. The Peierls distortion is an electronic effect that is associated with the top of the valence band/bottom of the conduction band, and which can be represented as a sum of different phonon modes. Thus if we inject an electron (or hole) into the system we would change the physical structure of the system as this would change the electronic structure at the bottom of the conduction band (top of the valence band). We can thus say that the Peierls distortion increases the magnitude of electron-phonon coupling.

If we just included electronic effects, then it would seem that the way to maximise the gain in energy would be to have two vastly different bonds, one with a very long (or infinite) bond length, the other with a very small (or zero) bond length. We need to balance the gain in electronic energy with the loss in elastic energy, so that the equilibrium

deformation  $u_0$  is given by the roots of

$$\frac{d}{du_0}(E_{\text{electronic}} + E_{\text{elastic}}) = 0. \quad (1.10)$$

There are two values of  $u_0$ . Thus there are *in extremis* two cases [114].

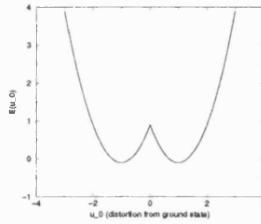


Figure 1.12: Twofold degeneracy of energy.

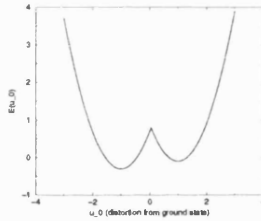


Figure 1.13: Near-twofold degeneracy of energy.

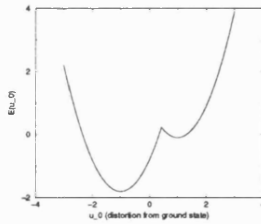


Figure 1.14: Near-onfold degeneracy of energy.

Firstly if the two values are exactly equal then the ground state of the one-dimensional metal is twofold degenerate (see Figure 1.12). That is that we can have two identical bond alternation patterns,  $1=2-3=4-5=6-7=8-9=10$ , and  $1-2=3-4=5-6=7-8=9-10$ , where  $-$  signifies a long bond and  $=$  signifies a short bond. This doubly degenerate ground state supports nonlinear excitations which can act as moving domain walls separating different phases. That is, in the chain it is possible to have two phases A ( $+u_0$ ) and B ( $-u_0$ ). These phases are shape-preserving excitations, thus they are called solitons [115].

Each phase has its own dimerisation parameter, one positive, the other negative. Where the two phases meet, the dimerisation will change sign (see Figure 1.15). This can be represented as  $a-a=a-a-a-X-b=b=b=b-b$ , where  $X$  is the discontinuity (see Figure 1.16).

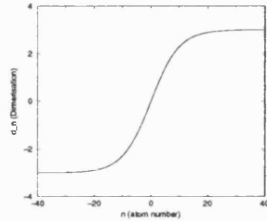


Figure 1.15: The dimerisation profile of a soliton.

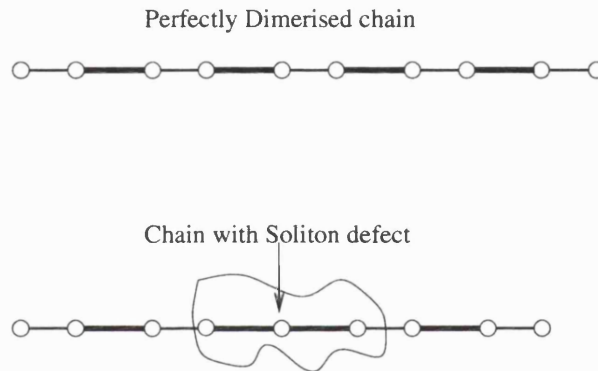


Figure 1.16: Structure of a soliton in a chain.

In the limit of a long chain, a soliton corresponds to a phonon field configuration that approaches the B phase as  $N \rightarrow \infty$ , approaches the A phase as  $N \rightarrow -\infty$ , and minimises the total energy. The width of a soliton  $\zeta$  depends on the competition of two effects, the electronic energy and the elastic energy per site. If the soliton is very narrow, then the sudden change in  $d_n$  from the  $-u_0$  to  $+u_0$  state (at  $n=0$  say) will cause the electronic energy to be large because of the uncertainty principle. If however,  $d_n$  changes very slowly from the  $-u_0$  state to the  $+u_0$  state, there will be a large region surrounding  $n=0$  where the elastic energy is greatly reduced again raising the energy [18].  $\zeta$  is the width of the soliton that minimises the the total energy. If  $\zeta$  is large compared to the average lattice spacing  $a$ , then as the soliton moves relative to the lattice the variation of the energy is small. This large soliton width also means that the soliton has an extremely small effective mass, of the order of an electron mass rather than an ionic mass. This means that if an electron (or hole) is injected into the chain then it would be energetically preferable for the charge to be transported along the chain as a soliton rather than as

a free electron as the effective mass is so much smaller. Note that as a moving soliton changes A-phase material to B-phase material and vice versa, that injected solitons can only be created or destroyed in pairs.

The presence of a soliton in the chain also affects the electronic spectrum. For each widely separated soliton there exists a normalised single-electron state of zero energy in the gap centre which can accommodate zero, one or two electrons and that has an extent of order  $\zeta$ . For a neutral soliton this state is singly occupied by an electron. Therefore we have a case where the neutral soliton has a spin of  $\frac{1}{2}$ . We would expect a spin  $\frac{1}{2}$  particle to have a charge of  $\pm e$ . Conversely when the soliton is charged the occupancy of the band gap state is 0 or 2 electrons, which means that it is carrying  $\pm e$  and has a spin of zero. This means that the soliton has reversed spin-charge relations.

Solitons have been observed to form in two ways, either by doping or by initial chain conditions. It has been observed that doping trans-polyacetylene with sodium ions leads to the spontaneous creations of solitons in the chain. Solitons are also formed naturally if the polyacetylene chain consists of an odd number of monomers. This would mean that one end of the chain would end in a single bond and the other end of the chain would end in a double bond. Polyacetylene would rather have a double bond at both ends of the chain, so a soliton is formed at one end of the chain and travels to the centre. Thus for odd numbered chains a soliton is formed in the ground state. It is possible to form a soliton-antisoliton pair  $S\bar{S}$  from an electron-hole pair. Functionally this pair resembles a *polaron* which is explained below.

For the more general case that the two values of  $u_0$  are nondegenerate (see Figures 1.13 and 1.14), the dominant charge carriers and excitations are polarons. A polaron is an electron-phonon excitation, in which the interaction of the electron with phonons allows the electron to be surrounded by a strain field and the movement of the electron is matched by the movement of the strain field. This has the effect of increasing the apparent mass of the electron [116]. Compared to the solitons considered previously, the formation of a polaron in the chain does not change the value of the dimerisation far away from the defect. The presence of a polaron merely induces a reduction in the local dimerisation (see Figure 1.17). There thus exist the following symmetries for the dimerisation  $d$  of the chain as a function of  $x$  when the defect (polaron or soliton) is at

$x_0$

$$d_P(-[x - x_0]) = d_P(x - x_0) \quad (1.11)$$

$$d_S(-[x - x_0]) = -d_S(x - x_0). \quad (1.12)$$

A polaron has two bound states associated with it and separated from the valence

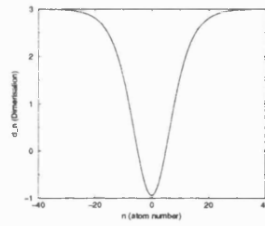


Figure 1.17: Dimerisation profile of a polaron.

band and the conduction band. This means that the formation of a polaron leads to a suppression of the band gap. A neutral polaron has two electrons in the lower state and none in the upper state. Conversely a hole polaron has only one state in the lower state and an electron polaron has two electrons in the lower state and a single electron in the upper state.

Polarons are also capable of being formed in metallic chains with exact ground state degeneracy. However, only one polaron at a time can exist in these chains, as the injection of a second electron/hole causes the breakup of the polarons and the formation of two solitons [18]. More generally if there is no exact degeneracy then it is possible for the two polarons to form an ordered pair known as a bipolaron.

The formation of either a polaron or a soliton will cause a deformation in the metallic chain as mentioned above, which can be represented as the action of a set of phonon modes. Not all phonon modes contribute an equal amount of energy to the distortion of the chain however. What is needed is a measure of how much a particular phonon modes contributes to the distortion. The strength of this phonon coupling is measured by the dimensionless Huang-Rhys constant [116, 117, 118]

$$S_{\text{ab}} = \frac{\text{deformation energy}}{\hbar\omega_q} = \frac{\frac{1}{2}M\omega_q^2(Q_{\text{a0}} - Q_{\text{b0}})^2}{\hbar\omega_q} = \frac{(Q_{\text{a0}} - Q_{\text{b0}})^2}{2(\hbar/M\omega_q)} \quad (1.13)$$

where  $\omega_q$  is the frequency of the phonon mode and  $(Q_{\text{a0}} - Q_{\text{b0}})$  is the change in displacement of lattice and  $q$  is the phonon mode. The stronger the value of the Huang-Rhys constant the stronger that phonon mode couples to the distortion (it is in a sense a measure of the electron-phonon coupling). The sum over all phonon modes should give an energy that is equal to the distortion energy caused by the soliton or polaron.

## 1.5 Concluding remarks

We have discussed the theoretical concepts that apply to devices that function at the nanoscale, including such ideas as mean free path, phase relaxation length, Peierls distortion and soliton/polaron formation. However we have not yet discussed how we would model the structure of atomic scale devices, or how once we have found the structure we would calculate the transport properties of such a device. An overview of the methods used to find the structural and electronic properties is given in the next chapter.

After we discuss the various theoretical methods used in this thesis, we then discuss three candidate atomic scale wires; the polyacetylene molecule, the silicon line on the  $\beta$ -SiC(001) surface and the  $(4\times 1)$ -Si(111)-In reconstruction. We do not calculate the conductivity characteristics of the polyacetylene molecule, rather we use the example of polyacetylene to sketch how we can calculate information that is used to calculate the conductivity for the other two candidate atomic scale wires and provide only a sketch of the conductivity characteristics of the polyacetylene molecule. For the other two atomic scale lines we show how we find the correct atomic and electronic structure, and then find the transport properties (although for the case of the indium-based reconstruction we can provide only a brief overview of the transport properties). We will then conclude this thesis with a discussion of further work that can be performed on the two systems.

# Chapter 2

## Theory

In this Chapter we detail the various theoretical methods used in this study, the techniques we used to find the physical and electronic structure of the candidate atomic scale wires and the methodology of calculating the conductivity of these atomic scale wires.

### 2.1 Modelling systems: Density Functional Theory

#### 2.1.1 Introduction

The description of many-particle systems is an important goal in contemporary condensed matter physics. Although analytic solutions of the Schrödinger equation are possible for a few simplified systems such as isolated atoms and simple molecules, it is not possible to find the exact analytic solution for complex systems due to the complicated electron-electron interactions. Instead, one is forced to rely on numerical schemes that can solve the Schrödinger equations for such systems. Although it is possible to use a Hartree-Fock scheme to find the ground state of a system, using Slater determinants to account for Fermi statistics [119, 120, 121] and configuration-interaction for the correlation effects [122], the large increase in the number of configurations with increasing electron number means that systems with a large number of electrons are unable to be modelled to a high degree of accuracy. For instance using a modern workstation it is only possible to model a cluster of approximately twenty atoms as storage of the various orbitals and permutations of orbitals requires orders of magnitude more CPU memory than any of the other techniques mentioned below. Although Hartree-Fock with Configuration-Interaction (HF-CI)

is computationally very expensive it does possess an advantage that none of the other methods discussed below possess, HF-CI can accurately calculate the electronic structure of excited states as well as ground states. No other electronic structure method can accurately calculate all excited states, although Density Functional Theory (also known as DFT, see below) can calculate some of these states [123, 124].

No other numerical technique (apart from HF-CI) models the ground state electronic structure of solids from first principles as accurately as Density Functional theory (DFT) (also known as *ab initio* DFT). This theory maps the ground state of an interacting electron gas onto the ground state of a noninteracting electron gas which experience an effective potential.

The Hamiltonian that describes the electrons is

$$\hat{H} = \hat{T} + \hat{V}_{ee} + \sum_{i=1}^N V_{ext}(r_i) \quad (2.1)$$

where  $\hat{T}$  and  $\hat{V}_{ee}$  are the kinetic and electron-electron interaction operators respectively and  $V_{ext}$  is the external potential the electrons move in.

The two basic theorems of DFT are

1. That there exists a functional  $F[n]$  of the electronic density  $n$  that represents the ground state energy  $E_{GS}$ . That is that  $E_{GS}$  is a functional of  $n$  ( $F[n] = \langle \hat{T} + \hat{V}_{ee} \rangle$ ). This is the existence theorem [125, 126].
2. That the only density which gives an energy equal to the energy of the ground state is the electronic density of the ground state  $n_{GS}$

$$\int dr V_{ext}(\mathbf{r})n_{GS}(\mathbf{r}) + F[n_{GS}] \equiv E_{GS}. \quad (2.2)$$

All other densities give ground state energies with a higher energy than the true ground state energy. The true electronic ground state can be found by a Levy-constrained search

$$F[n] \equiv_{\Psi \rightarrow n} \langle \Psi | \hat{T} + \hat{V}_{ee} | \Psi \rangle \quad (2.3)$$

This is the uniqueness theorem [125, 127].

$E[n]$  thus satisfies a variational principle.

We can use a separation of the Hamiltonian first devised by Kohn and Sham [120, 127], wherein we can write the energy as a sum of a set of functionals that depend on electron density

$$E[n] = T_0[n] + \int dr n(\mathbf{r})[V_{\text{ext}}(\mathbf{r}) + \frac{1}{2}\Phi(\mathbf{r})] + E_{\text{xc}}[n] \quad (2.4)$$

where  $T_0$  is the kinetic energy of a system with density  $n$  if there is no electron-electron interaction,  $\Phi$  is the classical Coulomb potential and  $E_{\text{xc}}$  is the exchange and correlation energy. There is no simple expression for the exchange and correlation energy. The exchange energy is the contribution to the energy that results from the Pauli principle, that no two electrons can have the same energy and have the same state (only electrons with opposite spins can fully occupy a state). This can be written analytically. The correlation energy cannot be written analytically. It is defined to be the difference in energy between the true ground state energy and the Hartree-Fock ground state energy.

The exchange and correlation energies thus depend on the electronic density  $n$ , which means that the energy as a functional of density depends in a nonlinear way on the density  $n$ , and what is worse is that we have no idea how  $E_{\text{xc}}[n]$  behaves. We are in the position of not knowing how to solve such complicated equations with so little data. The common way of solving the variational equations (2.4) is to make an approximation, the Local Density approximation (LDA) [128]. This approximation assumes that the exchange-correlation potential that an electron in a system experiences is equal to the exchange-correlation potential of an electron in a uniform gas of interacting electrons and can be inserted into the above equation as

$$E_{\text{xc}}^{\text{LDA}} = \int dr n(\mathbf{r})\epsilon_{\text{xc}}[n(\mathbf{r})] \quad (2.5)$$

where  $\epsilon_{\text{xc}}[n]$  is the exchange-correlation energy density of a homogeneous electron gas of density  $n$ . As the real world consists of a gas of electrons which are non-homogeneous, this would not seem to be a reasonable approximation. It is thus required that this approximation is used only when the electronic density varies only slowly with distance.

And yet it has been used on a large variety of systems and seems to work surprisingly well. Why is this?

### 2.1.2 The validity of the LDA

The exchange-correlation energy density can be written as [122]

$$E_{xc}[n] = \frac{e^2}{2} \int d^3r d^3r' n(\mathbf{r}) \frac{[\tilde{g}(\mathbf{r}, \mathbf{r}') - 1]}{|\mathbf{r} - \mathbf{r}'|} n(\mathbf{r}'). \quad (2.6)$$

The function  $\tilde{g}(\mathbf{r}, \mathbf{r}')$  is obtained by replacing the electron-electron interaction constant  $e^2$  by  $e^2\lambda$  and integrating over  $\lambda$

$$\tilde{g}(\mathbf{r}, \mathbf{r}') = \int_0^1 d\lambda g(\mathbf{r}, \mathbf{r}'; \lambda). \quad (2.7)$$

The function  $g(\mathbf{r}, \mathbf{r}'; \lambda)$  is the pair correlation function of the system with density  $n(\mathbf{r})$  and Coulomb interaction  $\lambda V_{ee}$ , i.e., it describes the response of the electron gas at  $\mathbf{r}$  due to a perturbation at  $\mathbf{r}'$ . The function  $n(\mathbf{r}')[g(\mathbf{r}, \mathbf{r}') - 1]$  describes the depletion in density due to the exchange-correlation hole around an electron at position  $\mathbf{r}$ . The quantity  $n(\mathbf{r}')[\tilde{g}(\mathbf{r}, \mathbf{r}') - 1]$  does the same with respect to  $\lambda$ . (2.6) is appealing as it allows us to formulate all approximations for  $E_{xc}[n]$  as ones for  $\tilde{g}(\mathbf{r}, \mathbf{r}')$ . The LDA can thus be represented as

$$n(\mathbf{r}')[\tilde{g}(\mathbf{r}, \mathbf{r}') - 1] \rightarrow n(\mathbf{r})[\tilde{g}_h(\mathbf{r} - \mathbf{r}'; n(\mathbf{r}')) - 1]. \quad (2.8)$$

This lets us see that the density depletion due to the exchange-correlation hole around an electron corresponds to exactly one particle, and this is independent of electron-electron coupling. This rule holds even for the LDA as  $n(r)[\tilde{g}_h(\mathbf{r} - \mathbf{r}') - 1]$  satisfies it. Equation (2.6) also shows that only a particular angular average of the pair-distribution function is involved with the calculation of  $E_{xc}[n]$ . Thus if we introduce the relative coordinate  $\mathbf{R} = \mathbf{r}' - \mathbf{r}$  then (2.6) can be written as

$$E_{xc}[n] = \frac{e^2}{2} \int d^3r n(\mathbf{r}) \int_0^\infty dR R n_{xc}(\mathbf{r}, R) \quad (2.9)$$

where

$$n_{xc}(\mathbf{r}, R) = \int d\Omega_{\mathbf{R}} n(\mathbf{r} + \mathbf{R}) [\tilde{g}(\mathbf{r}, \mathbf{r} + \mathbf{R}) - 1]. \quad (2.10)$$

The only part of the exchange-correlation hole that enters into the calculation of  $E_{xc}[n]$  is the spherically symmetric part. This is the key to the question of why should the LDA work as well as it does? The answer is that although the correct exchange-correlation energy density is non-symmetric,  $E_{xc}$  is only sensitive to the angular average of energy density. The average of the true exchange correlation energy density is symmetric and the LDA gives an energy density which is spherically symmetric as well and thus gives a very good agreement with the true non-symmetric exchange-correlation energy.

Finally when can we expect the LDA to work well? If we look at (2.9) and consider the integral

$$\int d^3R \frac{n_{xc}(\mathbf{r}, R)}{R} = - \left\langle \frac{1}{R} \right\rangle. \quad (2.11)$$

This describes the inverse extension of the exchange correlation hole. If this is approximated correctly then one would expect the LDA to work well. As a condition on the use of the LDA this is much less stringent than a requirement that the electronic density vary slowly.

### 2.1.3 Varieties of DFT method

There are various methodologies that have been developed to solve the one-particle Schrödinger equation of the LDA. There are three main classes: (i) the linear methods [129] developed by Andersen from the augmented-plane-wave (APW) method [130, 131], (ii) the pseudopotential method based on norm-conserving *ab initio* pseudopotentials invented by Hamann, Schlüter and Chiang [132] and (iii) the Gaussian basis set method, where Gaussians are used to expand the full-wavefunctions (the Gaussian methods are

mostly used by chemists, and although they embody the chemistry of the system, they do not describe surface states quite as well). The Gaussian method will not be expanded upon.

The linear methods deal with the full wavefunctions and can treat all elements in the periodic table, i.e.  $s$ -,  $p$ -,  $d$ - and  $f$ -electron systems equally. They range from the Linear Augmented-Plane-Wave method (LAPW) as the most accurate, to the Linear Muffin-Tin Orbital (LMTO) method as the most simplistic (in a simplified version, the LMTO method can be performed on *paper!*, allegedly).

The pseudopotential approach is based upon the realisation that the only part of the wavefunction  $\psi$  that is important in the binding of atoms is the part of  $\psi$  that is far away from the core of the atom. Near the core of the atom, the potential is strong enough to have bound ‘core’ levels. If we chose to expand  $\psi$  in terms of plane waves then the higher wavefunctions must be orthogonal to the lower wavefunctions, and the higher wavefunctions cannot have correctly converged energy eigenvalues until the lower wavefunctions are converged [133]. Thus if we are interested in the properties of the wavefunctions of the  $2p$  set of orbitals we also have to converge the wavefunctions for the  $1s$  and  $2s$  set of orbitals. As the  $1s$  state is so highly localised it requires a large number of plane waves to represent it. This is computationally very expensive. Can we avoid making such detailed calculations? The answer is yes as there does exist such a technique: the pseudopotential approach.

Instead of trying to solve the full Schrödinger equation

$$(\hat{T} + V_{\text{true}})\psi = E\psi \quad (2.12)$$

over all energies we can try and solve a Schrödinger equation accurately for a range of energies that are in the region of interest

$$(\hat{T} + V_{\text{pseudo}})\psi = E_{\text{range}}\psi. \quad (2.13)$$

$V_{\text{pseudo}}$  is the pseudopotential that for the energy range of interest gives energy eigenvalues that are identical with those of the true potential  $V_{\text{true}}$ . As the bands of interest (ones

involved with bonding) are quite low in energy then the potential that is needed to describe them is quite weak. The pseudopotential is created that gives the right scattering properties at low energies but gives the wrong scattering properties at high energies. The complicated potential at the core region is ‘smoothed off’ to give a pseudopotential which is much more amenable to analysis.

When the pseudopotential is used in combination with a plane-wave basis set it has the advantage of formal simplicity. However, if applied to systems with  $d$ - or  $f$ - electrons, pseudopotentials can become ‘hard’, so that either very large plane wave basis sets or very complicated basis sets have to be used which are not easily transferable. This is because of the norm-conservation condition [132, 134] that is required in order to make the obtained pseudo wavefunctions identical to the true wavefunctions. This requires that the total pseudocharge that is inside the core match that of the true wavefunction. This makes the core strongly repulsive, or “hard core” which means that it becomes impossible to construct a pseudowavefunction that is much smoother than the true wavefunction (i.e., such as O  $2p$  or Ni  $3d$  orbitals). If one relaxes the norm-conservation rule, then one can create ultra-soft pseudopotentials [135] that significantly improve the situation by increasing the size of the core region.

The ultrasoft pseudopotentials are created in the following way. We start with some all electron (AE) wavefunction that is found for a free atom. Cutoff radii  $r_{cl}$  and  $r_c^{loc}$  are chosen for the wavefunction and the local potential respectively and a radius  $R$  is chosen beyond which pseudo- and AE wavefunctions agree. AE wavefunctions  $\psi_i$  can solve the Schrödinger equation

$$(T + V_{AE} - \epsilon_i) |\psi_i\rangle \quad (2.14)$$

and a pseudowavefunction  $\phi_i$  is constructed that smoothly joins onto  $\psi_i$  outside  $r_{cl}$  and satisfies the norm conserving property  $\langle \phi_i | \phi_i \rangle_R = \langle \psi_i | \psi_i \rangle_R$ . A local wavefunction is also constructed

$$|\chi_i\rangle = (\epsilon_i - T - V_{loc}) |\phi_i\rangle. \quad (2.15)$$

The set of pseudowavefunctions  $|\phi_i\rangle$  can be generated from the AE wavefunctions  $|\psi_i\rangle$  with the condition that they obey the generalized norm-conserving condition  $Q_{ij}=0$ , where

$$Q_{ij} = \langle \psi_i | \psi_i \rangle_R - \langle \phi_i | \phi_i \rangle_R. \quad (2.16)$$

If we form the matrix  $B_{ij} = \langle \phi_i | \phi_j \rangle$  we can define a set of local wavefunctions

$$|\beta_i\rangle = \sum_j (B^{-1})_{ji} |\chi_j\rangle. \quad (2.17)$$

Using this set of local wavefunctions we can remove the condition on  $Q_{ij}$  by creating a nonlocal overlap operator

$$S = 1 + \sum_{ij} Q_{ij} |\beta_i\rangle \langle \beta_j| \quad (2.18)$$

which makes

$$\langle \phi_i | S | \phi_j \rangle_R = \langle \psi_i | \psi_j \rangle_R. \quad (2.19)$$

This means that the only constraint on  $\psi_i$  and  $\phi_i$  is for the matching of the two wavefunctions at the cutoff radius. We thus have the freedom of taking the cutoff radius to be well beyond the radial wavefunction maximum which means that it is now possible to perform computationally cheap simulations on atomic systems that would normally require a “hard core” pseudopotential, that is first-row and transition metal systems.

Another method that has been developed that bridges the divide between the LAPW methods and the pseudopotential methods (that combines the versatility of LAPW with the formal simplicity of pseudopotentials) is the Projector Augmented Wave method (or PAW method) [136]. In fact it has been shown that the LAPW method is a special case of the PAW method, and that the pseudopotential method is obtained by a well-defined approximation[136]. We have used the PAW method to perform the various *ab initio*

DFT calculations we have performed, and will provide the details of the PAW method in the next section.

#### 2.1.4 The PAW method: Wavefunctions

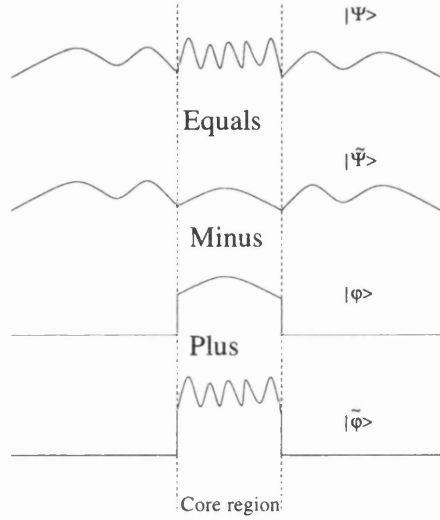


Figure 2.1: Schematic of the PAW scheme.

The main idea of the PAW method [136] is to split the all-electron (AE) wavefunction into three parts;

$$|\Psi\rangle = |\tilde{\Psi}\rangle + \sum_i (|\phi_i\rangle - |\tilde{\phi}_i\rangle) \langle \tilde{p}_i | \tilde{\Psi} \rangle. \quad (2.20)$$

$|\Psi\rangle$  is the AE wavefunction and  $|\tilde{\Psi}\rangle$  is a pseudo (PS) wavefunction analogous to the wavefunctions of the pseudopotential method, or the envelope functions of the linear method.  $|\phi_i\rangle$  are a set of AE partial waves within some core region, while  $|\tilde{\phi}_i\rangle$  are a set of smooth partial waves which coincide with the corresponding AE partial waves outside the core region.  $|\tilde{p}_i\rangle$  are projector functions localised within the core region which obey the relation  $\langle \tilde{p}_i | \tilde{\phi}_j \rangle = \delta_{ij}$ . As has been demonstrated previously there is thus a close connection to the ultrasoft pseudopotentials of Vanderbilt [135].

The AE wavefunction above is obtained by applying a transformation  $T$  to the PS wavefunction. This transformation is defined to act only on a region  $\Omega_R$  which encloses a volume around an atom. The transformation is

$$\hat{T} = 1 + \sum_R \hat{T}_R. \quad (2.21)$$

Within the augmentation region, every PS wavefunction can be expanded into a set of partial waves

$$|\tilde{\Psi}\rangle = \sum_i |\tilde{\phi}_i\rangle c_i. \quad (2.22)$$

As  $|\phi_i\rangle = \hat{T}|\tilde{\phi}_i\rangle$ , the corresponding AE wavefunction is of the form

$$|\Psi\rangle = \hat{T}|\tilde{\Psi}\rangle = \sum_i |\phi_i\rangle c_i \quad (2.23)$$

with identical coefficients  $c_i$ . This means that the linear transformation  $\hat{T}$  is defined as

$$\hat{T} = 1 + \sum_i \left( |\phi_i\rangle - |\tilde{\phi}_i\rangle \right) \langle \tilde{p}_i|. \quad (2.24)$$

Thence the full AE wavefunction can be expressed as

$$|\Psi\rangle = |\tilde{\Psi}\rangle + \sum_i \left( |\phi_i\rangle c_i - |\tilde{\phi}_i\rangle c_i \right) \quad (2.25)$$

As  $\hat{T}$  is linear, the coefficients are scalar products

$$c_i = \langle \tilde{p}_i | \tilde{\Psi} \rangle \quad (2.26)$$

of the PS wavefunctions with some fixed functions  $\langle \tilde{p}_i |$  which are called projector functions. We can then use this relation to obtain the full AE wavefunction as shown above.

### 2.1.5 The PAW method: Operators and energies

As the PS wavefunctions play the role of the variational parameters (instead of the AE wavefunctions) we need to be able to obtain observable quantities as the expectation values of the PS wavefunctions. Our representations of the wavefunctions have been changed, so we need to transform our operators into new ‘PS operators’. If we have some operator  $A$  that has an expectation value  $\langle A \rangle = \sum_n f_n \langle \Psi_n | A | \Psi_n \rangle$  where  $n$  is the band index and  $f_n$  is the occupation of the state, then the PS operator is  $\langle A \rangle = \sum_n f_n \langle \tilde{\Psi}_n | \tilde{A} | \tilde{\Psi}_n \rangle$ . For quasilocal operators such as  $-\nabla^2/2$  and  $|r\rangle\langle r|$ , which are needed to calculate the total energy and charge density, the PS operator has the form

$$\tilde{A} = T^\dagger A T = A + \sum_{ij} |\tilde{p}_i\rangle \left( \langle \phi_i | A | \phi_j \rangle - \langle \tilde{\phi}_i | A | \tilde{\phi}_j \rangle \right) \langle \tilde{p}_j|. \quad (2.27)$$

To arrive at this expand  $\hat{T}$  using (2.24) and delete terms that cancel as  $\sum_i |\tilde{\phi}_i\rangle\langle \tilde{p}_i| = 1$  within  $\Omega_R$  and  $|\tilde{\phi}_i\rangle = |\phi_i\rangle$  outside the augmentation region, remembering that the only terms which contribute are the on-site ones.

To then find the charge density we use a similar approach as to describe (2.27). The charge density at a point  $\mathbf{r}$  is the expectation value of the real space projection operator  $|r\rangle\langle r|$ . We can divide the charge density like so

$$n(\mathbf{r}) = \tilde{n}(\mathbf{r}) + n^1(\mathbf{r}) - \tilde{n}^1(\mathbf{r}) \quad (2.28)$$

where

$$\tilde{n}(\mathbf{r}) = \sum_n f_n \langle \tilde{\Psi}_n | r \rangle \langle r | \tilde{\Psi}_n \rangle, \quad (2.29)$$

and

$$n^1(\mathbf{r}) = \sum_{n,(i,j)} f_n \langle \tilde{\Psi}_n | \tilde{p}_i \rangle \langle \phi_i | r \rangle \langle r | \phi_j \rangle \langle \tilde{p}_j | \tilde{\Psi}_n \rangle, \quad (2.30)$$

and

$$\tilde{n}^1(\mathbf{r}) = \sum_{n,(i,j)} f_n \langle \tilde{\Psi}_n | \tilde{p}_i \rangle \langle \tilde{\phi}_i | r \rangle \langle r | \tilde{\phi}_j \rangle \langle \tilde{p}_j | \tilde{\Psi}_n \rangle. \quad (2.31)$$

Note that  $n^1$  contains the contribution of the core states  $\sum_n \langle \phi_n^c | r \rangle \langle r | \phi_n^c \rangle$  and that  $\tilde{n}^1$  and  $\tilde{n}$  contain the contribution of the PS states ( $\tilde{\phi}_n^c$  and  $\tilde{\Psi}_n^c$  respectively). We do not construct a PS core state for each state separately, but rather construct a PS core density.

The total energy functional

$$E = \sum_n f_n \langle \Psi_n | -\frac{1}{2} \nabla^2 | \Psi_n \rangle + \frac{1}{2} \int dr \int dr' \frac{(n + n^Z)(n + n^Z)}{|\mathbf{r} - \mathbf{r}'|} + \int dr n \epsilon_{xc}(n) \quad (2.32)$$

can also be divided in a similar way to the charge density:  $E = \tilde{E} + E^1 - \tilde{E}^1$ .  $\tilde{E}$  is evaluated in regular grids in Fourier (or real space) and  $E^1$  and  $\tilde{E}^1$  are one-centre contributions which are evaluated in radial grids in an angular momentum representation. The charge density of the nucleus is denoted by  $n^Z$  and the exchange and correlation energy by  $\epsilon_{xc}$ . The three contributions are

$$\begin{aligned} \tilde{E} &= \sum_n f_n \langle \tilde{\Psi}_n | -\frac{1}{2} \nabla^2 | \tilde{\Psi}_n \rangle \\ &+ \frac{1}{2} \int dr \int dr' \frac{(\tilde{n} + \hat{n})(\tilde{n} + \hat{n})}{|\mathbf{r} - \mathbf{r}'|} + \int dr \tilde{n} \bar{v} + \int dr \tilde{n} \epsilon_{xc}(\tilde{n}) \end{aligned} \quad (2.33)$$

$$\begin{aligned} E^1 &= \sum_{n,(i,j)} f_n \langle \Psi_n | \tilde{p}_i \rangle \langle \phi_i | -\frac{1}{2} \nabla^2 | \phi_j \rangle \langle \tilde{p}_j | \tilde{\Psi}_n \rangle \\ &+ \frac{1}{2} \int dr \int dr' \frac{(n^1 + n^z)(n^1 + n^z)}{|\mathbf{r} - \mathbf{r}'|} + \int dr n^1 \epsilon_{xc}(n^1) \end{aligned} \quad (2.34)$$

$$\begin{aligned} \tilde{E}^1 &= \sum_{n,(i,j)} f_n \langle \Psi_n | \tilde{p}_i \rangle \langle \tilde{\phi}_i | -\frac{1}{2} \nabla^2 | \tilde{\phi}_j \rangle \langle \tilde{p}_j | \tilde{\Psi}_n \rangle \\ &+ \frac{1}{2} \int dr \int dr' \frac{(\tilde{n}^1 + \hat{n})(\tilde{n}^1 + \hat{n})}{|\mathbf{r} - \mathbf{r}'|} + \int dr \tilde{n}^1 \bar{v} + \int dr \tilde{n}^1 \epsilon_{xc}(\tilde{n}^1). \end{aligned} \quad (2.35)$$

The potential  $\bar{v}$  is an arbitrary potential located in the augmentation region. It has no

contribution to the total energy as  $\tilde{n} = \tilde{n}^1$  within the region. The  $\hat{n}$  is the compensation charge density and is introduced so that the difference in the AE and PS one-centre contributions  $(n^1 + n^Z) - (\tilde{n} + \hat{n})$  to the charge density has vanishing electrostatic multipole moments and thus no longer interacts with charges outside the augmentation region.

This compensation charge density is of the form  $\hat{n} = \sum_R \hat{n}_R$  with

$$\hat{n}_R(\mathbf{r}) = \sum_L g_{RL}(\mathbf{r}) Q_{RL} \quad (2.36)$$

and is expressed as a sum of generalised Gaussians

$$g_{RL}(R) = C_l |\mathbf{r} - R|^l Y_L(\mathbf{r} - R) e^{-(|\mathbf{r} - R|/r_c)^2} \quad (2.37)$$

each of which is normalised so that its multipole moment is unity.

We finally need to evaluate the exchange-correlation energy for a one-centre expansion. We expand the energy density in the deviation of the one-centre charge density from its spherical part  $n_{R,l=0}^1$

$$\begin{aligned} \int dr n_R^1 \epsilon_{xc}(n_R^1) &= \int dr n_{R,l=0}^1 \epsilon_{xc}(n_{R,l=0}^1) \\ &+ \frac{1}{2} \sum_{L,l \neq 0} \int dr \frac{\partial \mu_{xc}(n_{R,l=0}^1)}{\partial n_R^1} (n_{R,L}^1)^2 + O((n_{R,L}^1)^3), \end{aligned} \quad (2.38)$$

where  $\mu_{xc}(n) = d[n\epsilon_{xc}(n)]/dn$ . A Taylor expansion up to second order is usually sufficient [137]. The PS charge density is treated identically.

To find the forces that are acting on each atom we use the Hellman-Feynman theorem [138, 139, 140], where the force on each atom can be reduced to

$$\frac{dE}{d\lambda} = \left\langle \Psi \left| \frac{\partial H}{\partial \lambda} \right| \Psi \right\rangle / \langle \Psi | \Psi \rangle + \left[ \left\langle \Psi | H - E | \frac{\partial \Psi}{\partial \lambda} \right\rangle + \left\langle \frac{\partial \Psi}{\partial \lambda} | H - E | \Psi \right\rangle \right] / \langle \Psi | \Psi \rangle. \quad (2.39)$$

If the eigenstates are exact, the Born-Oppenheimer approximation is in use or a plane wave basis set is used then only the first term in (2.39) is used (the Hellman-Feynman force). Otherwise all of the terms in (2.39) are used (the Hellman-Feynman force and

the Pulay force corrections).

We have mentioned that DFT is an accurate *ab initio* numerical method which is available for finding the electronic structure of a solid. However, with accuracy comes complexity. In full *ab initio* DFT one needs to calculate the potentials and energies self-consistently, and if this includes exchange and correlation terms this can become quite time consuming. Is there a method available which gives results which are almost as accurate as the results given by DFT but which is far less expensive in terms of time and computer power? The answer is yes, the *tight-binding* methodology.

## 2.2 Modelling systems: Tight-Binding

In the tight-binding formalism, we can expand the eigenstates of the Hamiltonian in terms of an atomic-like basis set,  $\phi_\mu$ , and we can replace the exact Kohn-Sham Hamiltonian with a parameterised Hamiltonian matrix [141]. In general the basis set is not constructed explicitly, but possesses the same symmetry properties as atomic orbitals, and only the atomic orbitals in the range of energies we are interested in are considered. For instance, when modelling silicon we can neglect the  $1s$ ,  $2s$  and  $2p$  orbitals and consider only the  $3s$  and  $3p$  orbitals. We start by taking the historical overview of how the tight-binding method was developed and then later on discuss the modern concept of the tight-binding approximation.

Consider the electronic structure of an extended system. Take an atomic orbital  $\phi_{i\alpha}(\mathbf{r} - R_i)$  located at  $R_i$ , and take the Bloch sum [142] over all periodic images of the orbital

$$N^{-\frac{1}{2}} \sum_{R_i} \exp[i\mathbf{k} \cdot R_i] \phi_{i\alpha}(\mathbf{r} - R_i) \quad (2.40)$$

where  $N$  is the number of periodic images. The atomic orbitals are not suitable for analysis purposes as they are not orthogonal to each other. It is possible to perform a transformation to these atomic orbitals that would create an orthogonal set, the Löwdin functions

$$\psi_{i\alpha} = \sum_{i'\alpha'} S_{i\alpha i'\alpha'}^{-\frac{1}{2}} \phi_{i'\alpha'} \quad (2.41)$$

where  $S$  is the overlap matrix. Compared to the atomic orbitals, the Löwdin functions  $\psi_{i\alpha}(\mathbf{r} - R_i)$  have a greater extent in space. These sums are then used to create the Hamiltonian matrix elements

$$H_{i\alpha j\beta} = N^{-1} \sum_{R_j, R_i} \exp[ik \cdot (R_i - R_j)] \times \int \psi_{i\alpha}^*(\mathbf{r} - R_i) H \psi_{j\beta}(\mathbf{r} - R_j) dr. \quad (2.42)$$

This can be simplified (by noting that one of the two sums cancels the  $N^{-1}$  factor) to

$$H_{i\alpha j\beta} = \sum_{R_j} \exp[ik \cdot (R_j - R_i)] \times \int \psi_{i\alpha}^*(\mathbf{r} - R_i) H \psi_{j\beta}(\mathbf{r} - R_j) dr. \quad (2.43)$$

What Slater and Koster did [143] is to replace this integral with a parameter which depends only on the internuclear distance  $[R_i - R_j]$  and the symmetry of the orbitals. It is common at this point to use the two-centre approximation, wherein the potential part of the Hamiltonian is replaced by the potential acting only on the two atoms  $i$  and  $j$ . The Löwdin functions are then replaced with a set of functions with well-defined angular momentum. This means that the Hamiltonian can be written as

$$H_{i\alpha j\beta} = \sum_{R_j, J} \exp[ik \cdot (R_j - R_i)] h_{\alpha\beta J}(|R_j - R_i|) G_{\alpha\beta J}(k, l, m) \quad (2.44)$$

where  $J$  represents the angular momentum of the bond which can have either value zero if the bond is an  $s$  orbital or zero or one if a  $p$  orbital. The direction cosines are represented by  $k, l$  or  $m$ . The tabulated function is  $h_{\alpha\beta, J}$ . We have thus replaced an integral with Löwdin functions that extend out to a large distance with a tabulated function that terminates much closer to the atom. Hence *tight-binding*.

The eigenstates of the Hamiltonian matrix are then obtained by solving

$$\hat{H}|\Psi_i\rangle = E_i|\Psi_i\rangle. \quad (2.45)$$

To then turn the electronic structure method into an atomistic method we need to be able to calculate the total energy and the forces acting on each atom. The band structure of a crystal is found by integrating the density of states  $n(E)$

$$E_{\text{band}} = \int^{E_f} E n(e) dE \quad (2.46)$$

where  $E_f$  is the Fermi level. All other contributions to the energy are described by a pairwise function

$$E_{\text{rep}} = \sum_{i \neq j} U_{ij}. \quad (2.47)$$

The total energy is thus the sum of these two terms [144, 145]. But why can we write the total energy as a pair of simple to evaluate terms? To see why we can do this we need to study the relationship between tight-binding and DFT.

Let us start with an approximate charge density  $\rho_f$  [141, 146, 147], and then construct the single-particle Kohn-Sham potential

$$\tilde{V} = v(\mathbf{r}) + V^f(\mathbf{r}) + \mu_{\text{xc}}^f(\mathbf{r}) \quad (2.48)$$

where  $v(\mathbf{r})$  is the ionic potential,  $V^f(\mathbf{r})$  is the Hartree potential and  $\mu_{\text{xc}}^f(\mathbf{r})$  is the exchange and correlation potential (the last two terms are due to  $\rho^f$ ). You can then add the kinetic energy operator and you will form the Kohn-Sham Hamiltonian which can then be solved self-consistently. The total energy  $E_{\text{KS}}$  can be written in a variational form

$$E_{\text{KS}} \approx \sum_n a_n \tilde{\epsilon}_n - \int d\mathbf{r} \rho(\mathbf{r}) \left[ \frac{1}{2} V^f(\mathbf{r}) + \mu_{\text{xc}}^f(\mathbf{r}) \right] + E_{\text{xc}}[\rho^f] + E_{\text{ii}} + O(N^2). \quad (2.49)$$

This can then be rewritten as (in basis-independent form)

$$E_{\text{KS}} \approx \text{Tr}[\rho^{\text{out}} H] - \text{Tr}\rho^f (V^f/2 + \mu_{\text{xc}}^f) + E_{\text{xc}}[\rho^f] + E_{\text{ii}}. \quad (2.50)$$

We can expand and manipulate (2.50) to obtain the energy in the tight-binding bond form (see Appendix A)

$$E_{\text{B}} \approx \text{Tr}(\rho^{\text{out}} - \rho^f) H + \Delta E_{\text{es}}[\rho^f] + \Delta E_{\text{xc}}[\rho^f] \quad (2.51)$$

where the energy is written in terms of the electrostatic energy, the exchange and correlation energy and the band energy.

So, can we make the approximation that any terms in the binding energy which are not in the sum of occupied eigenstates be approximated by a sum of pair terms? The change in electrostatic energy is already in that form. Thus the only term we need to consider is the exchange and correlation term. It is surprising that we could approximate this to a sum of pair terms as the exchange-correlation energy functional is nonlinear. Starting with the correlation energy, we can write this as [141, 148]

$$E_{\text{c}} = \frac{1}{2} \int \int d\mathbf{r} d\mathbf{r}' \rho(\mathbf{r}) \frac{h_{\text{c}}(\mathbf{r}, \mathbf{r}')}{|\mathbf{r} - \mathbf{r}'|} \rho(\mathbf{r}') \quad (2.52)$$

where  $h_{\text{c}}$  is related to the pair correlation function, but only weakly [148], so we can make the approximation that change in correlation energy upon forming the bulk is

$$\Delta E_{\text{c}} = \frac{1}{2} \sum_i \sum_{j \neq i} \int \int d\mathbf{r} d\mathbf{r}' \rho_i(\mathbf{r}) \frac{h_{\text{c}}(\mathbf{r}, \mathbf{r}')}{|\mathbf{r} - \mathbf{r}'|} \rho_j(\mathbf{r}') \quad (2.53)$$

which is a sum of pair terms.

The exchange energy can be written in the Hartree-Fock approximation (there is an external potential which gives rise to a Hartree-Fock density with  $\rho^{\text{HF}}(\mathbf{r}) = \rho^f(\mathbf{r})$ ) as

$$E_x[\rho] = -\frac{1}{2} \int \int d\mathbf{r} d\mathbf{r}' \frac{\rho^{\text{HF}}(\mathbf{r}, \mathbf{r}') \rho^{\text{HF}}(\mathbf{r}', \mathbf{r})}{|\mathbf{r} - \mathbf{r}'|}. \quad (2.54)$$

As  $\rho^{\text{HF}}(\mathbf{r})$  is equal to  $\rho^f(\mathbf{r})$  we can substitute  $\rho^f$  for  $\rho^{\text{HF}}$  in the above expression which leads to a sum of pair terms in the exchange energy.

We can thus explicitly write the total energy of the system as

$$E_{\text{tot}}(\{R_k\}) = E_{BS}(\{R_K\}) + E_{rep}(\{|R_k - R_l|\}) \quad (2.55)$$

$$= \sum_i n_i \epsilon_i(\{R_k\}) + \sum_k \sum_{<l} V_{rep}(|R_l - r_k|) \quad (2.56)$$

where  $n_i$  is the occupation number of orbital  $i$  and  $\epsilon_i$  is the eigenvalue of orbital  $i$ . The force on each atom can then be calculated by using the Hellman-Feynman theorem (2.39).

However, before any work is performed on solving the Hamiltonian and finding the total energy and thus the forces acting on each atom, we need to input information into the Hamiltonian, so that we can accurately represent the system we are modelling. In other words, the Hamiltonian needs to be *parameterised*, values need to be found for onsite and off-diagonal elements. In practice there are two ways this parameterisation can be performed, empirically or from *ab initio* techniques (the density-functional-tight-binding method first discussed by Porezag and Frauenheim [141, 149, 150, 151, 152, 153, 154]). An example of an empirically based tight-binding scheme is the SSH Hamiltonian [18, 57, 59], which shall be discussed in more detail in the next chapter, where values are given for the onsite energy, hopping parameter and electron-phonon coupling parameters. The *ab initio* DFTB (Density-Functional-Tight-Binding) technique is discussed in Chapter 5.

Before we can talk about how we calculate the conductivity of atomic scale wires we need a general overview of the problem so as to clarify a few issues, including the methodology of calculating conductance, the origin of resistance, measurement issues that in the real world could affect conductivity measurements, the details of how we calculate the transmission probability from the Green's function of an electron scattering through the wire and how we deal with size effects. For a more detailed review the

reader is advised to look at Datta [26] if they desire more information about the topic of calculating the conductivity characteristics of mesoscopic structures.

## 2.3 Transport in atomic scale wires: An overview

### 2.3.1 Introduction

We start with what is the most easy to visualise method of calculating the transport properties of the atomic scale wires, the *Landauer* approach [26]. This is to illustrate some of the basic concepts that are used in the calculation of transport properties, although we will stress that this is not how we calculated the transport properties of the various atomic scale wires themselves, as we work with wavefunctions.

In this approach the current through a conductor is expressed in terms of the probability that an electron is transmitted through the conductor. This is proportional to the number of modes that can be accessed by electrons in the valence band (or if holes, in the conduction band). And the number of modes is proportional to the size of the conductor. For a wide conductor there are many modes that can be accessed and the change in the number of modes available compared to the total number of modes is small, and thus the conductivity seems to go down smoothly. However as  $W$  (the width of the conductor) decreases the number of available modes decreases and the ratio of the change in number of modes to the total number becomes large and so the conductivity goes down in discrete steps.

It is not a trivial problem to calculate the transmission probability. For instance, one would think naively that if a device is smaller than the mean-free path, then the probability of an electron to travel through the device is unity, which would mean that the resistance of the device is zero. However, experimentally the current that is measured passing through the device is finite which indicates that the resistance of this device is nonzero. Where does this resistance come from? Note that in all of the examples that follow the transport properties are calculated at zero temperature, that is that current only flows in the energy range  $\mu_1 \leq E \leq \mu_2$  (where  $\mu_1$  is the chemical potential of contact 1 and  $\mu_2$  is the chemical potential of contact 2), and that the net current only flows from lead 1 to lead 2 and not vice versa (this is only true for zero temperature). Current flows in both directions but all terms cancel except in the energy range  $\mu_1 \leq E \leq \mu_2$ .

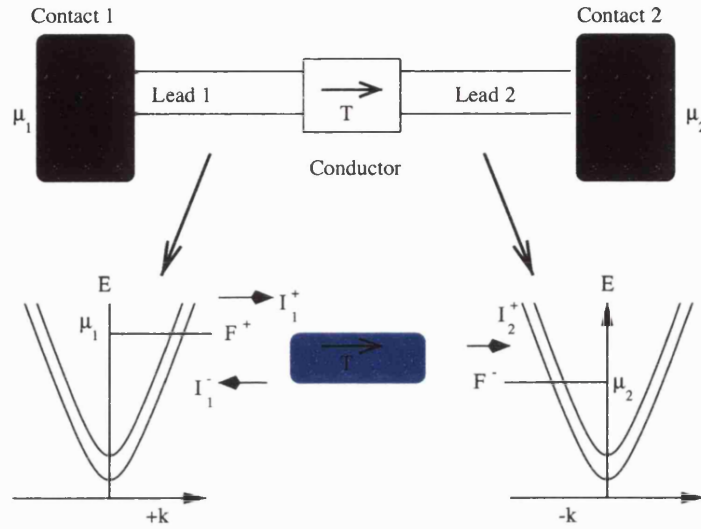


Figure 2.2: Typical experimental setup (top) involving an atomic scale conductor. Also shown is energy range (bottom) in which net current can flow. For definition of what  $F^+$  is see text.

How many electrons are involved in conduction between the terminals? We assume that the contacts are ‘reflectionless’. This is a simple situation,  $+k$  states in the conductor are only occupied by electrons in the left terminal, and  $-k$  states are occupied by electrons originating in the right terminal ( $k$  denotes wavenumber in the  $x$  direction). The quasi-Fermi level  $F^+$  (if the entire system is not in equilibrium as tends to be the case for transport problems, then there is not an uniform Fermi level across the system, so we have to use a local quasi-level which can vary in space  $F^+$ ) for the  $+k$  states is always equal to  $\mu_1$ . If both conductors are at the same chemical potential  $\mu_1$  then the potential of the electrons in the right lead (the  $-k$  electrons) is equal to  $F^+$ . Now suppose we change the potential at the right contact to  $\mu_2$ . The potential of the electrons  $F^+$  is unchanged, as electrons that are in the  $+k$  states originate in the left terminal, and no electrons from the right lead can access these states. Similarly, the quasi-Fermi level  $F^-$  for the  $-k$  states is solely determined by  $\mu_2$ . Therefore at low temperature the electrons that are involved with transport are all those electrons with  $+k$  wavevectors lying between  $\mu_1$  and  $\mu_2$  (see Figure 2.2).

Assuming zero temperature and assuming that the number of modes  $M$  is constant over the range  $(\mu_1 - \mu_2)$ , the influx of electrons from lead 1 is given by

$$I_1^+ = (2e/h)M[\mu_1 - \mu_2] \quad (2.57)$$

The outflux from lead 2 is given by multiplying the influx from lead 1 by the transmission probability  $T$

$$I_2^+ = (2e/h)MT[\mu_1 - \mu_2] \quad (2.58)$$

with the rest of the current reflected back into lead 1

$$I_1^- = (2e/h)M(1 - T)[\mu_1 - \mu_2]. \quad (2.59)$$

The net current  $I$  is thus the difference between  $I_1^+$  and  $I_1^-$ . The conductance is

$$G = \frac{I}{(\mu_1 - \mu_2)/e} = \frac{2e^2}{h}MT. \quad (2.60)$$

This term can be written as

$$G^{-1} = \frac{h}{2e^2M} \frac{1}{T} = \frac{h}{2e^2M} + \frac{h}{2e^2M} \frac{1 - T}{T} = C + \text{resistance}. \quad (2.61)$$

This gives us an intuitively pleasing result as the resistance of a conductor is related to the ease in which electrons can travel through the conductor, but there is also a constant term  $C$ . The physical meaning of this term is that this is the ‘contact’ resistance, that is the resistance due to the interface between the conductor and the contact of the leads. Experimentally it has been observed that even for the case of a ballistic conductor  $L \leq L_M$  (see Chapter 1), there is a finite resistance (the conductance saturates at some value  $G_c$ ). In the leads there are many modes that are accessible to the electrons, but in the atomic scale conductor there are only a few modes. To get from a mode in the lead to a mode in the conductor requires a redistribution of current in the modes in the lead.

We thus have a contact resistance  $G_c^{-1}$ . The more modes there are in the conductor the less redistribution of current is required in the leads and the lower the contact resistance.

### 2.3.2 Where does resistance come from?

So we have an expression of the resistance that is related to the ease with which electrons can travel through a conductor. But where does the resistance come from? Is it associated with the scatterer that is in the conductor that prevents electrons from travelling through the conductor? Is the potential drop across the scatterer?

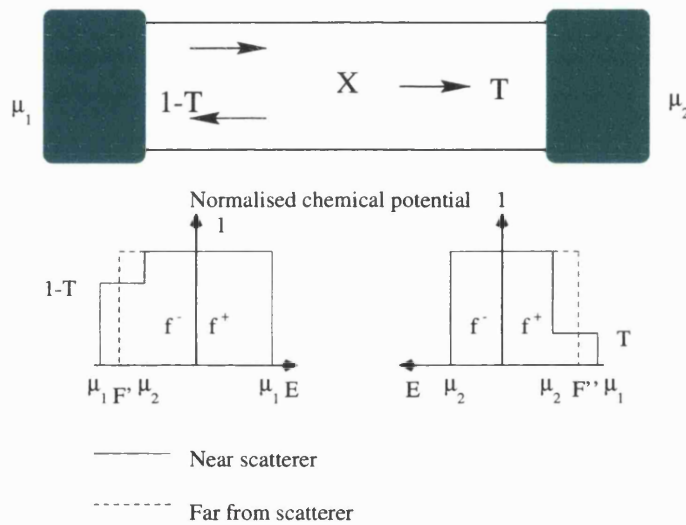


Figure 2.3: Illustration of the energy distribution of  $-k$  and  $+k$  states in a conductor with one scatterer  $X$  and a probability of transmission from left to right of  $T$ .

We need to consider the energy distribution of the carriers in the positive and negative  $k$ -states to the left and the right of the scatterer (see Figure 2.3). We will assume that we can treat the electrons as semiclassical particles, thus ignoring interference effects. The  $+k$  states to the left of the scatterer are occupied only by electrons coming in from the left contact. Thus these states have the same electrochemical potential as the left contact, that is  $\mu_1$ . At low temperatures we can write the distribution function as

$$f^+(E) \approx \theta(\mu_1 - E). \quad (2.62)$$

Equivalently the  $-k$  states to the right of the scatterer have the same electrochemical potential as the right contact  $\mu_2$  and the distribution function for  $f^-(E)$  for the  $-k$  states

is

$$f^-(E) \approx \theta(\mu_2 - E). \quad (2.63)$$

Now if we consider the  $-k$  states to the left of the scatterer or the  $+k$  states to the right of the scatterer the situation is more complicated. All states below  $\mu_2$  are fully occupied but the states in the energy range between  $\mu_2$  and  $\mu_1$  may only be partially filled. The distribution function of  $+k$  states to the right of the scatterer is (remembering that there is a probability  $T$  that the electrons propagate through the scatterer)

$$f^+(E) \approx \theta(\mu_2 - E) + T(\theta(\mu_1 - E) - \theta(\mu_2 - E)). \quad (2.64)$$

And for the  $-k$  states to the left of the scatterer

$$f^-(E) \approx \theta(\mu_2 - E) + (1 - T)(\theta(\mu_1 - E) - \theta(\mu_2 - E)). \quad (2.65)$$

Further away from the scatterer these distributions are not valid as the electrons are free to establish a Fermi type distribution

$$f^-(E) \approx \theta(F' - E) \quad (2.66)$$

$$f^+(E) \approx \theta(F'' - E). \quad (2.67)$$

The electrochemical potentials  $F'$  and  $F''$  are determined using the conservation of electron number

$$F' = \mu_2 + (1 - T)[\mu_1 - \mu_2] \quad (2.68)$$

$$F'' = \mu_2 + T[\mu_1 - \mu_2] \quad (2.69)$$

where we assume that there are relaxation processes that establish equilibrium for the  $+k$  states and among the  $-k$  states but that there is no energy transfer amongst the groups.

So how does the electrochemical potential vary with distance? To the left of the scatterer the potential is equal to  $\mu_1$  and to the far right it is equal to  $F''$ . But to the near right of the scatterer the potential is strongly distorted away from a Fermi function. In fact the electrochemical potential is not strictly well defined. We can define a potential such that integrating over energy would give us the total number of electrons, so that the potential to the near right of the scatterer is the same as the potential to the far right (but this will not tell us the energy distribution of the electrons). For the  $+k$  states this is

$$F^+ = \mu_1 \quad (\text{left}) \quad = F'' = \mu_2 + T[\mu_1 - \mu_2] \quad (\text{right}). \quad (2.70)$$

For convenience we can define normalised potentials  $\mu^+$  and  $\mu^-$  which are obtained from  $F^+$  and  $F^-$  by setting  $\mu_2 = 0$  and  $\mu_1 = 1$  which gives us

$$\mu^+ = 1 \quad (\text{left}) \quad (2.71)$$

$$\mu^+ = T \quad (\text{right}) \quad (2.72)$$

and for  $-k$  states

$$\mu^- = 1 - T \quad (\text{left}) \quad (2.73)$$

$$\mu^- = 0 \quad (\text{right}). \quad (2.74)$$

Thus we can see that there is a sharp drop across the scatterer (as expected for a

localised resistance) with the normalised potential drop equal to  $(1 - T)$ . The actual potential drop is the normalised potential drop multiplied by the applied potential  $(\mu_1 - \mu_2)$ . The rest of the applied bias  $T(\mu_1 - \mu_2)$  is dropped at the interface between the contacts and the leads (the contact resistance  $G_c^{-1}$ , see (2.61)).

### 2.3.3 Measurement issues

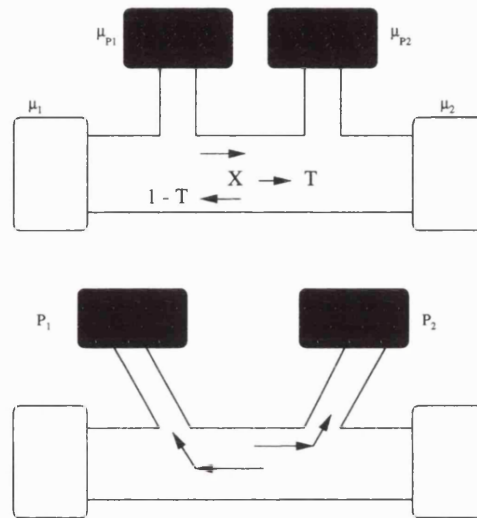


Figure 2.4: Schematic of an idealised system (top) and a more realistic situation (bottom).

It is standard procedure to measure the voltage drop across a conductor with a four terminal device. But measuring the voltage across an atomic scale device is not a simple matter. For macroscopic devices, the presence of these probes is a minor perturbation to the current, that is the presence of the probes does not change the properties of the device. However when we get to the atomic scale the presence of the probes represents a major perturbation, and they could be the dominant source of scattering or resistance. Another factor is that atomic scale probes are rarely identical. For instance, a probe  $P_1$  that is bent strongly to the left will couple far more easily to electrons coming from the right ( $-k$  states), than it would to electrons coming from the left (see Figure 2.4). The probe would thus measure a voltage close to that of a  $-k$  state  $\mu_{P1} \sim (1 - T)\Delta\mu$ , where  $\Delta\mu = \mu_1 - \mu_2$ . Similarly a probe  $P_2$  that is bent strongly to the right would couple strongly to  $+k$  states and would measure a potential  $\mu_{P2} \sim T\Delta\mu$ .

The measured resistance would then be

$$\frac{(\mu_{P1} - \mu_{P2})/e}{I} = \frac{h}{2e^2 M} \frac{1 - 2T}{T} \quad (2.75)$$

which for  $T$  greater than 0.5 gives negative resistance. The measured resistance will in actuality lie in the range

$$\frac{h}{2e^2 M} \frac{1}{T} \leq R \leq \frac{h}{2e^2 M} \frac{1 - 2T}{T} \quad (2.76)$$

which, if the conductor is very long (and thus  $T$  is very small) is of no relevance as 1 and  $1 - 2T$  are approximately identical.

We have thus seen that it is difficult even to measure the voltage drop across an atomic scale device. The interpretation of four terminal voltage measurements was for a long time in dispute. The methodology that was eventually used to solve this problem was to realise that there was no qualitative difference between the current and voltage measurements (it was Büttiker who first noted this [155]). We start with the simple two terminal linear response (or low bias regime where current is proportional to applied bias)

$$I = \frac{2e}{h} \bar{T} [\mu_1 - \mu_2] \quad (2.77)$$

where  $\bar{T}$  is the product of number of modes  $M$  and the transmission probability per mode  $T$  at the Fermi energy, assumed to be constant over the range  $(\mu_1 - \mu_2)$ . One can then treat all probes probes equally and extend (2.77) to include all terminals

$$I_p = \frac{2e}{h} \sum_q [\bar{T}_{q \leftarrow p} \mu_p - \bar{T}_{p \leftarrow q} \mu_p] \quad (2.78)$$

which can be rewritten (using  $V = \mu/e$ )

$$I_p = \sum_q [G_{qp} V_p - G_{pq} V_q] \quad (2.79)$$

where

$$G_{pq} \equiv \frac{2e^2}{h} \bar{T}_{p \leftarrow q}. \quad (2.80)$$

The various coefficients of  $G$  must obey the sum rule

$$\sum_q G_{qp} = \sum_q G_{pq} \quad (2.81)$$

so that when all of the potentials are equal no current flows through the device. We can use this sum rule to rewrite (2.81) as

$$I_p = \sum_q G_{pq} [V_p - V_q]. \quad (2.82)$$

The conductance coefficients also obey the relation (in a magnetic field  $B$ )

$$[G_{qp}]_{+B} = [G_{pq}]_{-B}. \quad (2.83)$$

If the magnetic field is zero then the coefficients are zero and (2.82) is what we would get if we applied Kirchoff's loop law to a network of conductors that connected every terminal  $p$  to every other terminal  $q$ . If a magnetic field is present then this relation does not follow, as in general  $G_{qp} \neq G_{pq}$ .

### 2.3.4 Calculating the transmission probability

How does one actually calculate the transmission function  $T$ ? In coherent transport (which we assume is the case, see Appendix B for more information on the validity of approximations we make) this is usually calculated from the scattering matrix  $S$ . This

relates the outgoing wave amplitudes to the incoming wave amplitudes at the different leads. The transmission probability  $T_{mn}$  is the square of the magnitude of the corresponding element in the  $S$ -matrix

$$T_{m \leftarrow n} = |s_{m \leftarrow n}|^2 \quad (2.84)$$

where  $m$  denotes a mode in lead  $q$  and  $n$  denotes a mode in lead  $p$ . The  $S$ -matrix is defined in terms of the ‘current amplitude’, which is equal to a wave amplitude times the square root of the velocity.

To conserve physical properties, the  $S$ -matrix must obey certain constraints. In order to conserve current, the  $S$ -matrix must be unitary. This makes sure that the sum rule for the conductance matrix is satisfied (for coherent transport). Also, for coherent transport the  $S$ -matrix must obey the reciprocity equation, i.e.,  $[S]_{+B} = [S^T]_{-B}$ .

The  $S$ -matrix tells us the response at one lead due to the excitation at another lead. This is similar to the Green’s function, which can tell us what the response is at any point in the conductor, due to an excitation at any other point. The Green’s function approach is extremely useful when we try to include the effect of interactions (such as electron-electron or electron-phonon interactions).

Whenever the response  $R$  is related to an excitation  $S$  by a differential operator  $D_{\text{op}}$  such that  $D_{\text{op}}R = S$ , we can define a Green’s function such that

$$R = D_{\text{op}}^{-1}S = GS. \quad (2.85)$$

The problems that we will want to solve are of the form

$$[E - H_{\text{op}}]\Psi = S \quad (2.86)$$

where  $\Psi$  is the wavefunction and  $S$  is an equivalent excitation due to an incident wave. The Green’s function corresponding to this problem would be

$$G = [E - H_{\text{op}}]^{-1}. \quad (2.87)$$

Depending on the boundary condition, the Green's function can either be retarded or advanced. A retarded Green's function is one in which the response progresses outwards from the point of excitation. An advanced Green's function is one in which the response progresses inwards to the point of excitation.

One can incorporate the boundary conditions into the equation itself, by adding an infinitesimal imaginary part. That is that instead of the above equation, we have  $G(S + i\eta) = R$  for the retarded function, where  $\eta \geq 0$ . This has the effect of making the retarded function grow exponentially as we move away from the point of excitation, which means that that solution is unphysical. Similarly, for the advanced function  $G(S - i\eta) = R$  where  $\eta \geq 0$ .

To directly relate the  $s$ -matrix to the Green's function we make use of the Fisher-Lee relation [156]. We consider a conductor attached to a set of leads as shown in Figure 2.5. The interface between lead  $p$  and the conductor is defined by  $x_p=0$ .  $G_{qp}^{\text{R}}$  denotes the Green's function between a point lying on the plane  $x_p=0$  and another point lying at  $x_q=0$

$$G^{\text{R}}(y_q; y_p) = G^{\text{R}}(x_q = 0, y_q; x_p = 0, y_p). \quad (2.88)$$

Assuming that the leads are one dimensional and that they are single moded, we know that the unit excitation at  $x_p=0$  gives rise to a wave of amplitude  $A_p^-$  away from the conductor and a wave of amplitude  $A_p^+$  towards the conductor. A wave travelling toward the conductor is scattered by the conductor into different leads. We can thus write

$$G_{qp}^{\text{R}} = \delta_{qp} A_p^- + s_{qp} A_p^+. \quad (2.89)$$

We then use the properties of one dimensional Green's functions that the function is continuous and the first derivative is discontinuous by  $2m/\hbar^2$ . We can rewrite this to

obtain

$$s_{qp} = -\delta_{qp} + i\hbar\sqrt{v_q v_p} G_{qp}^R \quad (2.90)$$

which thus relates the  $s$ -matrix to the Green's function. It is easy to generalise this argument to include multiple modes.

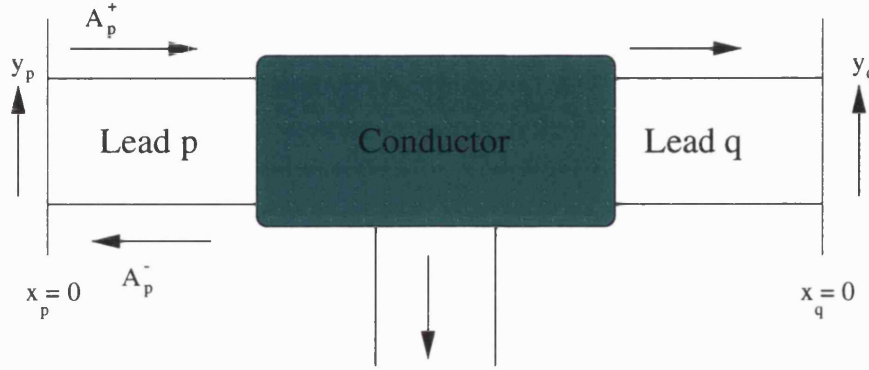


Figure 2.5: Unit impulse in lead p leads to an incident wave which is partially transmitted to the other leads.

### 2.3.5 Size effects

Now that we have detailed how to construct the Green's function from the Hamiltonian, how to obtain the  $S$ -matrix from the Green's function, and how to obtain the transmission function from the  $S$ -matrix, it would seem simple to setup the matrix  $[(E + i\eta) - H]$  and invert this to construct the Green's function  $G^R = [(E + i\eta) - H]^{-1}$ . The problem is that this matrix is infinitely dimensional as it includes the effects of the leads (which are infinitely long). If the matrix is just truncated at some point, then we get boundary conditions which reflect waves.

The Green's function can be partitioned into submatrices as follows

$$\begin{bmatrix} G_p & G_{pC} \\ G_{Cp} & G_C \end{bmatrix} = \begin{bmatrix} (E + i\eta)I - H_p & \tau_p \\ \tau_p^* & EI - H_C \end{bmatrix}^{-1} \quad (2.91)$$

where the matrix  $[(E + i\eta)I - H_p]$  represents the isolated lead and  $[EI - H_C]$  represents the isolated conductor. The coupling matrix is non-zero only for points which are adjacent

to each other  $\tau_p(p_i, i) = t$ .

Solving the linear equations for the submatrix  $G_C$  we find that we can write the Green's function for the isolated semi-conductor as

$$G_C = [EI - H_C - \tau_p^\dagger g_p^R \tau_p]^{-1} \quad (2.92)$$

where  $g_p^R = [(E + i\eta)I - H_p]^{-1}$ . All of the matrices in this expression are of finite size  $C \times C$ , with  $C$  the number of points inside the conductor. However, the effects of the infinite lead are taken into account exactly through the term  $\tau_p^\dagger G_p^R \tau_p$ . As  $g_p^R$  is the Green's function of an isolated lead it can be determined analytically.

We can thus write the Green's function as

$$G^R = [EI - H_C - \Sigma_R]^{-1} \quad (2.93)$$

where

$$\Sigma^R = \sum_P \Sigma_p^R(i, j) = \sum_P t^2 g_p^R(p_i, p_j). \quad (2.94)$$

Thus the effect of the leads is taken into account through the term  $\Sigma^R$  which is referred to as the self-energy of the leads.

## 2.4 Calculating the conductivity

To solve the problem of finding the conductivity of a long atomic scale wire including electron-phonon coupling, we used the method of Bonca *et al* [17], where we map the many-body problem in a large variational space exactly onto a one-body problem (see Figure 2.6), albeit for the case of one electron injected into the atomic scale wire at a time and assuming that the electron undergoes coherent and not diffusive transport. The real-space Schrödinger equation is then solved for the one-body problem. We assume that the Hamiltonian that needs to be solved consists of a kinetic energy term, a phonon creation/annihilation term (phonon energy term), and an electron-phonon coupling term

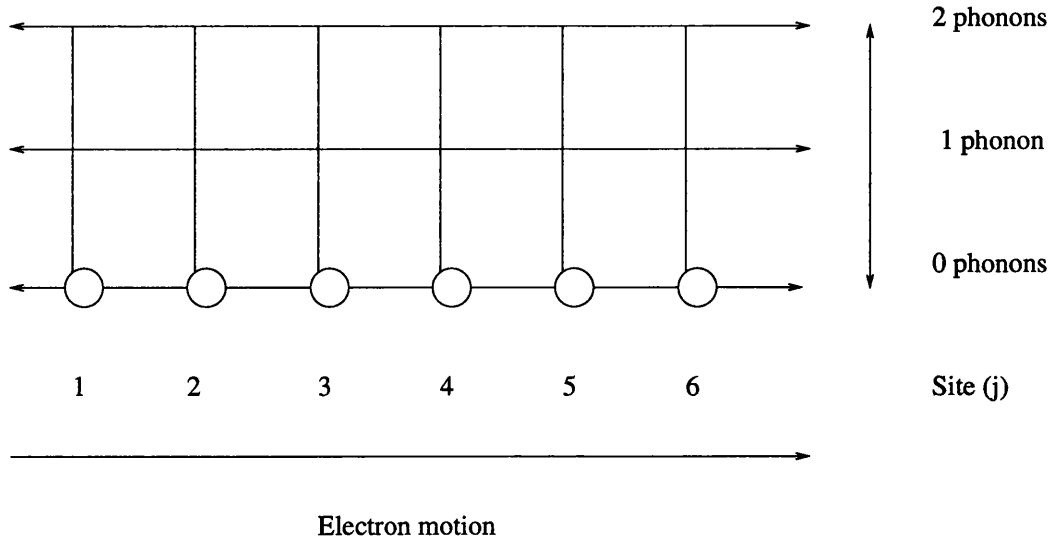


Figure 2.6: Schematic diagram showing model of mapping of many body system to one body system. Various energy channels shown, some of which can only be accessed by phonon scattering. For simplicity we only show the channels associated with one phonon mode.

[21, 157]. As an atomic wire is effectively one-dimensional, the Hamiltonian can be written as one-dimensional and so is dependent on one coordinate only,  $j$ . For a one-dimensional wire we are only concerned with the nearest neighbours, so we can replace an arbitrary index  $K$  by a term  $j + 1$  and  $j - 1$ . The interaction with the harmonic modes should be localised in the atomic wire. The Hamiltonian is thus generally (in eigenvector-space  $n$ )

$$H_W = \sum_l \epsilon_n c_n^\dagger c_n + \sum_q \omega_q a_q^\dagger a_q + \sum_{q,n,m} \gamma_{qnm} (a_q^\dagger + a_q) c_n^\dagger c_m. \quad (2.95)$$

where  $a_q^\dagger$  and  $a_q$  ( $c_n^\dagger$  and  $c_n$ ) are the creation and annihilation terms of the phonon mode  $q$  with frequency  $\omega_q$  (of the electron in state  $n$  with eigenenergy  $\epsilon_n$ ) and  $\gamma_{qnm}$  represents the coupling of phonon mode  $q$  from state  $n$  to state  $m$ . Nonlinear phonon modes or nonlinear phonon-phonon coupling can be added to the Hamiltonian by adding terms of higher than quadratic order, such as  $(a^\dagger)^5 + \text{H.c.}$ . Similarly nonlinear electron-phonon coupling can be added by adding terms such as  $c^\dagger c (a^\dagger)^2 + \text{H.c.}$  (by nonlinear we mean that there are terms which are not proportional to the quadratic).

We will generally use the following setup, that the atomic scale wire (containing  $N_a$  sites) described by (2.95) is embedded in a heterojunction and is connected to idealised

one-dimensional metallic leads (labelled L for left and R for right) whose Hamiltonians are

$$H_R = \sum_{j=N_a+1}^{+\infty} \epsilon_R d_j^\dagger d_j + \beta_R (d_j^\dagger d_{j-1} + d_{j-1}^\dagger d_j) \quad (2.96)$$

and

$$H_L = \sum_{j=-\infty}^0 \epsilon_L d_j^\dagger d_j + \beta_L (d_j^\dagger d_{j-1} + d_{j-1}^\dagger d_j) \quad (2.97)$$

via the coupling matrices

$$T_R = v_R (d_{N_a+1}^\dagger c_{N_a} + c_{N_a}^\dagger d_{N_a+1}) \quad (2.98)$$

and

$$T_L = v_L (d_0^\dagger c_1 + c_1^\dagger d_0). \quad (2.99)$$

We define the operators  $d_j^\dagger$  ( $d_j$ ) to create (annihilate) an electron on a site  $j$  inside the leads, with on-site energy  $\epsilon_{L,R}$  and nearest neighbour hopping integral  $\beta_{L,R}$ . The hopping matrix elements between the ends of the molecule and the right and left leads are denoted by  $v_{L,R}$ . Inside the atomic scale wire it is easy to transform from a site representation to an eigenstate representation by the operation  $c_n^\dagger = \sum_j Z_n^*(j) c_j^\dagger$ , where  $Z_n(j)$  are the components of the  $n$ th eigenstate on site  $j$ .

We perform the procedure to map the many-body problem onto a single-body problem with many channels by writing the total scattering wavefunction  $|\Psi(E)\rangle$  for the total energy  $E$  of the system as

$$|\Psi(E)\rangle = \sum_{j,(n_q)} \alpha_{j,(n_q)}(E) |j, (n_q)\rangle \quad (2.100)$$

and the basis set used to expand the scattering waves is

$$|j, (n_q)\rangle = c_j^\dagger \prod_q \frac{(a_q^\dagger)^{n_q}}{\sqrt{n_q!}} |0\rangle \quad (2.101)$$

where  $|0\rangle$  is the ground state of the neutral molecule and  $(n_q)$  is the set of phonon occupation (how many phonons are occupying each phonon mode). This means that we have not explicitly separated the electron and phonon degrees of freedom. For hole (or electron) propagation through the atomic scale wire each channel has a different set of phonon occupation numbers  $(n_q)$ . To find the total wavefunction  $|\Psi(E)\rangle$  we have to solve the Schrödinger equation with the total Hamiltonian

$$H|\Psi(E)\rangle = (H_W + T_L + H_L + T_R + H_R)|\Psi(E)\rangle = E|\Psi(E)\rangle. \quad (2.102)$$

The total energy  $E$  of the system (including electron injection energy) is conserved during the scattering process (this is only true for dissipationless systems)

$$E = E_{\text{in}} + \sum_q n_q \hbar \omega_q = E_{\text{out}} + \sum_q m_q \hbar \omega_q \quad (2.103)$$

where  $E_{\text{in}}$  and  $(n_q)$  are the initial energy and set of phonon occupation numbers and  $E_{\text{out}}$  and  $(m_q)$  are the final energy and set of phonon occupation numbers. Only if the process is elastic will  $(n_q) = (m_q)$ . We do not assume that this is the case.

The form of the wavefunction coefficients inside the leads is asymptotic, and corresponds to Bloch waves propagating inside the leads whose amplitudes are the reflection and transmission coefficients ( $r_{(m_q)}$  and  $t_{(m_q)}$  respectively) of the electron in different channels. For the left lead (where we inject an electron) the coefficients are (for  $j \leq -1$ )

$$\alpha_{j,(n_q)} = e^{ik_{(n_q)}^L j} \delta_{(n_q),(m_q)} + r_{(m_q)} e^{-ik_{(m_q)}^L j}. \quad (2.104)$$

For the right electrode  $j \geq N_a + 2$  the wavefunctions are described by

$$\alpha_{j,(m_q)} = t_{(m_q)} e^{ik_{(m_q)}^R j}. \quad (2.105)$$

The  $k_{(n_q)}^{L,R}$  are the wavevectors of the Bloch waves in different channels. To find the dispersion relations for these wavevectors we have to solve the Schrödinger equation  $\langle j|H|\Psi(E)\rangle = E\langle j|\Psi(E)\rangle$ . We find that for the incoming wave the wavevectors are

$$E_{\text{in}} = \epsilon_L + 2\beta_L \cos k_{(n_q)}^L, \quad (2.106)$$

for the outgoing reflected wave the wavevectors are

$$E_{\text{out}} = \epsilon_L + 2\beta_L \cos k_{(m_q)}^L \quad (2.107)$$

and for the transmitted wave the wavevectors are

$$E_{\text{out}} = \epsilon_R + 2\beta_R \cos k_{(m_q)}^R. \quad (2.108)$$

All our transport calculations take place in the limit of low temperature. This means that we can take the initial set of phonon occupation numbers  $(n_q)=0$ . If the injected electron's energy lies outside the channels defined above, that channel is not propagating and an electron has to tunnel through the gap between leads without any propagation through the wire.

We can relate the reflection or transmission coefficients to the wavefunction coefficients by solving  $\langle j|H|\Psi(E)\rangle = E\langle j|\Psi(E)\rangle$  at site  $j = 0$  and  $j = N_a + 1$ . The relations would be

$$r_{(m_q)} = -\delta_{(0),(m_q)} + \frac{v_L}{\beta_L} \alpha_{1,(m_q)} \quad (2.109)$$

and

$$t_{(m_q)} = \frac{v_R}{\beta_R} \alpha_{N_a, (m_q)} e^{-ik_{(m_q)}^R N_a} \quad (2.110)$$

where (0) is the elastic channel and  $(m_q) \neq 0$  are the inelastic channels.

Finally one needs to find the wavefunctions on sites  $j = 1 \dots N_a$ . As we have defined the wavefunctions in terms of a series of channels and as we are allowing electrons to propagate only via nearest neighbour sites, finding the wavefunctions thus becomes equivalent to solving the complex linear system of the form  $\underline{M} \underline{a} = \underline{d}$ , where  $\underline{a}$  are the  $\alpha_{j, (n_q)}$  and  $d$  is imaginary. The matrix  $M$  is by definition sparse, but if there is a large number of phonon modes with a lot of different occupations solving this linear system becomes unfeasible. One method of avoiding this numerical problem is to use the propagation matrix method (where we can use simpler tight-binding matrix equations), but as explained above, this can be rewritten as a Green's function method.

Using a Green's function method allows us to remove the leads by introducing embedding potentials. To then find the solution of the full scattering problem we want to propagate a source term  $|s(E)\rangle$  (which is an injected plane wave at energy  $E$ ) through the wire

$$|\alpha(E)\rangle = G_{\text{eff}}(E)|s(E)\rangle \quad (2.111)$$

where

$$|\alpha(E)\rangle = \sum_{n, (n_q)} \alpha_{n, (n_q)}(E) |n, (n_q)\rangle \quad (2.112)$$

is the wavefunction of the scattering state and

$$G_{\text{eff}}(E) = [E - H_W - \Sigma^L(E) - \Sigma^R(E)]^{-1} \quad (2.113)$$

is the effective Green's function of the wire connected to the leads.  $H_W$  is the Hamiltonian of the wire in eigenvector-space (2.95):  $\Sigma_L$  and  $\Sigma_R$  are the complex embedding potentials

of the two electrodes. These embedding potentials are diagonal matrices in the  $|n, (n_q)\rangle$  basis set with components

$$\Sigma_{n,(n_q)}^L(E) = Z_n(1)v_L g_{(n_q)}^L v_L Z_n(1) \quad (2.114)$$

and

$$\Sigma_{n,(n_q)}^R(E) = Z_n(N_a)v_R g_{(n_q)}^R v_R Z_n(N_a) \quad (2.115)$$

where  $g_{L,R}^S$  is the ‘surface’ Green’s function of the isolated leads (see also (2.94)). This is analytically given by  $g_{(n_q)}^{L,R}(E) = \exp(ik_{(n_q)}^{L,R}(E))/\beta_{L,R}$ .

We also need a form for the source term  $|s(E)\rangle$ . This has components given by

$$s_{n,(n_q)}(E) = \delta_{(0),(n_q)} \left( -2iv_L \sin k_{(0)}^L \right) Z_n(1). \quad (2.116)$$

We can simplify the solution of the system (2.113) by explicitly separating the real and imaginary parts of the vectors and matrices as follows

$$\begin{bmatrix} E - H_w - \Re \Sigma(E) & \Im \Sigma(E) \\ \Im \Sigma(E) & -E + H_w + \Re \Sigma(E) \end{bmatrix} \begin{bmatrix} \Re \alpha(E) \\ \Im \alpha(E) \end{bmatrix} = \begin{bmatrix} \Re s(E) \\ -\Im s(E) \end{bmatrix} \quad (2.117)$$

where  $\Sigma = \Sigma^L + \Sigma^R$ . This renders the matrix above real and symmetric and thus amenable to standard computational methods of solution (such as the conjugate gradients technique).

To find  $|\alpha(E)\rangle$  we solve  $G_{\text{eff}}^{-1}|\alpha\rangle = |s\rangle$ . The asymptotic outgoing waves on the right lead can be written as

$$\alpha_{j,(n_q)}^R(E) = t_{(n_q)}(E) e^{ik_{(n_q)}^R j}. \quad (2.118)$$

The transmission coefficients  $t_{(n_q)}$  are related to the value of  $|\alpha(E)\rangle$  at the last atomic site

of the wire connected to the right lead. We can relate these coefficients to the inelastic transmission amplitude  $t(E, E')$  where  $E'$  is the energy of an electron in an outgoing channel after it has been inelastically scattered. This is given by

$$t(E, E') = \sum_{(m_q)} t_{(m_q)}(E) \delta(E - E' - \sum_q m_q \hbar \omega_q). \quad (2.119)$$

The effective total transmission probability is then

$$T(E) = \sum_{(m_q)} |t_{(m_q)}(E)|^2 \frac{\beta_R \sin k_{(m_q)}^R}{\beta_L \sin k_{(0)}^L}. \quad (2.120)$$

To find the current which is leaving through the outgoing channels in the right electrode, (or reflected from the incoming channels in the left electrode) we use

$$J_{(m_q)}^R(E) = \frac{2e}{\hbar} \Im[\alpha_{j,(m_q)}^* \beta_R \alpha_{j+1,(m_q)}]. \quad (2.121)$$

As we are only considering hopping between adjacent sites, the current in each channel of the right electrode is found to be proportional to the transmission amplitudes.

$$J_{m_q}^R = 2\beta_R \sin(k_{(m_q)}^R) |t_{(m_q)}|^2 = 2\beta_R \sin(k_{(m_q)}^R \Delta) |\alpha_{n,(m_q)}|^2. \quad (2.122)$$

We have now discussed how we can find the structure of candidate atomic scale wires, and then having found the structure and obtained various pieces of physical information, how we can find the conductivity characteristics of these atomic scale wires, including electron-phonon effects. However we have not yet explained how to obtain such physical information such as the electron-phonon coupling  $\gamma_{qnm}$  or the phonon spectra. An illustration of how this information can be calculated shall be provided in the next chapter.

## Chapter 3

# The Polyacetylene molecule: An ideal testbed for studies of atomic scale wires

In this chapter we discuss the physical and transport properties of the polyacetylene molecule. This molecule is an ideal testbed for experimental and theoretical studies of molecular wires as it is such a simple molecule to study, both experimentally and theoretically. Experimentally it is quite easy to prepare a crystal of polyacetylene with the polymers in a highly anisotropic orientation [158], with a small number of crosslinks between polyacetylene molecules (meaning that these molecules are essentially isolated [18]). Thus if any electrons are injected into the crystal they it is likely would travel through a single molecule before leaving the crystal. This means that these polyacetylene molecules can be treated as isolated molecular wires at the atomic scale (and in fact we consider only a single polyacetylene molecule bridging the gap between two leads in our calculations). From a theoretical viewpoint these molecules are also easy to study as they can be modelled with a quite simple one-dimensional Hamiltonian such as the Su-Schrieffer-Heeger (SSH) Hamiltonian [57]. This chapter is structured in the following way. Firstly we provide more information on the experimental properties of the polyacetylene molecule and the different structural isomers of the molecule. We then detail the SSH Hamiltonian that can be used to model these molecules, how to solve the Schrödinger

equation using this Hamiltonian and what the various intrinsic defects that are formed in the chain under various boundary conditions look like. Next we discuss how we can calculate the classical phonon modes of the molecule and determine which of these phonon modes couple strongly to the defects that are formed when charge is injected. We then detail how to calculate the electron-phonon coupling constants that are required in order to calculate the transport properties of this molecule (2.95) and the transformation from ‘classical’ phonons to ‘quantum’ phonons (these are required so that we perform the transport calculation on a fully quantum mechanical level). We conclude this section by briefly discussing the transport properties of a polyacetylene molecule when a polaron is formed upon hole (or electron) injection into the chain.

### 3.1 Background Information

Polymers can be divided into two types; saturated polymers in which all four carbon valence electrons are tied up in covalent bonds and are thus insulators, and conjugated polymers where three of the electrons are in  $sp^2$  hybridized orbitals (two of the  $\sigma$ -type bonds connect neighbouring carbons while the third bonds to the neighbouring hydrogen side group) and the fourth electron is in a  $sp^2p_z$  hybridized orbital. This means that conjugated polymers can be expected to display semiconducting or metallic properties. As polyacetylene  $((CH)_x)$  is such a conjugated polymer it does not behave as a insulator, rather, because the  $\pi$  band is half filled and as there is strong intra-chain bonding ( $\sim 3.0$  eV) and weak inter-chain interactions ( $\sim 0.1$  eV) it behaves as a one dimensional metal. Such a one-dimensional metal is thus susceptible to a Peierls distortion (see Chapter One) [113, 159], and so polyacetylene molecules are dimerised, with an equilibrium bond modulation of the order of  $0.03$ - $0.04$  Å [18]. This renders polyacetylene a semiconductor, and due to the Peierls distortion there is a strong coupling between electrons and phonons. (This may not be strictly true as there is some debate in the literature whether the majority of the dimerisation that is observed in polyacetylene molecules is due to electron correlation effects [122, 160]. We choose to use the simple model of the SSH Hamiltonian to perform our calculations neglecting electron correlation effects which are in more sophisticated models such as the PPP Hamiltonian [161, 162], which is simply the SSH Hamiltonian but with an additional electron-electron interaction term describing the Coulomb repulsion between the  $\pi$  electrons occupying two different sites.

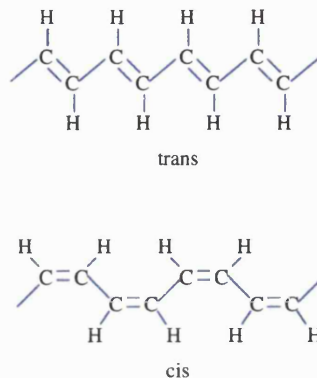


Figure 3.1: An illustration of the difference in chemical structure between *trans*-polyacetylene and *cis*-polyacetylene.

Polyacetylene also possesses a degenerate ground state whereas most other conjugated polymers do not (polyacetylene is the simplest degenerate conjugated polymer, other degenerate conjugated polymers have longer repeat distances). This means that solitons (as opposed to polarons) are the dominant charge storage species. This comes with a qualification however. As can be seen in Figure 3.1, there are two arrangements in which the polyacetylene molecule can form, with either two (*trans*-PA) or four (*cis*-PA) monomers per unit cell (where PA is shorthand for polyacetylene). Although you can easily have twofold degeneracy for *trans*-PA, in *cis*-PA no such symmetry exists. Hence the ground state of *cis*-PA is nondegenerate which means that the dominant charge species are polarons and not solitons.. Therefore it would be correct to say that only *trans*-PA has a degenerate ground state. Further discussion of PA will only detail *trans*-PA.

There is plenty of evidence that PA can be accurately modelled by one-dimensional tight-binding theory. The ratio of strong intra-chain coupling to weak inter-chain coupling has been confirmed by band calculations [163, 164]. The one dimensional band structure has been experimentally confirmed by resonance Raman scattering [165, 166, 167, 168, 169] and electron energy-loss spectroscopy [170]. Doping of the molecule with (for instance  $\text{Na}^+$  ions for *n*-type doping and  $\text{NO}^+\text{PF}_6^-$  for *p*-type doping [18]) will tend to introduce transient charge species such as polarons and bipolarons into the molecule. For a more detailed review of the properties of polyacetylene and other conjugated polymers, the reader is advised to refer to the review by Heeger *et al.* [18]. Our calculations only deal with neutral polyacetylene molecules that are undoped.

Our discussion of the polyacetylene molecule is limited by the extent to which we

can model the structure using a tight-binding method, and then using this tight-binding method to calculate the phonon spectrum and then transform these ‘classical’ phonons into ‘quantum’ phonons. We also delineate how we can then calculate electron-phonon coupling constants for the injection of a single electron or hole. However we do not then use this information to calculate the conductivity characteristics, as this work was performed in collaboration with Hervé Ness and the calculation of the transport properties of this molecule was performed by him. We thus briefly sketch the methods we could use to find the conductivity for the other two candidate atomic scale wires. For more information regarding the conductivity characteristics of polyacetylene molecules, the reader is advised to read the following papers [20, 21, 171]. However we first need to discuss how to model the structure of polyacetylene, with the commonly used Su-Schrieffer-Heeger Hamiltonian [57].

### 3.2 The Su-Schrieffer-Heeger (SSH) Hamiltonian

The SSH Hamiltonian is explicitly one-dimensional, and only the  $p_z$  or  $\pi$  orbitals are considered, as the  $\sigma$  and  $\sigma^*$  bands lie outside the region of interest. It explicitly possesses charge conjugation parity (that is the properties of particles with a positive charge and the properties of particles with a negative charge are identical). The only energy terms that are considered are a simple quadratic term in the bond lengths which represents the elastic energy stored when the  $\sigma$ -bond backbone is distorted, and the hopping integral between adjacent carbon atoms which is expanded linearly around its equilibrium value  $t_0$ . The SSH Hamiltonian is thus

$$\begin{aligned}
 H = & - \sum_j \sum_s (t_0 - \alpha(u_{j+1} - u_j)) [c_{j,s}^\dagger c_{j+1,s} + c_{j+1,s}^\dagger c_{j,s}] \\
 & + \frac{1}{2} K \sum_j (u_{j+1} - u_j + C)^2 + \frac{1}{2} M \sum_j \dot{u}_j^2
 \end{aligned}
 \tag{3.1}$$

where  $c_{j,s}^\dagger$  ( $c_{j,s}$ ) are creation (annihilation) operators that act on the  $p_z$  electrons on site  $j$  with spin  $s$  and  $u_j$  is the lattice position of atom  $j$  of the polyacetylene molecule. The electron-phonon coupling part of the Hamiltonian is in the term that contains  $\alpha$ , with the phonons that are modelled are classical.  $C$  is a constant that is added to the bond length ( $u_{j+1} - u_j$ ) so that the chain is not unstable with respect to overall

contraction. We also included the kinetic energy of the atoms so that we can later transform from real space  $j$  to classical space  $n$  (however throughout the rest of this section this term is neglected). From now on the spin part of the suffix is suppressed. As mentioned above we explicitly ignore electron-electron interaction (which are included in the PPP Hamiltonian [161, 162]). An optional term may be added which is proportional to  $\bar{u}_j \equiv (-1)^j u_j$ , but for a trans-polyacetylene molecule this evaluates to zero. This is to make the trans-polyacetylene molecule exactly doubly degenerate.

The parameters that need to be determined are  $\alpha$ ,  $K$  and  $t_0$ .  $K$  is chosen to be 42 eV  $\text{\AA}^{-2}$ , a value that has been adopted as the standard from Schugerl *et al.* [172]. The hopping parameter  $t_0$  is chosen so as to fix the total bandwidth  $4t_0$  at its experimental value of 10 eV [163], which gives a value for  $t_0$  of 2.5 eV. The average magnitude of dimerisation in the polyacetylene molecule is denoted by  $u_0$  and is chosen to be 0.025  $\text{\AA}$ . The parameter  $\alpha$  is chosen so that the bandgap  $8\alpha u_0$  is equal to the equal to the observed value of 1.4 eV. This gives a value of  $\alpha$  of 6.1 eV  $\text{\AA}^{-1}$ .

To then solve the Hamiltonian we need to use a two step recursive method. This is based on the explanation given by Wallace [59]. For a given starting geometry the Hamiltonian matrix is diagonalised, then the condition that  $\partial E / \partial u_j = 0$  for all  $j$  is used to generate new displacements. Note that we do not use periodic boundary conditions, instead choosing a finite length chain. A finite chain is used as we are interested in charge transport across the molecule, it is meaningless to consider charge transfer across a molecule if periodic boundary conditions are in place.

We start by expanding the eigenfunctions over the atomic  $p_z$  orbitals

$$c_n^\dagger = \sum_j Z_n(j) c_j^\dagger \quad (3.2)$$

where the matrix  $Z$  is assumed to be real (i.e., there is no external B-field),  $n$  represents the occupied states of the system and we neglect spin suffixes. The total energy of the system can then be written as

$$\begin{aligned}
E = & -2 \sum_j \sum_n^{\text{occ}} (t_0 - \alpha(u_{j+1} - u_j)) Z_n(j+1) Z_n(j) \\
& + \frac{1}{2} K \sum_j (u_{j+1} - u_j)^2 + \frac{1}{2} \sum_j M \dot{u}_j^2
\end{aligned} \tag{3.3}$$

although of course for the atomic sites  $j = 1$  and  $j = N_a$  where  $N_a$  is the number of atomic sites in the chain, the total energy contribution is different as this site is only onefold coupled instead of twofold coupled. This can be minimised with respect to  $(u_{j+1} - u_j)$ . We find that the self consistent equation we need to solve is

$$2\alpha \sum_n^{\text{occ}} (Z_n(j) Z_n(j-1) - Z_n(j+1) Z_n(j)) + K(2u_j - u_{j-1} - u_{j+1}) = 0, \tag{3.4}$$

which can be recast in terms of the one-electron eigenstates

$$2\alpha \sum_n^{\text{occ}} Z_n(j) (Z_n(j-1) - Z_n(j+1)) + K(2u_j - u_{j-1} - u_{j+1}) = 0, \tag{3.5}$$

where  $Z_n(j)$  are the components of the one-electron eigenstates with energy  $\epsilon_n$  of (3.1) for a given atomic configuration  $\{u_j\}$ .

(3.5) can be expressed in matrix form, and so we find that we have  $\underline{M}\underline{u} = \underline{F}$ , where

$$M_{ij} = -2\delta_{ij} + \delta_{i,j+1} + \delta_{i,j-1} \tag{3.6}$$

and

$$F_j = (2\alpha/K) \sum_n^{\text{occ}} Z_n(j) (Z_n(j-1) - Z_n(j+1)). \tag{3.7}$$

For a finite length chain the matrix  $M$  is tridiagonal. It can thus be easily solved with standard matrix solution techniques as found in [173]. For finite chains the boundary conditions are  $Z_n(j) = 0$  and  $u_j = 0$  when  $j \leq 1$  or  $j \geq N_a$ . In practice we also keep one of the two ends fixed in space so as to avoid uniform translation of the chain ( $u_1$  or

$u_{N_a} = 0$ ).

We now show the various dimerisation curves (see 1.7) that can be produced when solving (3.6) for an isolated polyacetylene molecule for various initial conditions, such as chain length  $N_a$  being an odd or even number, or whether any electrons or holes have been injected into the molecule. Firstly however we show the dimerisation curve of a neutral chain composed of a hundred atomic sites, see Figure 3.2. Note that for the majority of the chain interior the dimerisation curve is flat indicating that no defects are present. The dimerisation curve at the ends of the chain diverges from this uniformity however. This is a sign of edge effects, as near the edges the atoms are free to expand into space and thus increase their bond lengths. As the SSH Hamiltonian (3.1) possesses charge conjugation symmetry we get the same structure for hole or electron injection.

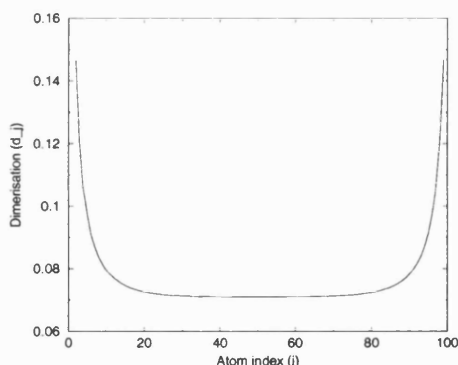


Figure 3.2: Dimerisation pattern of a neutral polyacetylene molecule with one hundred carbon atoms.

When an electron is injected into this chain we find that the electron localises in the middle of the chain and forms a polaron with a width of 28 atomic sites at FWHM, as shown in Figure 3.3.

The injection of (for instance) four electrons into the chain results in the formation of two bipolarons, spaced apart by a distance of approximately 28 atomic sites as shown in Figure 3.4. The reason why bipolarons form is that the SSH Hamiltonian does not include electron-electron effects. Therefore the SSH Hamiltonian cannot accurately model the structure of the polyacetylene molecule when multiple electrons are injected the chain.

For a neutral chain with an odd number of atoms the fact that the polyacetylene molecule prefers to have both ends terminated with a double bond results in the formation of a soliton as shown in Figure 3.5, where the dimerisation changes sign in the middle of the chain. The soliton forms in the middle of the chain as this minimises the total energy

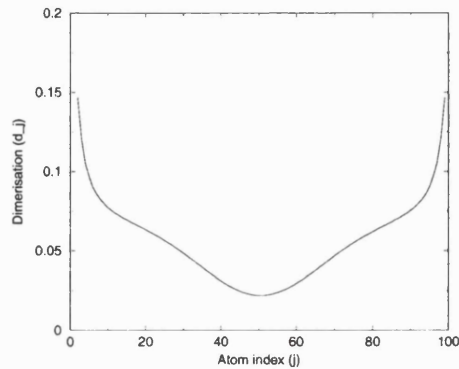


Figure 3.3: Dimerisation pattern of a singly charged (hole or electron) polyacetylene molecule with one hundred carbon atoms.

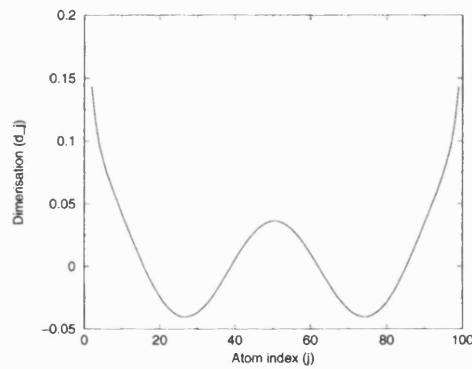


Figure 3.4: Dimerisation pattern of a multiply charged (four electrons or four holes) polyacetylene molecule with one hundred carbon atoms.

of the molecule.

When an electron is injected into the chain the dimerisation curve that is created is the same as for the neutral soliton case. This is because the formation of a soliton creates a state in the mid-gap that is (when the polyacetylene molecule is neutral) only half filled. As the SSH Hamiltonian possesses charge conjugation parity the injection of a single electron or a hole into the molecule must produce the same defect. Thus the filling or emptying of the state does not affect the structure of the chain as shown in Figure 3.6.

The injection of four electrons results in the creation of a soliton and a pair of bipolarons as shown in Figure 3.7.

Now that we have a formalism for calculating the forces that act on each atom and a method of finding the equilibrium structure for a set of starting conditions, it is now feasible to calculate the phonon modes that are present in the chain and determine which phonon modes are strongly involved in the distortion of the chain. Note that strictly

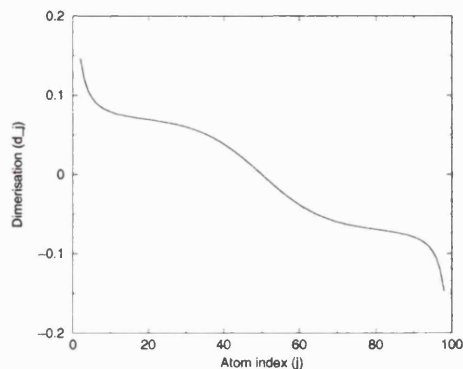


Figure 3.5: Dimerisation pattern of a neutral polyacetylene molecule with ninety nine carbon atoms.

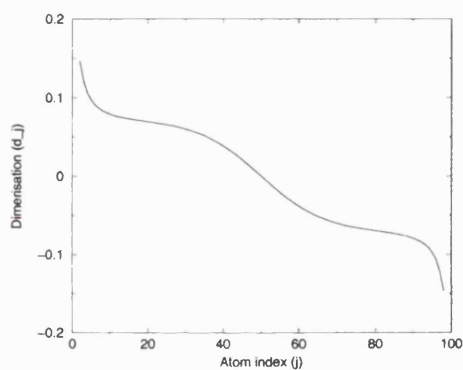


Figure 3.6: Dimerisation pattern of a singly charged (hole or electron) polyacetylene molecule with ninety nine carbon atoms.

speaking we are not calculating phonon modes as these are only defined for the case of an infinite molecule, but we use phonon as a shorthand for molecular vibration.

### 3.3 Calculating phonon modes, which ones are important?

We can find the phonon modes of the polyacetylene molecule by using a finite difference method or by using perturbation theory. In general we can use a finite difference technique to calculate the dynamic matrix, where we displace one atom by a small amount, calculate the forces induced on all the atoms by this displacement and then input all of these forces into the dynamical matrix (the forces so calculated are forces in the harmonic approximation). That is that the displacement of atom  $j$  by an amount  $x$  causes a force on atom  $i$  of amount  $F_i$  which means that the dynamical matrix is

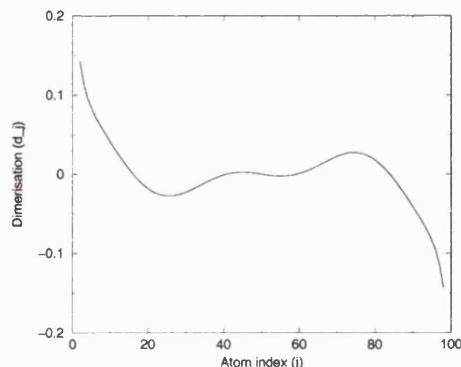


Figure 3.7: Dimerisation pattern of a multiply charged (four electrons or four hole) polyacetylene molecule with ninety nine carbon atoms.

$$K_{ij} = \frac{F_i}{x_j}. \quad (3.8)$$

This then needs to be diagonalised which can easily be done by any number of routines [173]. The eigenstates  $V_q(j)$  of (3.8) are the phonon modes of the finite molecular chain while the eigenvalues  $M\omega_q^2$  of (3.8) are related to the phonon frequency  $\omega_q$  ( $M$  is the mass of the CH group). We are neglecting the fact that the end groups are  $\text{CH}_2$  not CH.

There are several subtleties involved in the calculation of (3.8). One involves the size of the displacement  $x_j$  and one involves the fact that this is a finite difference method. The first problem is that (3.1) is a linear Hamiltonian (which means that the change in energy with distance is for large distances linear in distance), so to find terms proportional to the quadratic in  $x_j$  one needs to make small displacements. However if one makes the displacement  $x_j$  too small then the signal of the elastic force is drowned out by the noise. The dynamical matrix (3.8) should also be symmetric, however in practice it is not. This is due to the finite difference error in calculating the second derivative of energy with respect to distance. We assume that we can write (3.8) as the coefficient of  $\partial^2 E / \partial x^2$  which is not strictly true for a finite difference method. This error can be minimised by using a very small displacement  $x_j$  and then explicitly symmetrising the dynamical matrix. For the polyacetylene molecule discussed in this chapter, the equilibrium structure is found when the forces on every atom was less than  $10^{-7}$  Hartrees per Bohr and using a displacement  $x_j$  of order  $5 \times 10^{-5}$  Bohr.

However it is also possible to find the dynamical matrix analytically using perturba-

tion theory, which is what we do to find (3.8) for the case of (3.1). This is based on the method of Chao *et al.* [174] and the discussion of Wallace [59]. It is possible to write a time-dependent version of the SSH Hamiltonian as  $H = H_{\text{ST}} + H_{\text{PH}} + H_{\text{EP}}$  where  $H_{\text{ST}}, H_{\text{PH}}$  and  $H_{\text{EP}}$  are the static, phonon and electron-phonon coupling terms in the SSH Hamiltonian and are as written as follows

$$H_{\text{ST}} = - \sum_j (t_0 - \alpha(u_{j+1}^0 - u_j^0)) [c_{j+1}^\dagger c_j + c_j^\dagger c_{j+1}] + \frac{1}{2} K \sum_j (u_{j+1}^0 - u_j^0 + C)^2 \quad (3.9)$$

$$H_{\text{EP}} = \alpha \sum_j (x_{j+1} - x_j) [c_{j+1}^\dagger c_j + c_j^\dagger c_{j+1}] \quad (3.10)$$

$$H_{\text{PH}} = K \sum_j (x_{j+1} - x_j)(u_{j+1}^0 - u_j^0 + C) + \frac{1}{2} K \sum_j (x_{j+1} - x_j)^2 + \frac{1}{2} M \sum_j \dot{x}_j^2 \quad (3.11)$$

where we neglect all spin suffixes. The atomic displacements in the above equation have been written in terms of their equilibrium value  $u_j^0$  and their displacements from equilibrium  $x_j$ .

$H_{\text{EP}}$  is treated as a perturbation on the original electronic Hamiltonian. The condition that the chain is in equilibrium at  $u_j = u_j^0$  allows the cancellation of the first order term (of the expansion of E in powers of  $\alpha$ ) by the linear term in  $H_{\text{PH}}$  and the second order term gives the changes we must make to the calculated phonon frequencies. This second order correction is given by:

$$\Delta E = \sum_{\Phi \neq \Psi} \frac{|\langle \Phi | H_{\text{EP}} | \Psi \rangle|^2}{E(\Phi) - E(\Psi)} \quad (3.12)$$

where  $\Psi$  is the ground state.

We can write  $H_{\text{EP}}$  in (3.12) in terms of one-electron eigenstates  $|n\rangle$  for occupied states (or  $|m\rangle$  for unoccupied states)

$$H_{\text{EP}} = \alpha \sum_n^{\text{occ}} \sum_m^{\text{unocc}} \sum_j (x_{j+1} - x_j) (Z_m^*(j+1)Z_n(j) + Z_m^*(j)Z_n(j+1)) c_m^\dagger c_n. \quad (3.13)$$

Orthogonality means that we can ignore all  $|\Psi\rangle$  except those with one electron promoted to a different one-electron eigenstate. Thus

$$\langle \Phi | H_{\text{EP}} | \Psi \rangle = \alpha \sum_j (x_{j+1} - x_j) (Z_m^*(j+1)Z_n(j) + Z_m^*(j)Z_n(j+1)) \quad (3.14)$$

which means that (3.12) is

$$\begin{aligned} \Delta E &= \alpha^2 \sum_n^{\text{occ}} \sum_m^{\text{unocc}} \sum_{j,i} ((x_{j+1} - x_j) (Z_m^*(j+1)Z_n(j) + Z_m^*(j)Z_n(j+1))) \\ &\quad \times ((x_{i+1} - x_i) (Z_m^*(i+1)Z_n(i) + Z_m^*(i)Z_n(i+1)))^* \times \frac{1}{\epsilon(n) - \epsilon(m)} \end{aligned} \quad (3.15)$$

where  $\epsilon(m)$  and  $\epsilon(n)$  are one-electron energies. The above equation can then be rewritten as

$$\Delta E = \alpha^2 \sum_n^{\text{occ}} \sum_m^{\text{unocc}} \sum_{j,i} x_j x_i \frac{A_{j,n,m} A_{i,n,m}^*}{\epsilon(n) - \epsilon(m)} \quad (3.16)$$

where both  $A_{j,n,m}$  and  $A_{i,n,m}$  are of the form

$$A_{j,n,m} = (Z_m^*(j)Z_n(j-1) + Z_m^*(j-1)Z_n(j) - Z_m^*(j+1)Z_n(j) - Z_m^*(j)Z_n(j+1)). \quad (3.17)$$

$\Delta E$  can then be used to find the dynamical matrix in terms of  $\partial^2 E / (\partial x_j \partial x_i)$ , that is that a second order perturbation in  $H_{\text{EP}}$  gives a quadratic term in  $x_j$ . This is equivalent to (3.8) but without any finite difference errors.

This can then be rewritten in terms of the one-electron eigenstates of the system [171]. The dynamical matrix is written as

$$K_{ij} = K_{ji} = 2\alpha^2 \sum_m^{\text{unocc}} \sum_n^{\text{occ}} \frac{(F(i, m, n) - F(i + 1, m, n))(F(j, m, n) - F(j + 1, m, n))}{(\epsilon_n - \epsilon_m)}, \quad (3.18)$$

where  $F(j, m, n) = Z_m(j)Z_n(j - 1) + Z_n(j)Z_m(j - 1)$ .

To solve (2.111) using all of the phonon modes of the molecule would be prohibitively expensive. To demonstrate, assume a truncated phonon space up to a finite number of excitations  $n_{\text{occ}}^{\text{max}}$ , the size of the basis set is given by  $N_{\text{size}} = N_e \times (n_{\text{occ}}^{\text{max}} + 1)^{N_{\text{ph}}}$  with  $N_e$  ( $N_{\text{ph}}$ ) being the number of electronic states (phonon modes). Even for relatively short wires, the size ( $N_{\text{size}}$ ) of the basis set quickly becomes too large for tractable numerical calculations and/or reasonable computing times (as we have to diagonalise (2.111)). For example for  $N_a = 20$  atomic sites ( $N_{\text{ph}} = 19$  acoustic and optic phonon modes) with only  $n_{\text{occ}}^{\text{max}} = 2$ , we obtain  $N_{\text{size}} \gg 10^6$ .

Obviously we need to make sensible approximations that reduce the size of the basis set size. For the case of the SSH Hamiltonian (3.1) we can reduce the basis set by considering only the valence band or conduction band states only (this is because the SSH Hamiltonian has charge conjugation parity). This way we remove some of the complexity of the full basis set, and as we consider only the transport of one electron or hole in the molecule at a time we do not need the full complicated basis set anyway. There are also two other approximations that we can make to reduce the basis set size, both of which are quite general. These are (i) considering a limited but sufficient set of phonon modes and (ii) using only a few excitations in each phonon mode (truncated harmonic oscillator approximation).

In order to determine which phonon modes strongly contribute to the charge-induced deformation of the chain, we calculate the ground state atomic configurations for a neutral chain  $u_j^0$  and for a chain charged with one additional electron  $u_j^c$ . The lattice distortion is then projected onto the harmonic modes of vibration  $V_q$  of the neutral chain and the corresponding Huang-Rhys factor  $S_q$  (1.13) is calculated,

$$S_q = \frac{\frac{1}{2}M\omega_q^2\Delta_q^2}{\hbar\omega_q} \quad (3.19)$$

where  $\Delta_q = \sum_j V_q(j)(u_j^c - u_j^0)$ . These factors give the averaged number of phonons that would be needed to achieve the corresponding elastic energy of the lattice distortion (the lattice distortion can be expanded onto the harmonic phonon modes as  $u_j = u_j^0 + \sum_q V_q(j)\Delta_q$ ). For the polyacetylene molecule the largest values for these factors are obtained for the lowest energy (longest wavelength) optical phonon modes. In fact, the phonon mode that dominates the lattice distortion is the lowest optical phonon mode, which has a Huang-Rhys factor  $S_q \geq 0.8$ . For a one hundred atom chain the largest  $S_q$  is 0.825 and the next highest is  $3.66 \times 10^{-3}$ . We can thus reduce the basis set size by just considering the lowest wavelength optical phonon modes to describe the lattice deformation induced by the injection of an electron. The acoustic phonon modes do not couple to the polaron at all. To see what these phonon modes would look like for a hundred atom chain, see Figure 3.8.

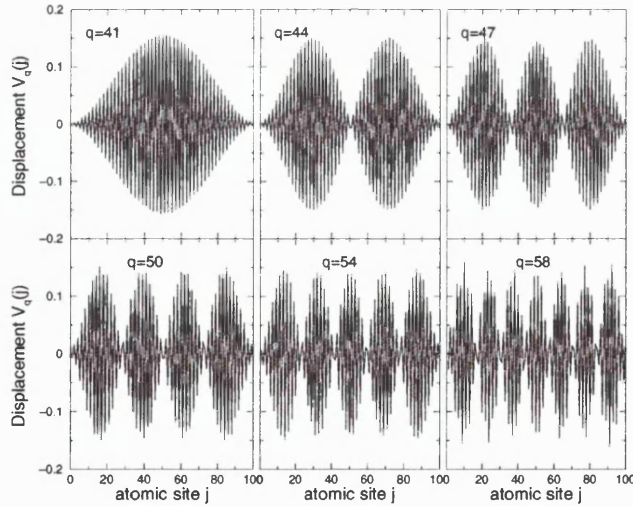


Figure 3.8: Lowest energy optical phonons  $V_q$  for a polyacetylene molecule containing one hundred carbon atoms. The indices are ordered so that as  $q$  increases the frequency of the phonon mode  $q$  increases.

We can check to see if the harmonic approximation is valid by comparing the energy gain of the chain with a polaron with the energy of the phonon modes that are needed to form the defect, that is comparing  $\Delta E = E_0[u_j^c] - E_0[u_j^0]$  with  $E_{harmonic} = \sum_q \frac{1}{2} M \omega_q^2 \Delta_q^2 = \sum_q \omega_q S_q$ . We use  $E_0[u_j^c]$  as the non-self consistent total energy of the chain with the polaron and  $E_0[u_j^0]$  is the self consistent energy of the neutral chain. Although the deformation of the lattice is not purely harmonic, we can use this check to see whether the energies are in the same order of magnitude. For short chains the

values of  $\Delta E$  and  $E_{\text{harmonic}}$  are almost identical (to within 5%) and for longer chains the discrepancy between  $\Delta E$  and  $E_{\text{harmonic}}$  increase but do not exceed 15%. Our phonons seem to be in the harmonic limit.

### 3.4 Calculation of electron-phonon coupling

So, once we set up our reference system (which is chosen to be a neutral polyacetylene chain with either an even or odd number of carbon atoms), we can write the Hamiltonians for the non-interacting electronic and *quantum* phonon degrees of freedom as

$$H_E = \sum_n \epsilon_n c_n^\dagger c_n \quad (3.20)$$

where  $c_n^\dagger = \sum_j Z_n(j) c_j^\dagger$  creates (or  $c_n$  annihilates) an electron in the  $n$ th electronic state with energy  $\epsilon_n$ . Neglecting the zero-point energy, the harmonic phonon Hamiltonian can be written as

$$H_{PH} = \sum_q \omega_q a_q^\dagger a_q \quad (3.21)$$

where  $a_q^\dagger$  creates a phonon in mode  $q$  with frequency  $\omega_q$  (and  $a_q$  annihilates a phonon). The basis set associated with a single added electron or hole  $H_E + H_{PH}$  is formed by the eigenstates  $|n, (n_q)\rangle = c_n^\dagger \prod_q \frac{(a_q^\dagger)^{n_q}}{\sqrt{n_q!}} |0\rangle$  with eigenvalues  $\epsilon_{n, (n_q)} = \epsilon_n + \sum_q n_q \omega_q$  and where  $|0\rangle$  is the original neutral state of the polyacetylene molecule and  $(n_q)$  the set of phonon occupation numbers.

To then find the electron-phonon coupling constants we expand the lattice deformations  $\delta u_j$  induced by an additional charge injected into the chain onto the phonon modes of the neutral chain:  $\delta u_j = \sum_q V_q(j) \Delta_q$ . The new lattice structure displaced from the original equilibrium structure  $u_j^0$  is  $u_j^0 + \delta u_j$ . Then the electron-phonon coupling terms of the SSH Hamiltonian (3.1) (assumed to be linear) are written in a quantum form by quantising the phonon field displacements

$$\delta_q = \sqrt{\frac{\hbar}{2M\omega_q}} (a_q + a_q^\dagger) . \quad (3.22)$$

Therefore the electron-phonon coupling Hamiltonian is

$$H_{E-PH} = \sum_{q,n,m} \gamma_{qnm} (a_q^\dagger + a_q) c_n^\dagger c_m , \quad (3.23)$$

where

$$\gamma_{qnm} = \sum_{j=2}^{N_a} \lambda_q(j) [Z_n(j)Z_m(j-1) + Z_n(j-1)Z_m(j)] , \quad (3.24)$$

and

$$\lambda_q(j) = \alpha[V_q(j) - V_q(j-1)] \times \sqrt{\frac{\hbar}{2M\omega_q}} . \quad (3.25)$$

The total Hamiltonian  $H_w$  for the molecular wire with quantum phonons and linear electron-phonon coupling inspired by the SSH model is given by the sum  $H_w = H_E + H_{PH} + H_{E-PH}$  as in (2.95).

For the particular case of the polyacetylene molecule modelled using the SSH Hamiltonian (3.1) the calculation of (3.24) can be greatly simplified by the use of selection rules.  $Z_n$  and  $V_q$  are even or odd functions with respect to the centre of the molecule. The quantity  $Z_n(j)Z_m(j-1) + Z_n(j-1)Z_m(j)$  is even (odd) when  $n+m$  is an even (odd) integer (indexing the eigenvectors  $Z_n$  by increasing eigenvalues and  $Z_{n=1}$  being even). Whenever the quantity under the site  $j$  summation in (3.24) is odd,  $\gamma_{qnm} = 0$  (this is equivalent to the property that the integration of an odd variable from  $-x$  to  $+x$  is zero). This can greatly reduce computational time when trying to calculate the transport properties of the polyacetylene molecule, as discussed in the next section.

Why do we perform the transformation from classical phonons to quantum phonons in the first place? It is because we are dealing with the full wavefunction of the electron. If we consider the wavepacket picture of an electron travelling through the molecule then when an electron meets the junction between the leads and the wire then part of the wavepacket is reflected away from the wire and part of the wavepacket is transmitted into the wire. The part of the wavepacket that is in the wire is treated as the full

electron, and it can only be treated as the full electron if we can include the vibrational part of the wavefunction. This requires us to use quantum phonons.

### 3.5 Transport properties: A brief discussion

We now provide a brief discussion of the transport properties of the chain when an electron or hole is injected into a chain with an even number of CH units and thus forms a polaron. For a more detailed review the reader is invited to read the papers of Ness *et al.* [20, 21, 171].

A major difference between our transport calculations and others, is that in our calculations the molecule responds to injection of charge by distorting. In the transport calculations of, for instance, Joachim *et al.* [13, 14, 15, 47, 77] the molecule is rigid while the charge carrier travels through the molecule. In order to represent this distortion we sum over the phonon modes  $\sum_q V_q(j)\delta_q$ . However as stated previously the basis set grows exponentially with the number of phonon modes that are present in the system. We used the Huang-Rhys factor to show that the dominant phonon mode is the lowest optical mode. However to describe the translation of the polaron through the molecule we need more phonons than the lowest optical mode, so in practice we use a set of the lowest optical phonon modes.

As stated in the last Chapter the current that is flowing through outgoing modes of the wire is given by (2.121), that is

$$J_{j \geq N_a}^{(m_q)} = 2\Im[\alpha_{j,(m_q)}^* \beta_{k,j} \alpha_{j+1,(m_q)}]. \quad (3.26)$$

for sites  $j \geq N_a$  that exist in the right lead (as we adopt the convention that the net current only flows from left to right). The total transmission probability is then given by (2.120).

We present results for the injection of an electron into the gap (transport by tunnelling effect) and also by resonant transport through the levels of the system above the gap (that is in the conduction band). We define the electron injection energy as positive with respect to the reference energy  $E=0$  for all lengths of molecule. The Fermi energy is assumed to be pinned at mid-gap in absence of any bias. We show typical results for

the effective total transmission  $T(E)$  showing the contribution from the elastic channel and one inelastic channel in Figure 3.9. As expected the transmission probabilities have an exponential behaviour in the tunnelling regime  $e^{2Kd}$  (which is below the first resonance peak). The main contribution is from the elastic channel and there are resonances throughout the system at higher energies. Note that the transmission probability at resonance does not equal one. This is because the interaction of many resonance levels in the molecule brings down the transmission probability [47].

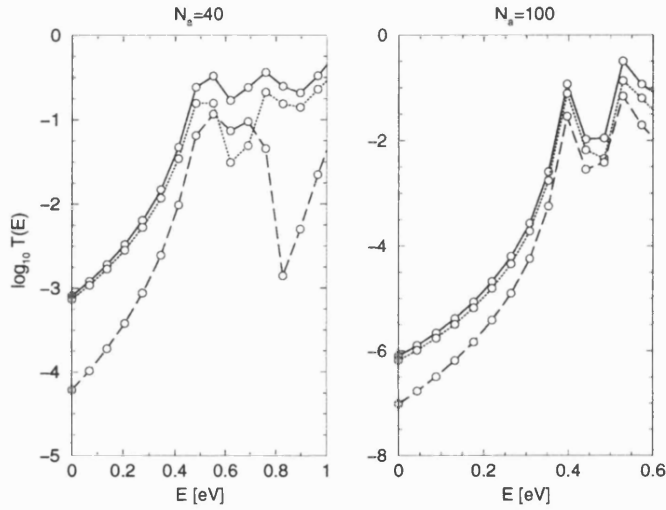


Figure 3.9: Effective transmission probability  $T(E)$  on a logarithmic scale vs electron injection energy  $E$  for two molecules with different lengths (one has 40 CH units with six phonon modes and a maximum phonon occupation of two phonons per mode, and one has 100 CH units with four phonon modes and a maximum phonon occupation of three phonons per mode). Total transmission probability is shown as the solid line, transmission from the elastic channel  $|t_{(0)}(E)|^2$  are the dotted lines and transmission from the first inelastic channel  $n_{q=1}=1$  and  $n_{q\geq 1}=0$  are shown as the dashed lines.

As can be seen below the first resonance, the contribution of the inelastic channels is negligible. Above the first resonance the inelastic contributions become as important as the contribution from the elastic channel. It should be noted that although the elastic channel dominates the transmission probability, the transport properties of our system are quite different from the calculated transmission probability of a molecule using just the elastic channel by itself. This is because as the coherent quantum electron-phonon coupling has a strong effect on the effective bandgap. This is due to the formation of the virtual polaron which reduces this effective bandgap [20, 171]. This is one of two effects that can reduce the effective bandgap. The other is that as the length of the molecule increases the effective bandgap reduces. This reaches an asymptotic limit when

the molecule becomes longer than a hundred CH units. Conversely this means that when a molecule is quite short ( $N_a \leq 10$ ) then the effective bandgap is quite large because of the variation of bandgap with length as mentioned above. If the molecule is shorter than this size then the injection of the electron into the chain cannot result in the formation of the polaron or the reduction of the bandgap that then results from the electron-phonon coupling. We do not discuss further the effects of the coherent electron-phonon coupling here, rather we refer the reader to the cited papers above.

### 3.6 Conclusion

In this chapter we have discussed the theoretical testbed molecular wire trans-polyacetylene and how we can use the simple SSH Hamiltonian to find the structure of a polyacetylene molecule under various conditions such as charge state or parity. We then detailed how to find the classical phonon modes of the molecule and which phonon modes couple strongly to the polaronic or solitonic defects that form in the molecule, and how to calculate the electron-phonon coupling constants that can strongly affect electron transport through the molecule. Finally we provided a small amount of detail about the transport properties of a molecule which has a virtual polaron injected into it and found that the coherent electron-phonon coupling strongly affected the transport properties.

However what other prospective atomic scale wires could demonstrate properties similar to the polyacetylene molecule such as a Peierls distortion, polaron formation etc.? In the next chapter we detail one such prospective atomic scale wire, the atomic silicon line on the  $\beta$ -SiC(001) surface. We discuss how this atomic line is formed, the various structural components that are believed to form this line and the surface it resides upon, the models of these components, the structure of these models, the electronic properties of these models and which model is thermodynamically favoured.

## Chapter 4

# Silicon carbide: *Ab initio* studies of the $(3\times 2)$ and $c(4\times 2)$ surfaces

This chapter describes the silicon atomic lines that form on the (001) face of cubic silicon carbide. We discuss the basic physical properties of the binary compound silicon carbide, and how these properties differ for various different polytypes. We then discuss the physical characteristics of the silicon atomic lines and how they are believed to form. This will then necessitate a discussion of the various models of the reconstructions which are believed to form the structural components of the line and the surface the line resides upon.

We will then discuss the work that we have performed using the PAW approach [136], starting off with various tests that we have performed on the utility of projectors in simulating the silicon carbide crystal, tests of our supercell and tests to see how well converged our calculations are with respect to plane wave cutoff,  $k$ -point sampling and vacuum gap spacing. We then start with the results of our *ab initio* simulations on the  $(3\times 2)$  surface for various models, and our analysis of the structural properties, the electronic properties and which of the various candidate models is thermodynamically preferred. After we have determined which is the preferred model for the structural components of the line we then turn to the analysis of our simulations of the  $c(4\times 2)$  reconstruction and again

analyse the structural, electronic and thermodynamic properties of the various models of the surface. We then finish this chapter with our general conclusions about the line and the surface it resides upon.

## 4.1 Review of silicon carbide

### 4.1.1 Background information on silicon carbide

Silicon carbide (SiC) is a binary compound consisting of two group-IV elements, silicon and carbon (it is in fact the only naturally stable group-IV compound [175]). It was first synthesised in 1891 by Eugene G. Acheson following the work of Jöns Jakob Berzelius on the possibility of a silicon-carbon bond [176]. Soon after its formation the phenomenon of polytypism (which will be discussed later) was discovered along with semiconducting electrical characteristics. However the Acheson method of preparation did not lend itself to industrial scale applications and so the use of silicon carbide as an industrial material was delayed until 1955 when Jan Antony Lely at Phillips perfected a new class of high temperature crystal furnace [177, 178]. Recently the development of such materials processing technologies as molecular beam epitaxy (MBE) and chemical vapour deposition (CVD) have enabled the fabrication of high quality device structures and increased research activity on the material (of which this thesis is one example). However we (as a species) should not feel pride in our ability to synthesise SiC crystals as microcrystals of the material have been found in meteorites which have been dated to before the formation of our Solar System.

The wide bandgap, high thermal conductivity, robust mechanical properties and resistance to radiation damage have made SiC an attractive material for such applications as high temperature, high power devices and nuclear power applications. SiC may also be a useful material for various optical applications such as blue and ultraviolet light emitting devices and detectors [178] (although GaN devices are more successful in this area). As a ceramic SiC has a very high hardness surpassed only by diamond and boron nitride. Finally SiC is one of the best bio-compatible materials, especially in regard to compatibility with human blood [109].

SiC is a tetrahedral compound with each silicon atom bonding to four surrounding carbon atoms (and vice versa, see Figure 4.1). Depending on the stacking of atoms in one

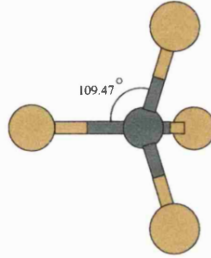


Figure 4.1: The bonding scheme of cubic silicon carbide. Each carbon atom (black) is bonded to four silicon atoms (yellow) in a tetrahedral arrangement. The bond angle is  $109.47^\circ$ .

direction SiC can possess more than one type of crystal structure (this polytypism is the one-dimensional variant of polymorphism [118]), ranging from purely cubic (zinc-blende) to the purely hexagonal (wurtzite) with more than two hundred polytypes in between [175].

We shall use the Ramsdell notation [179] to denote different types of crystal structure, using 3C for purely cubic crystals and 2H for purely hexagonal. The number refers to the number of atomic bilayers one has to stack perpendicular to the trigonal axis before recovering the original atomic position (so for cubic crystals the number of atomic layers is three in the (111) direction and for purely hexagonal crystals the number of atomic layers is two in the (0001) direction). This polytypism is due to the fact that successive planes along a trigonal axis can be displaced, and that there are three equivalent possibilities [118] (see Figure 4.2). These possibilities can be combined in any order, which results in the wide range of different polytypes that are available. Except for the cubic structure, all other polytypes represent hexagonal (H) or rhombohedral (R) combinations of these stacking sequences with  $n$  Si-C bilayers in the primitive cell. Examples would include 4H and 6H with four (six) double layers and eight (twelve) atoms in the primitive unit cell. It is possible to change the crystal structure from one polytype to another [180], but in our simulations we use one polytype only.

The three polytypes that have received the most attention are 6H-SiC, 3C-SiC and 4H-SiC. The first polytype to be manufactured at the industrial scale was 6H-SiC. 3C-SiC can be fabricated in bulk but is usually replete with defects. To minimise the number of defects in 3C-SiC it is a common practice to grow 3C-SiC epitaxially on a Si substrate.

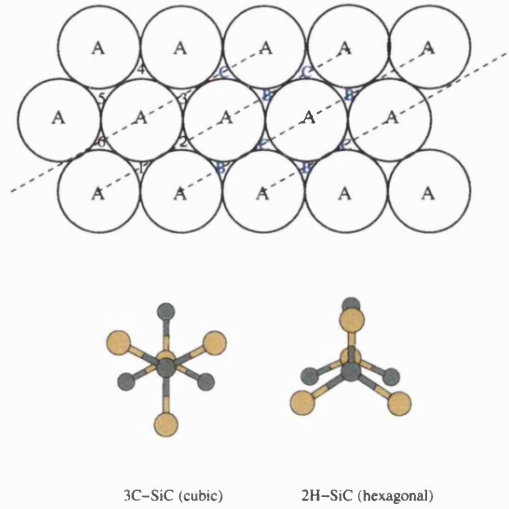


Figure 4.2: Illustration of polytypism based upon close packing of spheres (the spheres must be all of the same type: for silicon carbide they must all be silicon or carbon atoms only). Displaced initial layer contains spheres in A-type positions surrounded by six voids (top). Spheres of the next layer are situated either in the voids 1, 3 and 5 (B type) or in voids 2, 4 and 6 (C type positions). Spheres of any polytype have their centres located in parallel vertical planes whose interactions with the ground plane are represented by parallel lines (dashed lines). Taken from *Defects and Defect Processes in Nonmetallic Solids*, by W. Hayes and A. M. Stoneham, (1985). Other diagram shows bond orientation of the cubic (stacking sequence ABCA) and hexagonal (stacking sequence ABA) polytypes.

All polytypes of silicon carbide are wide bandgap semiconductors, with the gap indirect. However the bandgap is not the same for each polytype, rather there is a strong variation of bandgap with respect to polytype (in contrast to other semiconductors which possess polytypism, such as ZnS). The bandgap varies from 2.4 eV for 3C-SiC to 3.3 eV for 4H-SiC, with the increase in bandgap depending in a linear manner on the degree of ‘hexagonality’ involved (although this is only true up to a factor of 50% after which the variation with hexagonality is much less strong [181]). The degree of hexagonality is defined as the proportion of the unit cell which does not have a cubic stacking sequence [181].

In this thesis we are only interested in the specific polytype 3C-SiC, as the surface we want to study exists for this polytype. Experimentally the lattice parameter of the unit cell is found to be 4.36 Å with a surface lattice parameter of 3.08 Å [178]. The Young’s modulus in the literature is found to be in the region of 392-448 GPa [176]. The length of the silicon-carbon bond is 1.89 Å. The lattice parameter of 3C-SiC possesses a lattice mismatch of ~20% when compared with the lattice parameters of silicon or diamond (the carbon-silicon bond is ~20% longer than a carbon-carbon bond and ~20% shorter

than a silicon-silicon bond). This has several consequences: firstly that when 3C-SiC is grown as a film on a Si substrate, the interface between the two materials possesses an associated strain field. This strain is relieved by the formation of anti-phase boundaries that typically extend throughout a silicon carbide film for a  $\mu\text{m}$  [182]. Secondly, an unreconstructed Si or C-terminated SiC surface is under compressive or tensile stress. This stress is a driving force for significant reconstructions on both surfaces.

In the next section we detail one possible result of this stress on the silicon-rich surface of 3C-SiC, the formation of the  $(n \times 2)$  series of reconstructions. (A note on notation: throughout the following three chapters we will use the terms silicon carbide and SiC interchangeably, as well as  $\beta$ , 3C and cubic.)

#### 4.1.2 The $(n \times 2)$ series of reconstructions (silicon atomic lines):

##### Physical characteristics and method of formation

As mentioned above the specific polytype of silicon carbide that we study is the cubic or zinc-blende polytype. To minimise the high defect density that is present in bulk cubic silicon carbide it is common to grow thin ( $\approx 1\mu\text{m}$ ) SiC films by the chemical vapour deposition (CVD) of (for instance) acetylene ( $\text{C}_2\text{H}_2$ ) and silane ( $\text{SiH}_4$ ) molecules on vicinal ( $4^\circ$ ) Si(100) wafers [109, 183, 184]. This means that as we move along the [100] direction we encounter alternating atomic planes of carbon and silicon. The growth of these thin films on Si(100) leads to a high quality crystal with a much lower defect density [109], and as the film has a thickness of order micrometers the majority of the film can be treated as bulk silicon carbide rather than as a strained crystal.

This method of formation of cubic silicon carbide results in the surface of the crystal being initially covered by oxides, primarily silica ( $\text{SiO}_2$ ), and various graphitic carbon species [109]. To remove these contaminants it is common to anneal the surface at a temperature of 1300 K (that is heat the film to remove part of the surface and then cool down again). Removal of the contaminants results in the formation of the silicon-rich  $(3 \times 2)$  reconstruction [108, 109, 185, 186, 187, 188, 189], which is the most silicon-rich stable reconstruction of the (001) face of cubic silicon carbide [185, 190, 191]. This surface can itself be annealed to remove the  $(3 \times 2)$  reconstruction and form the less-silicon-rich  $c(4 \times 2)$  [106, 192, 193, 194, 195] (or the  $(2 \times 1)$  reconstruction [196, 197]). (The  $(3 \times 2)$  reconstruction can also be formed by Si deposition on the  $c(4 \times 2)$  surface at

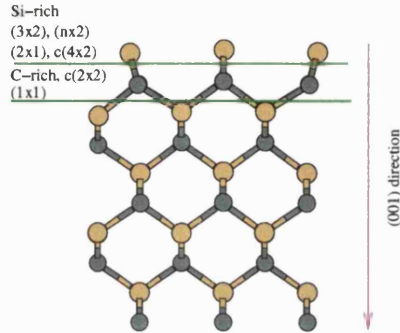


Figure 4.3: Schematic of alternating levels of silicon and carbon atoms (in the [001] direction) of the cubic polytype of silicon carbide. Different surface reconstructions correspond to various surface stoichiometries of silicon or carbon.

1200 K). Continued annealing of the (001) face results in the removal of the entire top silicon atomic layer and the formation of the carbon-rich  $c(2 \times 2)$  reconstruction [198, 199]. Annealing this surface results in the formation of the ideal  $(1 \times 1)$  reconstruction for the carbon-terminated surface [196, 200, 201]. The carbon atomic layer can once again be annealed to recover the  $(3 \times 2)$  reconstruction which is formed from the silicon atomic layer below (see Figure 4.3).

It has been found by STM that annealing the highly silicon-rich  $(3 \times 2)$  surface at 1300 K for several minutes leads to the formation of a grating of very long ( $\sim 1000$  Å), very straight, very stable (at 900 K) lines at the transition from the  $(3 \times 2)$  to  $c(4 \times 2)$  surface [108, 109, 188, 202, 203], with the separation between the lines of magnitude  $\sim 6$  Å. Additional heat treatment leads to the removal of this grating and the formation of widely separated atomic lines [105, 107, 108]. We refer to this sequence of structures as the  $(n \times 2)$  series of reconstructions where  $n$  is an odd number, thus we get the series  $(5 \times 2)$ ,  $(7 \times 2)$  etc.. These complex  $(n \times 2)$  reconstructions consist of two subunits: the structural elements corresponding to the area between the lines, and the structural elements corresponding to the lines themselves.

In STM images of these lines [107, 109] (see Figure 4.4) the bright regions appear to be  $\sim 9$  Å wide and the separation of these bright features along the line appears to be  $\sim 6$  Å. As stated before the surface lattice vector of the  $\beta$ -SiC (001) surface is 3.08

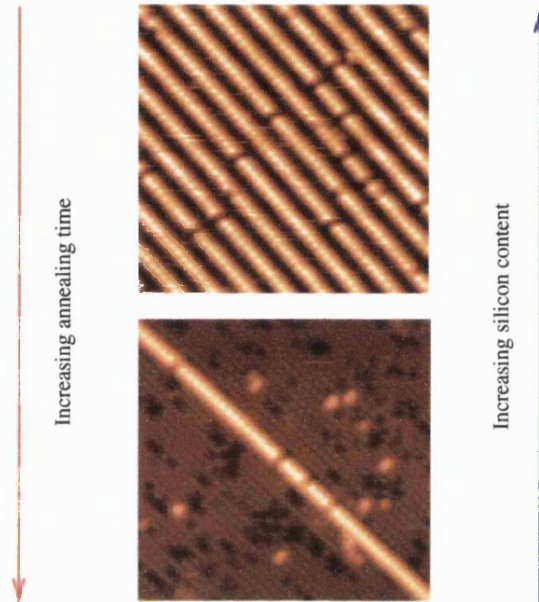


Figure 4.4: Formation of atomic-scale silicon lines on the (001) face of cubic silicon carbide. The top image is a STM scan of the surface after annealing at  $\approx 1300$  K and covers an area  $320 \text{ \AA}$  by  $320 \text{ \AA}$ . Bottom image shows a  $200 \text{ \AA}$  by  $200 \text{ \AA}$  topograph of the surface after annealing at a temperature of  $1350$  K. The next nearest silicon line is  $400 \text{ \AA}$  away. These STM scans are taken from Soukiassian *et al.* Phys. Rev. Lett. **79**, 2498, (1997).

$\text{\AA}$ . The dimensions of the repeat unit cell are very close to three by two lattice vectors, and so it is believed that these lines are formed from the same structural components as the silicon-rich  $(3 \times 2)$  reconstruction. The surface that is present between the silicon lines is believed to be the  $c(4 \times 2)$  reconstruction from inspection of the STM scans of the surface between the lines [109]. The silicon lines are straight and long (several hundred  $\text{\AA}$  in extent). The silicon line induces an antiphase relationship between the two  $c(4 \times 2)$  domains, that is that the periodicity of the  $c(4 \times 2)$  domain on one side of the line is shifted by  $\sim 3 \text{ \AA}$  compared to the  $c(4 \times 2)$  domain on the other side of the line. It is believed that the silicon lines are an intrinsic feature of the surface, they are not formed by spare silicon atoms decorating preexisting domain boundaries between two  $c(4 \times 2)$  domains.

We therefore use the following paradigm in our modelling of the silicon lines (see

Figure 4.5): that the structural components of the lines are identical to the  $(3 \times 2)$  reconstruction, and that the surface between the lines is composed of  $c(4 \times 2)$  unit cells (or parts thereof) (see Kitamura *et al.* [203] ), however we first of all need suitable models for the  $(3 \times 2)$  reconstruction and the  $c(4 \times 2)$  reconstruction.

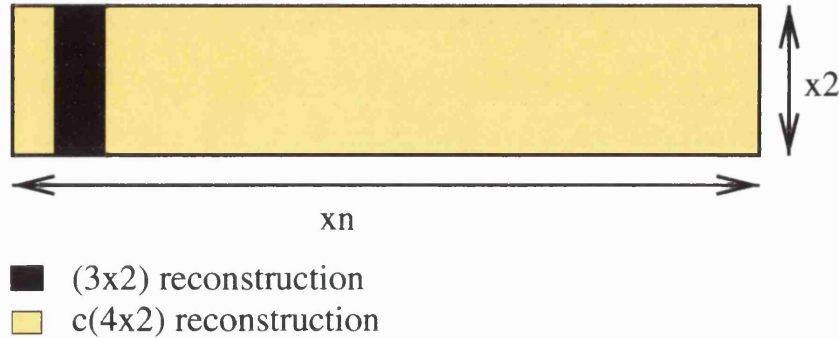


Figure 4.5: Paradigm of how we model the silicon lines (the  $(n \times 2)$ ) reconstruction. The line is composed of a single  $(3 \times 2)$  unit cell and the surface is composed of several  $c(4 \times 2)$  unit cells.

#### 4.1.3 Models of the $(3 \times 2)$ reconstruction and relevant experimental evidence

There are several different models of the  $(3 \times 2)$  surface, with a different silicon stoichiometry for each model. All of the models that have been proposed assume that the  $(3 \times 2)$  reconstruction consists of the surface atomic layer of the silicon carbide crystal proper (the *terminating layer*) consisting of silicon and that on the surface several silicon adatoms are present. When we quote the stoichiometry of a particular model of the surface reconstruction we will be quoting the stoichiometry of the Si adlayer. Several experiments have been performed that have tried to measure the stoichiometry of the  $(3 \times 2)$  surface and other  $(n \times 2)$  reconstructions ( $n = 5, 7$ ). MEIS results [185] confirm that as  $n$  increases the silicon content of the reconstruction falls and that the  $(3 \times 2)$  and  $(5 \times 2)$  reconstructions have  $\approx 0.36$  ML and  $\approx 0.16$  ML more silicon than the  $(2 \times 1)$  reconstruction. However there is a lack of experimental agreement on the actual stoichiometry of Si adatoms on the  $(3 \times 2)$  reconstruction [185, 191, 204].

The various models that have been proposed in the literature possess surface stoichiometries ranging from  $1/3$  ML to 1 ML of silicon. In order of increasing silicon content the models that we studied are the Additional Dimer Row Model (ADRM) [107,

109, 188, 191, 205, 206], the Double Dimer Row Model (DDRM) [183, 186, 187, 191, 207] and the Two Adlayer Asymmetric Dimer Model (TAADM) [208, 209]. In this section we detail the experimental evidence for each of the models. In all models we define the  $\overline{[110]}$  direction to refer to the  $\times 2$  direction and the  $[110]$  direction to refer to the  $\times 3$  direction.<sup>1</sup>

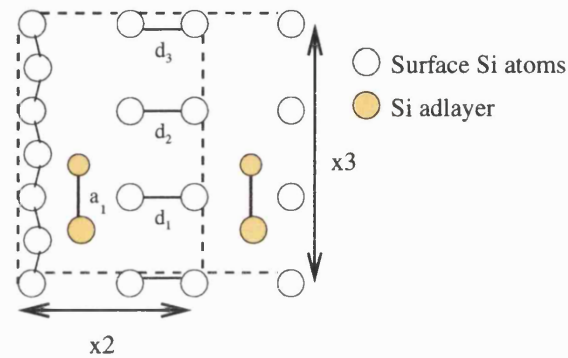


Figure 4.6: The Additional Dimer Row Model proposed by Yan *et al.*, Surf. Sci. **316**, 181, (1994) and Semond *et al.*, Phys. Rev. Lett. **77**, 2013, (1996). It consists of one silicon addimer per unit cell.

The ADRM possesses a silicon stoichiometry of  $1/3$  ML ( $\theta_{\text{Si}}^{\text{ad}} = 1/3$ ) with one silicon addimer per unit cell (see Figure 4.6). The Si atoms of the terminating layer are dimerised in the  $\times 2$  direction. The Si addimer is oriented perpendicular to the terminating layer Si dimers (or surface dimers). The model was first proposed by the theoretical work of Yan *et al.* [205, 206]; firstly by a Tersoff potential calculation [205] and then by an *ab initio* Carr-Parrinello DFT calculation [206]. This model has been used to analyse the STM data on high quality single domain surfaces obtained by Semond *et al.* [188]. Using an STM (and making sure that the results were reproducible and tip independent) Semond *et al.* imaged one oval spot per  $(3 \times 2)$  unit cell in filled states images and two oval spots per  $(3 \times 2)$  unit cell in empty states images (see Figure 4.7). If we are to apply the interpretation of the silicon (001) surface to the  $(3 \times 2)$  reconstruction of the (001) surface of cubic silicon carbide (the silicon rich reconstruction) then it would seem that Semond *et al.* are imaging a single addimer per unit cell with the filled states scan imaging the addimer and the empty states scan imaging the two silicon adatoms of the addimer. Scans along and across the  $(3 \times 2)$  unit cells seem to show that this addimer is asymmetric or buckled. The ADRM also matches the silicon stoichiometry data of

<sup>1</sup>This is consistent with the literature. We consistently use the  $\overline{[110]}$  direction to refer to the  $\times 2$  direction, no matter the orientation of the unit cell. This means that the  $\overline{[110]}$  directions of the  $(3 \times 2)$  and  $c(4 \times 2)$  unit cells are parallel and the  $\overline{[110]}$  directions of the  $(2 \times 3)$  and  $c(4 \times 2)$  unit cells are perpendicular.

Hara *et al.* [185] by giving a silicon adlayer stoichiometry of  $\approx 1/3$  ML for the  $(3\times 2)$  reconstruction and  $\approx 1/5$  ML for the  $(5\times 2)$  reconstruction. This apparent agreement depends upon the exact stoichiometry of the  $c(4\times 2)$  reconstruction, of which there are several models (see the next section).

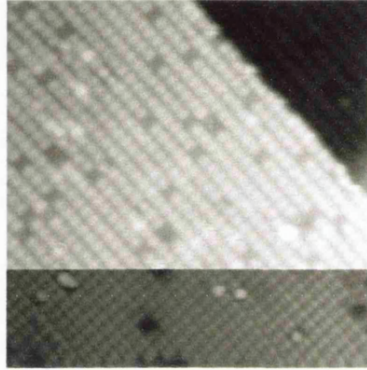


Figure 4.7: STM scan of the  $(3\times 2)$  surface using both filled (top) and empty (bottom) states. Taken from Semond *et al.*, Phys. Rev. Lett. **77**, 2013, (1996).

However, strictly speaking the ADRM is not a model of the  $(3\times 2)$  reconstruction but a model of the  $(2\times 3)$  reconstruction. LEED data [204] shows that the “ $\times 2$ ” direction is parallel to the “ $\times 2$ ” direction of the  $c(4\times 2)$  surface that is formed when the top silicon atomic layer reconstructs upon the removal of the  $(3\times 2)$  reconstruction. The ADRM has a “ $\times 2$ ” direction that would be perpendicular to the “ $\times 2$ ” direction of the  $c(4\times 2)$  reconstruction. The other two models that have been proposed do not share this problem. Another problem with the ADRM is the lack of agreement with the hydrogenated  $(3\times 1)$ -H reconstruction. In these experiments [186, 207, 210] the  $(3\times 2)$  surface is exposed to a hydrogen flux which breaks all dimer bonds and forms (reversibly) a  $(3\times 1)$ -H reconstruction and then a  $(1\times 1)$  reconstruction as found by LEED [186, 207, 210]. If the dimer bonds were broken in the ADRM then we would expect to get a  $(2\times 3)$ -H reconstruction, which is not observed to occur.

The DDRM possesses a silicon stoichiometry of  $2/3$  ML ( $\theta_{\text{Si}}^{\text{ad}} = 2/3$ ) with two silicon addimers per unit cell. The Si atoms of the terminating layer are dimerised in the  $\times 3$  direction, with the Si atoms between the Si addimers remaining undimerised. The Si addimers are oriented perpendicular to the direction of dimerisation on the surface and may be asymmetric, even buckled in different directions. This model was first proposed by Hara *et al.* [186] as set forth by Dayan *et al.* [207]. In this model the Si adatoms chemisorb as bridges between the atoms in the  $(2\times 1)$  or  $c(4\times 2)$  terminating layer (see

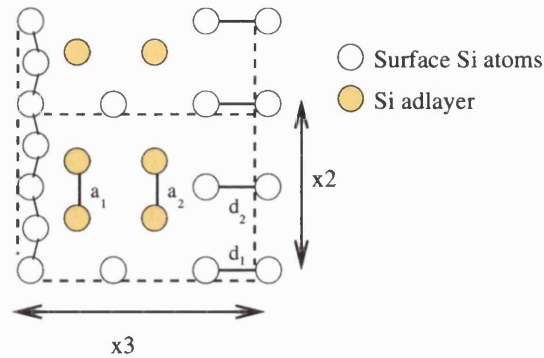


Figure 4.8: The Double Dimer Row Model proposed by Hara *et al.*, Phys. Rev. B **50**, 4548, (1994), and Dayan, J. Vac. Sci. Technol. A **4**, 38, (1985). It consists of two Si addimers per unit cell.

Figure 4.8). Every third adatom row is missing. As we increase  $n$  we simply increase the number of missing rows, so for instance the  $(7 \times 2)$  reconstruction has five missing rows, with the silicon atoms of the terminated layer becoming dimerised. This means that as we increase  $n$  the dangling bond density goes up as  $\frac{n-1}{n}$  [184], meaning that the order of stability decreases as  $n$  increases in agreement with experiment [186].

The DDRM gives a very natural explanation of the  $(3 \times 1)$  reconstruction that is observed when the  $(3 \times 2)$  surface is exposed to hydrogen. However it does not provide an explanation of the reversible transition to a  $(1 \times 1)$  reconstruction upon further exposure of the  $(3 \times 1)$ -H reconstruction to an additional hydrogen flux [210], as for a  $(1 \times 1)$  reconstruction to exist there must be at least 1 ML of Si adatoms. And it has been found that the total Si coverage is conserved in the transition  $(3 \times 2) \rightleftharpoons (3 \times 1) - H \rightleftharpoons (1 \times 1)$  [210]. It is also quite difficult to reconcile the DDRM with the STM scan data as we would have to assume that the STM filled states scans are imaging the pair of addimers and the empty states scans are imaging the individual addimers, in contradiction to the result that is expected from a comparison with the Si(100) surface.

The TAADM possesses a silicon stoichiometry of 1 ML ( $\theta_{\text{Si}}^{\text{ad}} = 1$ ) with three silicon addimers per unit cell (see Figure 4.9). The Si atoms of the terminating layer are dimerised in the  $\times 3$  direction with the middle Si atoms between the Si addimers non-dimerised. The addimers are arranged into two layers, with two silicon addimers chemisorbed as bridges between the atoms of the top silicon terminating layer and the top Si addimer above the two other Si addimers. The Si addimers of the lower layer are oriented perpendicular to the dimers of the terminated layer, while the addimer of the top adlayer is

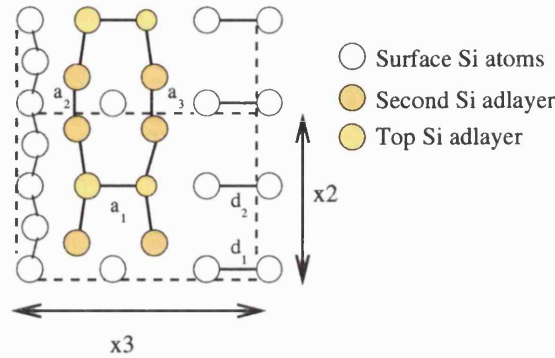


Figure 4.9: The Two Adlayer Asymmetric Dimer Model proposed by Lu *et al.*, Phys. Rev. B **60**, 2495, (1999). It consists of three addimers per unit cell.

oriented perpendicular to the addimers of the lower layer and parallel to the dimers of the terminating layer. Any or all of the addimers may in principle be asymmetric. This model was devised by Lu *et al.* [208] to bridge the experimental gap between the ADRM and DDRM models and seems to explain most of the experimental data. The LEED periodicity it gives is the same as the one obtained by Kaplan *et al.* [204] (and is identical to the DDRM). The simulated STM scans it would give are identical to the STM scan images of the ADRM. Reflectance Anisotropy Spectra (RAS) experiments have recently been performed on the  $(3 \times 2)$  surface [211]. These RAS curves are positive with a strong spectral feature at 4.2 eV. Only the TAADM model gives a positive RAS curve with a feature at 4.2 eV: both the ADRM and DDRM give RAS curves with positive and negative contributions [212].

However it is hard to explain the transition from the  $(3 \times 2)$  reconstruction to the  $(3 \times 1)$ -H reconstruction upon the imposition of a hydrogen flux. If we break all of the dimer bonds in the TAADM then we would expect the surface to maintain a  $(3 \times 2)$  periodicity which is in contradiction to the LEED data. This assumes that the orientation of the top addimer is unchanged following exposure to hydrogen. The TAADM provides an explanation of why the  $(3 \times 1)$ -H reconstruction can reversibly transform to a  $(1 \times 1)$  reconstruction upon further exposure to a hydrogen flux.

Several high quality photoemission studies have recently been performed on the  $(3 \times 2)$  [213, 214, 215] and  $(3 \times 1)$ -H [210] surface reconstructions. It is found that the  $(3 \times 2)$  reconstruction possesses four surface state bands which disappear upon hydrogen adsorption or silicon desorption [214]. All of the surface state bands have a small dispersion throughout the surface Brillouin zone, of magnitude  $\approx 0.2$  eV, with only two surface

states showing a measurable dispersion of 0.2 eV along the  $[\bar{1}10]$  direction and no dispersion along the  $[110]$  direction. Yeom *et al.* found that the only model which matches this data was the DDRM, however at the time the TAADM had not yet been proposed. Lu *et al.* found that the TAADM also matches the angular resolved photoemission (ARPES) data. It has been proposed that the small electronic dispersion is due to “unicellular disorder” [187, 216]. STM scans at room temperature have shown that there is no correlation between the buckle in one unit cell and the next unit cell in the  $\times 3$  or  $\times 2$  direction for a well covered surface. When vacancies are introduced onto the surface the disorder disappears and the addimers become “ferromagnetically” ordered. The ARPES experiments were performed on a fully covered surface.

Core level photoemission [215] finds that there are three surface Si  $2p$  components, in a ratio of 2:2:1. This can be fitted to either the DDRM or the TAADM. To fit to the DDRM the various components are assigned to the terminating Si layer atoms bonded to one Si adatom (4), the Si adatoms (4) and the terminating Si layer atoms bonded to two Si adatoms(2). To fit to the TAADM the components are assigned to Si atoms with four Si-Si bonds (4), Si atoms with two Si-Si bonds (4) and Si atoms with three Si-Si bonds (2). The Si atoms are in different electrostatic environments.

There have been many experiments performed on the  $(3\times 2)$  surface reconstruction and the interpretations of these experiments vary. For a summary of which experiments provide evidence for a particular model or refute a particular model see Table 4.1.

Table 4.1: Summary of the ability of different models to match experiments. + indicates agreement with the experiment, - indicates disagreement with experiment and o indicates ambivalent agreement with experiment.

Experimental Technique	ADRM	DDRM	TAADM
LEED [204]	-	+	+
STM [188, 186]	+	o	+
Photoemission [214]	o	+	+
RAS [211]	-	-	+
H adsorption [210]	-	o	o

In the interests of completeness we also mention the single dimer row model (SDRM) which is a unit cell which is a  $90^\circ$  rotation of the ADRM and which we found had a total energy 2.67 eV higher than the ADRM, and so is thermodynamically unfavourable compared to the ADRM; and the two-adlayer-asymmetric rotated dimer model (TAARDM) which is a unit cell which resembles the TAADM, but with the top addimer rotated so

that it is parallel to the second level addimers, and which we found had a total energy 0.68 eV higher than the TAADM and so is thermodynamically unfavourable when compared with the TAADM. We will not consider the SDRM or the TAARDM further.

What is unequivocally accepted by the experimental community is that the  $(3\times 2)$  surface reconstruction is more silicon rich than the  $c(4\times 2)$  or  $(2\times 1)$  surface reconstructions. Unfortunately there is disagreement about the exact silicon stoichiometry of these surfaces. Therefore it is important to find which model of the  $c(4\times 2)$  reconstruction is favoured as this model would provide a strong constraint on which model of the  $(3\times 2)$  surface reconstruction is favoured.

#### 4.1.4 Models of the $c(4\times 2)$ reconstruction and relevant experimental evidence

All AES (Auger Electron Spectroscopy) studies suggest that the  $(2\times 1)$  surface reconstruction (or alternatively, the  $c(4\times 2)$  reconstruction) has a lower silicon content than the  $(3\times 2)$  reconstruction [191]. The  $(2\times 1)$  reconstruction has been observed by LEED when the  $(3\times 2)$  reconstruction is annealed at high temperature ( $\sim 1300$  K) [196]. The LEED intensities have been fitted to several candidate structures but the one which fits the data best is a model that is very similar to the  $(2\times 1)$  reconstruction of the (001) face of silicon, where the terminating layer is silicon and the silicon surface reconstructs to form dimers which are buckled.

However there is also evidence for a  $c(4\times 2)$  reconstruction at the same silicon coverage levels [185, 195]. Soukiassian *et al.* performed STM scans on a well ordered  $c(4\times 2)$  surface and found that they could recover the  $(2\times 1)$  reconstruction by increasing the density of defects on the surface (missing dimers, steps etc.) [192]. Heating the surface to a temperature of  $\approx 650$  K causes a reversible phase transition between the  $c(4\times 2)$  reconstruction and the  $(2\times 1)$  surface reconstruction [217]. Aristov *et al.* assert that associated with this structural transition is a change in the electronic properties of the system, with the  $c(4\times 2)$  semiconducting surface becoming metallic in the  $(2\times 1)$  regime, according to STM spectroscopy and valence band emission [217, 218]. Angle resolved photoemission seems to show that the  $(2\times 1)$  reconstruction is semiconducting however [197, 219, 220].

Regardless of the electronic properties of the  $(2\times 1)$  surface it seems that the true

ground state of a well ordered surface is the  $c(4\times 2)$  reconstruction, and so we use this reconstruction to model the surface between the silicon lines. Two models have been proposed for the  $c(4\times 2)$  reconstruction, the Alternate Up Down Dimer (AUDD) model [192, 193, 202, 221] and the Missing Row Asymmetric Dimer (MRAD) model [194].

The AUDD model has a silicon stoichiometry of 0 ML ( $\theta_{\text{Si}}^{\text{ad}} = 0$ ). The Si atoms of the terminating layer form dimers in the  $\times 4$  ([110]) direction and are aligned in rows along the  $\times 2$  ( $\bar{1}\bar{1}0$ ) direction (see Figure 4.10). The silicon dimers are symmetric but are displaced vertically, with one dimer in the unit cell in an up configuration and the other dimer down. The height difference is of order 0.1 Å. The lengths of the up and down dimers may also differ [106]. The LEED pattern is caused by the dimers of the terminating silicon layer differing in height and length. To recover the  $(2\times 1)$  structure the up and down dimers have to be brought to the same height. This leads to a couple of problems however. Firstly that such a small change in the physical structure leads to such a large change in the electronic properties of the system. And secondly that when modelled using *ab initio* methods and a periodic supercell the  $(2\times 1)$  unit cell, not the  $c(4\times 2)$  unit cell is the thermodynamically preferred unit cell [222, 223, 224, 225]. The  $c(4\times 2)$  surface only becomes favourable when the unit cell is subjected to a tensile stress [225], and even then it is only lower than the ideal surface by 0.1 eV per unit cell which is within the error bar of *ab initio* calculations.

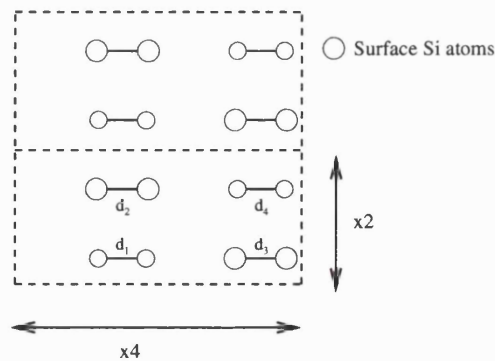


Figure 4.10: The Alternate Up Down Dimer model proposed by Soukiassian *et al.*, Phys. Rev. Lett. **78**, 907, (1997). There are no Si adatoms.

The MRAD model has a surface silicon stoichiometry of 0.5 ML ( $\theta_{\text{Si}}^{\text{ad}} = 1/2$ ). The silicon atoms of the terminating layer form dimers in the  $\times 4$  direction and the adatoms are adsorbed between the dimer rows (see Figure 4.11). These adatoms form addimers which can be either flat or buckled. The  $(2\times 1)$  reconstruction can be recovered simply

by breaking the addimer bonds, which would have the effect of making the  $(2\times 1)$  reconstruction substantially different from this model of the  $c(4\times 2)$  reconstruction. However core-level photoemission shows that the  $(2\times 1)$  reconstruction is Si-terminated with no Si adatoms present [215]. And although the calculated filled states images of the MRAD model match experiment the calculated empty state STM images do not. The STM cannot resolve in empty states imaging the upper adatoms of the MRAD model whereas Lu *et al.* present theoretical images (in the Tersoff-Haman approximation) which indicate that the upper adatom should be resolvable [221].

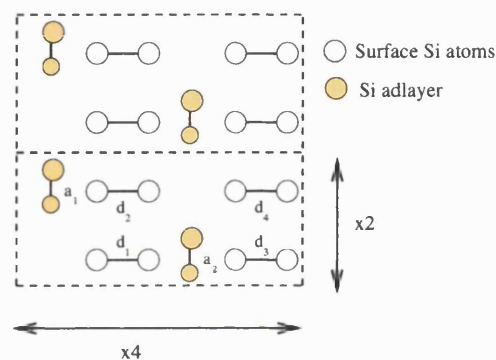


Figure 4.11: The Missing Row Asymmetric Dimer model proposed by Lu *et al.*, Phys. Rev. Lett **81**, 2292, (1998). The Si atoms in the terminating layer form dimers and the adatoms form addimers.

Both core level [226] and angle resolved valence-band photoemission [220] experiments have been performed on the  $c(4\times 2)$  reconstruction. The core level photoemission results found that there were only two different core level shifts, a result which favours the AUDD model (one shift for the up dimers, and one shift for the down dimers). The valence band photoemission data finds that there is a prominent surface state with a dispersion of 0.2 eV along the  $[110]$  direction and no dispersion in the  $[\bar{1}10]$  direction. An overview of how the two models match experiment and theory is shown in Table 4.2.

Table 4.2: Summary of the ability of different models to match experiments and theory considerations. + indicates agreement with the experiment, - indicates disagreement with experiment and o indicates ambivalent agreement with experiment.

Technique	AUDD	MRAD
STM [192, 221]	+	o
Photoemission [226, 220]	o	o
DFT [222]	-	+

## 4.2 Ab initio simulations of the (3×2) reconstruction

### 4.2.1 General points

The calculations were performed using *ab initio* density functional theory with the Projector Augmented Wave method (PAW) to handle the atomic cores [136] (see Chapter 2). We used the Perdew-Zunger parameterisation [227] of the Ceperley-Alder [228] treatment of the uniform electron gas. We solved the Kohn-Sham equations using the Car-Parrinello algorithm [229] (see Appendix C).

To check whether the PAW program accurately reproduced the physical properties of silicon carbide we calculated the variation of the total energy of a (1×1×1) unit cell of cubic silicon carbide with respect to the bulk lattice vector. The minimum of this curve corresponded to the bulk lattice vector of silicon carbide as found by PAW. These total energy differences are not accurate for unit cells with different volumes, unless the total energies are themselves converged [230]. A term can be added to the total energy which corrects for this error, the Francis-Payne correction [230]. This term is

$$\Delta E = \frac{2E_{\max}}{3} \left( \frac{\partial E_{\text{tot}}^k(c, E_{\max})}{\partial E_{\max}} \right)_c \ln \left( \frac{N_k^{\text{PW}}(c, E_{\max})}{g_\eta c} \right) \quad (4.1)$$

where  $c$  represents the lattice vector,  $k$  represents a particular  $k$ -point,  $E_{\text{tot}}^k$  is the total energy,  $E_{\max}$  is the plane wave cutoff,  $N_k^{\text{PW}}$  is the number of plane waves and  $g_\eta c$  is a variable dependent on the plane wave cutoff. The rate of change of total energy with respect to plane wave cutoff (the first term) was found to be -0.03255 Hartrees for a cutoff of 30 Rydbergs. The second term was calculated internally by PAW. The bulk lattice vector of SiC was found to be 8.30197 Bohrs which is within 0.7 % of the experimental bulk lattice vector of SiC (see Figure 4.12). The bulk modulus was found to be 456.77 GPa which compares favourably with the experimental value. In our PAW simulations we used the experimental lattice vector of SiC.

All models of both reconstructions were modelled using the surface slab technique with periodic boundary conditions. The simulation cells were six or ten atomic layers deep (six layers were used for preliminary checks, ten layers for the results quoted here); the bottom two layers were held in their bulk configuration while the other layers were allowed to relax, with the bottom carbon layer passivated with hydrogen atoms. If the bottom layer

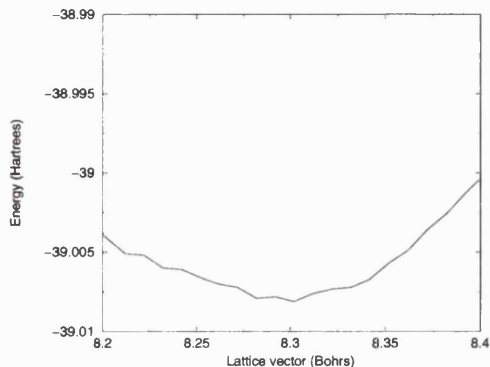


Figure 4.12: Plot of the corrected total energy of bulk cubic silicon carbide as a function of lattice vector in the PAW formalism for a  $(1 \times 1 \times 1)$  unit cell. The minimum is at 8.30197 Bohr.

consists of silicon atoms that are passivated with hydrogen we found that, as the silicon layer is under compression, the hydrogen-hydrogen distance is smaller than the silicon-hydrogen distance with the consequence that the hydrogen is unstable and dissociates from the surface with an artificial charge transfer takes place across the vacuum gap. With the bottom atomic layer consisting of carbon we found that the electronic charge density is confined to the slab with a negligible leakage across the vacuum gap (see Figure 4.13).

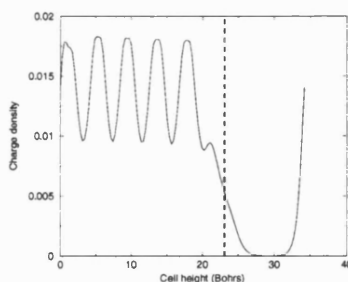


Figure 4.13: Plot of the total charge density as a function of cell height for the ADRM. The left side of the plot is the hydrogen terminated surface, the right side corresponds to the vacuum gap. Dashed line indicates the position of the top adatom.

In our calculations we sample four  $k$ -points of the surface Brillouin zone, corresponding to the  $\Gamma$ -point, the  $J'$ -point (in the  $[\bar{1}10]$  direction in real space), the  $J$ -point (in the  $[110]$  direction in real space) and the  $K$ -point (see Figure 4.14). For the  $(3 \times 2)$  unit cell these points are at the zone boundaries. We used a non-primitive rectangular cell to simulate the  $c(4 \times 2)$  reconstruction, which means that what we call the  $J$  point is halfway between the  $\Gamma$  and  $X$ -points of the surface Brillouin zone, the  $J'$ -point is 80% of the

way between the  $\Gamma$  and  $U$ -points and the  $K$ -point maps to the  $K$ -point of the primitive Brillouin zone. As the PAW program only uses pairs of real wavefunctions we can only sample four  $k$ -points.

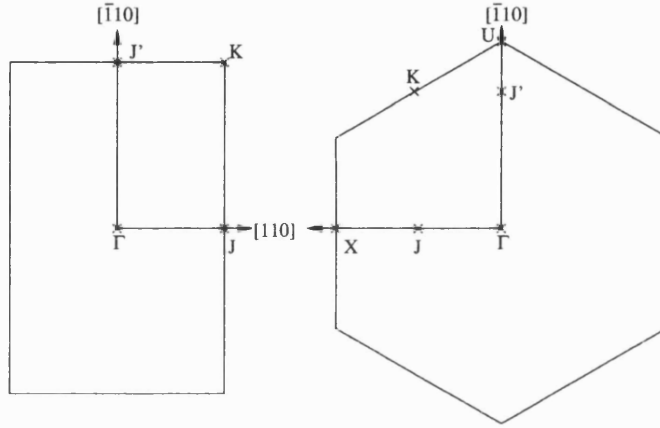


Figure 4.14: Schematic of the surface Brillouin zone and the four  $k$ -points that we sample for both reconstructions (not to scale). The left figure is the Brillouin zone of the  $(3 \times 2)$  reconstruction, right for the  $c(4 \times 2)$  reconstruction.

For our structural calculations we used a plane-wave cutoff of 20 Rydbergs, but for our electronic structure and total energy calculations we increased the cutoff to 30 Rydbergs. The vacuum spacing between slabs was set to 6.08 Å, and this thickness is defined as the distance from the top adlayer of one unit cell to the bottom hydrogen atoms of the next unit cell. This means that the vacuum spacing is different for different unit cells, dependent upon the number of adlayers (we return to this point later in this section). We set the criteria for convergence of relaxation such that the change in total energy per step is less than  $5 \times 10^{-6}$  Ha per iteration. The convergence of relaxed structures with respect to the number of atomic layers held in bulk position, plane wave cutoff,  $k$ -point sampling and vacuum spacing was checked.

To test whether the majority of the simulation slab acted as bulk silicon carbide we varied the number of atomic layers which are held in a bulk-like position. Decreasing the number of atomic layers which are held in bulk position (from two to one) has a major effect on the addimer bond length and asymmetries. Compared to the two atomic layer case the addimer bond lengths are increased by  $\approx 0.2$  Å and the asymmetries of buckled addimers are decreased by  $\approx 0.45$  Å. If we increase the number of atomic layers which are held in a bulk-like position (from two atomic layers to four) we found that there are only minor differences in the bond lengths and asymmetries of addimers (of at most  $\approx 0.1$  Å

difference). We can therefore conclude that our relaxed geometries are well converged with respect to the number of atomic layers which are held in a bulk-like position.

The difference between a relaxed unit cell with a plane wave cutoff of 20 Rydbergs and a relaxed unit cell of 30 Rydbergs was analysed and found to be negligible. There were minor differences in surface dimer length ( $\approx 0.10$  Å at most) and almost identical addimer length ( $\approx 0.01$  Å difference). Dimer buckling was found to be slightly increased for the higher cutoff compared to the case with the lower cutoff ( $\approx 0.06$  Å increase).

It was found that the relaxed structure of most of the models was accurately found by  $\Gamma$ -point sampling alone, with the differences in surface structure between  $\Gamma$ -point relaxed and multi  $k$ -point relaxed unit cells being of magnitude  $\sim 0.1$  Å at the most. However it was found that the structural and electronic properties of the TAADM were not properly represented by  $\Gamma$ -point sampling alone with differences in surface structure of order  $\approx 0.3$  Å. Consequently all relaxed structures that are presented here were found using four  $k$ -point sampling. Although we were not able to check for changes in the TAADM results with more than four  $k$ -points, we have also studied the  $k$ -point convergence of the tight-binding calculations (see next Chapter) and there we found that 4  $k$ -points are sufficient. All total energies that are quoted were found at 30 Rydbergs and four  $k$ -point sampling unless otherwise stated.

The effects of the vacuum thickness on the structure of relaxed unit cells was checked by performing a relaxation calculation on two identical unit cells, one with our standard vacuum thickness of 6.08 Å and one with a vacuum thickness of 7.88 Å. Comparison of the two relaxed unit cell structures revealed that the changes in structure were negligible, with surface and addimer bond lengths changing by at most 0.08 Å. Our relaxed structures are therefore well converged with respect to vacuum spacing.

Finally we consider the effects of vacuum spacing on the total energy of the unit cell. As stated previously the vacuum gap in our initial relaxation calculations was set to 6.08 Å from the top adlayer of the unit cell to the bottom hydrogen layer of the next cell. This means that the height of the ADRM and DDRM unit cells are different from the height of the TAADM unit cell (and similarly the height of the AUDD unit cell was different from the height of the MRAD unit cell). If we increase the height of the ADRM or DDRM unit cells so that it matches the height of the TAADM unit cell the total energy changes. We found that the total energy changes by only 0.05 eV which is less than the error of

LDA DFT. The effect of the slightly different vacuum spacing is negligible.

#### 4.2.2 Simulations of the ADRM model: Physical properties

The initial structure of the ADRM unit cell before relaxation was based upon the final structure proposed by Pizzagalli *et al.* [231], with a buckled addimer. It was found that unless the addimer was placed in this initially buckled state, the top addimer would relax into a metastable state wherein it would be flat and have a bond length of approximately 2.6 Å. This metastable state is 1.03 eV higher in energy than the final structure. Similar flat and weakly bound addimers have been found by Pizzagalli *et al.* [231] on the (3×2) surface and by Käckell [232] on the (2×1) surface. The silicon surface was initially in an undimerised state, but after relaxation the surface Si atoms were found to be dimerised. The final structure is shown in Figure 4.15.

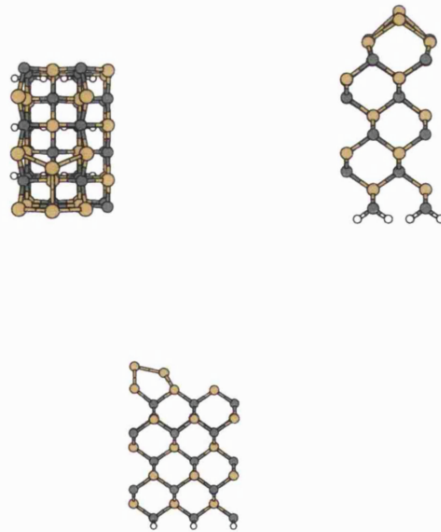


Figure 4.15: Relaxed structure of the ADRM model. Yellow represents silicon atoms, black represents carbon atoms and white represents hydrogen atoms. The top left picture is the view from above, the top right view is the view across the silicon line and the bottom view is along the silicon line.

The structure obtained for the ADRM is in agreement with previous *ab initio* [206, 208, 231], and tight-binding work [233], with a strongly bound and asymmetric addimer. The Si atoms of the first Si layer of the SiC crystal proper were also found to be dimerised (this is true for all (3×2) unit cells) in agreement with previous work [183, 184, 208,

231, 233]. The details of the surface structure of this model (and all other models) are presented in Table 4.3.

Table 4.3: Equilibrium bond lengths for the addimers and buckling of addimers (magnitude) in our total energy calculations and length of dimers in the terminating or surface layer. All distances are in Å. See Figures 4.6-4.9 for information on the nomenclature.

Model	Addimer bond length	Buckling of addimer	Surface dimer length
ADRM	2.30 ( $a_1$ )	0.50	2.59 ( $d_1$ ), 2.47 ( $d_2$ ), 2.49 ( $d_3$ )
DDRM	2.35 ( $a_1$ ), 2.34 ( $a_2$ )	0.51, 0.53	2.40 ( $d_1$ ), 2.41 ( $d_2$ )
TAADM	2.31 ( $a_1$ ), 2.44 ( $a_2$ ), 2.42 ( $a_3$ )	0.58, 0.01, 0.00	2.41 ( $d_1$ ), 2.41 ( $d_2$ )

### 4.2.3 Simulations of the DDRM model: Physical properties

The initial structure of the DDRM unit cell before relaxation was based upon the final structure proposed by Pizzagalli *et al.* [231], with two buckled addimers. It was found that unless the addimers were placed in initially buckled states, the addimers would relax into a metastable state wherein the addimers would be flat and have a bond length of approximately 2.6 Å. This metastable state is 0.99 eV higher in energy than the final structure. The silicon surface was initially in an undimerised state, but after relaxation the surface Si atoms were found to be dimerised.

As mentioned previously there are four separate configurations of the DDRM model, two where the addimers are aligned in the [110] direction (L) and have either identical (FM) or opposite (AFM) addimer buckling, and two configurations where the addimers are not aligned in the [110] direction (Z) and again have identical (FM) or opposite (AFM) addimer buckling directions. We studied all configurations and found that the model with lowest total energy at a plane wave cutoff of 20 Rydbergs and  $\Gamma$ -point sampling only was the LAFM-DDRM. If the initial unit cell was arranged in the LFM arrangement it was found that the unit cell would relax into the LAFM configuration. If the unit cell was placed into the ZAFM arrangement it was found that the unit cell would relax into the ZFM arrangement. The difference in total energy between the LAFM and ZFM arrangements was 0.17 eV. The relaxed structure of the LAFM-DDRM is presented in Figure 4.16.

The structure obtained for the DDRM is in disagreement with both previous *ab initio* [231], and tight-binding [233] results, as we found that both addimers are buckled and quite strongly bound. Our result corresponds to the LAFM-DDRM model studied

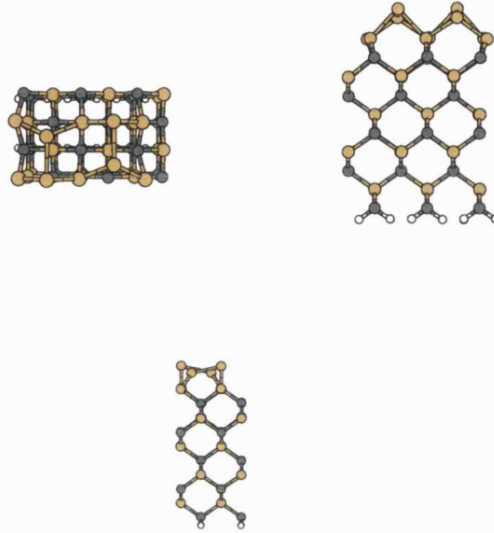


Figure 4.16: Relaxed structure of the DDRM model. See Figure 4.15 for colour coding. The top left picture is the view from above, the top right view is the view along the silicon line and the bottom view is across the silicon line.

previously using *ab initio* methods by Lu *et al.* [208] but unlike this work we found that the LAFM model is energetically preferred, rather than all arrangements having approximately the same energy. For the details of our surface structure see Table 4.3.

#### 4.2.4 Simulations of the TAADM model: Physical properties

The initial structure before relaxation corresponded to the initial structure of the TAADM as set forth by Lu *et al.* [208], but with one difference; the second level addimers were placed below the top addimer. After relaxation these addimer bonds were broken and new addimer bonds were formed. The relaxed structure of the unit cell is shown in Figure 4.17. This structure was in agreement with previous work [208]. There is an alternating arrangement of first layer and second layer addimers as we look along  $[\bar{1}10]$ , with the top layer addimer strongly bound and asymmetric, and the second level addimers strongly bound and flat. For the details of the surface structure see Table 4.3.

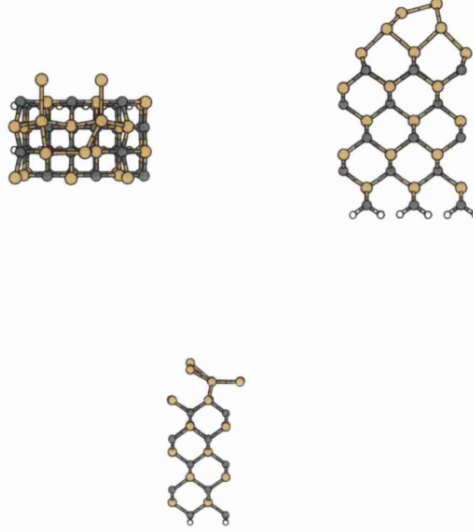


Figure 4.17: Relaxed structure of the TAADM model. See Figure 4.15 for colour coding. The top left picture is the view from above, the top right view is the view along the silicon line and the bottom view is across the silicon line.

Table 4.4: ‘Dispersion’ of HOMO state along  $[\bar{1}10]$  ( $\Gamma - J'$ ) and  $[110]$  ( $\Gamma - J$ ) directions, for various models. Also shown are values found in the literature. All values are in eV.

Author	ADRM	DDRM	TAADM
This work	0.18 ( $\Gamma J'$ ), 0.00 ( $\Gamma J$ )	0.01 ( $\Gamma J'$ ), 0.34 ( $\Gamma J$ )	0.13 ( $\Gamma J'$ ), 0.21 ( $\Gamma J$ )
Pizza. <i>et al.</i> [231]	$\leq 0.10$ ( $\Gamma J'$ ), $\leq 0.10$ ( $\Gamma J$ )	1.00 ( $\Gamma J'$ ), $\leq 0.10$ ( $\Gamma J$ )	
Lu <i>et al.</i> [208]	0.20 ( $\Gamma J'$ ), $\sim 0.00$ ( $\Gamma J$ )	$\sim 0.00$ ( $\Gamma J'$ ), $\sim 0.50$ ( $\Gamma J$ )	0.37 ( $\Gamma J'$ ), $\sim 0.00$ ( $\Gamma J$ )

#### 4.2.5 Simulations of the ADRM model: Electronic properties

We cannot comment in detail on the electronic structure of the ADRM (or any other model) as we are limited to sampling only four  $k$ -points in the surface Brillouin zone (this is because our PAW implementation is limited to FFT's of pairs of real wavefunctions). We found that at the  $\Gamma$ -point the gap between the highest occupied state and the lowest unoccupied state is 0.53 eV. For the flat addimer case this gap was 0.07 eV, which indicates that the buckling of the addimer is a Jahn-Teller-like distortion which lowers the energy by buckling the addimer and increasing the bandgap at at least the  $\Gamma$ -point. We found that there is one well defined occupied state above the valence band, and that there were three other states that are partially separated from the valence band. We define this to mean that in part of  $k$ -space these states are close in energy to the valence

band states (maximum 0.1 eV difference) and in other regions of  $k$ -space these states are well separated in energy (minimum 0.5 eV difference) from the valence band.

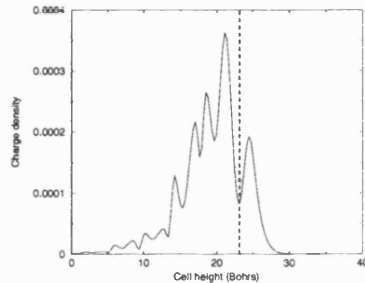


Figure 4.18: Plot of the charge density of the highest occupied state as a function of cell height for the ADRM. See Figure 4.13 for layout.

The top adatom of the addimer was found to have a large overlap with two of these states, the highest occupied state (or HOMO) and the third highest occupied state, with overlaps of 0.1425 and 0.1901 respectively (these numbers are actually the sum of the squares of the projectors  $p_i$  for the  $s, p_x, p_y$  and  $p_z$  orbitals used in (2.20), they provide a measure of the overlap). The distribution of the highest occupied state as a function of cell height (from the bottom of one hydrogen covered surface to the bottom of the next hydrogen covered surface) is shown in Figure 4.18. As can be seen the largest component of the HOMO state is localised in the middle of the slab, so it is not a surface state. This implies that the ADRM would not make a good atomic wire, as any holes that are injected into the HOMO state would quickly disperse into the bulk. This is because the HOMO state which is present on the up adatom is coupled into the bulk by the addimer, with a large component on the surface dimer. We can see this in our charge density plots of the HOMO state shown in Figure 4.19. The third HOMO state has a very similar distribution of charge density throughout the slab (see Figure 4.20), so if any holes are injected into this state and into the line then they would quickly disperse into the bulk.

We can calculate the differences (the ‘dispersion’) between the Kohn-Sham eigenvalues calculated at different points of the Brillouin zone, and compare these with recent photoemission experiments performed on the  $(3 \times 2)$  surface [200, 213, 214, 234]. Our results, and equivalent results in the literature are presented in Table 4.4. The magnitude of dispersion is approximately equal to the magnitude of dispersion measured [214] ( $\sim 0.2$  eV). The measured dispersion of the surface state bands is  $\sim 0.2$  eV along  $\Gamma - J'$ , with no measured dispersion along  $J$  [214]. The ADRM agrees with these photoemission

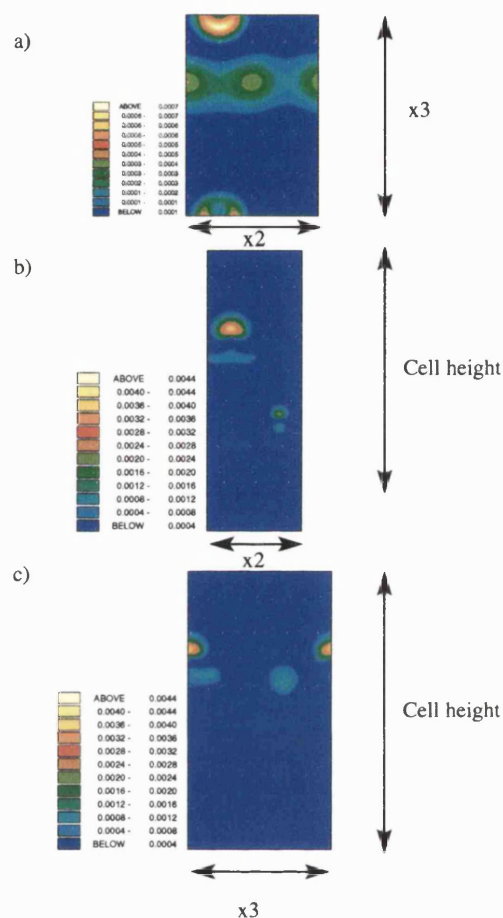


Figure 4.19: Three two-dimensional charge density plots of the ADRM. The top plot: a) is a plot of the charge density parallel to the surface at the height of the top adatom of the addimer. The second plot: b) is a plot of the charge density perpendicular to the surface and parallel to the  $\times 2$  direction of the unit cell, at the position of the top ad-atom. The third plot: c) is a plot of the charge density perpendicular to the surface and parallel to the  $\times 3$  direction at the position of the addimer.

results.

#### 4.2.6 Simulations of the DDRM model: Electronic properties

We found that at the  $\Gamma$ -point the gap between the HOMO and LUMO states is 0.79 eV. For the metastable flat addimer case this gap was 0.34 eV which again indicates that the buckling of the addimers is a kind of Jahn-Teller distortion which lowers the energy by buckling the addimers and increasing the bandgap, at at least the  $\Gamma$ -point. We found that there are two occupied states separated from the valence band, with another state partially separated from the valence band (see ADRM section on electronic properties

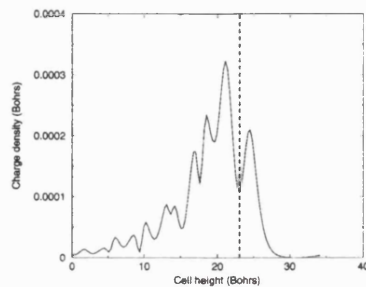


Figure 4.20: Plot of the charge density of the third highest occupied state as a function of cell height perpendicular to the surface for the ADRM. See Figure 4.13 for layout.

for definition).

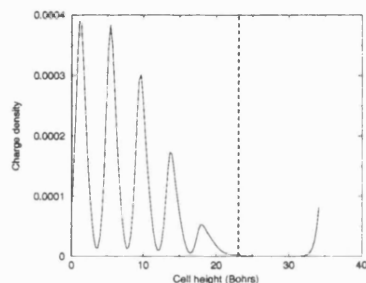


Figure 4.21: Plot of the charge density of the highest occupied state as a function of cell height perpendicular to the surface for the DDRM. See Figure 4.13 for layout.

We found that the top adatom of each addimer has an overlap with the HOMO state and the third HOMO state (with overlaps of 0.0882 and 0.1446 for the HOMO state, and 0.1429 and 0.1114 for the third HOMO state). The distribution of the highest occupied state as a function of height is shown in Figure 4.21. The largest component of the HOMO state is localised at one side of the slab, but this state is located on the side of the slab which is hydrogen terminated. The HOMO state is not associated with the adatoms. Thus if we attempted to inject a hole into the line then we would find that the hole disperses into the bulk. We can also see this in our charge density plots of the HOMO state as shown in Figure 4.22, where we see that the charge density is distributed throughout the unit cell and that this state is therefore not oriented along the  $\times 2$  direction, i.e., it is not “line-like”. The third HOMO state has a significant addimer component on the surface, although there is a large bulk component as well, as shown in Figure 4.23. This state is very isotropic and so is also not “line-like”.

Looking at the “dispersion” values for the HOMO state for the DDRM (see Table 4.4) we found that there is a large dispersion along  $\Gamma - J$ . We attribute this to our

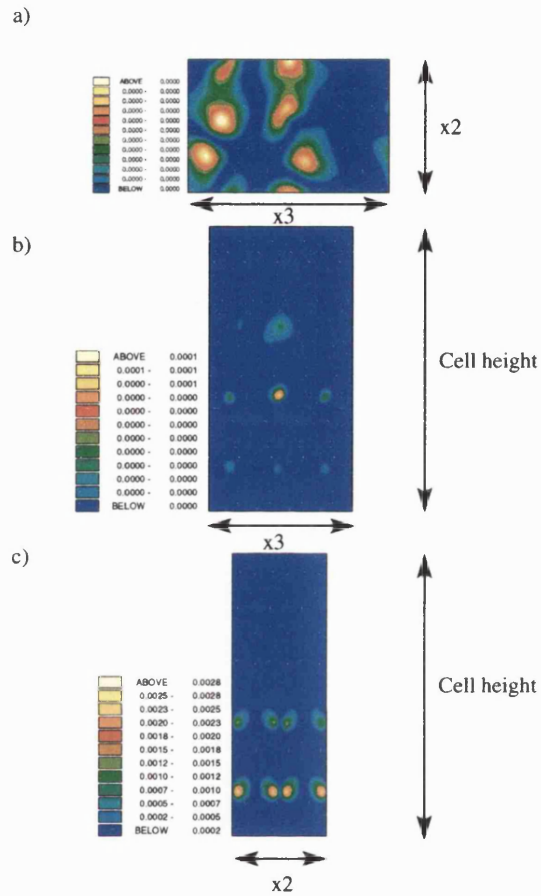


Figure 4.22: Three two-dimensional charge density plots of the DDRM. The top plot: a) is a plot of the charge density parallel to the surface at the height of the top adatom of an addimer. The second plot: b) is a plot of the charge density perpendicular to the surface and parallel to the  $\times 3$  direction of the unit cell, at the position of the top ad-atom of an addimer. The third plot: c) is a plot of the charge density perpendicular to the surface and parallel to the  $\times 2$  direction at the position of the addimer.

modelling of a perfectly ordered periodic  $(3 \times 2)$  surface, whereas the  $(3 \times 2)$  surface has been observed to be almost perfectly disordered [187, 216], in the sense that there is no observable correlation between the addimer tilt in one  $(3 \times 2)$  unit cell, and the next (in either the  $\times 3$  or  $\times 2$  direction). Our results suggest that the DDRM possesses a larger dispersion along  $\Gamma - J$  than along  $\Gamma - J'$ , which is contrary to the photoemission results (see above).

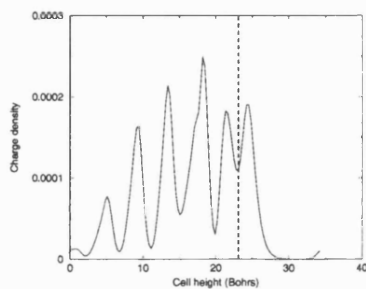


Figure 4.23: Plot of the charge density of the third highest occupied state as a function of cell height perpendicular to the surface for the DDRM. See Figure 4.13 for layout.

#### 4.2.7 Simulations of the TAADM model: Electronic properties

We found that the gap between the HOMO and LUMO states at the  $\Gamma$ -point is 1.00 eV. There are three occupied states separated from the valence band with one other state partially separated from the valence band (see ADRM section on electronic properties for definition).

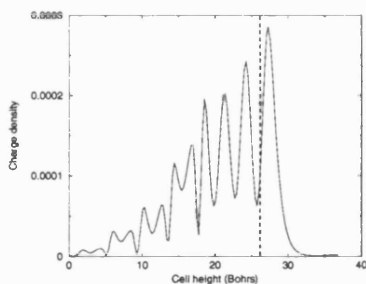


Figure 4.24: Plot of the charge density of the highest occupied state as a function of cell height for the TAADM. See Figure 4.13 for layout.

Of these states, only the HOMO state has a significant overlap with any of the adatoms, with an overlap of 0.3284. The distribution of the highest occupied state as a function of height in the unit cell is shown in Figure 4.24. The largest component of the HOMO state is localised above the top adatom and is confined to the top few atomic layers of the slab, so the HOMO state is a surface state. This is also shown in Figure 4.25 where we see that the HOMO state is mainly localised on the top adatom with very little dispersion into the bulk. We also see that part of the HOMO state is confined to the surface and has a “line-like” profile aligned along the  $\times 2$  direction, as can be seen in Figure 4.26, so the HOMO state is confined to the addimer part of the  $(3\times 2)$  unit cell and is delocalised along the line. Thus if a hole was injected into the line it would be

confined to the line and could disperse along it.

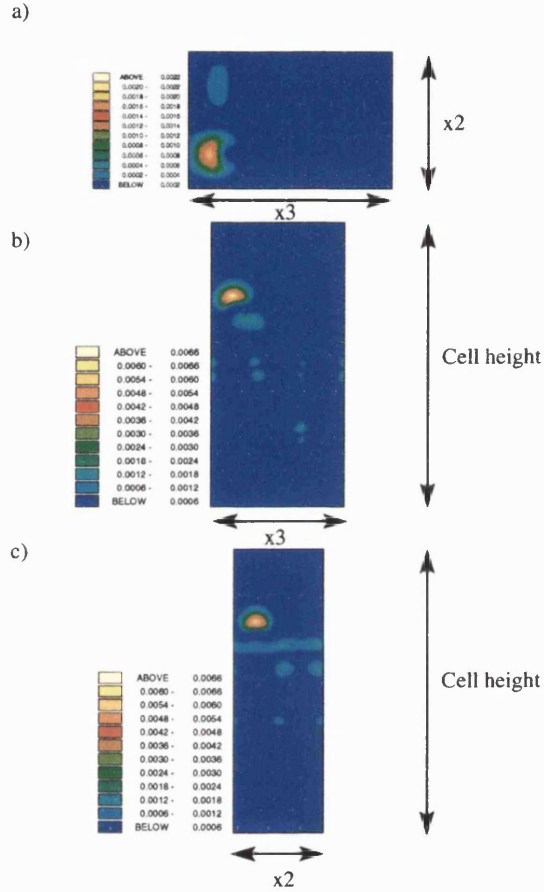


Figure 4.25: Three two-dimensional charge density plots of the TAADM. The top plot: a) is a plot of the charge density parallel to the surface at the height of the top adatom of the top addimer. The second plot: b) is a plot of the charge density perpendicular to the surface and parallel to the  $\times 3$  direction of the unit cell, at the position of the top adatom of the addimer. The third plot: c) is a plot of the charge density perpendicular to the surface and parallel to the  $\times 2$  direction at the position of the top addimer.

The dispersion of the HOMO state of the TAADM is shown in Table 4.4. Our results do not agree with the results of Lu *et al.* [208] who found that there is a greater magnitude of dispersion along the  $[\bar{1}10]$  direction than along the  $[110]$  direction, whereas we found that the HOMO state has a slightly greater dispersion along the  $[110]$  direction than along the  $[\bar{1}10]$  direction. We found that the HOMO state for the TAADM exists mostly in the vacuum of the simulation slab, and suggest that as we use plane waves to describe our electron wavefunction, as opposed to the localised Gaussian orbitals used by Lu *et al.* [208], our dispersion results may more accurately describe the dispersion of the surface

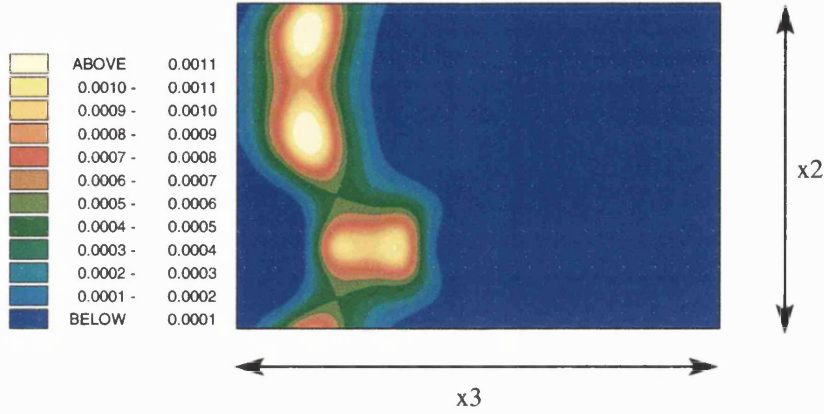


Figure 4.26: Charge density plot of the HOMO state of the TAADM. This is a slice which is parallel to the surface and is at the height of the bottom adatom of the top addimer. It clearly shows that the HOMO state is mediated from one unit cell to the other in the  $\times 2$  direction via the second level addimers.

state. Our results are of the same magnitude as the photoemission experiments [215] although the anisotropy of the dispersion is different, with our results showing a bigger dispersion along  $[110]$  than  $[\bar{1}10]$ .

#### 4.2.8 Thermodynamic results: Which $(3 \times 2)$ model is favoured?

We wish to use the total energies we calculated to discover which of the three candidate models is most stable. We assume that the formation of the different structures is determined by thermodynamic factors, but we cannot compare directly the total energies of models with different stoichiometries. A common method of comparing structures in these circumstances is to find the chemical potential  $\mu_{\text{Si}}$  for the silicon adatoms and then compare the grand potentials [235, 236]

$$\Omega = E - N_{\text{Si}}\mu_{\text{Si}}. \quad (4.2)$$

In this formula we neglect the finite temperature (entropic) contributions to the free energy. However, because of the experimental conditions that produce the  $(3 \times 2)$  surface

and because SiC is a two component system, it is nontrivial to calculate  $\mu_{\text{Si}}$ . Nevertheless we can estimate a value for the range of chemical potential that the silicon adatoms experience. We take the zero of chemical potential to correspond to the total energy of an isolated silicon atom. This varies depending on the formalism we use, and in the PAW formalism this corresponds to -3.808 Hartrees.

We must decide what physical/chemical process determines the value of  $\mu_{\text{Si}}$  in our system. We can make several choices. We choose to consider the incorporation of Si atoms into bulk SiC. The chemical potential  $\mu_{\text{Si}}$  would then become the chemical potential for a Si atom in SiC. However this cannot be calculated directly, because it is impossible to insert a single Si into SiC without creating a structural defect of some kind. We can, though, estimate the maximum range of  $\mu_{\text{Si}}$  that the Si adatoms experience [237]. We can write the chemical potential per unit cell of an ideal bulk system of SiC as

$$\mu_{\text{SiC}}^{\text{bulk}} = \mu_{\text{Si}} + \mu_{\text{C}}, \quad (4.3)$$

where  $\mu_{\text{Si}}$  and  $\mu_{\text{C}}$  are the (unknown) contributions from the Si and C atoms. In extremely Si-rich conditions,  $\mu_{\text{Si}}$  approaches the value of bulk Si. We can consider deviations from this bulk value  $\Delta\mu_{\text{Si}} = \mu_{\text{Si}} - \mu_{\text{Si}}^{\text{bulk}}$  (with a corresponding definition for  $\Delta\mu_{\text{C}}$ ). The allowed range is determined by the heat of formation of the SiC compound

$$\Delta H_f = \mu_{\text{SiC}}^{\text{bulk}} - \mu_{\text{C}}^{\text{bulk}} - \mu_{\text{Si}}^{\text{bulk}} = (\mu_{\text{Si}} - \mu_{\text{Si}}^{\text{bulk}}) + (\mu_{\text{C}} - \mu_{\text{C}}^{\text{bulk}}) = \Delta\mu_{\text{Si}} + \Delta\mu_{\text{C}} \quad (4.4)$$

The experimental value of  $\Delta H_f$  is 0.72 eV [238]. In a Si-rich environment  $\Delta\mu_{\text{Si}} = 0$ , and therefore  $\Delta\mu_{\text{C}} = \Delta H_f$ . Similarly, in a C-rich environment  $\Delta\mu_{\text{C}} = 0$  and  $\Delta\mu_{\text{Si}} = \Delta H_f$ . This means that furthest deviation the chemical potential of Si can make from the value for bulk Si is 0.72 eV. We show our results as a function of  $\mu_{\text{Si}}$  over the range from its value for bulk Si,  $\mu_{\text{Si}}(\text{Si})$ , to the value obtained by assuming that the chemical potential of SiC can be equally divided between the carbon and silicon atoms; we call this latter value  $\mu_{\text{Si}}(\text{C})$ . In the present case,  $\mu_{\text{Si}}(\text{C}) \leq \mu_{\text{Si}}(\text{Si}) - \Delta H_f \leq \mu_{\text{Si}}(\text{Si})$ .

We use calculated *ab initio* total energies, to find  $\Omega$  from equation (4.2) for the various models. The results presented (see Figure 4.27) are for our most converged simulations (30 Rydberg cutoff, 4  $k$ -points sampled). We first of all start off with the assumption that the Si adatoms are in equilibrium with the bulk. As can be seen, all crossover points

(that is the values of  $\mu_{\text{Si}}$  for which  $\Omega$  is equal for two separate models) are outside the maximum allowable range of  $\mu_{\text{Si}}$  as determined by  $\Delta H_f$ . We can thus unambiguously apply our calculations of  $\Omega$  to determine which model is thermodynamically preferred. Over the entire range of allowable chemical potentials, the TAADM model is favoured.

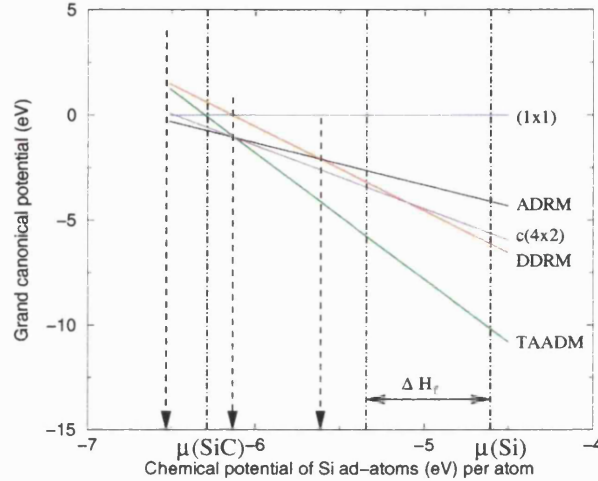


Figure 4.27: Plot comparing the grand canonical potentials  $\Omega$  per  $(3 \times 2)$  unit cell for the three  $(3 \times 2)$  candidate models, the ideal  $(1 \times 1)$  surface and a  $(3 \times 2)$  slice of the  $c(4 \times 2)$  reconstruction, as a function of chemical potential per Si atom  $\mu_{\text{Si}}$ . The zero of the grand canonical potential corresponds to the grand canonical potential of the ideal  $(1 \times 1)$  surface. Arrows pointing downwards indicate the critical value  $\mu_{\text{Si}}^*$  where  $\Omega$  is equal for a pair of  $(3 \times 2)$  models. Also indicated are the chemical potentials per atom of silicon and silicon carbide and the range of  $\Delta H_f$ , to illustrate the maximum range of allowable cohesive energies for the case where the Si atoms are assumed to be in equilibrium with the bulk.

Our results are in agreement with the previous work of Lu *et al.* [208], where it is found that the TAADM is the thermodynamically preferred model throughout the entire allowable range of  $\mu_{\text{Si}}$ . Regarding the relative stability of the ADRM and DDRM, we agree with other work [231, 233] where it is suggested that the ADRM is the favoured model (although the TAADM is not considered). We found that the ADRM is only favoured over the TAADM for values of  $\mu_{\text{Si}}$  which are close to  $\mu_{\text{Si}}^*(\text{SiC})$  (i.e., for extremely Si-poor conditions).

We have therefore found from our *ab initio* calculations of the grand potential that the TAADM is preferred over a large range of chemical potential and that the other two models can be discounted: with the DDRM never preferred and the ADRM only valid for a range of chemical potential which is non-physical.

## 4.3 Ab initio simulations of the c(4×2) reconstruction

### 4.3.1 Simulations of the AUDD model: Physical properties

The initial structure of the AUDD unit cell before relaxation was based upon the AUDD model proposed by Soukiassian *et al.* [192], with the atomic coordinates based on the specific structure of Pizzagalli *et al.* [193]. We found that this surface was locally stable with the surface dimers remaining strongly dimerised and flat. The presence of strong surface dimers is in contradiction to the results obtained on the related (2×1) surface by Käckell *et al.* [232], who found that the dimers are weakly bound with a length of 2.75 Å. The difference in height between the upper and lower surface dimers was found to be 0.21 Å, in agreement with Douillard *et al.* [202]; this difference is twice that found by Pizzagalli *et al.* [193]. The details of the structure of the relaxed unit cell are shown in Table 4.5. The relaxed structure is shown in Figure 4.28.

Table 4.5: Equilibrium bond lengths for the addimers and dimers in the terminating or surface layer and amount of buckling (magnitude) found in our total energy calculations. All distances are in Å. See Figures 4.10 and 4.11 for more.

Model	Dimer (or Ad-dimer) bond length	Amount of buckle
AUDD	2.40 ( $d_1, d_4$ ), 2.67 ( $d_2, d_3$ )	0.00 ( $d_1, d_4$ ), 0.00 ( $d_2, d_3$ )
MRAD	2.50 ( $d_1$ ), 2.50 ( $d_2$ ), 2.50 ( $d_3$ ), 2.50 ( $d_4$ ) 2.36 ( $d_5$ ), 2.36 ( $d_6$ )	0.00 ( $d_1, d_2, d_3, d_4$ ) 0.19 ( $d_5$ ), 0.18 ( $d_6$ )

### 4.3.2 Simulations of the MRAD model: Physical properties

The initial structure of the MRAD unit cell before relaxation was based on the structure proposed by Lu *et al.* [194]. We found that the surface was locally stable with the silicon atoms of the surface layer dimerising into short dimers and the addimers strongly bound and asymmetric. We found that the two addimers are only weakly buckled by 0.19 Å ( $d_5$ ), and 0.18 Å ( $d_6$ ) respectively, whereas Lu *et al.* [194] found that the addimers are buckled by  $\sim 0.54$  Å. For more structural information see Table 4.5. The relaxed structure is shown in Figure 4.29.

### 4.3.3 Simulations of the AUDD model: Electronic properties

As for the (3×2) reconstruction we do not possess a large amount of information on the electronic structure of the various models as we only sample four  $k$ -points of the surface

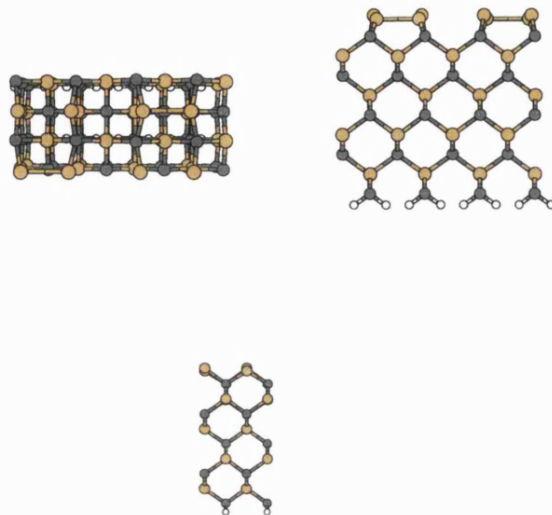


Figure 4.28: Relaxed structure of the AUDD model. See Figure 4.15 for colour coding. The top left picture is the view from above, the top right view is the view along the  $[\bar{1}10]$  direction and the bottom view is the view along the  $[110]$  direction.

Brillouin zone. There are two occupied states separated from the valence band. The bottom surface dimers have a significant overlap with the HOMO states (0.1064) while the top surface dimers have a significant overlap with the second HOMO state (0.1538). This implies that for such a small difference in physical structure the top and bottom surface dimers have different electronic characteristics. Both states have a significant surface component, as can be seen in Figures 4.30-4.31.

We found that the highest occupied state disperses by 0.04 eV as we move along both the  $[110]$  and  $[\bar{1}10]$  directions; this is in contradiction with recent photoemission work [220], wherein it was found that a prominent surface state shows a dispersion of 0.2 eV along the  $[110]$  direction, and no noticeable dispersion along the  $[\bar{1}10]$  direction. We found that at all four of the  $k$ -points we sample in the surface Brillouin zone, the HOMO and second HOMO states are degenerate, which is in agreement with photoemission data [220], where it is found that there is only one surface state (called  $S_1$  in the cited reference) from  $M - \Gamma - X$ . Finally, as there are only two types of dimer on the surface (the top surface dimer and the bottom surface dimer), we would expect there to be only two core-level shifts, which is in agreement with the core-level photoemission results of

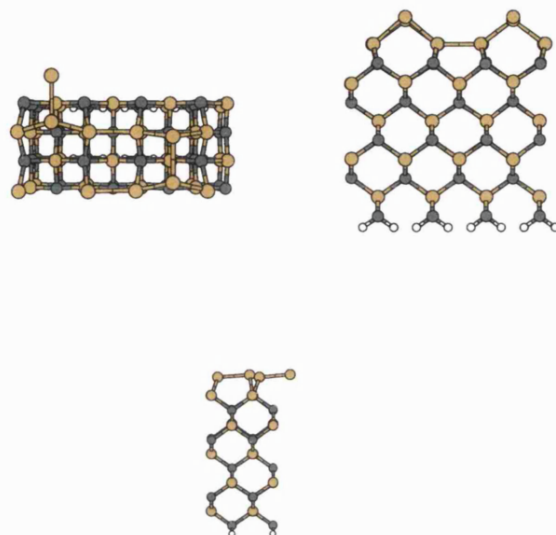


Figure 4.29: Relaxed structure of the MRAD model. See Figure 4.15 for colour coding. The top left picture is the view from above, the top right view is the view along the  $[\bar{1}10]$  direction and the bottom view is the view along the  $[110]$  direction.

Aristov *et al.* [226].

#### 4.3.4 Simulations of the MRAD model: Electronic properties

We found that one state is separated from the valence band and one state is partially separated from the valence band (for our definition of how we decide which states are separated from the valence band and which states are not, see the ADRM subsection on electronic properties). We found that there is a significant overlap between the adatoms

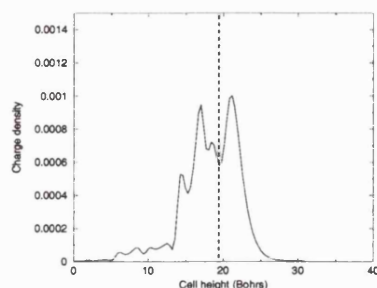


Figure 4.30: Plot of the charge density of the highest occupied state as a function of cell height perpendicular to the surface for the AUDD. See Figure 4.13 for layout. The dashed line indicates the position of the top surface dimer.

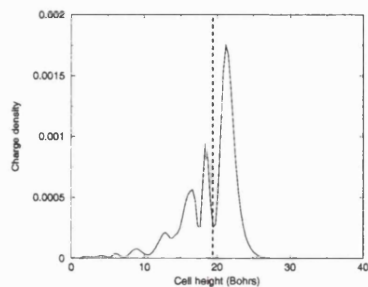


Figure 4.31: Plot of the charge density of the second highest occupied state as a function of cell height perpendicular to the surface for the AUDD. See Figure 4.13 for layout. The dashed line indicates the position of the top surface dimer.

and the highest occupied state (0.1006) and that there is a strong overlap between the second highest occupied state and the adatoms (0.1651). There is surprisingly little difference between the overlaps for up adatoms and down adatoms. As can be seen in Figure 4.32 the HOMO state does have a large surface component but there is also a significant bulk component. The second HOMO state (as shown in Figure 4.33) does not have a large surface component but it does instead have a large component in the bulk.

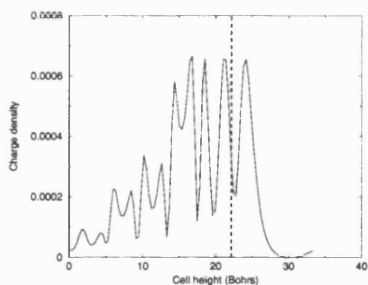


Figure 4.32: Plot of the charge density of the highest occupied state as a function of cell height perpendicular to the surface for the MRAD. See Figure 4.13 for layout.

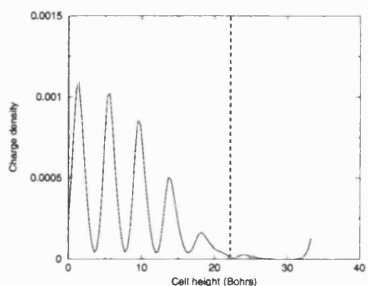


Figure 4.33: Plot of the charge density of the highest occupied state as a function of cell height perpendicular to the surface for the MRAD. See Figure 4.13 for layout.

We found that for the MRAD model the highest occupied state disperses by 0.05 eV along the [110] direction, and by 0.40 eV along the  $[\bar{1}10]$  direction. The dispersion found for the MRAD model is in contradiction with photoemission experiments [220], wherein it was found that a prominent surface state shows a dispersion of 0.2 eV along the [110] direction, and no noticeable dispersion along the  $[\bar{1}10]$  direction. However we also found that at the  $J$  and  $J'$  points in the Brillouin zone, the HOMO and second highest occupied states are degenerate which does match photoemission data [220]. As we found a weakly buckled ad-dimer, the surface possesses only two essentially different electrostatic environments for Si, in agreement with the experimental results of Aristov *et al.* [226].

#### 4.3.5 Thermodynamic results: Which $c(4\times 2)$ model is favoured?

A comparison of  $\Omega$  over the entire range of allowed chemical potential  $\Delta H_f$  for both models is presented in Figure 4.34. As can be seen, the MRAD model is the thermodynamically preferred model over the entire allowable range of chemical potential. Our results thus agree with those of Lu *et al.* [194], who also found that the asymmetric MRAD model was energetically preferred. We also found that the ideal  $(1\times 1)$  reconstruction is energetically preferred over the reconstructed  $c(4\times 2)$  reconstruction. This is in agreement with Catellani *et al.* [225], who found that for an unstressed clean surface,  $c(4\times 2)$  reconstructions would always reconstruct into a weak  $p(2\times 1)$  reconstruction with a total energy a few meV per atom less than the ideal surface. We therefore conclude that the MRAD is the preferred model for the  $c(4\times 2)$  surface reconstruction.

## 4.4 Conclusions

From analysis of our plots of grand canonical potential (see Figures 4.27 and 4.34) as a function of chemical potential of the Si atoms involved, we found that the favoured model for the  $(3\times 2)$  reconstruction is the TAADM and the favoured model for the  $c(4\times 2)$  model is the MRAD model. For the  $(3\times 2)$  reconstruction we can comprehensively rule out the other models. The DDRM is not stable over the range of physically valid chemical potentials. The ADRM is only favoured over the TAADM for values of  $\mu_{\text{Si}}$  which are close to  $\mu_{\text{Si}}(\text{SiC})$  (i.e., for extremely Si-poor conditions). But there is no evidence for a  $(2\times 3)$  reconstruction, such as the ADRM, which is less silicon-rich than the  $c(4\times 2)$

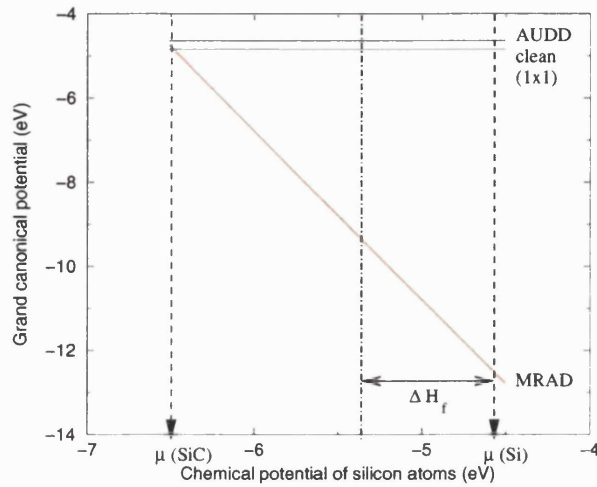


Figure 4.34: Plot comparing the grand canonical potentials  $\Omega$  per  $(4 \times 2)$  unit cell for the two models as a function of the chemical potential of Si atoms, with an arbitrary zero. Also indicated are the cohesive energies per atom of silicon and silicon carbide and the range of size  $\Delta H_f$  within which  $\mu_{\text{Si}}$  is constrained to lie.

reconstruction. We found that (contrary to observations) the  $c(4 \times 2)$  reconstruction is only preferred over a very narrow range of  $\mu$  when the ADRM is included. This indicates that the formation of the ADRM reconstruction must be inhibited by kinematic effects.

However, how adequate are our thermodynamical calculations in determining the favoured model for both the  $(3 \times 2)$  and  $c(4 \times 2)$  reconstructions? The adequacy of our thermodynamic calculations is determined by two factors: firstly the accuracy of LDA DFT calculations of the total energy and secondly the suitability of our zero temperature calculations for modelling the energetics of the growth process. The error in LDA DFT is composed of three terms: an error in the density functional, an error in the plane wave cutoff and an error in  $k$ -point sampling. We have previously shown that our calculations are well converged with respect to plane wave cutoff and  $k$ -point sampling. The error in our density functional is difficult to quantify but we believe this error to be small ( $\approx 0.1$  eV).

The formation of this polytype of SiC takes place at a high temperature and consequently the chemical potential of the silicon adatoms may be determined by entropic factors instead of energetic factors. We neglect any entropic effects. The contribution of any entropic effects would be of magnitude  $k_B T$ . A temperature of approximately 1000 K would lead to entropic effects of order 0.1 eV. By inspection, the grand canonical

curves of the TAADM and ADRM that we plot in Figure 4.27 differ from each other by a much greater amount than this within the region of chemical potential  $\mu_{\text{Si}}$  that is determined by the heat of formation (and similarly for the AUDD and MRAD models).

It is also possible that the structure of the  $(3 \times 2)$  reconstruction is determined by kinematic factors instead of energetic factors. High temperature STM scans [105] show that the Si adatoms are quite mobile but are also ordered. Therefore the structure of the low temperature  $(3 \times 2)$  reconstruction is identical to the high-temperature  $(3 \times 2)$  reconstruction and at such high temperatures it is unlikely that the individual Si adatoms would be kinematically trapped in any specific configuration. This suggests that the chemical potential of the surface reconstruction is determined by energetic factors. Therefore, thermodynamic considerations should be the determining factor in the formation of this surface.

A problem with both of our thermodynamically favoured models is that it remains to reconcile the dispersion of our Kohn-Sham eigenvalues with the experimentally observed photoemission data [214, 220]. The photoemission curves are not generated from one-electron states however, but are generated from many-electron quasiparticle states. Our dispersion results for the TAADM are within the experimental error bars of photoemission results ( $\pm 0.1$  eV), so it is conceivable that our dispersion results do match the real dispersion values. The dispersions of the MRAD model are more problematic, as they do not match photoemission data, but as they are generated from single-particle eigenstates which are compared to many-particle eigenstates the comparison is not ideal. Also the grand canonical potential of the MRAD model is lower than the AUDD model over the entire range of allowable chemical potential and has a higher chemical potential than the ideal  $(1 \times 1)$  surface.

Therefore when we consider the formation of the  $(n \times 2)$  reconstruction in the next Chapter, we take as the structural component of the line (the  $(3 \times 2)$  reconstruction) the TAADM model and the structural component of the surface (the  $c(4 \times 2)$  reconstruction) the MRAD model. We have shown that the TAADM model possesses a highest occupied state that is confined to the line and is “wire-like”. The TAADM possesses a larger dispersion along the  $\times 3$  direction than the  $\times 2$  direction, which means it is easier for an injected electron (or hole) to disperse across the line than along it (by making a simple analogy to tight-binding where the dispersion relation is  $E = E - 2t \cos(ka)$  where  $t$  is the

hopping integral). The  $(3 \times 2)$  reconstruction corresponds to the case where the silicon lines are next to each other. In order to separate the silicon lines we need to add part of the  $c(4 \times 2)$  surface to the unit cell, in order to form a  $(n \times 2)$  unit cell. This  $(n \times 2)$  unit cell requires the use of a larger unit cell. To perform these calculations using DFT would be computationally expensive, instead we use a tight-binding method. This is the subject of our next chapter, the tight-binding study of the  $(n \times 2)$  series of reconstructions.

## Chapter 5

# Silicon carbide: Tight-binding analysis of the structure of the $(n \times 2)$ series of reconstructions

We have found that the favoured model for the  $(3 \times 2)$  reconstruction is the TAADM model (see Figure 4.27) and that the favoured model for the  $c(4 \times 2)$  reconstruction is the MRAD model (see Figure 4.34). We now want to model widely separated silicon lines, which means that we want to construct a  $(n \times 2)$  unit cell by combining the two sets of reconstructions (see Figure 4.5). To model such large unit cells necessitates the use of a less accurate formalism than the DFT method we used for the last chapter. We use a non-self-consistent-charge tight-binding methodology for the simulation of such large unit cells.

In this chapter we first of all introduce the tight-binding method (using the TRO-CADERO code) that we use, the tests we performed to check whether this method accurately simulated silicon carbide and the convergence of our simulations with respect to  $k$ -point sampling. We then compare our tight-binding simulations of the  $(3 \times 2)$  reconstruction with the DFT simulations of the  $(3 \times 2)$  reconstruction to check whether they agree. We then construct and simulate  $(n \times 2)$  unit cells (where  $n$  varies in odd numbers from 3 to 11). We present the details of two structures, a ground-state structure and a metastable structure. We study the effects of the increase in separation of the lines on the

structural and electronic properties of the lines, and present details of a structural transition that occurs for the metastable state when  $n \geq 7$ . Finally we show what happens if we increase the size of the unit cells we are studying by performing calculations on the  $(7 \times 4)$  unit cell, which corresponds to a larger slice of the line and allows distortions with a  $\times 4$  periodicity to occur. This allows the ‘metastable’ structure to relax to a structure with a lower total energy than the ground-state structure. We analyse the structural and electronic properties of such a large unit cell. We then present our conclusions.

## 5.1 Tight-binding: Formalism

### 5.1.1 Tight-binding: Parameterisation

As discussed in Chapter 2, the tight-binding method can be recovered from standard DFT methods by neglecting second order corrections to the total energy [146]. We can thus write the Hamiltonian as  $\hat{H} = \hat{T} + V_{\text{eff}}(r)$ , where we can write the one-electron potential as a sum of spherical atomic contributions:

$$V_{\text{eff}}(r) = \sum_k V_0^k(|r - R_k|) \quad (5.1)$$

where  $V_0$  is the Kohn-Sham potential of a neutral pseudoatom. We can write the wavefunctions of an extended system as

$$\psi_n(r) = \sum_{\alpha, k} c_{\alpha, k}(n) \phi_{\alpha}(r - R_k), \quad (5.2)$$

where  $\phi_{\alpha}(r - R_k)$  are the atomic-like valence orbitals ( $\alpha$ ) of a single pseudo-atom (located at site  $k$ ) within DFT. They are found explicitly by solving the Kohn-Sham equation with the Hamiltonian

$$\left[ -\frac{\hbar^2}{2m_e} \nabla^2 + V_{pa}(r) \right]. \quad (5.3)$$

In this Hamiltonian,  $V_{pa}(r)$  corresponds to a pseudo-atom potential which has the same scattering properties as the atomic DFT potential. The Kohn-Sham equations can then be transformed into a set of algebraic equations

$$\sum_{\alpha,k} c_{\alpha,k}(n)(H_{\alpha\beta} - \epsilon_n S_{\alpha\beta}) = 0, \quad (5.4)$$

where  $H_{\alpha\beta} = \langle \phi_\alpha | \hat{H} | \phi_\beta \rangle$  and  $S_{\alpha\beta} = \langle \phi_\alpha | \phi_\beta \rangle$ . We can then find the single particle energies  $\epsilon_n$  by solving the generalised eigenvalue problem, and thus find the total energy and thence the force acting on each atom. In practice we use the non-self-consistent-charge parameterisation first utilised by Gutierrez *et al* [151], with the Hamiltonian matrix and the overlap matrix parameters fitted to DFT calculations on diatomic molecules, specifically the C-C, Si-Si, Si-H, Si-C, C-H and H-H diatomic molecules (this is known as Density-Functional-Tight-Binding, DFTB). We use four basis functions corresponding to the four valence orbitals  $s, p_x, p_y$  and  $p_z$  of silicon and carbon. Hydrogen of course only uses the  $s$ -orbitals. For more information about the various tight-binding methods that are available, the reader is invited to read the following review articles [141, 153, 154].

### 5.1.2 Tight-binding: Tests

We need to check whether our tight-binding parameterisation gives us an accurate value of the lattice parameter of silicon carbide. The lattice parameter is calculated by finding the minimum of binding energy with respect to lattice parameter. We find that the binding energy is converged when we model a bulk SiC unit cell with 64 atoms, that is that proceeding from 64 to 128 atoms produces a negligible change in the binding energy per atom. We sampled the  $\Gamma$ -point only, as with Brillouin zone folding we are sampling a large part of  $k$ -space. We found that our tight-binding formalism gives a bulk lattice vector of 4.384 Å (see Figure 5.1) which is 0.55% greater than the experimental value. The bulk modulus was found to be 693.82 Gpa. In all of our simulations, we use this theoretical lattice parameter.

We also want to check how many  $k$ -points we need to sample in the surface Brillouin zone in order to make certain that our relaxed structures are well converged. We use a Monkhorst-Pack net [239] to sample the surface Brillouin zone in our tight-binding

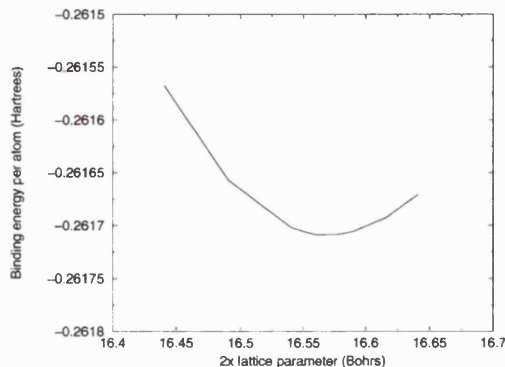


Figure 5.1: Plot of binding energy of bulk cubic silicon carbide as a function of lattice vector for the tight-binding formalism. This is for a simulation of a  $(2 \times 2 \times 2)$  unit cell. The minimum is at 16.56562 Bohr.

simulations. We found that as we increase the  $k$ -point sampling from a  $(221)$  net to a  $(441)$  net and relax the unit cell, that there is a negligible difference in surface structure. The largest change in addimer bond length is  $0.016 \text{ \AA}$  and the largest change in addimer buckling is  $0.0056 \text{ \AA}$ . We conclude that our surface structures are well converged with respect to  $k$ -point sampling using a  $(221)$  net. This also implies that our DFT calculations of the TAADM in the last chapter should be well converged with respect to  $k$ -point sampling as they too sampled four  $k$ -points. We use a  $(221)$   $k$ -point net for all of our tight-binding simulations.

### 5.1.3 Tight-binding: Correspondence with DFT results

All simulation results we present here use simulation cells which are ten atomic layers thick, with the bottom carbon atomic layer passivated with hydrogen. We want to check whether our tight-binding code successfully reproduces the gross structural and thermodynamic results of DFT. We present the details of the structure and deviation from DFT results in Table 5.1 for the  $(3 \times 2)$  models.

Analysing our structural results model by model we see that TROCADERO accurately finds the structure of the ADRM model, with a strongly bound and asymmetric addimer. Our tight-binding formalism does tend to overestimate the amount of buckling. TROCADERO finds a different structure to our DFT results for the DDRM model, with one short and strongly buckled addimer and one longer and flatter addimer. Interestingly our DDRM structure is similar to the structures obtained by Pizzagalli *et al.* [231], who used *ab initio* molecular dynamics, and Gutierrez *et al.* [233], who used a self-consistent-

Table 5.1: Structure of the various (3×2) models as found in our tight-binding scheme and how they compare to DFT simulations. See Figures 4.6-4.9 for the meaning of labels.  $\Delta z$  refers to the buckle of an addimer. All distances are in Å.

Model	Tight-binding results	Deviation from DFT
ADRM	2.3320 ( $a_1$ ), 0.6295 ( $\Delta z$ )	0.0307 ( $a_1$ ), 0.127 ( $\Delta z$ ),
	2.6015 ( $d_1$ ), 2.5710 ( $d_2$ ), 2.6620 ( $d_3$ )	0.0000 ( $d_1$ ), 0.0961 ( $d_2$ ), 0.1658 ( $d_3$ )
DDRM	2.6380 ( $a_1$ ), 0.2441 ( $\Delta z$ )	0.2882 ( $a_1$ ), 0.2654 ( $\Delta z$ )
	2.3239 ( $a_2$ ), 0.6645 ( $\Delta z$ )	0.0259 ( $a_2$ ), 0.1318 ( $\Delta z$ ),
	2.3417 ( $d_1$ ), 2.6323 ( $d_2$ )	0.0587 ( $d_1$ ), 0.2319 ( $d_2$ )
TAADM	2.6199 ( $a_1$ ), 0.6473 ( $\Delta z$ )	0.3008 ( $a_1$ ), 0.0558 ( $\Delta z$ )
	2.6132 ( $a_2$ ), 0.0000 ( $\Delta z$ )	0.1619 ( $a_2$ ), 0.0000 ( $\Delta z$ )
	2.5904 ( $a_3$ ), 0.1252 ( $\Delta z$ )	0.1693 ( $a_3$ ), 0.1252 ( $\Delta z$ )
	2.3409 ( $d_1$ ), 2.3367 ( $d_2$ )	0.0640 ( $d_1$ ), 0.0678 ( $d_2$ )

charge DFTB code. For the TAADM model we find that the gross structure agrees with our DFT results with the similar addimer buckling (0.59 Å and 0.65 Å), although the addimer bond lengths are longer. The largest difference is for the top addimer  $a_1$ .

One possible source for the difference in calculated addimer bond lengths is the charge transfer that occurs when the addimer tilts. In a system which is charge self-consistent, the addimer atoms become oppositely charged and attract one another, reducing the addimer bond length. We posit that this is why in our DFT calculations the flat addimer length is 2.60 Å while the buckled addimer bond length is  $\approx 2.35$  Å. Our non-self consistent code cannot accurately reproduce this effect and so overestimates the addimer bond length. However it does capture the tilt. This is not surprising as the tilt is a kind of Jahn-Teller (JT) distortion which depends upon the symmetry of the highest occupied states, and the near degeneracy of these states is not strongly dependent on the charge distribution of the system. In other words, if the system fulfils the conditions for a JT distortion, it will distort and lower its energy both according to DFT and DFTB, although the structural details of the distortion will be slightly different in each case.

Does TROCADERO reproduce the thermodynamic results that were obtained from our DFT simulations? We used the same thermodynamic arguments as were used in our last chapter, although as the total energy of an isolated silicon atom in TROCADERO is different from PAW we set the zero of silicon chemical potential to -1.0782 Hartrees. Our results are presented in Figure 5.2. As for our DFT calculations, we found that the preferred model for the (3×2) reconstruction over the entire range of allowable silicon chemical potential is the TAADM model. We found that the DDRM model is never thermodynamically preferred. The ADRM model is only allowed for values of chemical

potential that correspond to a silicon-poor  $(3 \times 2)$  unit cell. We also found that the MRAD model is favourable for most regions of the allowable chemical potential.

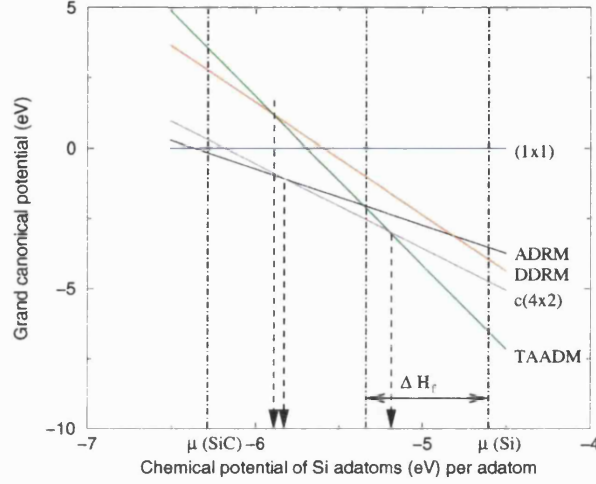


Figure 5.2: Plot comparing the grand canonical potentials  $\Omega$  per  $(3 \times 2)$  unit cell for the three  $(3 \times 2)$  candidate models, the ideal  $(1 \times 1)$  surface and a  $(3 \times 2)$  slice of the  $c(4 \times 2)$  reconstruction, as a function of chemical potential per Si atom  $\mu_{\text{Si}}$ . The zero of the grand canonical potential corresponds to the grand canonical potential of the ideal  $(1 \times 1)$  surface. Arrows pointing downwards indicate the critical value  $\mu_{\text{Si}}^*$  where  $\Omega$  is equal for a pair of  $(3 \times 2)$  models. Also indicated are the chemical potential per atom of silicon and silicon carbide and the range of  $\Delta H_f$ , to illustrate the maximum range of allowable cohesive energies, for the case where the Si atoms are assumed to be in equilibrium with the bulk. This is calculated with TROCADERO, and is in agreement with Figure 4.27.

We have therefore found that our tight-binding formalism reproduces the gross structure of the favoured TAADM model of the  $(3 \times 2)$  reconstruction, by reproducing the magnitude of the top addimer buckling. We have also found that TROCADERO reproduces the thermodynamic results of our DFT simulations. We therefore feel that TROCADERO does reproduce the essential physics of this face of silicon carbide.

## 5.2 Structural properties of the $(n \times 2)$ series

In our relaxations of the  $(n \times 2)$  series of unit cells we used the same initial conditions as for the TAADM and MRAD models. When the difference in total energy per relaxation step is less than  $10^{-5}$  Ha we then say that the structure is fully relaxed.

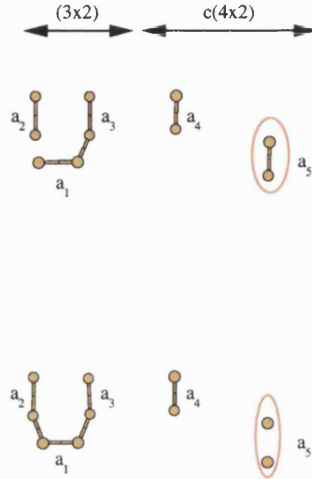


Figure 5.3: Illustration of the two different states of the  $(n \times 2)$  series of reconstructions (this reconstruction corresponds to the  $(7 \times 2)$  reconstruction). We show only the adatoms of the surface. The top diagram shows the ground-state system, while the bottom diagram shows the metastable system. Note that the length and asymmetry of one of the two surface dimers is different in the two schematics (indicated by the red rings).

### 5.2.1 Variation of line structure with $n$

We modelled unit cells with  $n$  ranging in odd steps from 3 to 11, with all odd  $n$  in between. We found two stable states, a ground-state and a metastable state (see Figure 5.3). The true ground-state was not obtainable directly from our initial structure, but was obtained by a process of perturbing one of the addimers of the  $c(4 \times 2)$  part of the surface, by placing the two adatoms of the flat addimer of the surface into the position of the buckled addimer of the surface. We first detail the structure of the ground-state of the  $(n \times 2)$  series of reconstructions. The structure of the ground-state of the entire series of  $(n \times 2)$  reconstructions is essentially identical for all  $n$ . The top addimer of the line was buckled, the second-level addimers of the line are flat and all the addimers of the surface (the MRAD addimers) were buckled. This motif is maintained for all the values of  $n$  we modelled. The structure of the  $(5 \times 2)$  reconstruction was in agreement with previous theoretical work [209].

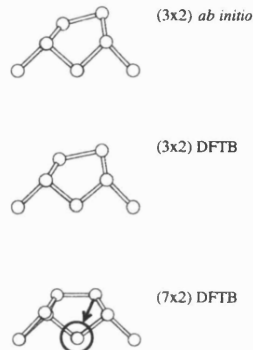


Figure 5.4: Illustration of the different addimer structures we obtain for different unit cells and different, methods of calculation (*ab initio* and DFTB). Note that the addimer for the  $(7 \times 2)$  unit cell is flat, compared to the  $(3 \times 2)$  unit cell (obtained by both methods). The arrow indicates where the electron localises, see Section 5.3.2.

In contrast, the metastable state that we initially find upon relaxation exhibits a structural transition of the line and the surface when  $n \geq 7$ . For  $n \leq 5$  the addimer of the line is buckled, in agreement with the ground-state structure and Lu *et al.* [208, 209]. However, we found that for  $n \geq 7$  the top addimer becomes symmetric and the addimer bond length becomes shorter, with a bond length of  $2.35 \text{ \AA}$  (see Figure 5.4). This matches STM topographs of the lines, which show that the lines are composed of symmetric units [106, 240]. The bond angles between the top addimer and the top-ad-layer-to-second-ad-layer bonds all become  $\sim 109.5^\circ$ , compared to  $\sim 85^\circ$  and  $125^\circ$  for the buckled addimer case. We present the details of the structure of the ground-state  $(7 \times 2)$  and metastable  $(7 \times 2)$  unit cells in Table 5.2. The two major differences in the metastable structure are that 1) the top addimer of the line is flat and much shorter in the metastable state, and 2) that one of the addimers of the surface is flat and longer (this addimer is the closest MRAD addimer to the up adatom of the line). This configuration of the surface addimer roughly corresponds to the configuration of the  $(2 \times 1)$  surface found in previous work [194]. We also found that there is a higher-energy structure of the metastable state that had a buckled addimer. This had a total energy 0.3 eV higher than the flat addimer structure of the metastable state.

The ground-state structure (which has a buckled addimer) had a total energy  $\approx 0.3$  eV lower in energy than the metastable structure. The total energy difference between

Table 5.2: The addimer structure of our two structures of the  $(7 \times 2)$  unit cell; the ground-state (GS) and metastable state (MS). We also show the buckling of the addimers. See Figure 5.3 for the definition of  $a_1 - a_5$ .

State	Addimer bond lengths	Buckling of addimers ( $\Delta z$ )
GS	2.6201 ( $a_1$ ), 2.6153 ( $a_2$ ), 2.6065 ( $a_3$ ) 2.3413 ( $a_4$ ), 2.3409 ( $a_5$ )	0.6507 ( $a_1$ ), 0.0000 ( $a_2$ ), 0.0000 ( $a_3$ ) 0.6383 ( $a_4$ ), 0.6399 ( $a_5$ )
MS	2.3490 ( $a_1$ ), 2.5981 ( $a_2$ ), 2.4156 ( $a_3$ ) 2.3406 ( $a_4$ ), 2.6448 ( $a_5$ )	0.0000 ( $a_1$ ), 0.0000 ( $a_2$ ), 0.1114 ( $a_3$ ) 0.6400 ( $a_4$ ), 0.0000 ( $a_5$ )

the two structures is less than the total thermal energy of the surface silicon atoms at room temperature. Both states could be accessible to the surface.

## 5.2.2 Thermodynamic results

We plotted the grand canonical potential of the  $(n \times 2)$  series of reconstructions as a function of chemical potential in a similar manner to our plot for the candidate models of the  $(3 \times 2)$  and  $c(4 \times 2)$  reconstructions, by using (4.2). These plots are shown in Figure 5.5 for the ground-state system. We found that the  $(3 \times 2)$  reconstruction is the thermodynamically preferred model for chemical potentials that are silicon rich, and that otherwise the  $c(4 \times 2)$  reconstruction is preferred. The  $(n \times 2)$  series of reconstructions is favoured for a very narrow range of chemical potential and over the range of interest of silicon chemical potential, the grand canonical potentials (for  $(1 \times 1)$  unit cells) are very similar. Therefore once the silicon lines are formed then it is relatively easy to increase their separation. However we do not take into account entropic effects, which as the grand canonical potentials are so similar could make a significant difference to moving the crossover points.

## 5.3 Electronic properties of the $(n \times 2)$ series

### 5.3.1 Variation of bandgap and HOMO state with $n$

We analysed the variation in electronic structure as  $n$  was increased, which corresponds to increasing the separation of the lines. The analysis of the unit cell was performed using a (771)  $k$ -point Monkhorst-Pack net. We were interested in finding if the semiconducting nature of the surface changed with  $n$  and whether the dispersion of the HOMO state changed (remember that the dispersion of the HOMO state is important if we consider

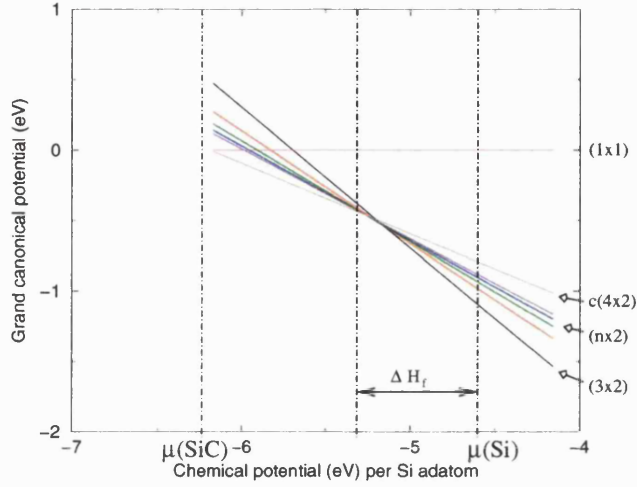


Figure 5.5: Plot comparing the calculated grand canonical potentials  $\Omega$  per  $(1 \times 1)$  cell for the  $(n \times 2)$  series of lines (where  $n$  varies in odd numbers from 3 to 11) with the ideal  $(1 \times 1)$  surface and a  $(1 \times 1)$  slice of the  $c(4 \times 2)$  reconstruction, as a function of  $\mu_{\text{Si}}$ . The zero of the grand canonical potential corresponds to the grand canonical potential of the ideal  $(1 \times 1)$  surface. Also indicated are the experimental cohesive energies per atom of silicon and silicon carbide and the range of  $\Delta H_f$ , to illustrate the maximum range of allowable cohesive energies, for the case where the Si atoms are assumed to be in equilibrium with the bulk. All  $(n \times 2)$  reconstructions have an identical grand canonical potential at  $\mu_{\text{Si}} \approx -5.24$  eV.

Table 5.3: The variation of electronic structure with  $n$  for the ground-state system. We show the dispersion of the HOMO state along the  $\times n$  and  $\times 2$  directions and the range of band gap. All units are in eV.

Value of $n$	Dispersion ( $\times n$ )	Dispersion ( $\times 2$ )	Variation of bandgap
5	0.14	0.02	0.99-1.27
7	0.07	0.04	1.06-1.24
9	0.03	0.01	0.98-1.18
11	0.02	0.02	0.84-1.15

hole injection into the lines, similarly the LUMO state is important for electron injection into the lines).

We found for the  $(3 \times 2)$  unit cell the HOMO state has a dispersion of 0.44 eV along the  $[110]$  (or  $\times 3$ ) direction and a dispersion of 0.07 eV along the  $[\bar{1}10]$  (or  $\times 2$ ) direction. This dispersion was in qualitative agreement with our DFT results for the dispersion on the HOMO state. The HOMO-LUMO (highest-occupied-molecular-orbital lowest-unoccupied-molecular-orbital) gap varies from 1.04 eV at the zone boundary to 1.48 eV at the zone centre. We show how the HOMO dispersion and the bandgap vary with  $n$  for the ground-state system (see Table 5.3) and the metastable state (see Table 5.4).

Table 5.4: The variation of electronic structure with  $n$  for the metastable state system. We show the dispersion of the HOMO state along the  $\times n$  and  $\times 2$  directions and the range of band gap. All units are in eV.

Value of $n$	Dispersion ( $\times n$ )	Dispersion ( $\times 2$ )	Variation of bandgap
5	0.06	0.45	0.03-0.84
7	0.05	0.48	0.23-0.87
9	0.03	0.42	0.33-0.82
11	0.01	0.48	0.22-0.84

Table 5.5: Dispersion of the LUMO state for the metastable structure in eV.

Value of $n$	Dispersion ( $\times n$ )	Dispersion ( $\times 2$ )
5	0.22	0.51
7	0.00	0.14
9	0.00	0.04
11	0.00	0.07

Inspection of Table 5.3 shows that as we increase  $n$  for the ground-state system, the HOMO-LUMO gap of the surface (which is approximately  $\approx 1$  eV for all unit cells) is unaffected. The dispersion of the HOMO state becomes smaller and more isotropic as  $n$  increases, although there is still a larger dispersion along the  $[110]$  direction than along the  $[\bar{1}10]$  direction. The ground-state system does not make a good atomic scale wire.

For the metastable state we found that as we separate the lines there is a change in the HOMO-LUMO gap (see Table 5.4). The minimum HOMO-LUMO gap narrows and the unit cell becomes a narrow-band-gap semiconductor, although the maximum value of the HOMO-LUMO gap is approximately the same as for the ground-state. This is because the surface has a mostly  $c(4\times 2)$  character. We also found that the anisotropy of dispersion of the HOMO state changes; as we separate the silicon lines the HOMO state became quasi-one-dimensional and was aligned along the  $\times 2$  direction of the unit cell and its dispersion became predominantly along the same direction. This implied that the HOMO state is confined along the line and has become “wire-like” for the metastable system. It seemed as if the metastable system could make a good candidate atomic scale wire for hole injection.

We found that the  $(3\times 2)$  unit cell has a larger LUMO dispersion along the  $\times 3$  direction (0.03 eV) than the  $\times 2$  direction. How does increasing the separation of the silicon lines affect the LUMO dispersions? A comparison of the LUMO dispersions for the metastable and ground-state structures is shown in Tables 5.5-5.6. We found that for both structures as we increased the silicon lines the LUMO state becomes more anisotropic with a large

Table 5.6: Dispersion of the LUMO state for the ground-state structure in eV.

Value of $n$	Dispersion ( $\times n$ )	Dispersion ( $\times 2$ )
5	0.01	0.15
7	0.00	0.15
9	0.00	0.16
11	0.00	0.31

dispersion along the line. For the metastable structure the dispersion along the line decreased with  $n$ . Conversely the dispersion along the line for the ground-state structure increased with  $n$  (for the range of  $n$  we consider). Both ground-state and metastable structures would make good atomic scale wires for electron injection.

### 5.3.2 Density matrix analysis

We need to know how the electronic properties of the system are related to the structural changes we observed. One way of studying the local bonding is to calculate the bond order between two atoms in the unit cell, so as to explain the difference in bond length for the flat and buckled addimers of the line. This is derived from the density matrix. The density matrix also lets us calculate the charge density of a particular atom (the charge on an atom) and find the overlap of any state with the atoms of the unit cell.

The density matrix is found by evaluating the integral [241]

$$\rho(x) = \sum_n \langle x | \Psi_n \rangle \langle \Psi_n | x \rangle \quad (5.5)$$

where  $|\Psi_n\rangle$  is the normalised eigenstate and  $|x\rangle$  is a position eigenstate. We can write  $|\Psi_n\rangle$  as

$$|\Psi_n\rangle = \sum_{j\alpha} c_{j\alpha}(n) |\phi_{j\alpha}\rangle, \quad (5.6)$$

where  $c_{j\alpha}(n)$  is the expansion coefficient of the  $n$ th state in the atomic orbital  $\alpha$  on atom  $j$ . This means that we can write the density matrix as

$$\rho_{p\beta j\alpha} = \sum_n \sum_{j\alpha} \sum_{p\beta} c_{j\alpha}(n) c_{p\beta}^*(n) |\phi_{j\alpha}\rangle \langle \phi_{p\beta}| \quad (5.7)$$

The density matrix consists of two terms, a diagonal term ( $p = j$ ) that corresponds to the charge density on an atom  $j$  (the occupation) and an off-diagonal term ( $p \neq j$ ) that corresponds to the charge density between a pair of atoms  $j, p$  (the bond order). This derivation of the density matrix is for orthogonal states, however as our tight-binding formalism is based on DFT calculations we use non-orthogonal states (atomic orbitals) along with a second reciprocal basis set which uses a mixed tensors basis set [242].

To construct the full wavefunction  $|\Psi_n\rangle$  we expand in terms of the linearly independent basis vectors  $|\phi_{j\alpha}\rangle$  to get

$$|\Psi_n\rangle = \sum_{\alpha} c_{j\alpha}(n) |\phi_{j\alpha}\rangle. \quad (5.8)$$

We define an overlap matrix that has elements

$$S_{j\alpha p\beta} = \langle \phi_{j\alpha} | \phi_{p\beta} \rangle = S_{j\alpha p\beta}^*. \quad (5.9)$$

We can also construct a dual set from the original basis set vectors

$$|\phi^{j\alpha}\rangle = \sum_{p\beta} |\phi_{p\beta}\rangle (S^{-1})^{p\beta j\alpha} \quad (5.10)$$

which are orthogonal to the original basis set vectors

$$\langle \phi^{j\alpha} | \phi_{p\beta} \rangle = \sum_{r\gamma} (S^{-1})^{j\alpha r\gamma} \langle \phi_{r\gamma} | \phi_{p\beta} \rangle = \sum_{r\gamma} (S^{-1})^{j\alpha r\gamma} S_{r\gamma p\beta} = \delta_{p\beta}^{j\alpha} \quad (5.11)$$

where  $r\gamma$  is a dummy index. The use of the contravariant index notation is extremely useful for analysis. For instance the mixed-basis element  $H_{p\beta}^{j\alpha}$  is simply

$$\langle \phi^{j\alpha} | H | \phi_{p\beta} \rangle = \sum_{r\gamma} (S^{-1})^{j\alpha r\gamma} H_{r\gamma p\beta}. \quad (5.12)$$

For the case of our DFTB scheme the density matrix  $\rho_{p\beta}^{j\alpha}$  is calculated as

$$\rho_{p\beta}^{j\alpha} = \sum_n \langle \phi^{j\alpha} | \Psi_n \rangle \langle \Psi_n | \phi_{p\beta} \rangle = \sum_{r\gamma n} c^{j\alpha}(n) c^{*r\gamma}(n) S_{r\gamma p\beta}. \quad (5.13)$$

If we do not perform the sum over states in equation (5.13) we obtain the crystal orbital overlap population (or COOP) [243, 244]. We can then evaluate the bond order and charge density terms by summing the COOP (5.13) for all occupied states. To evaluate the bond order terms we need to rotate the off-diagonal elements from their original coordinate frame where the contributions to the  $\sigma$  and  $\pi$  bonds are mixed to a coordinate frame where these contributions are not mixed and where the  $\sigma$  bonds are aligned along the addimer direction (along the  $x$  direction which is equivalent to the  $\times 7$  direction). This is accomplished by the unitary transformation  $U \rho_{p\beta}^{j\alpha} U^{-1}$ , where  $U$  is a unitary matrix transformation through the three orthogonal Euler axes [245].

We started by investigating the bond order of the top addimer of the line, summing over all occupied eigenvalues. Why is this addimer shorter when the addimer becomes flat? We find that the flat addimer of the  $(7 \times 2)$  unit cell (the smallest unit cell with a flat addimer) has a shorter bond length than the buckled addimer of the  $(3 \times 2)$  or  $(5 \times 2)$  unit cells because there is a stronger  $\sigma$  bond and a much stronger  $\pi$  bond. There are much stronger  $ss$  (0.218 for the  $(7 \times 2)$  vs -0.062 for the  $(3 \times 2)$ ),  $sp_x$  (-0.302 vs 0.004) and  $p_x p_x$  (-0.521 vs 0.005) overlaps for the  $(7 \times 2)$  unit cell. Representative COOP are shown in Figures 5.6-5.7.

We have also compared the bond order between the top adatom of the line and one of the adatoms of the second adlayer for the buckled addimer case (for the flat addimer case this corresponds to one of the level adatoms). This analysis shows that as the addimer becomes flat this bond becomes much stronger, with larger  $\sigma$  and  $\pi$  components. There are much stronger  $ss$  (0.200 for the  $(7 \times 2)$  unit cell vs 0.076 for the  $(3 \times 2)$  unit cell) and  $p_z p_z$  (0.450 vs 0.253) overlaps for the  $(7 \times 2)$  unit cell (see Figures 5.8-5.9). Evaluating the diagonal terms of the density matrix we find that associated with this stronger bond

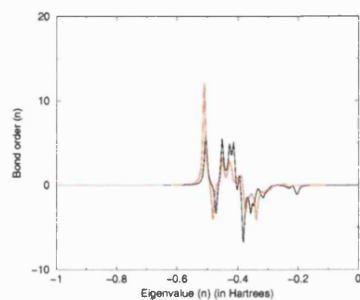


Figure 5.6: Plot of the COOP for all occupied states as a function of eigenvalue  $n$  for the overlap of the  $s$  orbitals on the top pair of adatoms of the line. Black indicates the  $(3 \times 2)$  unit cell and red the  $(7 \times 2)$  unit cell.

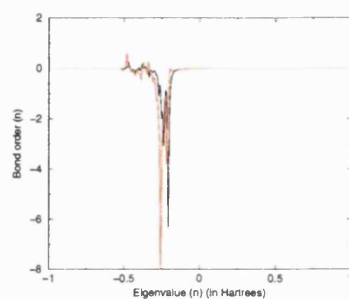


Figure 5.7: Plot of the COOP for all occupied states as a function of eigenvalue  $n$  for the overlap of the  $p_x$  orbitals on the top pair of adatoms of the line. See Figure 5.6 for layout.

between top ad-layer and second ad-layer is the loss of an electron from the top addimer. This electron is transferred to the surface silicon atoms directly below the ad-dimer as shown in Figure 5.4.

Using the density matrix we can also evaluate the overlap of various states on atoms of the unit cell. We calculated the overlap of the HOMO state on all atoms of the surface of the unit cell. We found that for the  $(3 \times 2)$  unit cell the HOMO state is quite diffuse, with the largest component on the second-level addimers, and large components on the top adatom of the top adlayer and the silicon atoms on the surface between the second layer addimers.

When we look at the overlap of the HOMO state on the ground-state  $(n \times 2)$  series of reconstructions (see Figure 5.3), we find that the highest overlap is on the top adatom of the top addimer of the line structure ( $a_1$ ). There is a large overlap of the HOMO state with the other adatoms ( $a_2, a_3$ ) of the line and the two silicon atoms of the surface that are in the middle of the line. The HOMO state for this structure is localised on the line part of the  $(n \times 2)$  reconstruction.

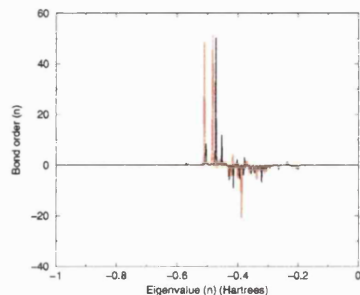


Figure 5.8: Plot of the COOP for all occupied states as a function of eigenvalue  $n$  for the overlap of the  $s$  orbitals between the top adatom of the line and a second-level adatom. See Figure 5.6 for layout.

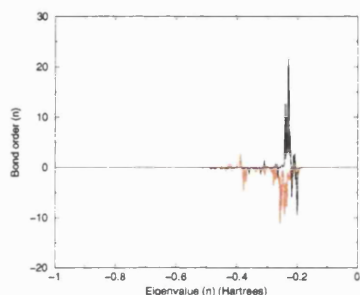


Figure 5.9: Plot of the COOP for all occupied states as a function of eigenvalue  $n$  for the overlap of the  $p_z$  orbitals between the top adatom of the line and a second-level adatom. See Figure 5.6 for layout.

For the metastable structures we find that the HOMO state is strongly localised on two of the adatoms, the surface addimer that is flat and weakly bound (see the encircled addimer  $a_5$  in Figure 5.3) and the second-level addimer that is nearest this surface addimer ( $a_2$ ). The overlap of the HOMO state on other surface and adlayer Si atoms is negligible. The HOMO state resides upon the flat surface addimer. It appears that this surface addimer is responsible for the unit cell acting as a narrow bandgap semiconductor. This  $(2 \times 1)$  part of the surface (from now on called the silicon string) may also act as an atomic scale wire.

### 5.3.3 Proposed mechanism of structural transition for the metastable reconstruction

We observe three changes that happen together for the metastable state: the HOMO state becomes quasi-one-dimensional in character, the top adatom of the buckled addimer of the line moves down, and there is a transfer of an electron from the top adlayer to the

top layer of the silicon carbide crystal proper. We offer one possible rationalisation for this structural transition: that as we increase the separation of the lines, the HOMO state associated with the  $(2\times 1)$  part of the surface becomes quasi-one-dimensional. The HOMO state in one unit cell ceases to interact with the HOMO state in the next unit cell along the  $(\times n)$  direction. This makes the HOMO state interact more strongly with the line, which means that there is an extra contribution to the second adlayer to top adlayer bonds of the line. This forces the top adatom closer to the surface, and flattens the buckle of the top addimer. As the dangling bond state rises in energy as the addimer becomes flat, a state of the top adatom becomes depopulated, and an electron leaves the top addimer to reside in the silicon atoms of the top layer of the silicon carbide crystal directly below the addimer (as indicated in Figure 5.4). However we are aware that the charge transfer which is involved in this structural transition could be inaccurately treated, as the tight-binding method we use is a non-charge-self-consistent scheme.

## 5.4 Discussion on the ground-state and metastable structures

We have shown that the  $(n\times 2)$  series of reconstructions is a complex series of reconstructions which exhibit a rich variety of behaviour. There exists a ground-state which possesses an insulating character and a metastable state that exhibits a quasi-one-dimensional near-metallic behaviour. For the ground-state structures all silicon addimers on the surface are strongly bound and asymmetric. The metastable structure on the other hand has a weakly bound, flat, silicon addimer (the silicon string) on the surface, as well as several strongly bound and buckled addimers. This silicon string roughly corresponds to the configuration of the  $(2\times 1)$  surface in previous work [194].

Our treatment of the  $(n\times 2)$  series of reconstructions relies on treating the surface between the lines as composed of  $c(4\times 2)$  structural components. However the  $c(4\times 2)$  reconstruction is only stable for surfaces which have a very low defect density and which exists at low ( $\leq 600$  K) temperature. Our  $(n\times 2)$  series of reconstructions does not correspond to a well ordered  $c(4\times 2)$  surface, as defects are present. These defects are the silicon lines. It is questionable whether we should assume that the local structure of the surface is that of a well-ordered  $c(4\times 2)$  surface. We posit that the formation of the

metastable state is caused by the influence of the silicon lines on the surface. Evidence for such a metastable state is provided by the STM topographs of Douillard *et al.* who found that the silicon lines of the  $(8 \times 2)$  unit cell (composed of a  $(5 \times 2)$  and a  $(3 \times 2)$  unit cell) were flat. These are the only STM topographs of the silicon lines which have been published.

Also, we do impose the constraint that the basic surface reconstruction of the surface and line has a repeat lattice vector of  $\times 2$  along the  $[\bar{1}10]$  direction. This means that the near-metallic and quasi-one-dimensional silicon string-like surface cannot reduce its energy via a Peierls-like transition. The “stable” structure is only more stable than the “metastable” structure if it is constrained to a  $\times 2$  periodicity. This is not necessarily the case for larger unit cells, as we show in the next section.

## 5.5 Larger unit cells: $(7 \times 4)$ unit cell

### 5.5.1 Structural properties of the $(7 \times 4)$ unit cell

We use the relaxed structures obtained from our simulations of the  $(7 \times 2)$  unit cell and place two unit cells next to each other to form a larger unit cell with dimension  $(7 \times 4)$ . We found that our ground-state structure did not undergo any significant structural relaxation in this new unit cell. A structure derived from the metastable structure did undergo a significant structural transition however. The silicon addimer of the surface string of one  $(7 \times 2)$  unit cell bonds to the silicon string of the other  $(7 \times 2)$  unit cell to form a structure which is  $\approx 8 \text{ \AA}$  long. The previously flat surface silicon strings become asymmetric, with the atoms at the ends of the string  $0.5 \text{ \AA}$  higher than the atoms in the middle of the string (see Figure 5.10).

We also found that the addimers of the second adlayer of the line become dimerised, (see (1.7)) with a repeat lattice vector of  $\times 4$  surface lattice vectors, (we have tested this for a  $\times 8$  unit cell and found that the basic structural motif still has a repeat lattice vector of  $\times 4$  lattice vectors, see Figure 5.10). The long addimers have a bond length of  $2.60 \text{ \AA}$  while the short addimers have a bond length of  $2.38 \text{ \AA}$ , the magnitude of change in bond length is of order  $0.22 \text{ \AA}$ . We also found that there is a height difference between the short and long addimers, the long addimers are  $\approx 0.05 \text{ \AA}$  higher than the short addimers (see Figure 5.11). This relaxation of the metastable structure is  $0.53 \text{ eV}$  lower in total

energy than the relaxed ground-state structure.

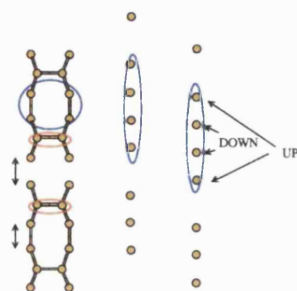


Figure 5.10: Structure of the Si adlayer for the  $(7 \times 8)$  unit cell constructed from the flat addimer case for the metastable structure. We indicate the differing bond lengths of the second-level addimers with the black arrows. The structure of the  $(7 \times 8)$  unit cell is composed of two  $(7 \times 4)$  unit cells. The blue ellipses indicate atoms on the surface where there is a large overlap with the HOMO state, the red ones atoms on the surface where there is a large overlap with the LUMO state.



Figure 5.11: Asymmetry of height for the short and long addimers of the line for the  $(7 \times 8)$  unit cell. This asymmetry has been exaggerated.

If we took the buckled addimer structure of the metastable state of the  $(7 \times 2)$  unit cell and construct a  $(7 \times 4)$  unit cell, we found that this too undergoes a structural transition which is similar to the flat addimer structure. The second-level addimers of the line became dimerised. The flat silicon addimer of the silicon string reconstructs in a similar way to the silicon string for the flat addimer case, with the end adatoms of the string  $0.5 \text{ \AA}$  higher than the middle adatoms of the string. The structure is shown in Figure 5.12.

This structure is 0.09 eV lower in energy than the ground-state structure but is 0.42 eV higher in energy than the flat addimer structure of the metastable structure.

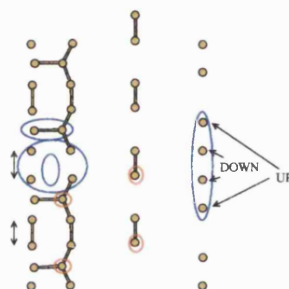


Figure 5.12: Structure of the Si adlayer for the  $(7\times 8)$  unit cell constructed from the buckled addimer case for the metastable state. We indicate the differing bond lengths of the second-level addimers with the black arrows. The structure of the  $(7\times 8)$  unit cell is essentially composed of two  $(7\times 4)$  unit cells. See Figure 5.10 for colour coding.

This structural transition with a doubling of the basic repeat lattice vector is indicative of a Peierls transition (see chapter 1), and is the reason why the relaxed “metastable”  $(7\times 4)$  unit cell has a lower total energy than the relaxed “ground”  $(7\times 4)$  unit cell. How does this affect the electronic structure?

### 5.5.2 Electronic properties of the $(7\times 4)$ unit cell

We compared the electronic properties of a dimerised  $(7\times 4)$  unit cell to an undimerised  $(7\times 4)$  unit cell using a (771) Monkhorst-Pack net. Our results are shown in Table 5.7 for the flat addimer and buckled addimer structures of the metastable structure. The HOMO state is still quasi one-dimensional and aligned along the direction of the line after dimerisation for the flat addimer structure. For the buckled addimer structure the anisotropy of the HOMO state changed direction and was aligned across rather than along the line. After dimerisation the LUMO state of the flat addimer structure is quasi-one-dimensional and more dispersive along the silicon line than before dimerisation. Before dimerisation the LUMO state of the buckled addimer structure is more dispersive along the  $\times 7$  than the  $\times 4$  direction although the magnitude of dispersion along both directions

Table 5.7: Dispersion for the HOMO (and LUMO in brackets) states for the “metastable” structures before and after dimerisation along the  $\times 7$  and  $\times 4$  directions and the range of the HOMO-LUMO gap in eV. We present results for the flat addimer (top pair) and buckled addimer structures (bottom pair).

Dimerisation?	Dispersion ( $\times 7$ )	Dispersion ( $\times 4$ )	Variation in bandgap
No	0.03 (0.00)	0.14 (0.07)	0.03-0.28
Yes	0.00 (0.00)	0.02 (0.10)	0.64-0.77
No	0.07 (0.07)	0.15 (0.03)	0.02-0.05
Yes	0.04 (0.07)	0.00 (0.00)	0.34-0.38

is of the same magnitude. After dimerisation the LUMO state is quasi-one-dimensional with a much larger dispersion across the silicon line (the  $\times 7$  direction) than along the silicon line (the  $\times 4$  direction).

We find in both cases that the dimerisation increases the gap between the HOMO and LUMO states. It seems as if we can treat the dimerisation (in at least the flat addimer system) as a Peierls-like transition. We use Peierls-like rather than simply Peierls transition, as the surface is a narrow bandgap semiconductor not metallic. A Peierls transition is only valid for metallic systems.

### 5.5.3 Density matrix analysis

We analysed the off-diagonal density matrix elements to find the bond order for the long and short addimers for our flat and buckled addimer dimerised structures. We do not present results for the undimerised structure that is obtained from the ground-state ( $7\times 4$ ) system as its electronic properties are essentially identical to those of the ( $7\times 2$ ) unit cell. We found that there are much stronger  $\sigma$  bonds and  $\pi$  bonds for the short addimer of the line than for the long addimer. The  $ss$  overlap in particular (0.388 for the short addimer vs 0.282 for the long addimer) is much stronger for the short addimer case (see Figure 5.13), and there is also a larger  $\pi$  ( $p_x p_x$ ) overlap (0.214 vs 0.145) for the short addimer (see Figure 5.14).

We have also evaluated the occupation of the electronic states on the short and long addimers of the line to see if there is a charge density wave present in the second-level addimers. We found that there is a difference in the occupation of states on atoms in the long addimer when compared with atoms of the short addimer. We found that the for the flat addimer system of the metastable structure the long addimers have  $\approx 0.1$  more of an electron than the short addimers; for the buckled addimer system of the

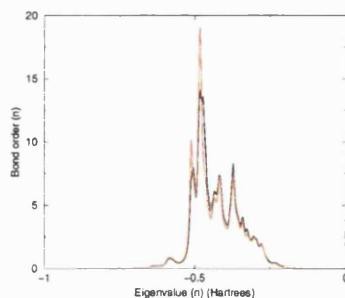


Figure 5.13: Plot of the COOP for all occupied states as a function of eigenvalue  $n$  for the overlap of the  $s$  orbitals for the second-level addimers of the line for a  $(7 \times 8)$  dimerised unit cell.

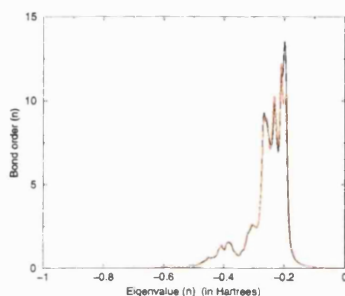


Figure 5.14: Plot of the COOP for all occupied states as a function of eigenvalue  $n$  for the overlap of the  $p_x$  orbitals for the second-level addimers of the line for a  $(7 \times 8)$  dimerised unit cell. See Figure 5.13 for colour coding.

metastable structure there is  $\approx 0.4$  more of an electron on the long addimers than on the short addimers. In both cases this additional contribution for the long addimers fills the antibonding part of the  $ss$  and  $p_x p_x$  orbitals. We think that the reason there appears to be more charge difference between the long and short addimers for the buckled addimer of the metastable case is that the flat top addimer case involves a lot of charge transfer, with the electron transferred from the top addimer localising on the second-level addimers. This extra charge is found predominantly on the shorter second level addimers.

When we looked at which atoms of the surface of the unit cell had a large overlap with the HOMO state for the flat addimer system, we found that the largest overlap is on the adatoms that form the silicon string. The up adatoms of the silicon string have a larger overlap with the HOMO than the down atoms of the silicon string. There is also a large overlap of the HOMO state with the short ( $\approx 2.38 \text{ \AA}$ ) addimers of the line (see Figure 5.10). The HOMO state is tightly bound to structures that are oriented along the  $\times 4$  direction as it was in the  $(7 \times 2)$  structure, this is why the HOMO state is still quasi-one-dimensional. The LUMO state is tightly bound to the top addimers of the line

for the flat addimer structure. Any electrons or holes that are injected into this system would propagate along the string (or line).

For the buckled addimer case we find that the HOMO state has a strong overlap with the long ( $\approx 2.60 \text{ \AA}$ ) second level addimers of the line, the silicon atoms of the surface that are between these addimers, one of the top level addimers of the line and the flat silicon string of the surface (see Figure 5.12). Similarly the LUMO state has strong overlaps with the surface addimers. This HOMO (or LUMO) state is much more diffuse than the tightly localised HOMO (or LUMO) state of the flat addimer system, with a very large overlap across the line. This is why the HOMO (or LUMO) state has a much larger dispersion in the  $\times 7$  direction than across the  $\times 4$  direction. Any charges that are injected into this system would disperse across the string or the line.

## 5.6 Conclusions

We have tested our tight-binding parameterisation against DFT results and found that our relaxed structures are in general agreement with the DFT structures. We have used the thermodynamically favoured models of the  $(3\times 2)$  and  $c(4\times 2)$  unit cells as the structural components of the  $(n\times 2)$  series of reconstructions. We have found that we could obtain two classes of structure, a ground-state structure with a well defined and buckled  $c(4\times 2)$  surface, and a metastable structure where the surface has a partial  $(2\times 1)$  character. The ground-state structures were found to be wide bandgap semiconductors with a nearly isotropic and weakly dispersive HOMO state which had a slightly larger dispersion along the  $\times n$  than the  $\times 2$  direction. The LUMO state was found to have a strong dispersion along the  $\times 2$  direction and a weak dispersion along the  $\times n$  direction. The metastable structures are narrow bandgap semiconductors with an anisotropic and more strongly dispersive HOMO state. For these metastable states a structural transition occurs when  $n \geq 7$ ; the top addimer of the line becomes flat. The HOMO state then has a large dispersion along the  $\times 2$  direction and a small dispersion along the  $\times 7$  direction and so is quasi-one-dimensional. Similarly the LUMO state has a weak dispersion along the  $\times n$  direction and a stronger dispersion along the  $\times 2$  direction. A tentative explanation of the structural transition is proposed on the basis that, as we increase  $n$ , we increase the separation between the HOMO states of neighbouring unit cells that are localised on the silicon string. This makes this state interact more strongly with the nearest silicon

line, and makes it energetically possible for the top addimer to flatten.

We then use our ground-state and metastable structures to construct and relax a  $(7\times 4)$  unit cell. The results depend on whether the ground-state or metastable  $(7\times 2)$  structure is used. We found that the ground-state  $(7\times 2)$  unit cell does not dimerise and the  $(7\times 4)$  unit cell has a structure composed of two  $(7\times 2)$  unit cells. We also found that the metastable structure does dimerise to form a  $(7\times 4)$  unit cell. This dimerised unit cell has a lower total energy than the  $(7\times 4)$  unit cell derived from the  $(7\times 2)$  ground-state. Thus the dimerised  $(7\times 4)$  unit cell is thermodynamically favoured. This dimerisation also increases the bandgap, implying that it is a Peierls-like transition. The HOMO state is still quasi-one-dimensional and is confined to the silicon string and the silicon line.

Clearly the  $(n\times 2)$  series of reconstructions is a complex series with a rich variety of behaviours depending upon the details of the surface structure. However are we modelling the surface accurately? We are aware that the charge transfer which is involved in the metastable surface structure could be inaccurately treated, as the tight-binding method we use is a non-charge-self-consistent scheme. Currently we have been unable to test our structures using a more accurate *ab initio* formalism.

The silicon string (the surface addimer) and the silicon line (the line addimers) are codependent in the metastable system. The presence of the line causes a silicon string to form which then causes the structural transition in the silicon line. If we strongly buckle the silicon string then we buckle the top addimer of the line. Is it reasonable that the string-like structure forms in the first place on the  $c(4\times 2)$  part of the surface? As stated in the last chapter, the  $c(4\times 2)$  surface is only formed in defect-poor regions of the silicon rich (001) face of cubic silicon carbide. The silicon lines do constitute defects on this surface. As  $n$  increases the surface between the lines does become more  $c(4\times 2)$ -like. However the surface near the silicon lines should not be  $c(4\times 2)$ -like but  $(2\times 1)$ -like (as shown in section 4.1.4 of Chapter 4). We found this is what happens. Therefore we propose that the silicon string formation, which makes the silicon line symmetric, may occur on the surface. There is some experimental evidence that the silicon lines are symmetric [106, 240, 216]; STM scans along and across the lines show that the line is composed of symmetric units. However compared to the various surfaces we have modelled there is a paucity of experimental evidence on the silicon lines. There is no experimental evidence that the surface near the lines has a  $(2\times 1)$ -like character, but STM

scans near the line may be strongly affected by the presence of the line.

We have found a  $(7 \times 4)$  unit cell with two line-like features (the silicon string and the silicon line) which appears to have undergone a Peierls-like transition and has a quasi-one-dimensional electronic character with a narrow bandgap. Is this system a good candidate atomic scale wire? To find out we need to calculate the transport properties of this system. This is the subject of the next chapter, which concerns polaron formation and the effects on the electronic structure of the system.

## Chapter 6

# Transport properties of the silicon lines

We have found that there exists a metastable state for the  $(n \times 2)$  unit cell on the (001) face of cubic silicon carbide which possesses a quasi-one-dimensional HOMO state. This state is localised on a silicon atomic string with a significant overlap with the second level addimers of the line. This surface reconstruction is found to be unstable with respect to a Peierls-like transition which doubles the length of the repeat lattice vector along the line direction, increases the bandgap and which is thermodynamically favoured over the ground-state. This seems to indicate that we can treat the silicon atomic string and/or the silicon atomic line as a Peierls distorted atomic scale wire. What are the transport properties of such a system?

In this chapter we inject charge into the  $(7 \times 8)$  unit cell to investigate whether the charge localises to form a polaron. We find that this is indeed the case. We investigate how the formation of this polaron affects the physical and electronic structure of the system. We calculate the dynamical matrix of the system and see which phonon modes couple strongly to the system. We then use the information we obtained from our calculation of the dynamical matrix to calculate the electron-phonon coupling constants of the system in real space, and transform these constants into eigenvector-space. We also transform the original long ranged atomic orbitals of the system into tightly localised Wannier functions. We then assess the effective mass of the polaron defect to determine whether the defect would undergo coherent or diffusive transport. Finally we analyse

these results and discuss whether this system is a good atomic scale wire.

## 6.1 Effects of charge injection into system

In this section we discuss the effects of injecting an electron or a hole into a large slice of the line (using the TROCADERO code). We used a  $(7\times 8)$  unit cell to make certain that if any polaron-like defect is formed, then each polaron in the line is well separated from its image in the neighbouring unit cells. The use of such a large unit cell requires us to use a six atomic layer thick unit cell to make our calculations tractable on a DEC-Alpha EV6 workstation. The bottom two layers were constrained in bulk atomic positions. The initial structure of this  $(7\times 8)$  unit cell is the relaxed structure in a neutral charge state. This is identical to two dimerised  $(7\times 4)$  unit cells stacked upon each other in the  $\times 4$  direction. We call this structure the reference structure (in which we denote the vector of atomic positions by  $u^0$ ).

In order to make certain that the polaron localises on the surface we distorted one of the atoms of the silicon line (see the last chapter for which atoms these are). The atom that is distorted has a large overlap with the HOMO state (for hole injection) or the LUMO state (electron injection), the magnitude of distortion is given in the next subsection. Charge is then injected into the system. All structural relaxations were performed using a  $(221)$  Monkhorst-Pack mesh [239]. Analysis of the electronic structure of the relaxed unit cell was performed using a  $(771)$  M-P mesh.

### 6.1.1 Structural effects of charge injection: Polaron formation

We have performed relaxation calculations using our ground-state  $(7\times 4)$  unit cell as the basis for a  $(7\times 8)$  unit cell (the reference structure). The reference structure is one where the top addimer of the line is flat and the unit cell is dimerised.

For the hole polaron defect we distort an atom which has a strong overlap with the HOMO state so as to distort the symmetry. This is either an atom of the silicon line or of the silicon string, in both cases making the Si-Si bond length shorter by  $0.21 \text{ \AA}$ . In both cases we find that if we allow a  $(7\times 8)$  unit cell to relax when a hole is injected into the system, a small polaron-like defect is formed. The addimer structure is shown in Figure 6.1. The polaron defect is confined to the silicon line.

We found that the hole polaron defect has a small structural effect on the  $(7\times 8)$  unit

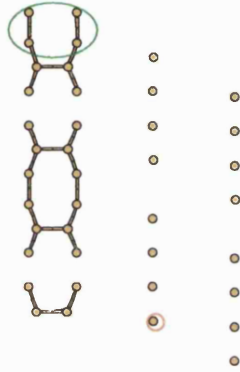


Figure 6.1: Structure of the Si adlayer for the  $(7 \times 8)$  unit cell when a hole is injected into the system (top view). The light green ellipse indicates the structural defect where a polaron is formed. The red ellipse indicates where we initially inject a hole.

cell. When compared to the initial reference structure the two (short) addimers that are affected by the polaron are shorter by  $\approx 0.04 \text{ \AA}$  each. One of the short addimers is asymmetric by  $0.03 \text{ \AA}$ . These two short addimers are  $0.04 \text{ \AA}$  higher than the short addimers of the reference structure, which means that they are higher than the long addimers (see Figure 5.11). When compared with the charged reference system, the system with the polaron defect has a lower total energy with the difference in total energies of order  $0.05 \text{ eV}$ . As the polaron defect is localised on the second level addimers of the silicon line it seems likely that the defect would not be directly observable by STM scans.

We can distort an adatom which has a strong overlap with the LUMO state and inject an electron into the system to observe whether electron polaron formation occurs. We distort a flat adatom of the line by moving it up by  $0.3 \text{ Bohrs}$ . We found that if an electron is injected into the system that it localises on the line. The polaron is tightly localised on an adatom of the top addimer of the line and a second level addimer of the line (see Figure 6.2). Unlike the hole polaron, the structural deformation induced by the polaron is large. The top addimer of a slice of the line becomes buckled by  $0.30 \text{ \AA}$  with

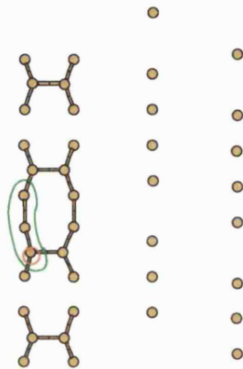


Figure 6.2: Structure of the Si adlayer for the  $(7 \times 8)$  unit cell when an electron is injected into the system (top view). The light green ellipse indicates the structural defect where a polaron is formed. The red ellipse indicates where we initially inject an electron.

the top addimer becoming  $0.02 \text{ \AA}$  longer. The second level addimer that was distorted is  $0.03 \text{ \AA}$  longer. The difference in total energy between this charged polaron structure and the charged reference structure was  $0.07 \text{ eV}$ , with the polaron structure possessing a lower total energy. As this defect had a large component on the top addimer of the line with a large distortion, it seems likely that this defect would be observable to STM scans if it remains localised for long enough.

However our calculation of the electron polaron system is less accurate than our calculation of the hole polaron system. The electron polaron system is a negatively charged ground-state. The tight-binding parameterisation that we use is based upon LDA-DFT calculations of diatomic molecules. The LDA accurately reproduces the behaviour of ground-state systems regardless of charge, but our tight-binding parameterisation is fitted to occupied-state properties such as the bond length. Injection of an electron involves occupying conduction band states that may well be less well described.

### 6.1.2 Effect of polaron formation on electronic structure

Does the formation of the structural defect localise the hole or electron that has been injected into the system? This was checked by performing a charge analysis (see equation (5.13)) using the structure of the polaron system and the structure of the reference system, when both systems are neutral and then when they are charged. If we compare the occupation of atoms for the two different unit cells in the two different charge states we can see whether the formation of the defect localises charge or not.

For the hole polaron system we found that the hole is strongly localised on six atoms associated with the line, the four silicon adatoms of the line and the two silicon atoms of the terminating layer between these silicon addimers (see Figure 6.3). Before the formation of the polaron defect (in the reference system) only 0.09 of the hole was localised on these six atoms. After the formation of this polaron defect, 0.42 of the hole was localised on these six atoms. This indicates that the formation of this polaron localises the hole. We get a large amount of charge localisation for a small amount of deformation.



Figure 6.3: Structure of the Si adlayer for the  $(7 \times 8)$  unit cell when a hole is injected into the system (top view). The magenta ellipse indicates the six atoms of the unit cell where the hole is localised.

For the electron polaron we found that the electron was strongly localised on the three adatoms that are deformed from the reference structure when the polaron was formed (see Figure 6.2). Before the formation of the polaron only 0.11 of the electron was localised on these three adatoms. After the formation of the polaron 0.58 of the electron was localised on these three adatoms. Unlike the hole polaron there is both a

large amount of charge localisation and a large amount of deformation on a few adatoms of the line.

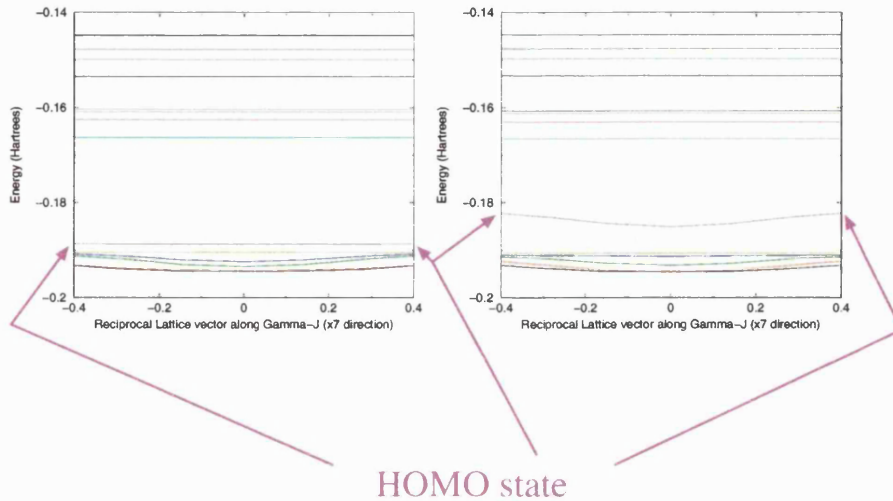


Figure 6.4: Band structure of the reference system (left diagram) and the hole polaron system (right diagram) along the  $\Gamma - J$  (or  $[110]$ ) direction. We also indicate the HOMO state.

How does the formation of the hole polaron affect the electronic structure of the  $(7 \times 8)$  unit cell? We compare the electronic structures of the polaron system and the reference system along the  $\times 7$  and  $\times 8$  directions, see Figures 6.4 and 6.5. As can be seen in these two figures the formation of the polaron reduces the HOMO-LUMO gap by pushing the HOMO state into the gap. This is a defining characteristic of a polaron state, as stated in Chapter 1. The magnitude of dispersion of the HOMO state along the  $\times 7$  direction or across the silicon line is 0.080 eV, while along the line the HOMO dispersion is 0.001 eV. The HOMO state is quasi-one-dimensional, but is more dispersive across than along the line.

The formation of the electron polaron structure also had an effect on the electronic structure. The LUMO state is pushed away from the conduction band and into the gap (see Figures 6.6 and 6.7). This significantly reduces the HOMO-LUMO gap. The magnitude of dispersion along the line (the  $\times 8$  direction) is 0.003 eV while the magnitude of dispersion across the line (the  $\times 7$  direction) is 0.00008 eV. The HOMO state is quasi-one-dimensional and is more dispersive along the line than across the line.

We found that the dispersion characteristics of the hole polaron structure and the electron polaron structure differ from each other, with the hole polaron structure having

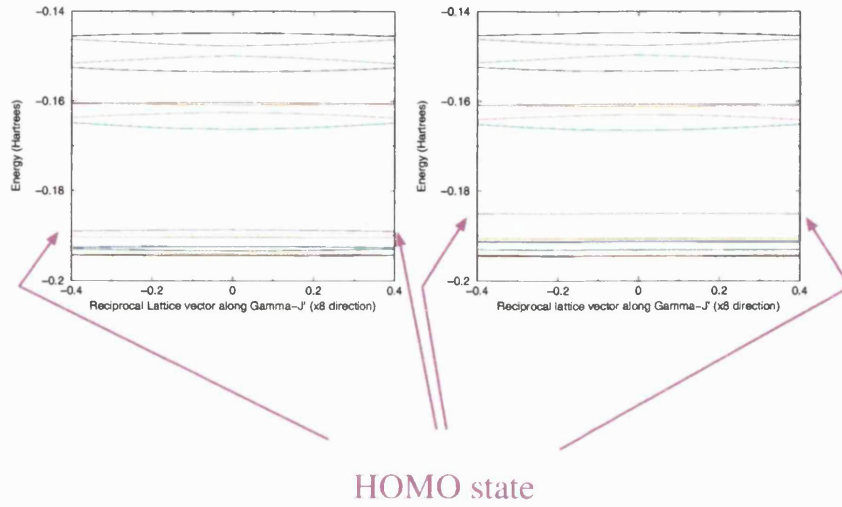


Figure 6.5: Band structure of the reference system (left diagram) and the hole polaron system (right diagram) along the  $\Gamma - J'$  (or  $[\bar{1}10]$ ) direction. We also indicate the HOMO state.

a stronger dispersion across the line than along it and the electron polaron having a stronger dispersion along the line than across it. We attribute this to the distribution of the HOMO and LUMO states in the  $(7 \times 8)$  unit cell. The HOMO state is localised on the silicon strings of the surface and the short second level addimers of the line. If we inject a hole into the line it forms a polaron that is localised on the second level addimers (see Figure 6.1). It is easier for this polaron to move across the line than along the line as the distance from a set of short second level addimers to a neighbouring silicon string is less than the distance from one set of short second level addimers to the next set of short second level addimers ( $\times 2$  surface lattice vectors vs  $\times 4$  surface lattice vectors). In contrast, the electron polaron is localised on the top addimer of the line and a second level addimer next to this addimer (see Figure 6.2). For this polaron to move from one such site to the next equivalent site along the line is a shorter distance than to move from one equivalent site to another across the line ( $\times 4$  vs  $\times 7$  surface lattice vectors). It seems as if the electron polaron is confined to the line and acts quasi-one-dimensionally while the hole polaron can spread across the surface.

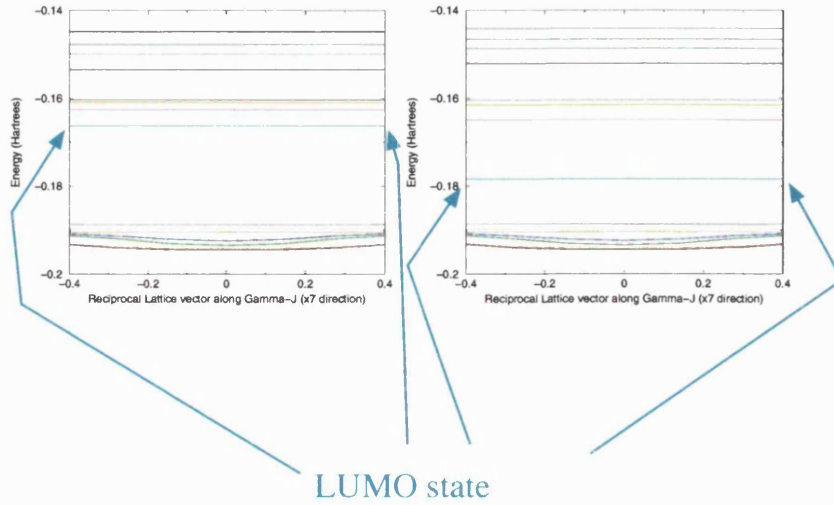


Figure 6.6: Band structure of the reference system (left diagram) and the electron polaron system (right diagram) along the  $\Gamma - J$  (or  $[110]$ ) direction. We also indicate the LUMO state.

## 6.2 Which phonon modes couple strongly to the polaron?

We have found that when we inject charge into the silicon line that a polaron forms, a defect which localises charge. Polarons which form in a Peierls-like distorted chain couple strongly to phonon modes. How well does the polaron couple to the phonon modes of the equilibrium system?

### 6.2.1 Calculation of phonon modes: Formalism and tests

In order to calculate the phonon modes of the reference system we need to find the eigenvectors of the dynamical matrix (equation (3.8)). We calculated the elements of the dynamical matrix numerically, using

$$K_{i(k),j(l)} = \frac{\Delta F_{i(k)}^1 - \Delta F_{i(k)}^2}{2\Delta x_{j(l)}} \quad (6.1)$$

where  $i$  labels any atom in the unit cell and  $j$  labels the particular atom that is displaced by a distance  $\Delta x$ . We displace each atom first one way along one direction (1 in (6.1)) then in the opposite direction (2) (i.e., positive and negative displacements). This lets us

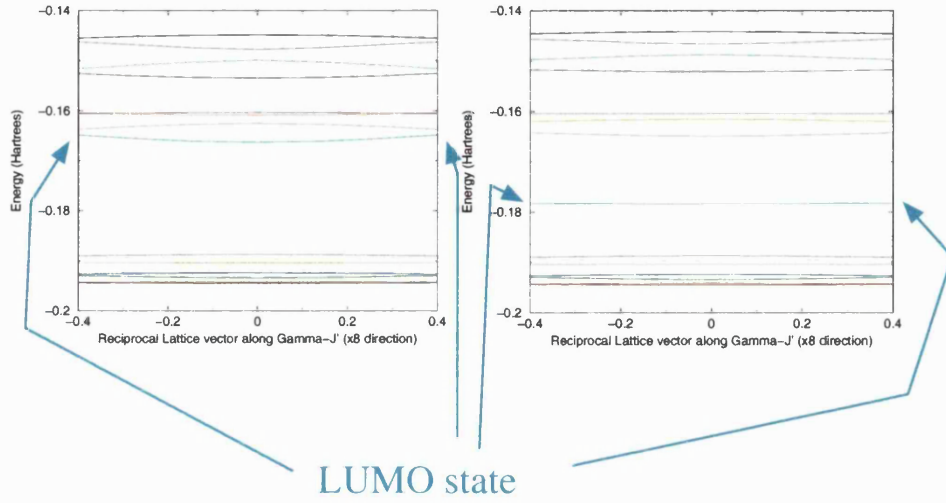


Figure 6.7: Band structure of the reference system (left diagram) and the electron polaron system (right diagram) along the  $\Gamma - J'$  (or  $[\bar{1}10]$ ) direction. We also indicate the LUMO state.

calculate the differential of force with respect to displacement using a centered-difference method. As our unit cell is three dimensional we have  $3N$  phonon modes in our dynamical matrix; we thus use the indices  $k$  and  $l$  to label direction of the induced force on atom  $i$  and the displacement of atom  $j$  respectively. To then find the phonon modes and frequencies we diagonalise the resulting dynamical matrix. The eigenvalues  $V_q$  we calculate are not the phonon mode frequencies, rather they are  $M_j \omega_q^2$  where  $M_j$  is the mass of the atom we are displacing.

Firstly we needed to determine how small a displacement we can make to any individual atom and remain within the harmonic limit, while also producing a restoring force on the atom which was larger than the numerical noise. We found that a distortion of 0.01 Bohrs is within the harmonic limit (see Figure 6.8) and yet gave a force which is 20 times larger than the numerical noise. As we use numerical differentiation there will be a small asymmetry in the dynamical matrix. Diagonalisation of this dynamical matrix (6.1) will result in eigenvectors which are complex and eigenvalues which are imaginary. This is obviously unphysical. We explicitly symmetrise the dynamical matrix to obtain real eigenvectors.

As we have 488 atoms in our unit cell any program that calculates the phonon modes of the entire system will take an extremely long amount of time. We therefore needed to make an approximation to make this calculation tractable in a reasonable amount of

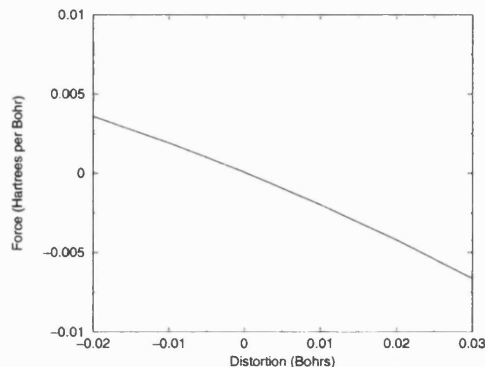


Figure 6.8: Plot of force against displacement for an equilibrium structure. The force is approximately linear for displacements within 0.01 Bohrs.

time. We assume that the only atoms which are coupled to the polaron defect are the silicon adatoms of the line (from four ( $3 \times 2$ ) unit cells, 24) and the silicon atoms of the surface under the line (as above, 24). We tested whether this approximation reproduces the polaron structure by performing the same relaxation calculation as were performed in the last section for the hole polaron system, but this time constraining all atoms apart from the 48 atoms mentioned above. We found that the gross physical structure of the polaron defect is retained in this approximation but that the differences from the reference structure are smaller: the two addimers are  $0.03 \text{ \AA}$  shorter than the same addimers in the reference structure, the buckle of one of the addimers is only  $0.01 \text{ \AA}$  and the two addimers are only  $0.02 \text{ \AA}$  higher than the equivalent addimers of the reference structure. As the gross structure of the defect is reproduced by this approximation we assume that this limited (or minimal) phonon calculation is a valid approximation.

### 6.2.2 Huang-Rhys factor analysis

After we calculated the phonon modes and frequencies for our reference unit cell using a minimal number of phonons, we calculated how strongly each (reference) phonon mode couples to the polaron. This was accomplished by calculating the Huang-Rhys factor (1.13) [117]

$$S_q = \frac{\frac{1}{2} M \omega_q^2 \Delta_q^2}{\omega_q} \quad (6.2)$$

Table 6.1: Significant Huang-Rhys factors for hole polaron system. Phonon modes are arranged in increasing frequency (there are 144 phonon modes in total).

Phonon mode ( $q$ )	Huang-Rhys Factor ( $S_q$ )
12	0.1535
39	0.4654
42	0.2708
54	0.2249
58	0.1886
61	0.2780
62	0.2672
63	0.1041
66	0.2036
67	0.4029
69	0.2347
70	0.2397
77	0.4203
103	0.1390

where  $\Delta_q = \sum_j V_q(j)(u_j^c - u_j^0)$ , which is the projection onto mode  $q$  of the difference in atomic positions  $j$  between the reference system ( $u^0$ ) and the polaron system ( $u^c$ ). As we only calculated phonon modes for a specific set of atoms in the unit cell, all of the same species, we drop the index  $j$  on  $M$ .  $S_q$  represents the number of phonons that are needed to produce the polaron defect. As we are using atomic units we have set  $\hbar$  to unity.

The most significant Huang-Rhys factors ( $S_q \geq 0.1$ ) for the hole polaron are shown in Table 6.1. The vast majority of the phonon modes which have a large Huang-Rhys factor are phonon modes which are in the middle of the frequency range. The total number of phonons (3.8) needed to recreate the polaron distortion is  $\gg 1$ , which means that this system is quite strongly coupled [118]. No phonon mode contributes a full phonon to the deformation, which reduces the parameter space needed if we are to perform a coherent transport calculation (see Chapter 3). There are three significant modes with  $S_q \geq 0.3$ , these are the phonon modes  $q = 39, 77$  and  $67$  in decreasing order. We need only three phonon modes to reproduce the polaron.

Similarly we have calculated the Huang-Rhys factors for the electron polaron structure. The Huang-Rhys factors  $\geq 0.1$  are shown in Table 6.2. Unlike the hole polaron system the phonon modes which have a large Huang-Rhys factor are low frequency acoustic phonon modes. As these phonon modes are low frequency, in order to obtain the polaron structure more phonons are needed. Like the hole polaron system the electron polaron structure is strongly coupled, with the total number of phonons (7.4) needed to recreate

Table 6.2: Significant Huang-Rhys factors for electron polaron system. Phonon modes are arranged in increasing frequency (there are 144 phonon modes in total).

Phonon mode ( $q$ )	Huang-Rhys Factor ( $S_q$ )
4	0.2654
5	0.4726
7	0.1282
8	0.4542
9	0.1752
10	0.8034
11	0.1502
13	1.1990
15	0.1961
19	0.1020
21	0.4265
22	0.1936
23	0.4181
25	0.1876
26	0.1159
30	0.1004
31	0.9604
32	0.9847
75	0.1154

the distortion  $\geq 1$ . The electron polaron structure is more strongly coupled to the phonon modes than the hole polaron structure. There are four significant phonon modes that couple strongly to the phonon, in order of decreasing  $S_q$  these are  $q = 13, 32, 31$  and 10. All of these phonon modes contribute approximately one phonon mode to the deformation. Four other phonon modes also have strong Huang-Rhys factors ( $S_q \geq 0.3$ ), in order of decreasing  $S_q$  these are the phonon modes  $q = 5, 8, 21$  and 23. Thus, as a bare minimum we need eight phonon modes to reproduce the polaron defect

How well can the hole polaron defect be modelled by the harmonic phonon modes that we have calculated? This was checked by comparing the deformation energy  $\Delta E$  to the harmonic distortion energy  $E_{\text{harm}} = \sum_q \frac{1}{2} M \omega_q^2 \Delta_q^2 = \sum_q \omega_q S_q$  (all units are in atomic units). The true (anharmonic) deformation energy  $\Delta E = E(u_j^c) - E(u_j^0)$ , where  $E(u_j^0)$  is the total energy of the reference system and  $E(u_j^c)$  is the total energy of a neutral system which has the same structure as the hole polaron. If the two energies are approximately equal then the polaron defect can be represented by a set of harmonic phonon modes. We found that for the hole polaron system the harmonic energy is 218% of the deformation energy. The overestimate is due to the hole polaron residing outside the harmonic regime. This can be seen if we make an interpolation between the reference and

hole polaron structures, calculating the harmonic and distortion energies for each step (see Figure 6.9). The harmonic and true distortion energies converge only for structures which are less than 20% of the way to the hole polaron structure.

We think that hole polaron is outside the harmonic limit because the hole polaron resides near to the surface of the silicon carbide crystal. We do not include phonon modes that result from the displacement of other atoms on the surface or deeper in the slab. However, as our minimal phonon set reproduced the gross structural properties of the polaron deformation and gave us a harmonic energy which was of the same order of magnitude as the deformation energy we consider that our phonon modes do reflect the essential physics of polaron formation.

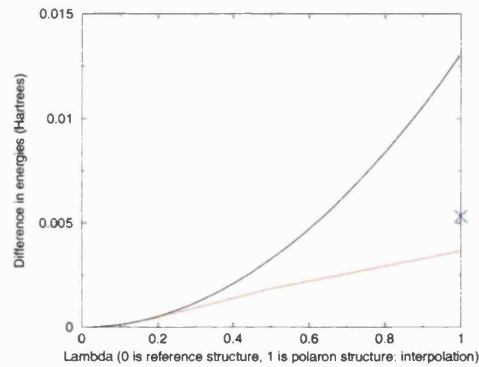


Figure 6.9: Comparison of harmonic (black) and deformation (red) energies for structures which are interpolations between the reference structure ( $\lambda=0$ ) and the polaron structure ( $\lambda=1$ ). The two energies converge for  $\lambda \leq 0.2$ . Also shown (blue cross) is the difference in energy between the dimer structure and a structure where the atoms that we use to create the phonon modes use the hole polaron positions and all other atoms are in the reference cell positions.

In contrast we found that the electron polaron structure is well reproduced by the harmonic phonon modes that we calculate. Comparing the harmonic and deformation energies for the electron polaron system we find that the two energies are in close agreement; they differ by only only 3%. This is because the electron polaron is localised on the addimers of the line, and our dynamical matrix calculation includes all the adatoms of the line.

### 6.3 Electron-phonon coupling

As the electron polaron system shows signs of strong coupling to phonon modes and is quasi-one-dimensional, it may be desirable to perform transport calculations on the silicon lines. In order to perform transport calculations that include inelastic effects we needed to evaluate the electron-phonon coupling constants  $\gamma_{qnm}$  (see equation (2.95)). We use an atomic-like basis set in real space, so firstly we had to evaluate  $\gamma_{i\alpha j\beta q}$  and then transform to eigenvector space.

The electron-phonon coupling is related to the displacement of phonons in phonon space [246]. This can be written as the displacement of the Hamiltonian matrix  $H_{i\alpha j\beta}$  in phonon space  $\lambda$ , where  $i$  labels an atomic site on which orbital  $\alpha$  is located and  $j$  labels an atomic site where orbital  $\beta$  is located. The parameter  $\lambda$  is found by the relation

$$\lambda = V^T y \quad (6.3)$$

where  $V$  is the phonon mode matrix and  $y$  is a scaled version ( $y_i = M_i^{1/2} x_i$ ) of the actual phonon displacements  $x_i$ . The displacement of phonons in phonon space is related to the displacements of atoms in real space by the formula

$$\frac{\partial H_{i\alpha j\beta}}{\partial \lambda_q} = \sum_{kC} \frac{\partial H_{i\alpha j\beta}}{\partial R_{kC}} U_{(kC)q} \quad (6.4)$$

where  $U$  is the transformation matrix,  $R$  is the real atomic displacement that we use to calculate the phonon modes,  $k$  denotes the atomic site that is been displaced and  $C$  labels the coordinate in which the atom is been displaced.

If we use the relation (6.3) and consider that  $V$  is orthogonal, we found that the transformation matrix can be derived by using

$$\frac{\partial H}{\partial \lambda} = \frac{\partial H}{\partial x} \frac{\partial x}{\partial y} \frac{\partial y}{\partial \lambda} = \frac{\partial H}{\partial R} M^{-1/2} V. \quad (6.5)$$

This means that if we compare (6.5) to (6.4), that the transformation matrix is  $U_{ij} = M_i^{-1/2} V_{ij}$ . Individual coupling elements are given by

$$\gamma_{i\alpha j\beta q} = \left( \frac{1}{2\omega_q} \right) \left\langle \frac{\partial H_{i\alpha j\beta}}{\partial \lambda_q} \right\rangle \quad (6.6)$$

as we use atomic units  $\hbar$  is equal to unity.

For a (7×8) unit cell the entity  $\gamma_{i\alpha j\beta q}$  is extremely large. If we included electrostatic, exchange and correlation terms then the number of matrix elements that are affected by the displacement of one atom is very large. However as we used the tight-binding approximation then these terms are represented by sums of pair terms (see the section in Chapter 2 regarding tight-binding). This means that the only nonzero elements of the entity  $\gamma_{i\alpha j\beta q}$  are those elements which involve the atom  $k$  which is been displaced ( $i$  or  $j = k$ ). This massively reduced the number of elements we need store in our workstation.

Once we calculated the electron-phonon coupling constants in real space we needed to transform these constants into eigenvector space. This is done simply by performing an overlap with the wavefunctions of the system

$$\gamma_{qnm,\underline{k}} = \langle \Psi_n(\underline{k}) | \hat{\gamma}_q | \Psi_m(\underline{k}) \rangle \quad (6.7)$$

where  $\underline{k}$  is the  $k$ -point sampled and  $\hat{\gamma}_q$  represents the real space electron-phonon coupling.

The nonorthogonal wavefunctions  $\phi_{n\alpha}$  that are used in our tight-binding method are long ranged in extent. Thus if we are to model the transport of charge through the silicon atomic line using these wavefunctions then we would need to include phase factors when charge flows from one (7×8) unit cell to another, as the  $\phi_{n\alpha}$  on one site are not orthogonal to the  $\phi_{n\alpha}$  on another site. This complication can be removed by transforming these wavefunctions into Wannier functions which are much more localised in nature [25]. As our calculations sample a limited number of  $k$ -points in the surface Brillouin zone we simply use the following transformation

$$W_{n,i\alpha}(R_l) = \sum_{\underline{k}} \exp^{-i(\underline{k} \cdot R_l)} \langle \phi^{i\alpha} | \Psi_n(\underline{k}) \rangle \times \text{weighting} \quad (6.8)$$

where  $R_l$  is the unit cell lattice vector. As we calculate the Wannier functions for each

unit cell separately the exp term is equal to unity. It is then easy to calculate onsite and hopping terms for the Wannier functions by finding the overlaps of the Wannier functions for functions on the same site (onsite) and on two neighbouring sites (hopping).

## 6.4 Transport properties

With the formation of the electron polaron and the calculation of the electron-phonon coupling and Wannier functions completed, the transport properties of the silicon atomic line were considered. Firstly, we should consider whether the polaron can travel through the silicon atomic line coherently or whether transport can occur diffusively. Effective mass can be checked by calculating the effective mass of the polaron; if the effective mass is small then polaron transport will be coherent at low temperatures, but if it is large then coherent polaron transport will not occur.

The effective mass of the polaron is the product of two factors, a factor dependent on the bandwidth of the bands the polaron can interact with, and a factor dependent on the reduction factor which measures the contribution of the phonons to the effective mass [247]. The bandwidth dependent factor  $m_{bw}^*$  can be derived from the relation [116]

$$\frac{\hbar^2}{m_{bw}^*} = \frac{\partial^2 E}{\partial k^2} \Big|_{\min} = 2a^2t, \quad (6.9)$$

where  $t$  is the hopping integral between two sites for any Wannier band and  $a$  is the lattice parameter. This relation can be rearranged to obtain the bandwidth dependent part  $m_{bw}^*$ . The total bandwidth available to the polaron defect is  $4t$ . This means that the bandwidth dependent part of the effective mass is

$$m_{bw}^* = \frac{\hbar^2}{2a^2t}. \quad (6.10)$$

The phonon dependent part of the effective mass is inversely proportional to the reduction factor of the electron matrix element in the Condon approximation. This is the Ham effect [247]. The reduction factor is expressed as

$$m_{ph}^* = \exp\left(\frac{M\omega}{2\hbar}(Q_{a0}-Q_{b0})\right) \quad (6.11)$$

where  $(Q_{a0} - Q_{b0})$  is the displacement in the lattice. This can be related to the Huang-Rhys factor (1.13), so that the the phonon field contribution to the effective mass of the polaron is

$$m_{ph}^* = \exp(\sum_q S_q). \quad (6.12)$$

Within the Condon approximation the final effective mass of the polaron is approximately the product of (6.10) and (6.12) (although the Condon approximation is not that good as the polaron bandwidth drops).

Evaluating both contributions to the effective mass of the polaron we found that the effective mass of the polaron is large. The bandwidth of the polaron is the sum of the bandwidths of all states that are available to the polaron. The bandwidth of any particular band is equal to the hopping element between one site and the neighbouring site. The bandwidth is simply the dispersion in the  $\times 8$  direction. The hopping element can be derived from the Wannier functions as

$$t = \langle W_n(a) | H | W_n(a+R) \rangle \quad (6.13)$$

This can be expanded in terms of atomic orbitals as

$$\begin{aligned} t &= \sum_{\underline{k}, \underline{k}'} \exp^{i\underline{k}a} \langle \Psi_n(\underline{k}) | H | \Psi_n(\underline{k}') \rangle \exp^{-i\underline{k}'(a+R)} = \sum_{\underline{k}, \underline{k}'} \exp^{i\underline{k}a} \epsilon_n \delta_{\underline{k}, \underline{k}'} \exp^{-i\underline{k}'(a+R)} \\ &= \sum_{\underline{k}} \epsilon_n(\underline{k}) \exp^{-i\underline{k}R}. \end{aligned} \quad (6.14)$$

This is a Fourier transform, and as we only sample two  $k$ -points in our relaxation and phonon calculations we find that this is equal to the dispersion along the  $\times 8$  direction.

We found that the total bandwidth is  $1.35234 \times 10^{-3}$  Hartrees. This means that the

bandwidth fraction of the polaron effective mass is evaluated to be 0.6729 times the mass of an electron.

The phonon contribution to the effective mass is large. The total Huang-Rhys factor for the electron polaron defect is 7.4. This means that the phonon contribution to the effective mass is  $\exp^{7.4} \times$  the mass of the electron, or  $\approx 1600$  times the mass of the electron. This is approximately equal to the mass of an atom, which is much larger than the mass of a an electron. The phonon fraction of the effective mass dominates the effective mass of the polaron. The total effective mass of the polaron is  $\approx 1100$  electron masses.

As the effective mass of the polaron is so much larger than the effective mass of an electron we conclude that if polaron transport occurs it will not be coherent. This means that we will not be able to use the methodology outlined in Chapter 2, section 4 concerning the transport of polarons in coherent systems. However the energy of relaxation of the polaron is quite small, of order 0.07 eV (0.00257 Hartrees). Might it be possible that polaron transport along the line be possible by thermally activated diffusion?

Dimensional analysis indicates that a good expression for the diffusion constant to within an order of magnitude is

$$D_c = \omega_q \exp\left(-\frac{E_r}{k_B T}\right) a^2 \quad (6.15)$$

where  $E_r$  is the energy of relaxation for the electron polaron defect and  $k_B T$  is the thermal energy (we assume room temperature transport). The distance is the lattice parameter of the unit cell in Bohrs along the  $\times 4$  direction of the unit cell, this is the minimal distance the polaron can travel before it localises on an equivalent site. We pick the frequency with the strongest Huang-Rhys factor, this is  $q = 13$ , giving a frequency of  $8.2865 \times 10^{-4}$  atomic units. We find that the diffusion constant is  $\approx 0.02993$  Bohr<sup>2</sup> per atomic unit of time. In S.I. derived units the diffusion constant is 0.03467 cm<sup>2</sup> per second.

We can compare this to the diffusion constant for electrons in bulk-like 3C-SiC. The carrier mobility has been measured by electron cyclotron resonance experiments on 10  $\mu\text{m}$  thick films [248]. The carrier mobility  $\mu$  was found to be 300 cm<sup>2</sup>/Vs. The diffusion

constant can be calculated from the carrier mobility by the Einstein relation [249]

$$D_c = \frac{\mu k_b T}{q}, \quad (6.16)$$

where  $q$  is the charge of the carrier, for polarons this is equal to one. Using this data we found that the electron diffusion constant in bulk 3C-SiC is 7.714 cm<sup>2</sup> per second. This is approximately 300 times greater than the diffusion constant of polarons along the silicon line. This suggests that thermally activated polaron diffusion along the silicon line is much harder than electron diffusion in the bulk. The silicon line would be the slow link in any electronic device constructed on SiC.

We can also use (6.16) to calculate the mobility of the silicon line and compare it with typical mobilities of other materials. We find that the polaron mobility is 1.3483 cm<sup>2</sup>/Vs for the silicon line. This is quite close to the mobility of copper, where the mobility is of order 20 cm<sup>2</sup>/Vs [250]. When compared with conducting polymer mobilities however this mobility is quite small, as experiments performed on partially oriented and doped (with iodine or AsF<sub>5</sub>) polyacetylene films have found that these films possess a high mobility of order 60 cm<sup>2</sup>/Vs [251]. Conducting polymers are another class of prospective atomic scale wires, and for other prospective atomic scale wires to compete with them they would need equivalent electron mobilities. This is not the case for the silicon atomic line. We have ignored such aspects as easy integration with silicon, but as any silicon based atomic scale electronic device would have to have an interface with the silicon carbide surface in order to utilize the atomic lines such devices would be under a large surface stress. This could be detrimental to the performance of such devices.

## 6.5 Conclusions

We have performed calculations on the (7×8) reconstruction of the (001) face of cubic silicon carbide when charge is injected into the line. We find that for both electron and hole injection a polaron forms on the silicon line which is energetically favoured compared to the original reference structure and which localises charge. The hole polaron structure is more diffuse than the electron polaron structure and possesses a HOMO state which disperses more across the silicon line than along the silicon line. This implies that the

hole polaron is not strongly confined to the silicon line, which is not a desirable property for an atomic scale wire. In contrast the electron polaron does have an anisotropic state associated with it which has a quasi-one-dimensional dispersion along the line. This implies that the electron polarons are strongly coupled to the silicon line.

The phonon modes of the reference system were then calculated for a limited number of silicon atoms of the line and the surface. We found that the hole polaron distortion was not well described by the resulting set of phonon modes but that the electron polaron distortion was. Both kinds of polaron are strongly coupled to phonon modes. The electron-phonon coupling constants for the reference system were also calculated in preparation for making a coherent transport calculation on the silicon line for the electron polaron system.

In order to check whether it is practical to make a fully quantum mechanical transport calculation on the silicon line system we calculated the effective mass of the electron polaron. Although the contribution to the effective mass from bandwidth effects is relatively small (of order 0.7 electron masses), as the polaron is strongly coupled to the phonon modes of the system we found that the total effective mass of the polaron is of the order of an atomic mass ( $\approx 1100$  electron masses). Therefore if there is any polaron transport along the silicon line it will not be coherent, except at extremely low temperatures.

The energy of trapping for the electron polaron is quite small (of order 0.07 eV). It may be possible for the electron polaron to diffuse along the line by thermal activation. We evaluated the diffusion constant for the electron polaron and found that it was 0.03467 cm<sup>2</sup> per second, and compared it to the diffusion constant for electrons in bulk 3C-SiC. The polaron diffusion constant was found to be much smaller than the diffusion constant for electrons in bulk 3C-SiC. A polaron would diffuse more slowly along the silicon line than an electron would diffuse throughout the bulk silicon carbide crystal, as also illustrated by a comparison of mobility. This would have the effect of making the silicon line the slow component in any electronic device manufactured from silicon carbide. This is not a desirable feature for an atomic scale wire. The mobility of the silicon atomic line is also much less than the mobility of a crystal of doped and ordered polyacetylene molecules, which are another class of prospective atomic scale wires. We therefore conclude that the transport properties of the silicon atomic line are not conducive for atomic scale transport.

## Chapter 7

# Ab initio study of the In atomic chain on the (111) face of silicon

In this chapter we discuss the indium atomic chain reconstruction on the (111) face of silicon, the  $(4\times 1)$ -Si(111)-In reconstruction. This atomic scale chain structure is a promising atomic scale wire candidate. We provide background experimental information on this system, the electronic structure of the system, indium and silicon stoichiometries, structural information and hydrogenation data. We discuss several models that have been proposed by experimentalists for this reconstruction and narrow the selection models down to two models which fit the largest set of experimental data. We then provide the details of the two competing models that we will study, showing which experimental data each model is in agreement or disagreement with.

We then test our projectors of silicon and indium to discover whether they are accurate. These projectors are used to model the well understood  $(\sqrt{3} \times \sqrt{3})$ -Si(111)-In reconstruction to check whether our results match those in the literature. After these tests we perform *ab initio* simulations on the two competing models for the  $(4\times 1)$ -Si(111)-In reconstruction and present our structural, electronic and thermodynamic results. We then conclude with our findings on whether this would make a good atomic scale wire.

## 7.1 Background information

### 7.1.1 The Si(4×1)-In reconstruction

The electronic and physical properties of metal adsorbates on silicon surfaces have been the object of studies for over thirty years [252, 253, 254]. These studies are useful as they provide a valuable insight into the interface formation of silicon with the simple (Group III) metals Al, Ga and In. This is a problem of interest as the evolution of the metal-induced semiconductor surface structures from a semiconducting to metallic regime with increasing adatom coverage is an important tool in understanding the formation of the Schottky barrier; the Schottky barrier of a metal-semiconductor system reaches its macroscopic value at adatom coverages at which the surface becomes metallic [88]. Thus the surface reconstructions of a metal-semiconductor system at approximately monolayer coverage (the typical coverage for a semiconducting to metallic transition) determine the electrical properties of a metal-semiconductor interface, which are used extensively in electronic systems. The In-Si interface in particular is often used as a test interface to study these complex phenomena of coverage-driven reconstructions, as the In-Si interface is nonreactive [255], but with sufficient adatom-substrate coupling to support a large number of structures [88].

Depending on the surface stoichiometry of indium there exists a large variety of surface reconstructions, ranging from a (7×7) reconstruction at sub-monolayer coverages to a combination of (1×1), ( $\sqrt{7} \times \sqrt{3}$ ) and (4×4) reconstructions at supermonolayer coverages. A surface phase diagram of In on Si(111) is shown in Figure 7.1. Several surface reconstructions share the same indium stoichiometry (hence the overlap), this may be because one surface is a defect induced reconstruction of another ground state surface. The Si(4×1)-In reconstruction in particular has a wide range of measured In stoichiometry, ranging from 0.5 to 1 ML. There are two different routes available to form the (4×1) reconstruction by indium deposition. Firstly there is a “low temperature” irreversible route ( $\approx 500$  K) in which there is a transition from a ( $\sqrt{3} \times \sqrt{3}$ ) reconstruction to the (4×1) reconstruction. Secondly there is a “high temperature” reversible route ( $\approx 700$  K) in which there is the transition ( $\sqrt{3} \times \sqrt{3}$ )  $\iff$  ( $\sqrt{31} \times \sqrt{31}$ )  $\iff$  (4×1) upon indium deposition [256]. Upon further deposition of indium upon the (4×1) reconstruction the surface forms a ( $\sqrt{7} \times \sqrt{3}$ ) reconstruction [88, 255, 256, 257, 258, 259, 260].

As the (4×1) reconstruction may have an indium surface stoichiometry of 1 ML

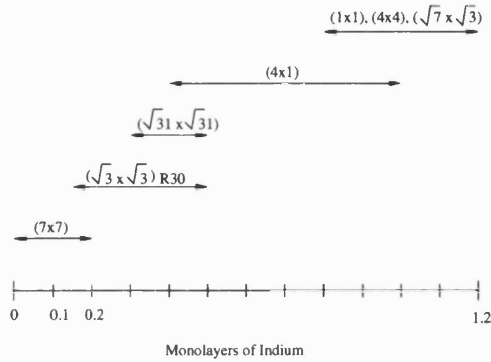


Figure 7.1: Diagram of experimental uncertainty of indium coverage for the In-Si(111) system taken at a temperature of 700 K. This diagram is taken from Kraft *et al.*, Phys. Rev. B **55**, 5384, (1997).

and thus be of use in analysing the Schottky barrier problem, considerable experimental attention has focused on it. STM imaging of the surface revealed that the indium adatoms form atomic chains [88, 90, 92, 93, 94, 95] that are aligned along the  $[01\bar{1}]$  direction and are separated by  $13.3 \text{ \AA}$  along the  $[2\bar{1}1]$  direction, see Figure 7.2<sup>1</sup>. The difference in height between the rows and the trench between rows has been measured by STM to be  $1.5 \text{ \AA} \pm 0.2 \text{ \AA}$  [261] and X-ray diffraction also finds that there is a height difference of order  $1 \text{ \AA}$  [262].

As indium is a metal and silicon is a semiconductor, a naive assumption would be that these indium atomic scale chains act as atomic scale wires which confine states near the Fermi level to the chains. This assumption depends on two factors; firstly whether the  $(4 \times 1)$  reconstruction is metallic and secondly whether the surface possesses states which are quasi-one-dimensional.

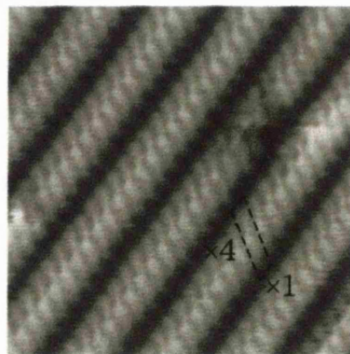


Figure 7.2: STM image of the filled states of the  $(4 \times 1)$  reconstruction of the Si(111) reconstruction. An individual  $(4 \times 1)$  unit cell is delineated. This image is taken from H. W. Yeom *et al.*, Phys. Rev. Lett. **82**, 4898, (1998).

Analysis of the electronic structure of the  $(4\times 1)$  reconstruction is complicated by the problem of deconvolving information about the electronic structure of the one-domain surface from the electronic structure of the three-domain surface. An incorrect interpretation of the electronic structure of the three domain  $(111)$  surface can lead to a misinterpretation of experiments that investigate the surface structure of the  $(4\times 1)$  reconstruction.

STM spectroscopy has been performed on a three domain  $(4\times 1)$  surface [261]. Analysis of the  $(dI/dV)(I/V)$  curves shows that the surface is semiconducting with a bandgap of 0.8 eV. This is in agreement with the angular resolved photoemission and inverse photoemission experiments which have been performed on a three domain Si(111) surface by Öfner *et al.* [263], who found that there was one empty interface state in the bandgap and that there were three filled surface bands. The surface was found to be semiconducting. Hill *et al.* [86] suggested that this was because the experimental setup did not probe all of the reciprocal space of the  $(4\times 1)$  unit cell. Inverse photoemission of a three domain [86] surface does indeed find that there is a Fermi level crossing in the Brillouin zone meaning that the surface is metallic. This is in agreement with the STS curves of the three domain surface obtained by Kraft *et al.*, who found that the  $(4\times 1)$  surface has a finite density of states at the Fermi level [88].

Experiments performed on the single-domain surface are far more conclusive. Inverse photoemission experiments by Hill *et al.* show that the surface is metallic with a Fermi level crossing at  $0.6 \bar{\Gamma} - \bar{X}$  (see Figure 7.10). Core level photoemission experiments by Abukawa *et al.* [264] also show that the surface is metallic and that the In adatoms are metallic in nature while the Si atoms are semiconducting. This implies that if any charge is injected into the indium atomic chains then the charge would be confined to the chains and would find it easier to disperse along the chain than across the chain. How one dimensional are the electronic states associated with these indium atomic chains?

RAS curves obtained from single-domain samples show that there is a significant optical anisotropy of 1.65 % at a photon energy of 1.9 eV [91]. This anisotropy is uncharacteristic of semiconductor systems and is indicative of strong electron confinement in the  $[2\bar{1}\bar{1}]$  direction, i.e., perpendicular to the indium atomic chains. Additional support for this is provided by detailed angle-resolved photoemission spectroscopy performed on

<sup>1</sup>The  $(4\times 1)$  reconstruction is rectangular. Therefore on the Si(111) surface it is threefold degenerate. If the Si(111) surface is miscut by a couple of degrees towards the  $[01\bar{1}]$  direction (for instance) then terraces form that break this threefold symmetry and form single-domain surfaces [257, 261].

the single-domain  $(4\times 1)$  surface [95, 265]. Three surface state bands are observed which cross the Fermi level and all three surface states have quasi-one-dimensional dispersions which are aligned along the  $\times 1$  direction. The magnitude of dispersion along the  $\times 1$  direction is  $\approx 0.2$  eV for the highest occupied state,  $\approx 0.4$  eV for the second highest state and  $\approx 0.7$  eV for the third highest state. The dispersions along the  $\times 4$  direction are  $\approx 0.1$  eV for the HOMO state,  $\approx 0.0$  eV for the second highest state and  $\approx 0.2$  eV for the third highest state [265]. Inverse photoemission found that the unoccupied states also have the same quasi-one-dimensionality of dispersion with the unoccupied states confined to the indium atomic chains [87].

If the atomic wire is quasi-one-dimensional and metallic then it is susceptible to a Peierls-like transition which doubles the repeat spacing along the wire and makes the surface semiconducting. STM and RHEED observations show that below room temperature the  $(4\times 1)$  metallic structure becomes a  $(4\times 2)$  semiconducting structure [95]. However this result is in dispute, as there are angle-resolved electron-energy-loss spectra which indicate that the transition at low temperature is from a metallic  $(4\times 1)$  surface to a  $(8\times 2)$  semi-metallic surface [266]. There is also evidence for this in the X-ray diffraction results of Kumpf *et al.* [267], although this experiment was performed on a three domain surface. There have been suggestions that this is an indication of a Fermi liquid to Luttinger liquid transition, although it may be a less exotic ground state transition.

In summary it seems as if the  $(4\times 1)$  surface reconstruction acts in many respects as an atomic scale wire. In order to estimate what its transport properties are we need to know the structure of the indium atomic chain. What models of the  $(4\times 1)$  reconstruction exist, and for what indium stoichiometries?

### 7.1.2 Models

As has been shown in Figure 7.1 the uncertainty in the indium surface stoichiometry is quite large for the  $(4\times 1)$  surface. As the  $(4\times 1)$  is not a surface solution, i.e., its indium surface stoichiometry is fixed [268], the indium stoichiometry of the  $(4\times 1)$  unit cell must consist of an integer number of In adatoms. The lower limit for the number of In adatoms per unit cell is 2, as the less indium-rich  $(\sqrt{3} \times \sqrt{3})$  unit cell is an extremely well characterised surface with a surface indium stoichiometry of one indium atom per unit cell (1/3ML In) [88, 93, 258, 269, 270, 271]. The upper limit is four indium adatoms

per unit cell (1ML In) [88]. The range of indium stoichiometry is therefore 0.5 to 1 ML. Unfortunately there is a lot of conflicting experimental evidence on the indium stoichiometry of the (4×1) surface.

Experimental support for a 1/2 ML indium coverage is provided by the impact-collision ion-scattering spectrometry (ICISS) results of Cornelison *et al.* [83], who found that the best fit with experiment was a model with two In adatoms occupying two inequivalent sites on the (111) face, the  $H_3$  and  $T_4$  sites. There was no evidence for substitutional In atoms in the top atomic layer of the silicon crystal. Additional ICISS experiments were performed by Stevens *et al.* [261] on the single-domain surface, who also found that the best fit to experimental data was the mixed-site model with 0.5 ML of indium (see Figure 7.3, a)).

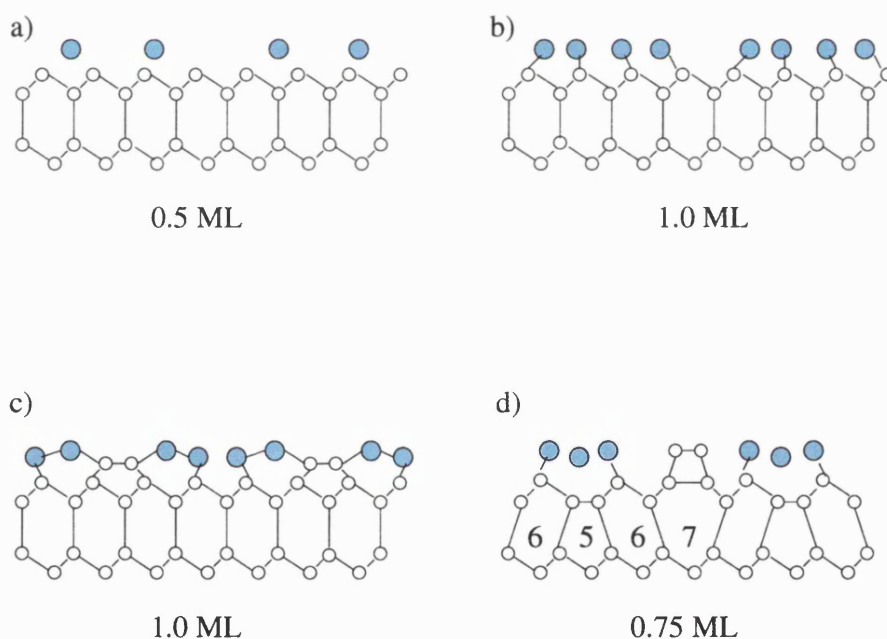


Figure 7.3: Comparison of various models that have been proposed for the (4×1) surface. Structures proposed a) Stevens *et al.*, Phys. Rev. B **47**, 1453, (1993), b) Abukawa *et al.*, J. Elec. Spec. Rel. Phen. **80**, 233, (1996), c) Bunk *et al.*, Phys. Rev. B **59**, 12228, (1999) and d) Saranin *et al.*, Phys. Rev. B **60**, 14372, (1999). Open circles are silicon atoms, light blue circles are indium adatoms.

A one monolayer model has been proposed by Abukawa *et al.*[264] (see Figure 7.3, b)), who found that core level photoemission spectra show that the Si  $2p$  components are symmetric with no significant core level shift. This is interpreted as evidence for an almost ideal one-to-one bonding of the top layer of silicon with indium. The core-level shifts also

show that there are two kinds of In bonding, metallic In-In bonding and covalent In-Si bonding. This model is consistent with angle resolved photoemission data [265]. This ARPES data is interpreted to rule out models with 3/4 or 5/4 ML indium coverages, although this interpretation does not include any excess silicon atoms on the surface. The model proposed by Abukawa is in agreement with X-ray diffraction data obtained by Finney *et al.* on three domain surfaces [262, 272]. The model proposed by Finney (see Figure 7.3b)) also assumes an unreconstructed substrate. Micro-probe Auger electron spectroscopy and RHEED also found that the indium coverage is 1 ML with no excess silicon. An In coverage of 3/4 ML was ruled out by symmetry considerations (although the observed indium stoichiometry is 0.8 ML which is a lot closer to a stoichiometry of 0.75 ML than to 1 ML [89]).

The assumption that the silicon substrate is unreconstructed and that there is no excess silicon present on the surface is, however, wrong. Exposure of the (4×1) surface to hydrogen results in the desorption of indium adatoms and the adsorption of hydrogen atoms [92]. Since this occurs without any change in the periodicity as measured by LEED, it is reasonable to assume that the hydrogen atoms replace the indium adatoms without significantly disturbing the silicon atoms. It was found by STM, AES and LEED that upon hydrogen adsorption the (4×1)-In reconstruction is replaced by a (4×1)-H reconstruction [92, 94]. This indicates that the silicon substrate is itself reconstructed. Saranin *et al.* proposed that the substrate reconstruction is similar to the Si(111)-(3×1)-Me reconstructions (where Me is a metal like Al, Ge or Li) that have been observed. Erwin proposed that these (3×1) reconstructions are composed of units that are extensions of the Pandey model that is accepted as the atomic geometry of the clean Si(111)-(2×1) surface [273]. A clean unreconstructed Si(111) surface consists of six-member rings of silicon. The (2×1) Pandey model replaces these six membered rings with alternating seven- and five-membered rings (7575...). The Erwin model for the (3×1) reconstruction inserts a six-membered ring (765765...). The Saranin model (see Figure 7.3, d)) simply inserts another six membered ring into the sequence (76567656...) [94]. This is referred to as a  $\pi$ -bonded-chain-stacking-fault model ( $\pi$ -SF).

The original Saranin model proposed that this  $\pi$ -SF substrate reconstruction has an indium overlayer with an indium stoichiometry of 0.75 ML [94]. Experimental evidence for this indium stoichiometry is provided by Auger spectroscopy [94], STM imaging of the

unit cell [256] and determination of the stoichiometry of the  $(4\times 1)$  surface by STM [274]. Two of the indium adatoms form the indium rows that are observed by STM (see Figure 7.2) and are covalently bound to the silicon substrate. The third indium atom resides in the trough between the rows [256] and has only metallic bonds with neighbouring indium adatoms. Protrusions which correspond to these fully metallic indium adatoms have been imaged by empty state STM scans of the  $(4\times 1)$  surface [256]. It has been suggested that displacements of these middle adatoms are what is responsible for the possible Peierls transition that has been observed.

So far we have assumed that the silicon stoichiometry is ideal, only In varies. But in principle silicon stoichiometry may change too. Surface X-ray diffraction experiments have been performed on the  $(4\times 1)$  reconstruction by Bunk *et al.* [82]. They found that the reconstruction was quasi-one-dimensional but with chains of silicon atoms alternating with zig-zag chains of indium adatoms on an unreconstructed silicon substrate. There is an excess silicon stoichiometry of 0.5 ML relative to the ideally terminated surface. There are three In-In interatomic distance vectors in the Patterson function (a measure of the pair-correlation function of the electron density) which means that there must be three different indium sites involved in the reconstruction. This rules out any models which have a surface indium stoichiometry of 0.5 ML. The original model proposed by Saranin also shows a poor fit to the data. The model which best fits the experimental data is a model with four indium adatoms and two silicon atoms on the surface per unit cell (see Figure 7.3, c)). The silicon atoms are arranged in a  $\pi$ -bonded chain and the indium adatoms are arranged in two rows, each row containing two adatoms, one of which is higher than the other. There are thus two inequivalent types of indium adatoms which is in agreement with core-level photoemission results [89]. This model is also in agreement with inverse photoemission results [275].

Additional STM experiments by Saranin *et al.* have confirmed the presence of these silicon atomic lines [274] in the Si(111)- $(4\times 1)$ -H reconstruction. Scans along the  $\times 4$  direction show that there is a protuberance in filled states imaging with a  $\times 4$  repeat spacing. Therefore Saranin *et al.* have proposed the modified Saranin model in which there are three indium adatoms and two silicon atoms on the surface per unit cell (this is the structure shown in Figure 7.3, d)). The silicon atoms are placed above the sevenfold ring. It is expected that this model would better fit X-ray diffraction data.

Table 7.1: Summary of the ability of different models to match experiments. + indicate agreement with the experiment, - indicates disagreement with experiment and o indicates ambivalent agreement with experiment.

Experimental Technique	Bunk model	Saranin model (modified)
STM [256, 259, 90, 261, 274]	+	+
ICISS [261, 83]	-	-
PES [264]	+	o
XRD [262, 82, 272]	+	o
hydrogenation [92, 94, 274]	+	+
RHEED [89]	+	-
AES [94, 262, 89]	-	+
AED [89]	-	+
IPES [275]	+	-

The experimental evidence suggests that the indium coverage of the  $(4 \times 1)$  surface reconstruction is either 0.75 ML or 1.0 ML with no substitutional indium in the silicon substrate. There is also a surface silicon stoichiometry of 0.5 ML. Of all the structural models proposed only two models fit the majority of the experimental data, the Bunk model (1.0 ML In) and the modified Saranin model (0.75 ML In). A summary of how each model matches experimental data is shown in Table 7.1 and a comparison of the adatom structure of both models is shown in Figure 7.4. As the only difference in surface stoichiometry is that one model has one more indium adatom than the other we can easily calculate the difference in grand canonical potentials. Therefore we perform *ab initio* calculations on these two models in order to determine the geometric and electronic structure and find which model is thermodynamically favoured. We first of all need to determine whether the PAW formulation we use can accurately model the indium-silicon system.

## 7.2 PAW simulations: Tests

### 7.2.1 Projector test: Lattice parameters of Si and InAs

We have to check whether our PAW formalism accurately models both silicon and indium correctly. As a first test we determine whether PAW correctly calculates the bulk lattice vectors of solids containing silicon and indium. This was tested in the same way that we calculated the bulk lattice vectors of silicon carbide in Chapter 4, by varying the bulk lattice vectors  $a$  ( $1 \times 1 \times 1$ ) of the crystal, applying the Francis-Payne plane wave correction to the total energy (4.1) and finding the lattice vector which corresponds to

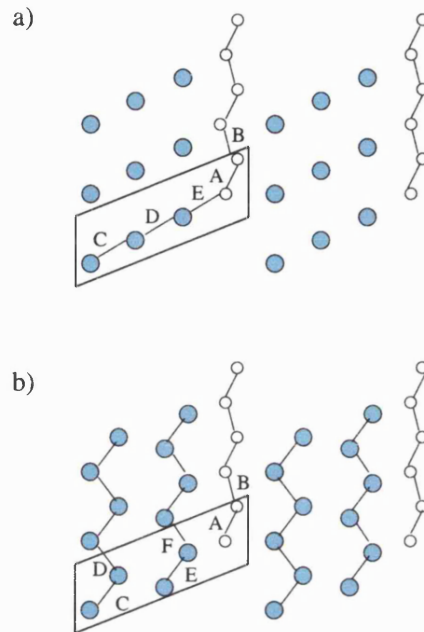


Figure 7.4: Comparison of the surface structure of the two most likely models. See Figure 7.3 for colour coding. a) is the Saranin model, b) is the Bunk model.

the minimum of total energy. The plot of total energy at a plane wave cutoff of 30 Rydbergs with respect to the bulk lattice vector for silicon is shown in Figure 7.5. We found that the PAW lattice vector for bulk silicon is within 0.3 % of the experimental value. We also found that the bulk modulus of silicon was 85.59 GPa, which is within 15% of the experimental value. Our PAW formalism thus accurately represents silicon. In our simulations we use the experimental values for the surface lattice vectors of silicon.

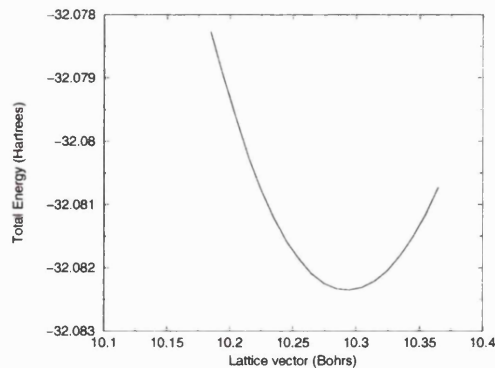


Figure 7.5: Plot of corrected total energy vs bulk lattice vector for silicon in PAW.

Our PAW formalism is much less suited for modelling pure indium as we can only sample a limited number of  $k$ -points in the Brillouin zone (4). Unfortunately the ground

state properties of metals cannot be accurately converged for such a small number of  $k$ -points. In order to accurately determine the bulk lattice vectors of indium we would therefore have to use a large number of primitive unit cells and sample a large portion of the Brillouin zone by backfolding. The memory requirements for such a calculation are beyond the capacity of current workstations. We therefore chose to find the bulk lattice vectors of the semiconductor compound indium arsenide, using a well tested arsenide projector. The indium projector uses the  $s$  and  $p$  states, placing the  $d$  states in the core. Our plot of corrected total energy for a plane wave cutoff of 30 Rydbergs as a function of bulk lattice vector for a  $(1 \times 1 \times 1)$  unit cell is shown in Figure 7.6. We found that the theoretical value for the bulk lattice vector is 14% less than the experimental value. This is a large error.

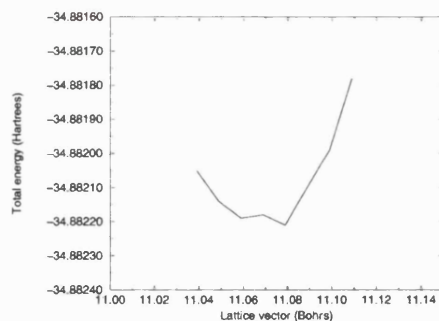


Figure 7.6: Plot of corrected total energy vs bulk lattice vector for indium arsenide in PAW.

How well can we trust our indium projectors? We can test our indium projector on another reconstruction on the (111) face of silicon, the  $(\sqrt{3} \times \sqrt{3})R30^\circ$  reconstruction.

### 7.2.2 Simulation of the $(\sqrt{3} \times \sqrt{3})\text{Si}(111)$ -In reconstruction

The  $(\sqrt{3} \times \sqrt{3})R30^\circ$  reconstruction is a well characterised and uncontroversial reconstruction. The surface indium stoichiometry is 0.33 ML: there is one In adatom per unit cell. No excess silicon has been observed. The indium adatom is located in the  $T_4$  site above a second layer Si atom [88, 269]; an alternative geometry with the indium atom located in the  $H_3$  site has a total energy 0.2 eV higher than the  $T_4$  site when modelled using pseudopotentials in the LDA [269].

This well known unit cell was modelled in the PAW formalism using a plane wave cutoff of 30 Rydbergs and sampling four  $k$ -points in the surface Brillouin zone. We use

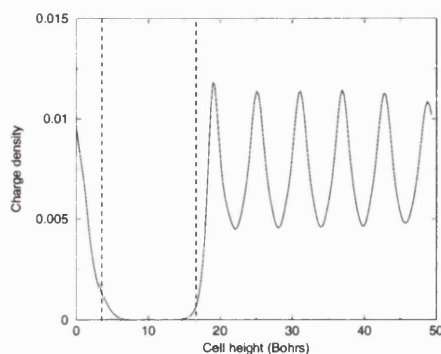


Figure 7.7: Plot of total charge density as a function of cell height for a  $(\sqrt{3} \times \sqrt{3})R30^\circ$  unit cell. Space between dashed lines is the vacuum.

a surface slab which is eleven atomic layers thick, with the bottom silicon atomic layer passivated by hydrogen. The vacuum gap is 17.00621 Bohrs in thickness. The charge density is confined to the slab as shown in Figure 7.7.

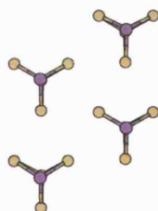


Figure 7.8: Surface structure (top two layers, several unit cells) of the relaxed  $(\sqrt{3} \times \sqrt{3})R30^\circ$  with the In atom in the  $T_4$  position. Yellow circles are surface silicon atoms, purple circles are indium adatoms.

We performed *ab initio* DFT calculations on the  $T_4$  and  $H_3$  reconstructions. The relaxed structures are shown in Figures 7.8 and 7.9. We found that our results are in close agreement with the previous literature. For the  $T_4$  model we found that the average In-Si distance between the In atom and the three surrounding Si atoms of the top layer is 2.48 Å, whereas previous theoretical results indicate that this distance is 2.63 Å [269]. The distance between the In atom and the Si atom directly beneath it is 2.43 Å, whereas the literature result is 2.59 Å [269]. For the  $H_3$  model the average In-Si distance between the In atom and the three surrounding Si atoms is 2.45 Å, the literature result is 2.62 Å [269]. We found that the  $T_4$  site has a lower total energy than the  $H_3$

site, with the difference in total energies 0.22 eV. We emphasize that as these previous literature results are 12 years old that their density functionals are much cruder than the density functionals that we use. Our energetic results are in excellent agreement with the literature.

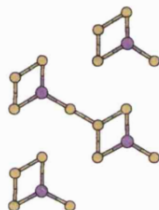


Figure 7.9: Surface structure (top two layers, several unit cells) of the relaxed  $(\sqrt{3} \times \sqrt{3})R30^\circ$  with the In atom in the  $H_3$  position. See Figure 7.8 for colour coding.

As our simulations agree so well with previous results in the literature, in particular with regard to the total energy difference in excellent agreement, we conclude that our simulations of the indium-silicon systems will probably be accurate. We posit that the reason why our indium projector does not accurately model the indium arsenide system is because the indium projector does not include contributions from the  $d$ -electrons. In contrast the indium on silicon systems are well modelled by the indium projector because these systems do not display evidence that  $d$ -electrons are involved. Only  $s$  and  $p$  orbitals are involved in the bonding [95, 265].

### 7.3 Ab initio simulations of the $(4 \times 1)$ unit cell: General points

Our simulations of the Bunk and Saranin models were performed on single  $(4 \times 1)$  unit cells with a plane wave cutoff of 30 Rydbergs and sampling four  $k$ -points in the surface Brillouin zone, the  $\Gamma$ ,  $K$ ,  $X$  and  $X'$  (see Figure 7.10). The surface slab is eleven atomic layers thick with the bottom silicon layer passivated by hydrogen to avoid artificial charge transfer. The vacuum part of the simulation cell is 19.18715 Bohrs thick.

The convergence of our simulations with respect to plane wave cutoff was checked by

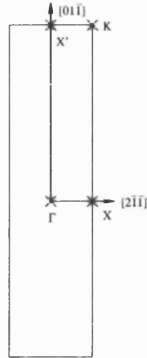


Figure 7.10: Surface Brillouin zone of the  $(4\times 1)$  surface and the four  $k$ -points sampled.

calculating the forces on the ions for the relaxed structure at 30 Rydbergs and comparing with ionic forces calculated for the same structure at a plane wave cutoff of 35 Rydbergs. We found that the largest difference in forces was for the indium atoms on the surface. This difference in forces was of order 0.00025 Hartrees per Bohr, which is a small difference in forces. We therefore conclude that our calculations are well converged with respect to plane wave cutoff.

## 7.4 Simulation of the Bunk model

### 7.4.1 Physical structure

The relaxed structure of the Bunk model is shown in Figure 7.11. The surface is locally stable. The indium atomic chains are  $0.3285 \text{ \AA}$  higher than the silicon atomic chain. The silicon atomic chain is buckled by  $0.0622 \text{ \AA}$ . The indium atomic chains are strongly buckled, with the average buckle distance  $0.2648 \text{ \AA}$ . The indium adatoms which are close to the silicon atomic chain are higher than the indium adatoms which are in the ‘inside edge’ of the atomic chains. The separation between the two indium atomic chains is  $4.1186 \text{ \AA}$ , this is in good agreement with the inferred separation between the atomic rows [275]. The details of the structure are shown in Table 7.2.

Table 7.2: Equilibrium bond lengths for the indium and silicon addimers. All distances are in  $\text{\AA}$ . See Figure 7.4 for nomenclature.

Model	Bond length
Bunk	2.2555 (A), 2.2465 (B), 2.6761 (C), 2.6823 (D), 2.6868 (E), 2.6854 (F)
Saranin	2.3666 (A), 2.4638 (B), 3.4160 (C), 3.1320 (D), 2.6127 (E)

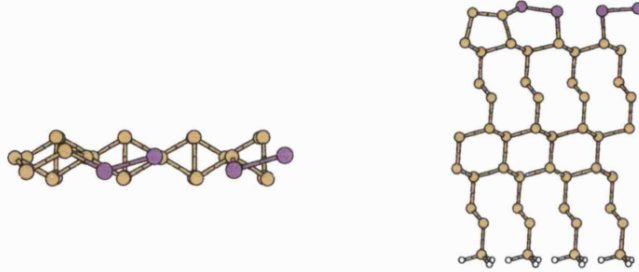


Figure 7.11: Relaxed structure of the Bunk model. Left diagram is view from above the surface, right diagram is view along the  $x_1$  direction. See Figure 7.8 for colour coding.

We can compare our structural results with the work of Miwa *et al.* [276] and the work of Nakamura *et al.* [277]. Both of their calculations were performed with density functional theory and used pseudopotentials to treat the electron-ion interaction. In both cases the Brillouin zone sampling is much better than the  $k$ -point sampling scheme we use, with Miwa *et al.* sampling 16  $k$ -points in the surface Brillouin zone and Nakamura *et al.* sampling 25  $k$ -points in the Brillouin zone. The plane wave cutoff used by Miwa *et al.* was 16 Rydbergs, while the plane wave cutoff used by Nakamura *et al.* was 25 Rydbergs. In both cases this is less than the plane wave cutoff we use.

We found that our structural results compare well with the results of both Miwa *et al.* and Nakamura *et al.*. The spacing we found between indium chains (4.12 Å) is less than that found by Miwa (4.4 Å). Our indium to silicon bond lengths were found to be shorter than the indium to silicon bond lengths found in the literature, with our indium-silicon bond lengths of order 2.45 Å and the indium-silicon bond lengths in the literature of order 2.65 Å. We think this underestimate of the bond length is due our smaller  $k$ -point sampling set.

#### 7.4.2 Electronic structure

As has already been mentioned we cannot comment in detail on the electronic structure of the Bunk model as our implementation of PAW is limited to sampling only four  $k$ -points in the surface Brillouin zone. There is also the problem that we cannot accurately

calculate the properties of excited states because of the LDA. At the four  $k$ -points sampled we found that the gap (defined as the difference in K-S eigenvalues) at select parts of the Brillouin zone varies from 0.18 eV at the  $X$ -point to 0.96 eV at the  $K$ -point. This indicates that the Bunk model has a narrow bandgap with a large range and may be metallic.

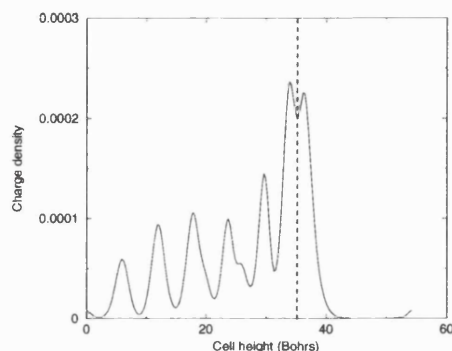


Figure 7.12: Plot of the charge density of the HOMO state as a function of cell height. Left side is bottom of the unit cell. Dashed line is position of the top of the unit cell.

Our simulations of the Bunk model show that there are two surface state bands separated from the valence band, with another band which is partially separated from the valence band; this is in agreement with angle-resolved photoemission experiments [263, 265]. The distribution of these states in the unit cell as a function of cell height is shown in Figures 7.12-7.14. The three highest occupied states all have quasi-one-dimensional dispersions with large dispersions along the  $\times 1$  direction (1.16 eV, 1.18 eV and 1.23 eV from HOMO to 3rd HOMO state) and much smaller dispersions along the  $\times 4$  direction (0.4 eV, 0.23 eV and 0.21 eV from HOMO to 3rd HOMO state). These dispersions are the differences in Kohn-Sham eigenvalues at different points of the Brillouin zone.

We found that the highest occupied state has a large overlap (we define the overlap by the sum of the squares of the projectors  $p_i$  for the  $s$ ,  $p_x$ ,  $p_y$  and  $p_z$  orbitals used in (2.20)) with the indium adatoms (see Figure 7.4 for layout). The HOMO state has a very strong overlap with the middle pair of indium adatoms (0.8909 for the left middle In adatom, 0.4806 for the right middle In adatom) and the indium adatom on the left (0.2355). The third HOMO state also has a large overlap with these three indium adatoms, with an overlap of 0.3294 on the left middle indium adatom, 0.1820 on the right middle indium adatom and an overlap of 0.1569 on the top left indium adatom. The second highest state does not have a strong overlap with any of the adatoms on the surface. The silicon

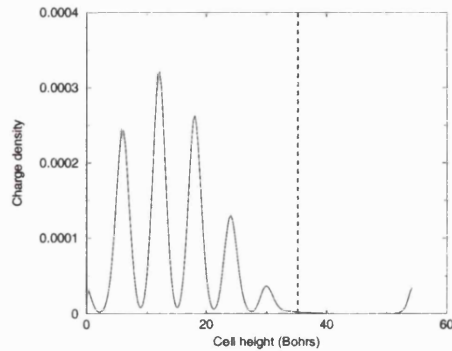


Figure 7.13: Plot of the charge density of the second HOMO state as a function of cell height. See Figure 7.12 for layout.

chain does not have a strong overlap with any of these states.

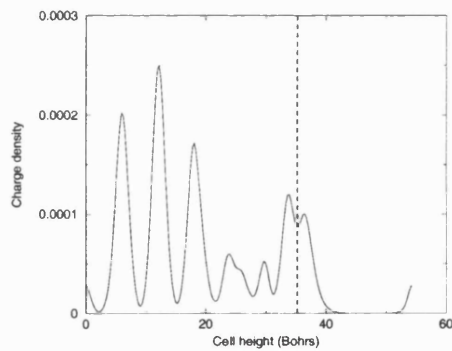


Figure 7.14: Plot of the charge density of the third HOMO state as a function of cell height. See Figure 7.12 for layout.

A plot of the charge density of the HOMO and 3rd HOMO states also shows that they are strongly associated with the middle pair of indium adatoms and that there is a very strong connection from one  $(4 \times 1)$  unit cell to the next along the  $\times 1$  direction. These charge density plots are shown in Figure 7.15. Along with the dispersion characteristics of these states and the large surface components these states possess this strongly implies that if a hole is injected into these indium adatoms it would diffuse easily along the  $\times 1$  direction and would be confined to the indium atomic chain. The Bunk model would make a good atomic scale wire.

We cannot compare in detail our electronic structure with the theoretical electronic structural results that have been published in the literature because we sample only a small set of  $k$ -points, whereas other theoretical studies have used a large set of  $k$ -points [276, 277]. Our electronic structure results agree in general with the results published

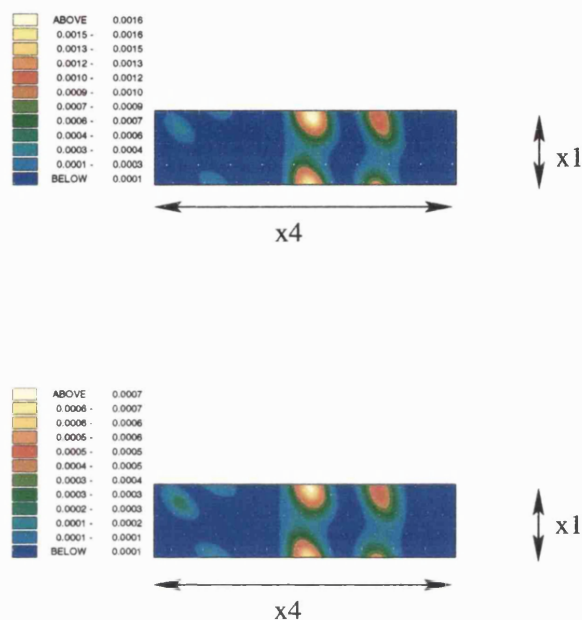


Figure 7.15: Plot of the charge density of the HOMO state (top) and 3rd HOMO state (bottom). This is a slice parallel to the surface at a point 3 Å above the surface.

in the literature, where both Miwa *et al.* and Nakamura *et al.* finding that the three highest occupied states possess quasi-one-dimensional behaviour and are confined to the indium atomic chains.

## 7.5 Simulation of the Saranin model

### 7.5.1 Physical structure

The relaxed structure of the Saranin model is shown in Figure 7.16. The surface is locally stable. We found that the silicon atomic chain is 0.5081 Å higher than the indium atomic chains. The silicon atomic chain is strongly buckled by 0.4501 Å. The indium atomic chain is also strongly buckled with the average buckle distance 0.6045 Å, with the two outer indium adatoms higher than the inside indium adatom. The separation between the two outer indium adatoms is 6.2715 Å, which is not in good agreement with the inferred separation between the atomic rows [275]. The indium atomic chain is not

equidistant between two silicon atomic chains with the separation from one side 2.5632 Å and from the other side the separation is 4.9649 Å. This asymmetry is not observed in STM images. The silicon substrate is in a (7665...) arrangement. The details of the structure are shown in Table 7.2. Unlike the Bunk model, we cannot compare our atomic and electronic structures with results published in the literature as no simulations of the Saranin model have been presented. This also means that this work features the first analysis of the relative thermodynamic stability of the two competing models of the (4×1) surface reconstruction.

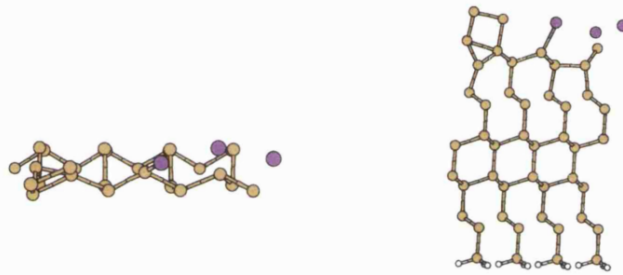


Figure 7.16: Relaxed structure of the Saranin model. See Figure 7.11 for layout.

### 7.5.2 Electronic structure

Although we cannot comment in detail on the electronic structure of the Saranin model we found that this system has a very small bandgap at all four  $k$ -points in the Brillouin zone. The bandgap varies from 0.14 eV at the  $\Gamma$ -point to 0.32 eV at the  $X'$  point. This indicates that the bandgap for the Saranin model is small and that the unit cell may be metallic.

Our simulations of the Saranin model show that there are four surface state bands separated from the valence band and there is another band which is partially separated from the valence band. This is in disagreement with angle-resolved photoemission experiments [263, 265], which shows that there are only three surface state bands. The distribution of the three highest states in the unit cell as a function of cell height is shown in Figures

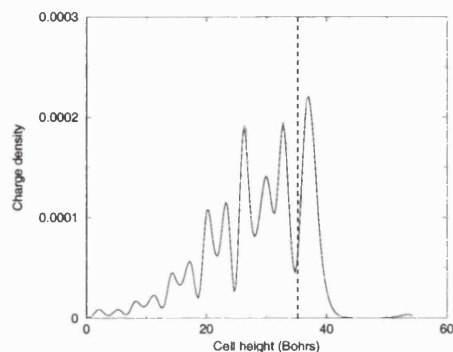


Figure 7.17: Plot of the charge density of the HOMO state as a function of cell height. See Figure 7.12 for layout.

7.17-7.19. The five highest occupied states all have quasi-one-dimensional dispersions with large dispersions along the  $\times 1$  direction (0.68 eV, 0.97 eV, 1.18 eV, 1.24 eV and 1.25 eV from HOMO to 5th HOMO state) and much smaller dispersions along the  $\times 4$  direction (0.39 eV, 0.17 eV, 0.22 eV, 0.23 eV and 0.20 eV from HOMO to 5rd HOMO state).

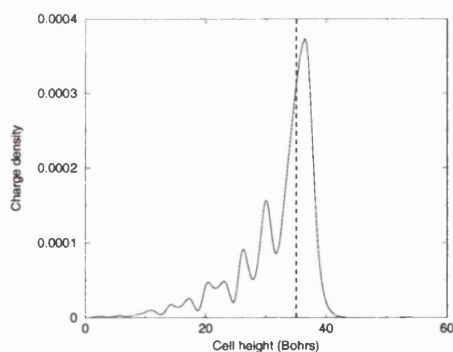


Figure 7.18: Plot of the charge density of the second HOMO state as a function of cell height. See Figure 7.12 for layout.

We found that the highest occupied state has a large overlap on all three indium adatoms (see Figure 7.4 for layout). The HOMO state has a very strong overlap with the middle indium adatom (0.9137), and weaker overlaps with the other two indium adatoms (0.6391 for the right In adatom and 0.1887 for the left In adatom). The second HOMO state has a very large surface component, with very large overlaps on the two outer indium adatoms (1.1054 on the left In adatom and 0.7455 on the right In adatom). There is also a large overlap of this state with the middle In adatom (0.5067) and on the silicon atomic chain, with overlaps of 0.1515 on the higher Si atom and 0.1882 on the

lower In atom. There is a negligible overlap between the surface atoms and the 3rd and 4th HOMO states, but there is a large overlap with the 5th HOMO state and several other high energy states.

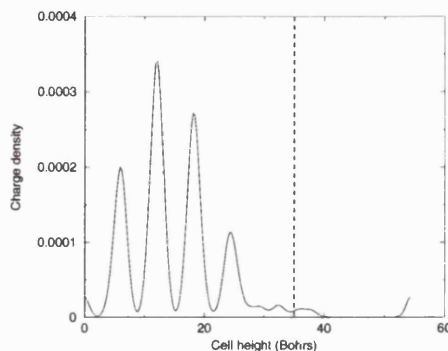


Figure 7.19: Plot of the charge density of the third HOMO state as a function of cell height. See Figure 7.12 for layout.

A plot of the HOMO and second HOMO states is shown in Figure 7.20. The HOMO state shows a strong connection along the  $\times 1$  direction mediated by the right atom of the indium chain. Similarly the second HOMO state shows a strong connection along the  $\times 1$  direction mediated by the indium atomic chain. We have therefore found that the two highest energy states have very large surface components and are strongly associated with the indium atomic chain. These states possess quasi-one-dimensional dispersions and, along with charge density plots, these seem to indicate that if a hole is injected into the line it would find it easy to disperse along the  $\times 1$  direction and would be confined to the indium atomic chain. The Sarasin model would make a good atomic wire.

## 7.6 Thermodynamic results: Which model is favoured?

We can use our calculated total energies to calculate which model of the  $(4\times 1)$  reconstruction is thermodynamically favoured, i.e., possesses the lower grand canonical potential [235, 236] over a range of chemical potential of the indium adatom (as the total surface stoichiometries differ by one indium atom, see equation (4.2)). We assume that the formation of the  $(4\times 1)$  reconstruction is constrained by thermodynamic factors. Our calculation of the canonical potential of indium adatoms takes place at zero temperature, we neglect entropic factors. We take the zero of chemical potential to correspond to the total energy of an isolated In atom in the PAW formalism, this is -1.98918 Hartrees.

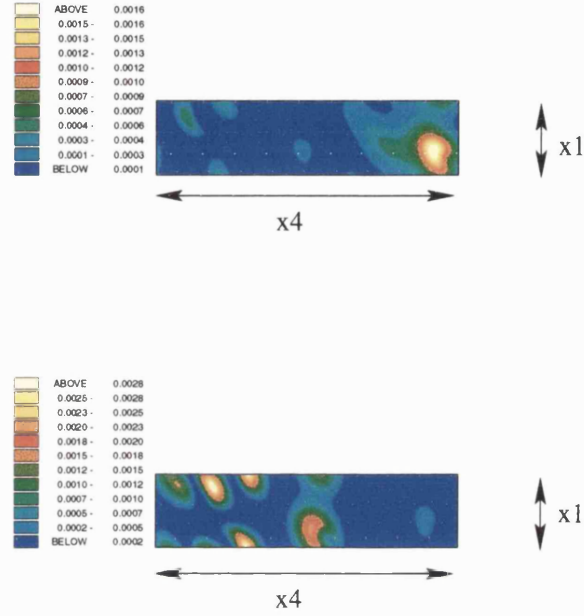


Figure 7.20: Plot of the charge density of the HOMO state (top) and 3rd HOMO state (bottom). This is a slice parallel to the surface 3 Å above the surface.

The chemical potential of the indium adatoms could either be in equilibrium with each other (the chemical potential of the indium adatoms is equal to the chemical potential of indium adatoms in bulk indium), or the indium adatoms could be in equilibrium with the indium gas phase. One of these bounds is already determined by the cohesive energy per atom of indium in bulk indium (-2.6 eV) [116, 278], the other bound is determined by the chemical potential of an ideal gas (as a first approximation) [279]. This is equal to

$$\mu_{\text{In}}^{\text{gas}} = \mu_{\text{In}}^{\text{atom}} - k_B T \ln \left( \frac{V}{V_{DB}} \right), \quad (7.1)$$

where  $\mu_{\text{In}}^{\text{atom}}$  is the chemical potential of an atom in bulk indium,  $k_B$  is Boltzmann's constant,  $T$  is the temperature at which indium is deposited (550° C),  $V$  is the average volume each indium atom occupies when in the process of being deposited on the surface

and  $V_{DB}$  is the De Broglie volume.

We can calculate the average volume each In atom occupies during the process of forming the (4×1) reconstruction by looking at the deposition rate at which the indium is deposited. The average deposition rate is 0.2 ML per minute (where 1 ML is the ideal Si density on the (111) plane,  $7.8 \times 10^{18} \text{m}^{-2}$  [93]). This means that per second of time (and assuming that when indium is deposited it sticks) the average spacing between atoms is  $6.2 \times 10^{-9} \text{m}$  from which we can determine the average volume each indium atom occupies. The De Broglie wavelength is given by [279]

$$\lambda_{DB} = \left( \frac{2\pi}{3} \right)^{\frac{1}{2}} \left( \frac{h^2}{2\pi m k_B T} \right)^{\frac{1}{2}} \quad (7.2)$$

which corresponds to  $8.22 \times 10^{-12} \text{m}$  and from which we can determine the De Broglie volume. Substituting these two volumes into (7.1) we find that the correction to the chemical potential of indium is -1.41 eV. The range of chemical potential that the indium adatoms could inhabit ranges (to a first approximation) from -2.6 to -4.01 eV.

The plot of  $\Omega$  as a function of  $\mu_{\text{In}}$  is shown in Figure 7.21. This is compared with the total energy of an ideal (4×1) unit cell with two silicon atoms in a chain structure, shifted down by 1.6 eV so as to match the relaxation energy of the (7×7) unit cell (0.4 eV per (1×1) unit cell [280, 281]), which is the ground state structure of the silicon (111) surface.

For the range of chemical potential that lies between bulk indium and the indium as an ideal gas we found that the Bunk model is thermodynamically preferred. The difference in grand canonical potentials in this range of chemical potential is 3-5 eV. This is much larger than any contributions to the grand canonical potential from entropic factors. We found that the Saranin model only becomes thermodynamically favoured when the chemical potential is equal to -7.89 eV. At this chemical potential the (7×7) surface with the silicon atomic chain positions that are used as the starting point for both models is thermodynamically favoured. We thus conclude that the Bunk model is the thermodynamically favoured model over the entire range of allowable chemical potential.

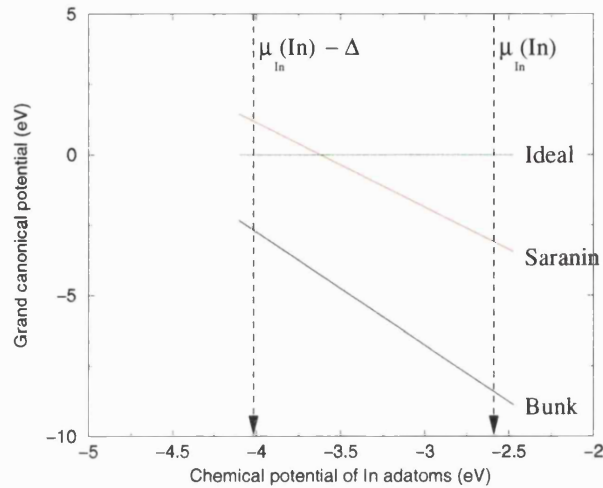


Figure 7.21: Plot comparing the grand canonical potentials  $\Omega$  per  $(4 \times 1)$  unit cell for the two  $(4 \times 1)$  candidate models and a  $(4 \times 1)$  component of the  $(7 \times 7)$  surface, as a function of chemical potential per In atom  $\mu_{\text{In}}$ . The zero of the grand canonical potential corresponds to the grand canonical potential of the ideal  $(7 \times 7)$  surface.

## 7.7 Conclusions

We have performed detailed *ab initio* calculations on the  $(4 \times 1)$  indium rich reconstruction on the  $(111)$  face of silicon. We have performed calculations on the Bunk and Saranin models of this  $(4 \times 1)$  reconstruction and have found that the Bunk model is thermodynamically preferred. The Bunk model also matches experimental photoemission data that shows that there are three occupied surface states while the Saranin model has five occupied surface states. We also found that in the Saranin model the silicon atomic line is higher than the indium atomic chain, but STM topographs of the In-rich  $(4 \times 1)$  reconstruction do not show a repeating feature along the  $\times 4$  direction with a repeat distance of 4 lattice vectors, rather it shows two features separated by  $\approx 4 \text{ \AA}$  with a repeat distance of 4 lattice vectors. The Bunk model matches the majority of the experimental evidence. We therefore conclude that the Bunk model is the favoured model for the  $(4 \times 1)$  surface.

How good an atomic scale wire is the Bunk model? We have found that the bandgap (at four points in the Brillouin zone) is enormously variable with a large bandgap at the  $K$ -point and a narrow bandgap at the  $X$ -point. The surface at least behaves as a narrow bandgap semiconductor and due to our limited  $k$ -point sampling we cannot confirm whether it is or is not metallic. The HOMO and third HOMO states have quasi-one-dimensional dispersions and are strongly associated with the indium atoms of the

indium atomic chain, specifically the two middle indium atoms. We conclude that the combination of a small bandgap, quasi-one-dimensional electronic states associated with the indium atomic chain and strong surface confinement indicate that the  $(4\times 1)$  reconstruction is an extremely good candidate for an atomic scale wire. As presented in the literature review there is a lot of experimental evidence for this conclusion. Suggestions for further work will be presented in the conclusions chapter.

# Chapter 8

## Conclusions and suggestions for further work

We have presented the results of detailed calculations on the physical and electronic structure of three prospective atomic scale wire systems, the trans-polyacetylene molecule, the silicon lines on the (001) face of cubic silicon carbide (the  $(n \times 2)$  series of reconstructions) and the indium atomic chains on the (111) face of cubic silicon carbide (the  $(4 \times 1)$ -In reconstruction). In this final chapter we present our conclusions on the utility of these systems as atomic scale wires and suggest further work that can be performed on these systems.

### 8.1 The polyacetylene molecule

#### 8.1.1 Conclusions

The polyacetylene molecule was modelled (at zero temperature) using the empirically based SSH Hamiltonian. The structure of the molecule under various boundary conditions (number of charges present and number of CH units) was calculated, and, depending on the initial boundary conditions polaron and/or soliton defects were observed to form. Harmonic phonon modes and frequencies were calculated for an equilibrium system using perturbation theory and the Huang-Rhys factors were calculated for a molecule with a single polaron present. The polaron structure is well represented by using the six lowest optical branch phonons. The electron-phonon coupling constants for the equilibrium

system were calculated in real space and were transformed into eigenvector space. Using these coupling constants and the phonon modes which strongly couple to the electron, a fully quantum mechanical transport calculation was made. It was found that although the elastic channel dominates the transmission probability (for the tunnelling regime), the coherent electron-phonon coupling has a strong effect on the effective bandgap. This is due to the creation of the virtual polaron that propagates through the molecule. The formation of this virtual polaron increases the tunnelling transport probability.

Transport in one-dimensional molecular wires is not the same as transport in three-dimensional semiconducting molecular crystals, as the propagating particles are not electron-like but are polaron-like (an electron strongly coupled to the phonon modes of the molecule). The electron-phonon coupling for this system increases the tunnelling transport probability. The methods used to find the transport properties of the polyacetylene molecule are of general applicability to other one-dimensional systems which have undergone a Peierls distortion and generate polarons when charge is injected into the system. This work is the first work which calculates (fully quantum mechanically) the effects of polaron formation on the transport properties of atomic scale wires.

### 8.1.2 Suggestions for further work

How can we take our study of the polyacetylene molecule further? There are several things that we can do; investigate the transport properties of soliton defects in a polyacetylene molecule, investigate the effects of finite temperature on the transport properties, investigate the properties of polyacetylene molecules when they are coupled to more realistic contacts, consider the real dynamics of charge injection and consider how we may experimentally measure the transport properties of the molecule.

A polyacetylene molecule at a finite temperature would change the initial set of phonon occupation numbers. In our zero temperature calculation the only phonon modes which are initially occupied are those phonon modes which are needed to form the polaron. The phonon modes which would be excited at room temperature would be acoustic phonon modes (thermal energy is  $\approx 1/40$  eV, optical phonon energies are approximately 200 meV). Although these acoustic phonon modes do not couple to the electron they would deform the molecule, thus altering the electron states. The effects of finite temperature would also affect the statistical averages that we use to calculate the transport

properties of the polyacetylene molecule.

Charge injected into a polyacetylene molecule with an odd number of CH units is expected to interact with the soliton defect which is already present. The formation of soliton defects improves the transport properties of the polyacetylene molecule, as the soliton creates a state in the middle of the bandgap [282], and for very long molecules is even mobile. Charge injection into a polyacetylene molecule with an even number of CH units may also result in the formation of a charged soliton which would increase the conductivity of the polyacetylene molecule.

We can consider the effects of more accurate modelling of the coupling between the contacts and the polyacetylene molecule. We include the effects of these contacts by including a self energy term into the Hamiltonian. We could model more realistic 3D contacts by using clusters (for instance gold [283]). These clusters would need to be relaxed using a tight-binding or DFT method. These contacts are not allowed to exchange particles with the polyacetylene molecule, it is assumed that before charge injection into the molecule the polyacetylene molecule and the contacts are both electrically neutral. In a real system this is almost certainly not the case as the chemical bonding between the end groups of the polyacetylene molecule and the contacts will result in some charge transfer, resulting in a charged molecule. This charging of the molecule will alter the transport properties. To a first approximation we can consider the effects of charging by calculating the amount of charging that particular chemical bonds (such as C-S-Au) would cause to the polyacetylene molecule. Then for this particular charge state we can find the relaxed structure using the method outlined in Chapter 3. The phonon modes and electron-phonon coupling constants would then be calculated for this structure and the transport properties would be calculated.

We have also completely neglected many body electron-electron effects in our transport calculations. There are two main areas where many body effects can manifest. Firstly, these effects can manifest themselves in the polyacetylene molecule itself. The strong coupling between electrons induced by the quasi-one-dimensionality of the line can make the excitations of the electronic system act as if they were bosons, that is they behave as a Luttinger liquid rather than as a Fermi liquid. Currently there is no information on how a Luttinger liquid coupled to a surface behaves, so we assume that the eigenstates of the polyacetylene molecule are Fermi states. The other many body effect

that is neglected is for the case where the chemical bonding between the polyacetylene molecule and the contacts leads to the molecule becoming charged by an odd number of electrons. If a molecule with an odd number of electrons is able to exchange electrons with the contacts, then a Kondo resonance would be able to bring the molecule into resonance. This would change the transport properties of the molecule, making the molecule a better conductor of charge (and a good atomic scale wire).

Currently in our injection of charge into the molecule we have assumed that the wavefunction is a plane wave. This is an approximation to the real dynamics of the system. Instead of the plane wave we could model the injected electron as a wavepacket instead.

How can experimentalists measure the transport properties of polyacetylene molecules (and other conducting polymers)? Transport measurements have been performed on molecules which have been suspended between two contacts [284, 285, 286]. However there is doubt whether these transport experiments measure only the transport properties of the molecule or include a bulk contribution. Recently Langlais *et al.* [287] have used an STM to image the penetration of metallic electronic states through a molecular wire. Although the polaron propagates through the molecule extremely quickly (much quicker than the STM could image the carrier) it may be possible to use the STM tip to trap the polaron and analyse the effects of polaron formation on a conjugated molecule. This would be a major theoretical and experimental undertaking.

There is a lot of additional work that can be performed on the polyacetylene molecule.

## 8.2 The silicon lines on silicon carbide

### 8.2.1 Conclusions

The  $(n \times 2)$  series of reconstructions were studied at zero temperature using both DFT and DFTB codes. This series of reconstructions corresponds to silicon atomic lines that have been observed on the (001) face of cubic silicon carbide. The component parts of the  $(n \times 2)$  series of reconstructions (the  $(3 \times 2)$  reconstruction which is the structural parent of the line and the  $c(4 \times 2)$  reconstruction which is the structural parent of the surface) were modelled using the PAW method. We found that the unambiguously thermodynamically favoured model for the  $(3 \times 2)$  surface reconstruction is the TAADM model, which has

an excess surface silicon stoichiometry of 1 ML. The unambiguously thermodynamically favoured model for the  $c(4\times 2)$  surface reconstruction is the MRAD model, which has an excess surface silicon stoichiometry of 0.5 ML.

The favoured models for the line and the surface were then used in tight-binding simulations of the large ( $n\times 2$ ) unit cells (where  $n$  varied from 3 to 11). We present in this thesis the first simulations of these widely separated silicon atomic lines, as well as considering the effects of modelling larger unit cells. Two types of structure were observed, a “ground”-state structure where all of the addimers of the surface and the top addimer of the line were strongly buckled and flat and a “metastable” structure where one of the addimers of the surface is flat and less strongly bound (this addimer is referred to as the silicon string). A structural transition was also observed for the metastable structure, as  $n$  is increased the top addimer of the silicon line flattens. With the flattening of this silicon line the HOMO state of the metastable structure becomes quasi-one-dimensional and dispersive in the  $\times 2$  direction (along the line). The dispersion of the HOMO state of the ground state structure become smaller in magnitude and anisotropic with increasing  $n$ . The LUMO states of both structures becomes quasi-one-dimensional with increasing  $n$ , with a large dispersion along the  $\times 2$  direction. The metastable structures also have a much smaller bandgap than the ground-state structures, with a bandgap varying from 0.23 to 0.86 eV.

$(7\times 4)$  unit cells composed of ground-state and metastable  $(7\times 2)$  unit cells were also studied using tight-binding techniques. It was found that the  $(7\times 4)$  unit cell made from the metastable  $(7\times 2)$  unit cell undergoes a Peierls-like transition where the repeat lattice vector along the line increases to  $\times 4$  surface lattice vectors. This Peierls-like transition also increases the bandgap of the  $(7\times 4)$  unit cell, the range varying from 0.64 to 0.77 eV. The HOMO state of this Peierls-like distorted system is still quasi-one-dimensional and aligned along the line direction.

The effects of hole and electron injection into the line were investigated by relaxing a charged  $(7\times 8)$  unit cell. It was found that both the hole and the electron localised on the line and formed polarons. The hole polaron was localised on the second level addimers of the line with a small structural deformation. The electron polaron localised on the top addimer of the line with a large structural deformation. The formation of hole and electron polarons decreases the bandgap by pushing the HOMO (or LUMO for

electron polaron systems) state into the bandgap. The formation of the hole polaron system altered the anisotropy of the HOMO state, with a larger dispersion in the  $\times 7$  direction (across the line) than along the  $\times 8$  direction (along the line). The electron polaron defect does not alter the anisotropy of the LUMO state; it is still more dispersive along than across the line. The energy of relaxation for both polaron systems is quite small (of order 0.05 eV).

The phonon modes (a minimal set) and electron-phonon coupling constants of the equilibrium system (before charge injection) were calculated. It was found that both polaron deformations were strongly coupled to the system, with the hole polaron requiring four phonons to recreate the structural defect and the electron polaron requiring eight phonons to recreate the defect. A consequence of this is that the effective mass of both polaron systems is quite large, with the effective mass of the electron polaron (the polaron which disperses along the line) of order 1100 electron masses. This means that if transport is to occur along the line then it will not be coherent. The techniques that were used to find the transport properties of the polyacetylene molecule are not valid for this system. The mobility and diffusion constants for thermally activated diffusion of the electron polaron were calculated and were found to be 300 times smaller than the diffusion constants for bulk cubic silicon carbide. The calculated mobility was also found to approximately 60 times smaller than the mobility of polyacetylene, the testbed atomic scale wire.

Our final conclusions are that the silicon line on silicon carbide is not a good candidate for use as an atomic scale wire. If electronic devices are manufactured using silicon carbide then the silicon atomic wire would be a slow link in the process, as it would be easier for electrons to propagate through the bulk SiC crystal than through the silicon line. This silicon line also possesses a lower mobility than a competing atomic wire, iodine and AsF<sub>5</sub> doped polyacetylene. Therefore the silicon atomic line is not a good candidate atomic scale wire. However it may be useful as a template for a conducting molecule. This, and other possible applications are discussed in the next section.

### 8.2.2 Suggestions for further work

What additional tests can be performed on the ( $n \times 2$ ) series of unit cells? Our calculations of the large ( $n \times 2$ ) unit cells was performed using a non-self-consistent Density-

Functional-Based-Tight-Binding implementation. Some of the structures that we found have involve a large amount of charge transfer. To check the results of this calculation we could perform a test calculation using a charge self-consistent-code, such as PAW. However, as these systems are so large it is computationally intractable using current workstations. With Moore's law in operation however, this calculation will be possible in a couple of years. And we could use  $O(N)$  *ab initio* codes to perform these calculations on these large unit cells using a parallel machine.

The results we present for the electron polaron system are less accurate than the results we present for the hole polaron system. The electron polaron system is the ground state of a charged system. The tight-binding parameterisation that we use is based upon LDA-DFT calculations of diatomic molecules. The LDA does not accurately reproduce excited states, and so our calculation of the electron polaron structure is less accurate than our calculation of the hole polaron structure. Until a more accurate method of dealing with the exchange and correlation terms is invented we cannot improve on these results (and even then the one-particle Kohn-Sham eigenstates that are used in DFT do not give the correct eigenvalues for excited states).

We calculated only a minimal set of the phonon modes of the reference system. This approximation did not have a major effect on the electron polaron system, but it did have a major effect on the hole polaron system. This is because the only atoms that are perturbed in order to calculate phonon modes are atoms of the silicon line. The hole polaron resides close to the surface, and so may couple strongly to phonon modes of the entire surface, not just phonon modes of the line. The only constraint that prevents us from calculating more phonon modes is the limit imposed by the CPU time that it takes to calculate the dynamical matrix that we use to calculate the phonon modes of the system. Increasing the number of atoms that are perturbed would increase the number of phonon modes we sample and would more accurately model the hole-polaron coupling and thus provide a better estimation of the effective mass. However as the hole polaron system has a stronger dispersion across the silicon line than along the silicon line, the hole polaron transport is not confined to the line, meaning that for hole polaron injection the silicon line is not an effective atomic scale wire. We conclude that additional phonon mode calculation is not needed.

The electron polaron system results show that although the polaron that forms has

a large spatial deformation and is localised on the silicon line, it is not very mobile (as indicated by calculations of the effective mass and mobility). The silicon line is not an effective atomic scale wire. What applications can the silicon line be used for? We suggest two applications, using the silicon lines as a template for the growth of conducting polymers or other structures on silicon carbide and using the polaron defects which occur under electron injection to store information.

There have been several recent experiments that have studied the assembly of atomic scale lines on a silicon substrate. For instance Lopinski *et al.* [288] have used an STM tip to manipulate the (100) surface of silicon to induce the self-directed growth of lines of styrene molecules. The silicon atomic lines that are observed on the (001) face of silicon carbide can be manufactured macroscopically for a well defined annealing temperature and time. They could be used as templates for the growth of conducting polymers. Currently no experiments have been performed to check whether conducting polymers would have strong bonds to the silicon line. We expect that as there are two dangling bonds per unit cell (associated with the top addimer) these line components are chemically reactive, and the electronic states associated with the lines are aligned along the line. DFT simulations of the reaction of a small monomer unit to a (3×2) unit cell could be performed to calculate the adhesion energy, and to determine whether the bonding of the molecule to the silicon carbide surface significantly affects the electronic properties of the conducting molecule.

The formation of (relatively) immobile polarons on the silicon lines of the ( $n \times 2$ ) surface raises an intriguing possibility for the use of injected polarons as a one-time-only means of storing information. The formation of the electron polarons causes a large buckle of magnitude 0.3 Å in the silicon line where no buckle previously existed. There are two easily distinguishable states for the top addimer to be in; the buckled state and the flat state. These can be treated as a 0 and 1 state respectively. Once the addimer has been placed in a buckled state it does not spontaneously relax back to a flat addimer state (see Chapter 6). We can envisage using an STM tip as a read/write head operating on a (7×4) surface. The STM tip scans along and across the silicon line injecting electrons into the silicon line to write data into the surface (with each sector well separated from the next along the line). The STM tip then later reads the data by measuring the buckle of each sector. The effective mass of the polaron is approximately equal to that of an

atom, but unlike the atoms of the silicon carbide crystal the polaron is mobile. At room temperature we estimate that each polaron diffuses  $1.86 \times 10^{-3}$  m up and down the line in a second. The diffusion distance per second is much longer than the average length of a silicon atomic line. To reduce the amount of silicon line that a polaron diffuses along per second it is necessary to reduce the operating temperature. For a diffusion length of the order of nanometres per second an operating temperature of magnitude 50 K would be needed. This operating temperature is not suitable for mass consumer technological applications.

A final possibility for further work that suggests itself is the study of the possible formation of a soliton on the silicon line. A soliton will be supported if the Peierls-like transition produces two degenerate ground states, the distortion is degenerate. As we are using periodic boundary conditions to model this surface this means that the  $(n \times 4)$  series of reconstructions must possess translational invariance. This implies that the ground state is degenerate. Considering our experience with the polarons on this line, we suspect that the solitons would also possess a large effective mass and be unsuitable for atomic scale transport.

## 8.3 Indium atomic chains on silicon

### 8.3.1 Conclusions

The intriguing indium-rich  $(4 \times 1)$  surface on the  $(111)$  face of silicon was simulated using DFT. This is the first time that this surface has been simulated. This surface reconstruction has been observed by STM to possess indium atomic chains that are evenly spaced apart. This surface is metallic, with a very strong quasi-one-dimensional character and electronic states that are strongly confined to the indium atomic chains. Out of two competing models the Bunk model (with a 1 ML indium surface stoichiometry and a 0.5 ML silicon surface stoichiometry) was found to be the thermodynamically favourable model over the entire range of indium chemical potential. The Bunk model was also found to possess a narrow bandgap, with the indium atomic chain possessing very strong overlaps with the highest-occupied-states that are quasi-one-dimensional in nature (and are localised on the surface). The  $(4 \times 1)$  surface seems to be a very promising candidate atomic scale wire.

### 8.3.2 Suggestions for further work

Of all the systems that we have studied the  $(4\times 1)$  reconstruction is the system which has the most potential for additional work. This further work can be divided into two parts; checks of the results that we have obtained and suggestions for further work. In our calculations of the  $(4\times 1)$  surface we have sampled only a limited part of the surface Brillouin zone. The  $(4\times 1)$  surface has been observed to be metallic, therefore in order to fully explore the electronic structure we would need to sample many more  $k$ -points than we have already used ( $\approx 50$ ). Our implementation of the PAW formalism is however only limited to sampling only four  $k$ -points of the surface Brillouin zone, in order to check the convergence of our  $k$ -point sampling scheme we would have to use a different DFT code (such as VASP) or modify the  $k$ -point sampling scheme of our PAW implementation. We could also further check our projectors by including the  $d$ -electron states. However as the  $(4\times 1)$  surface does not show any evidence of  $d$ -electron bonding [265], we suspect that the addition of  $d$ -electron states to the projector will not make a large difference to the atomic structure of the two competitive models.

After our calculations of the  $(4\times 1)$  surface have been fully tested we can then fully evaluate the potential of the indium atomic chain to act as an atomic scale wire. That is; firstly whether the indium atomic chains undergo a Peierls transition and secondly whether the injection of charge into the lines results in the formation of a polaron.

First of all we need to find out whether a Peierls transition occurs, as this will determine the route which further research will take (and is in itself an extremely controversial topic). Experimentally there is disagreement whether a  $(4\times 1) \iff (4\times 2)$  transition occurs, or whether a  $(4\times 1) \iff (8\times 2)$  transition occurs. To account for the possibility of there being a structural transition to an  $(8\times 2)$  surface we have to model an  $(8\times 2)$  unit cell composed of four  $(4\times 1)$  unit cells. If the metallic  $(4\times 1)$  surface reconstructs to a semiconducting  $(4\times 2)$  surface then the surface would have undergone a Peierls transition. On the other hand if there is a transition from a metallic  $(4\times 1)$  surface to a less metallic  $(8\times 2)$  surface then the surface may have undergone another kind of structural transition. This may be a Fermi liquid to Luttinger liquid transition, which would mean that we would not be able to perform transport calculations using the transport techniques outlined in Chapter 2 (a Luttinger liquid system is very different from a Fermi liquid system), or could be another type of structural transition. Regardless of the possible

structural transitions that may occur, the relaxation of an  $(8 \times 2)$  unit cell would be an extremely large computational calculation to perform, as this unit cell is very large (248 atoms). In order to perform *ab initio* calculations on a simulation cell of this size we would need to use a parallel machine.

If the indium atomic chains do become dimerised then we can use the formalism we have presented in Chapter 2 to calculate the transport properties of the indium atomic chain. This requires that when charge is injected into the chain that it localises on the atomic chain and that it forms a polaron. To check whether this occurs we need to perform relaxation calculations on the relaxed  $(4 \times 2)$  structure that may have previously been obtained, but with the addition/removal of one charge. If a polaron does form then we can check how many phonons couple to the polaron defect by calculating the dynamical matrix of the initial Peierls distorted system by the displacement of individual atoms (as shown in Chapter 6) and calculating the Huang-Rhys factors. If the Huang-Rhys factors are small (all phonon modes contribute less than one phonon) then the size of the Hamiltonian that needs to be solved will also be quite small, and a transport calculation will be possible. Alternatively if a large number of phonon modes possess Huang-Rhys factors which are large (some phonon modes contribute more than one phonon) then a transport calculation will not be feasible (as the Hamiltonian size increases as the exponent of the number of phonons per phonon mode). If the polaron is strongly coupled to the phonon modes of the system then the phonon contribution to the effective mass will be large (although the bandwidth contribution to the effective mass could be small). If the effective mass of the polaron is small then the polaron will be mobile enough for a transport calculation to be viable.

If it appears practicable to perform a transport calculation then the next step that we should perform is to find the electron-phonon coupling constants in real space and transform these constants into  $k$ -space. In order to reduce the size of the arrays that would store these constants we would use the tight-binding approximation as set out in Chapter 6, where the only nonzero elements of the electron-phonon coupling are the elements that involve the atom that is been displaced. The final step we would have to perform to obtain all the elements that we need to perform a transport calculation would be to transform the long ranged atomic basis set orbitals into short ranged Wannier functions. Once all of these calculations have been performed then we will have

enough information to perform coherent quantum mechanical transport calculations on the indium atomic chain. We could then perform transport calculations for systems with hole polarons, electron polarons (assuming that the structural defect is different from the structural defect of the hole polaron) and solitons (as the unit cell is periodic there does not seem to be any problem in forming a soliton defect).

The indium-rich ( $4\times 1$ ) reconstruction is an extremely promising candidate atomic scale wire. We have outlined a programme of work in which we determine whether the indium atomic chains relax due to a Peierls transition or whether there is a complicated Fermi liquid to Luttinger liquid transition. If a Peierls transition does occur then a detailed program of work is presented. If the structural transition is the result of a Fermi to Luttinger liquid transition then our options for further work are limited in the short term. This is because the study of possible Luttinger liquid formation in realistic quasi-one-dimensional structures is still in its infancy as the many-body Hamiltonian used is difficult to solve (although of course this also means that the prospects for interesting physics are good in the long term). The possible formation of a Luttinger liquid could be useful for the fitting of parameters to models of how quasi-one-dimensional structures couple to substrates [289].

A final possibility that suggests itself is the possible use of these indium atomic chains as the foundation for a quantum computer. An atomic wire which facilitates coherent transport may possess states which have a very low coupling to the substrate. These states could have a very long decoherence time. Long decoherent states could be manipulated into performing quantum logic operations. Compared to other proposals for quantum computers the indium atomic chains can be easily incorporated into solid state architectures. However we have not yet proposed any method of constructing quantum logic gates. The design of these quantum logic gates is another possibility for long term research.

## 8.4 Final remarks

We have presented the results of simulations on three different prospective atomic scale wires. Although the conclusions regarding the three systems are different we can draw general conclusions. One, that a Peierls distorted semiconducting system which supports polaron formation will be a better conductor than a semiconducting system which does

not support polaron formation. Two, that the lower the coupling of the polaron to the phonon modes (and consequently the lower the effective mass) the better. And three, that the most promising atomic scale wires (to this writer at least) are those wires which are metallic and form large scale surface reconstructions (this minimises the effort that is needed to form the atomic wire).

Atomic scale wires are fascinating physical systems. The problem of determining the transport properties of such systems is not a trivial problem and requires the collaboration of both theorists and experimentalists, so that the synergistic effects of collaboration are fully utilized. Part of the intention of this thesis is to provoke debate and lead to renewed study (both experimental for the case of the silicon lines and theoretical for the case of the indium atomic chains) on the systems that we study here. If this thesis accomplishes only this and nothing else, then it will have succeeded in its aims.

## Appendix A

# Binding energy in the tight-binding bond form

This appendix details how to formulate the binding energy in the tight-binding bond form so as to illustrate the connection between the tight-binding method and DFT. As this is quite involved we have placed this part of the discussion here rather than in the main part of the thesis. We start with the energy in the basis-independent form (2.50) which is

$$E \approx \text{Tr}[\rho^{\text{out}} H] - \text{Tr}\rho^f (V^f/2 + \mu_{\text{xc}}^f) + E_{\text{xc}}[\rho^f] + E_{\text{ii}}. \quad (\text{A.1})$$

Now if we take the assumed charge density to be the superposition of the free-atom charge densities [146]  $\rho^f = \sum_i \rho_i$  then we can write the above equation as the sum of four terms

$$E \approx A + B + C + D \quad (\text{A.2})$$

where

$$A = \text{Tr} (\rho^{\text{out}} - \rho^f) H \quad (\text{A.3})$$

and

$$B = \text{Tr} \sum_i \rho_i \left( \sum_{i \neq j} V_j^f / 2 + v_j \right) + E_{ii} \quad (\text{A.4})$$

and

$$C = E_{\text{xc}}[\rho^f] - \sum_i E_{\text{xc}}[\rho_i] \quad (\text{A.5})$$

and finally

$$D = \sum_i \left( \text{Tr} \rho_i \left( T + V_i^f / 2 + v_i \right) + E_{\text{xc}}[\rho_i] \right). \quad (\text{A.6})$$

If we look at this complex expression term by term we see that the first term is the sum of occupied eigenstates in the system ( $E_{\text{band}}$ ) minus the sum of occupied eigenstates in the free atoms ( $E_{\text{band}}^{\text{free}}$ ). This means that it is the promotion energy, that is the increase in energy due to promotion of electrons from the lowest energy orbitals in isolation to form hybrid orbitals in the bulk, plus the bonding energy (the reduction of energy due to the mixing of hybridised states to form bonding and antibonding orbitals).

The second term is the change in the total electrostatic energy due to the condensation from isolated atoms to the bulk. The third term is the change in the total exchange and correlation energy, and the fourth term is the total energy of the isolated atoms. If we subtract this total energy from the both sides of (A.6) we can find the binding energy in the tight-binding bond form

$$E_{\text{B}} \approx \text{Tr} (\rho^{\text{out}} - \rho^f) H + \Delta E_{\text{es}}[\rho^f] + \Delta E_{\text{xc}}[\rho^f]. \quad (\text{A.7})$$

We can then use this expression to show explicitly that the tight-binding formulation is an approximation to DFT (see Chapter 2).

## Appendix B

# Validity of approximations used in calculation of transport?

How badly does our approximation that the system is at zero temperature affect our derivation of the Landauer formula? We have also implicitly assumed that the current is only carried by a single energy channel at the Fermi level in our explanation of the Büttiker formula (although in practice we consider the effects of electron-phonon coupling that can scatter electrons from one channel to another). This allowed us to write the current as a linear response function (2.77) (this is the preferred expression to use as it is much more difficult to apply (2.78) to conductors with floating probes).

To model the more realistic situation of transport at finite temperature, we simply need to include injection from both contacts. The influx of electrons from lead 1 per unit energy is

$$i_1^+(E) = (2e/h)M f_1(E), \quad (\text{B.1})$$

where  $M$  is the number of modes in lead 1, and the influx from lead 2 is

$$i_2^-(E) = (2e/h)M'f_2(E) \quad (\text{B.2})$$

where  $M'$  is the number of modes in lead 2. The outflux from lead 2 is

$$i_2^+(E) = Ti_1^+(E) + (1 - T')i_2^-(E), \quad (\text{B.3})$$

where  $T$  is the probability of transmission from lead 1 to lead 2, and similarly the outflux from lead 1 is

$$i_1^-(E) = (1 - T)i_1^+(E) + T'i_2^-(E), \quad (\text{B.4})$$

where  $T'$  is the probability of transmission from lead 2 to lead 1. The net current  $i(E)$  in any point in the device is

$$i(E) = i_1^+ - i_1^- = i_2^+ - i_2^- \quad (\text{B.5})$$

$$= Ti_1^+ - T'I_2^- \quad (\text{B.6})$$

$$= \frac{2e}{h}[M(E)T(E)f_1(E) - M'(E)T'(E)f_2(E)] \quad (\text{B.7})$$

which can be simplified by defining the transmission function as  $\bar{T}(E) = M(E)T(E)$ . The total current in the device is thus

$$I = \int i(E)dE = \int \frac{2e}{h}\bar{T}(E)[f_1(E) - f_2(E)] \quad (\text{B.8})$$

assuming that  $\bar{T}(E) = \bar{T}'(E)$ . This approximation is valid (even in the presence of magnetic fields) so long as there is no inelastic scattering from one energy to another. If there are multiple terminals, then we can modify this expression to get

$$I_p = \int i_p(E) dE = \int \frac{2e}{h} \sum_q [\bar{T}_{qp} f_p(E) - \bar{T}_{pq} f_q(E)]. \quad (\text{B.9})$$

which can be written as

$$I_p = \int i_p(E) dE = \int \frac{2e}{h} \sum_q \bar{T}_{pq} [f_p(E) - f_q(E)]. \quad (\text{B.10})$$

which is only true if  $\sum_q \bar{T}_{qp} = \sum_q \bar{T}_{pq}$ , that is that there is no net inelastic scattering from one energy to another. Note that the transmission function  $\bar{T}_{p \leftarrow q}$  is found by summing all the transmission probabilities for all modes  $m$  in lead  $q$  and all modes  $n$  in lead  $p$ .

$$\bar{T}_{p \leftarrow q} = \sum_{\text{all } m} \sum_{\text{all } n} T_{n \leftarrow m}. \quad (\text{B.11})$$

Is it valid to ignore inelastic scattering? A constraint that prevents electrons from arbitrarily scattering from one state to another is the Pauli exclusion principle, wherein no two electrons cannot be in the same state (neglecting spin factors). Thus if we include inelastic scattering then we would need to take into account the Pauli exclusion principle. The answer to the question depends on how strong the coupling is between the conductor and the leads. If the coupling is weak, so that we have a state in lead 1 and another state with the same energy in lead 2, then the exclusion principle does affect transport, as the state in lead 2 needs to be unoccupied so that the electron in lead 1 can travel through the conductor [26]

However, if the coupling between the leads and the conductor is strong, that is if we can define a single wavefunction that extends from one lead to another, then the above expression is valid. This means that if transport is coherent throughout the conductor then *the exclusion principle has no effect on transport*.

If transport throughout the conductor is incoherent, what effect does this have on the transport properties? We can imagine dividing the current into two parts, a coherent and an incoherent part. This can be described by

$$i_p = \frac{2e}{h} \sum_q \bar{T}_{pq}(E)[f_p(E) - f_q(E)] + \frac{2e}{h} \bar{T}_\phi[f_p(E) - f_\phi(E)] \quad (\text{B.12})$$

where  $q$  denotes all real terminals and  $\phi$  denotes an imaginary phase-breaking terminal (see Chapter 1 for more information on phase-breaking). The current at the fictitious terminal is

$$i_\phi(E) = \frac{2e}{h} \sum_q \bar{T}_{\phi q}(E)[f_\phi(E) - f_q(E)] \quad (\text{B.13})$$

and can be either positive or negative. However, this phase-breaking terminal cannot extract or inject current. The net current over all energies sums to zero  $\int i_\phi(E)dE = 0$ .

This current denotes ‘vertical’ flow, i.e., the flow of current from one energy level to another. The actual distribution of vertical flow is quite complicated (see Figure B.1).

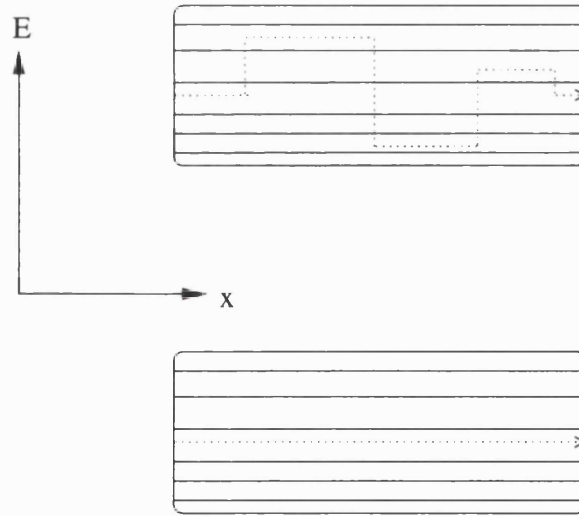


Figure B.1: How vertical flow occurs in a real system (top diagram), and how we neglect it (bottom diagram)

Thus, if the transport through a conductor is coherent, then the current through a conductor per unit energy is *rigorously* given by

$$i_p(E) = \frac{2e}{h} \sum_q \bar{T}_{pq}(E)[f_p(E) - f_q(E)]. \quad (\text{B.14})$$

We assume that transport occurs through a series of independent energy channels.

# Appendix C

## The Car-Parrinello algorithm

The Car-Parrinello (CP) algorithm was devised in 1985 and was a great step forward in the development and use of density functional techniques and molecular dynamics as it is a scheme that unifies the two concepts. The effect that it had on density functional calculations is that it allowed the application of DFT techniques to much larger systems than could previously be studied, and it let DFT be applied to the computation of interatomic forces in molecular dynamics which were previously limited to empirical interatomic potentials. In this appendix we describe the formulation of the CP algorithm and how it is used.

We start by writing the electron density in terms of the single electron orthonormal orbitals (the Kohn-Sham (KS) equations [127])  $n(\mathbf{r}) = \sum_i |\psi_i(\mathbf{r})|^2$ . To then find the minimum of the potential energy surface (for a specific geometry) the functional

$$E[\psi_i, R_I, \alpha_\nu] = \sum_i \int_{\Omega} d^3r \psi_i^*(\mathbf{r}) \left[ -\frac{\hbar^2}{2m} \nabla^2 \psi_i(\mathbf{r}) + U[n(\mathbf{r}), R_I, \alpha_\nu] \right] \psi_i(\mathbf{r}) \quad (\text{C.1})$$

must be minimised with respect to  $\psi_i(\mathbf{r})$ . Here  $R_I$  are the set of nuclear coordinates and  $\alpha_\nu$  are all possible external constraints imposed on the system (volume  $\Omega$ , strain etc.). The functional  $U$  contains the Coulomb repulsion of the atomic nuclei, and the effective potential of the electrons, thus including the Hartree, nuclear and exchange and correlation terms.

If we minimise (C.1) with respect to the orbitals  $\psi_i$  (subject to orthonormality) we get the self-consistent KS equations

$$\left(-\frac{\hbar^2}{2m}\nabla^2 + \frac{\delta U}{\delta n(\mathbf{r})}\right)\psi_i(\mathbf{r}) = \epsilon_i\psi_i(\mathbf{r}). \quad (\text{C.2})$$

This matrix then needs to be diagonalised which scales as  $O(N^3)$ . Also, this procedure has to be repeated for each new geometry and this means that it is extremely difficult to find computationally the equilibrium geometry of the system if this is not known experimentally. However, we can take a different approach to this problem (as Car and Parrinello showed).

We can regard the minimization of the KS functional as an optimisation problem which can be solved by a simulated annealing algorithm [290]. An objective function  $O(\beta)$  is minimised with respect to the set of parameters  $\beta$ , by generation of a set of  $\beta$  with a Boltzmann-type probability distribution which is proportional to  $\exp(-O(\beta)/T)$  via a Monte Carlo procedure. As  $T \rightarrow 0$  the state of the lowest  $O(\beta)$  is reached (unless there is some metastable system).

For our case the objective function is (C.1) and the variational parameters are the coefficients of the KS orbitals in some convenient basis set (and, depending on whether we are using the Born-Oppenheimer approximation or not,  $R_I$  and  $\alpha_\nu$ ). The most efficient method of minimising (C.1) is a strategy based on molecular dynamics rather than the example outlined above (this is known as ‘dynamical simulated annealing’). This also allows us to perform calculations at a finite temperature if we so desire.

We construct (C.1) to be time-dependent and introduce the Lagrangian

$$L = \sum_i \frac{\mu}{2} \int_{\Omega} d^3r |\dot{\psi}_i|^2 + \sum_I \frac{1}{2} M_I \dot{R}_I^2 + \sum_{\nu} \frac{1}{2} \mu_{\nu} \dot{\alpha}_{\nu}^2 - E[\psi_i, R_I, \alpha_{\nu}] \quad (\text{C.3})$$

where  $\psi_i$  has to satisfy the constraint

$$\int_{\Omega} d^3r \psi_i^*(\mathbf{r}, t) \psi_j(\mathbf{r}, t) = \delta_{ij} \quad (\text{C.4})$$

and  $\mu$  and  $\mu_{\nu}$  are arbitrary parameters. All derivatives are with respect to time.

The Lagrangian (C.3) generates the dynamics for the parameters  $\psi_i, R_I$  and  $\alpha_{\nu}$

through the equations of motion

$$\mu\ddot{\psi}_i(\mathbf{r}, t) = -\frac{\delta E}{\delta\psi_i^*(\mathbf{r}, t)} + \sum_k \Lambda_{ik}\psi_k(\mathbf{r}, t) \quad (\text{C.5})$$

$$M_I\ddot{R}_I = -\nabla_{R_I} E \quad (\text{C.6})$$

$$\mu_\nu\ddot{\alpha}_\nu = -\frac{\partial E}{\partial\alpha_\nu} \quad (\text{C.7})$$

where  $\Lambda_{ik}$  are Lagrange multipliers which are need in order to satisfy (C.4). The dynamics of the three equations of motion are fictitious and are only used as tools to perform the dynamical simulated annealing. The classical kinetic energy is given by

$$K = \sum_i \frac{\mu}{2} \int_{\Omega} d^3r |\dot{\psi}_i|^2 + \sum_I \frac{1}{2} M_I \dot{R}_I^2 + \sum_\nu \frac{1}{2} \mu_\nu \dot{\alpha}_\nu^2. \quad (\text{C.8})$$

The equilibrium value  $\langle K \rangle$  of the kinetic energy is calculated as the temporal average over the trajectories generated by the equations of motion and can be related to the temperature of the system by a suitable normalization. As we vary the velocities  $\dot{\psi}_i$ ,  $\dot{R}_I$  and  $\dot{\alpha}_\nu$ , the temperature of the system can be slowly reduced and as  $T \rightarrow 0$  the ground state of energy  $E$  is reached. At equilibrium  $\ddot{\psi}_i = 0$  and (C.5) is within a unitary transformation of the KS equations (C.2) and the eigenvalues of  $\Lambda_{ik}$  are coincident with the occupied KS equations. It is only at this point that the Lagrangian (C.3) describes a real physical system.

The advantages of this algorithm over a standard diagonalization approach are the following. One, that for large systems this scheme is more efficient than the standard diagonalization techniques [229]. And two, that diagonalization, self-consistency, ionic relaxation, and volume and strain relaxation are performed simultaneously. It is this that allows us to perform structural calculations that relax the geometry towards a minimum state of energy, and thus let us present the results that we present in this thesis.

# List of Figures

1.1	Interference patterns around a mesoscopic ring in a zero magnetic field. . .	15
1.2	Interference patterns around a mesoscopic ring in a non-zero magnetic field.	15
1.3	Quantization of states in a narrow potential well. . . . .	18
1.4	Change in height of a barrier under the influence of an electric field. . . .	19
1.5	quantum well embedded in a molecule with top of valence band and bot- tom of conduction band shown. The CH <sub>2</sub> groups represent the potential barriers, and the benzene groups in the middle represent the quantum well.	21
1.6	Schematic of an atomic relay (obtained from Goldhaber <i>et al</i> , Proc. IEEE <b>85</b> , 521, (1997)). . . . .	22
1.7	An example of a molecular switch. . . . .	23
1.8	Dimerisation of a molecule. . . . .	25
1.9	A dangling bond wire (image taken from Hitosugi <i>et al</i> , Phys. Rev. Lett. <b>82</b> , 4034, (1999)). . . . .	27
1.10	Plot of energy as a function of wavevector for a regular undimerised atomic chain. . . . .	28
1.11	Plot of energy as a function of wavevector for a dimerised semimetallic chain.	29
1.12	Twofold degeneracy of energy. . . . .	30
1.13	Near-twofold degeneracy of energy. . . . .	30
1.14	Near-onfold degeneracy of energy. . . . .	30
1.15	The dimerisation profile of a soliton. . . . .	31
1.16	Structure of a soliton in a chain. . . . .	31
1.17	Dimerisation profile of a polaron. . . . .	33
2.1	Schematic of the PAW scheme. . . . .	43

2.2	Typical experimental setup (top) involving an atomic scale conductor. Also shown is energy range (bottom) in which net current can flow. For definition of what $F^+$ is see text. . . . .	54
2.3	Illustration of the energy distribution of $-k$ and $+k$ states in a conductor with one scatterer $X$ and a probability of transmission from left to right of $T$ . . . . .	56
2.4	Schematic of an idealised system (top) and a more realistic situation (bottom). . . . .	59
2.5	Unit impulse in lead $p$ leads to an incident wave which is partially transmitted to the other leads. . . . .	64
2.6	Schematic diagram showing model of mapping of many body system to one body system. Various energy channels shown, some of which can only be accessed by phonon scattering. For simplicity we only show the channels associated with one phonon mode. . . . .	66
3.1	An illustration of the difference in chemical structure between trans-polyacetylene and cis-polyacetylene. . . . .	75
3.2	Dimerisation pattern of a neutral polyacetylene molecule with one hundred carbon atoms. . . . .	79
3.3	Dimerisation pattern of a singly charged (hole or electron) polyacetylene molecule with one hundred carbon atoms. . . . .	80
3.4	Dimerisation pattern of a multiply charged (four electrons or four holes) polyacetylene molecule with one hundred carbon atoms. . . . .	80
3.5	Dimerisation pattern of a neutral polyacetylene molecule with ninety nine carbon atoms. . . . .	81
3.6	Dimerisation pattern of a singly charged (hole or electron) polyacetylene molecule with ninety nine carbon atoms. . . . .	81
3.7	Dimerisation pattern of a multiply charged (four electrons or four hole) polyacetylene molecule with ninety nine carbon atoms. . . . .	82
3.8	Lowest energy optical phonons $V_q$ for a polyacetylene molecule containing one hundred carbon atoms. The indices are ordered so that as $q$ increases the frequency of the phonon mode $q$ increases. . . . .	86

3.9	Effective transmission probability $T(E)$ on a logarithmic scale vs electron injection energy $E$ for two molecules with different lengths (one has 40 CH units with six phonon modes and a maximum phonon occupation of two phonons per mode, and one has 100 CH units with four phonon modes and a maximum phonon occupation of three phonons per mode). Total transmission probability is shown as the solid line, transmission from the elastic channel $ t_{(0)}(E) ^2$ are the dotted lines and transmission from the first inelastic channel $n_{q=1}=1$ and $n_{q \geq 1}=0$ are shown as the dashed lines.	90
4.1	The bonding scheme of cubic silicon carbide. Each carbon atom (black) is bonded to four silicon atoms (yellow) in a tetrahedral arrangement. The bond angle is $109.47^\circ$ .	94
4.2	Illustration of polytypism based upon close packing of spheres (the spheres must be all of the same type: for silicon carbide they must all be silicon or carbon atoms only). Displaced initial layer contains spheres in A-type positions surrounded by six voids (top). Spheres of the next layer are situated either in the voids 1, 3 and 5 (B type) or in voids 2, 4 and 6 (C type positions). Spheres of any polytype have their centres located in parallel vertical planes whose interactions with the ground plane are represented by parallel lines (dashed lines). Taken from Defects and Defect Processes in Nonmetallic Solids, by W. Hayes and A. M. Stoneham, (1985). Other diagram shows bond orientation of the cubic (stacking sequence ABCA) and hexagonal (stacking sequence ABA) polytypes.	95
4.3	Schematic of alternating levels of silicon and carbon atoms (in the [001] direction) of the cubic polytype of silicon carbide. Different surface reconstructions correspond to various surface stoichiometries of silicon or carbon.	97
4.4	Formation of atomic-scale silicon lines on the (001) face of cubic silicon carbide. The top image is a STM scan of the surface after annealing at $\approx 1300$ K and covers an area $320 \text{ \AA}$ by $320 \text{ \AA}$ . Bottom image shows a $200 \text{ \AA}$ by $200 \text{ \AA}$ topograph of the surface after annealing at a temperature of $1350$ K. The next nearest silicon line is $400 \text{ \AA}$ away. These STM scans are taken from Soukiassian <i>et al.</i> Phys. Rev. Lett. <b>79</b> , 2498, (1997).	98

4.5	Paradigm of how we model the silicon lines (the $(n \times 2)$ ) reconstruction. The line is composed of a single $(3 \times 2)$ unit cell and the surface is composed of several $c(4 \times 2)$ unit cells. . . . .	99
4.6	The Additional Dimer Row Model proposed by Yan <i>et al.</i> , Surf. Sci. <b>316</b> , 181, (1994) and Semond <i>et al.</i> , Phys. Rev. Lett. <b>77</b> , 2013, (1996). It consists of one silicon addimer per unit cell. . . . .	100
4.7	STM scan of the $(3 \times 2)$ surface using both filled (top) and empty (bottom) states. Taken from Semond <i>et al.</i> , Phys. Rev. Lett. <b>77</b> , 2013, (1996). . .	101
4.8	The Double Dimer Row Model proposed by Hara <i>et al.</i> , Phys. Rev. B <b>50</b> , 4548, (1994), and Dayan, J. Vac. Sci. Technol. A <b>4</b> , 38, (1985). It consists of two Si addimers per unit cell. . . . .	102
4.9	The Two Adlayer Asymmetric Dimer Model proposed by Lu <i>et al.</i> , Phys. Rev. B <b>60</b> , 2495, (1999). It consists of three addimers per unit cell. . . .	103
4.10	The Alternate Up Down Dimer model proposed by Soukiassian <i>et al.</i> , Phys. Rev. Lett. <b>78</b> , 907, (1997). There are no Si adatoms. . . . .	106
4.11	The Missing Row Asymmetric Dimer model proposed by Lu <i>et al.</i> , Phys. Rev. Lett <b>81</b> , 2292, (1998). The Si atoms in the terminating layer form dimers and the adatoms form addimers. . . . .	107
4.12	Plot of the corrected total energy of bulk cubic silicon carbide as a function of lattice vector in the PAW formalism for a $(1 \times 1 \times 1)$ unit cell. The minimum is at 8.30197 Bohrs. . . . .	109
4.13	Plot of the total charge density as a function of cell height for the ADRM. The left side of the plot is the hydrogen terminated surface, the right side corresponds to the vacuum gap. Dashed line indicates the position of the top adatom. . . . .	109
4.14	Schematic of the surface Brillouin zone and the four $k$ -points that we sample for both reconstructions (not to scale). The left figure is the Brillouin zone of the $(3 \times 2)$ reconstruction, right for the $c(4 \times 2)$ reconstruction. . . .	110
4.15	Relaxed structure of the ADRM model. Yellow represents silicon atoms, black represents carbon atoms and white represents hydrogen atoms. The top left picture is the view from above, the top right view is the view across the silicon line and the bottom view is along the silicon line. . . . .	112

4.16	Relaxed structure of the DDRM model. See Figure 4.15 for colour coding. The top left picture is the view from above, the top right view is the view along the silicon line and the bottom view is across the silicon line. . . . .	114
4.17	Relaxed structure of the TAADM model. See Figure 4.15 for colour coding. The top left picture is the view from above, the top right view is the view along the silicon line and the bottom view is across the silicon line. . . . .	115
4.18	Plot of the charge density of the highest occupied state as a function of cell height for the ADRM. See Figure 4.13 for layout. . . . .	116
4.19	Three two-dimensional charge density plots of the ADRM. The top plot: a) is a plot of the charge density parallel to the surface at the height of the top adatom of the addimer. The second plot: b) is a plot of the charge density perpendicular to the surface and parallel to the $\times 2$ direction of the unit cell, at the position of the top ad-atom. The third plot: c) is a plot of the charge density perpendicular to the surface and parallel to the $\times 3$ direction at the position of the addimer. . . . .	117
4.20	Plot of the charge density of the third highest occupied state as a function of cell height perpendicular to the surface for the ADRM. See Figure 4.13 for layout. . . . .	118
4.21	Plot of the charge density of the highest occupied state as a function of cell height perpendicular to the surface for the DDRM. See Figure 4.13 for layout. . . . .	118
4.22	Three two-dimensional charge density plots of the DDRM. The top plot: a) is a plot of the charge density parallel to the surface at the height of the top adatom of an addimer. The second plot: b) is a plot of the charge density perpendicular to the surface and parallel to the $\times 3$ direction of the unit cell, at the position of the top ad-atom of an addimer. The third plot: c) is a plot of the charge density perpendicular to the surface and parallel to the $\times 2$ direction at the position of the addimer. . . . .	119
4.23	Plot of the charge density of the third highest occupied state as a function of cell height perpendicular to the surface for the DDRM. See Figure 4.13 for layout. . . . .	120

4.24	Plot of the charge density of the highest occupied state as a function of cell height for the TAADM. See Figure 4.13 for layout. . . . .	120
4.25	Three two-dimensional charge density plots of the TAADM. The top plot: a) is a plot of the charge density parallel to the surface at the height of the top adatom of the top addimer. The second plot: b) is a plot of the charge density perpendicular to the surface and parallel to the $\times 3$ direction of the unit cell, at the position of the top adatom of the addimer. The third plot: c) is a plot of the charge density perpendicular to the surface and parallel to the $\times 2$ direction at the position of the top addimer. . . . .	121
4.26	Charge density plot of the HOMO state of the TAADM. This is a slice which is parallel to the surface and is at the height of the bottom adatom of the top addimer. It clearly shows that the HOMO state is mediated from one unit cell to the other in the $\times 2$ direction via the second level addimers. . . . .	122
4.27	Plot comparing the grand canonical potentials $\Omega$ per $(3\times 2)$ unit cell for the three $(3\times 2)$ candidate models, the ideal $(1\times 1)$ surface and a $(3\times 2)$ slice of the $c(4\times 2)$ reconstruction, as a function of chemical potential per Si atom $\mu_{\text{Si}}$ . The zero of the grand canonical potential corresponds to the grand canonical potential of the ideal $(1\times 1)$ surface. Arrows pointing downwards indicate the critical value $\mu_{\text{Si}}^*$ where $\Omega$ is equal for a pair of $(3\times 2)$ models. Also indicated are the chemical potentials per atom of silicon and silicon carbide and the range of $\Delta H_f$ , to illustrate the maximum range of allowable cohesive energies for the case where the Si atoms are assumed to be in equilibrium with the bulk. . . . .	124
4.28	Relaxed structure of the AUDD model. See Figure 4.15 for colour coding. The top left picture is the view from above, the top right view is the view along the $[\bar{1}10]$ direction and the bottom view is the view along the $[110]$ direction. . . . .	126
4.29	Relaxed structure of the MRAD model. See Figure 4.15 for colour coding. The top left picture is the view from above, the top right view is the view along the $[\bar{1}10]$ direction and the bottom view is the view along the $[110]$ direction. . . . .	127

4.30	Plot of the charge density of the highest occupied state as a function of cell height perpendicular to the surface for the AUDD. See Figure 4.13 for layout. The dashed line indicates the position of the top surface dimer. . .	127
4.31	Plot of the charge density of the second highest occupied state as a function of cell height perpendicular to the surface for the AUDD. See Figure 4.13 for layout. The dashed line indicates the position of the top surface dimer.	128
4.32	Plot of the charge density of the highest occupied state as a function of cell height perpendicular to the surface for the MRAD. See Figure 4.13 for layout. . . . .	128
4.33	Plot of the charge density of the highest occupied state as a function of cell height perpendicular to the surface for the MRAD. See Figure 4.13 for layout. . . . .	128
4.34	Plot comparing the grand canonical potentials $\Omega$ per $(4 \times 2)$ unit cell for the two models as a function of the chemical potential of Si atoms, with an arbitrary zero. Also indicated are the cohesive energies per atom of silicon and silicon carbide and the range of size $\Delta H_f$ within which $\mu_{\text{Si}}$ is constrained to lie. . . . .	130
5.1	Plot of binding energy of bulk cubic silicon carbide as a function of lattice vector for the tight-binding formalism. This is for a simulation of a $(2 \times 2 \times 2)$ unit cell. The minimum is at 16.56562 Bohrs. . . . .	136
5.2	Plot comparing the grand canonical potentials $\Omega$ per $(3 \times 2)$ unit cell for the three $(3 \times 2)$ candidate models, the ideal $(1 \times 1)$ surface and a $(3 \times 2)$ slice of the $c(4 \times 2)$ reconstruction, as a function of chemical potential per Si atom $\mu_{\text{Si}}$ . The zero of the grand canonical potential corresponds to the grand canonical potential of the ideal $(1 \times 1)$ surface. Arrows pointing downwards indicate the critical value $\mu_{\text{Si}}^*$ where $\Omega$ is equal for a pair of $(3 \times 2)$ models. Also indicated are the chemical potential per atom of silicon and silicon carbide and the range of $\Delta H_f$ , to illustrate the maximum range of allowable cohesive energies, for the case where the Si atoms are assumed to be in equilibrium with the bulk. This is calculated with TROCADERO, and is in agreement with Figure 4.27. . . . .	138

5.3	Illustration of the two different states of the $(n \times 2)$ series of reconstructions (this reconstruction corresponds to the $(7 \times 2)$ reconstruction). We show only the adatoms of the surface. The top diagram shows the ground-state system, while the bottom diagram shows the metastable system. Note that the length and asymmetry of one of the two surface dimers is different in the two schematics (indicated by the red rings). . . . .	139
5.4	Illustration of the different addimer structures we obtain for different unit cells and different, methods of calculation ( <i>ab initio</i> and DFTB). Note that the addimer for the $(7 \times 2)$ unit cell is flat, compared to the $(3 \times 2)$ unit cell (obtained by both methods). The arrow indicates where the electron localises, see Section 5.3.2. . . . .	140
5.5	Plot comparing the calculated grand canonical potentials $\Omega$ per $(1 \times 1)$ cell for the $(n \times 2)$ series of lines (where $n$ varies in odd numbers from 3 to 11) with the ideal $(1 \times 1)$ surface and a $(1 \times 1)$ slice of the $c(4 \times 2)$ reconstruction, as a function of $\mu_{\text{Si}}$ . The zero of the grand canonical potential corresponds to the grand canonical potential of the ideal $(1 \times 1)$ surface. Also indicated are the experimental cohesive energies per atom of silicon and silicon carbide and the range of $\Delta H_f$ , to illustrate the maximum range of allowable cohesive energies, for the case where the Si atoms are assumed to be in equilibrium with the bulk. All $(n \times 2)$ reconstructions have an identical grand canonical potential at $\mu_{\text{Si}} \approx -5.24$ eV. . . . .	142
5.6	Plot of the COOP for all occupied states as a function of eigenvalue $n$ for the overlap of the $s$ orbitals on the top pair of adatoms of the line. Black indicates the $(3 \times 2)$ unit cell and red the $(7 \times 2)$ unit cell. . . . .	147
5.7	Plot of the COOP for all occupied states as a function of eigenvalue $n$ for the overlap of the $p_x$ orbitals on the top pair of adatoms of the line. See Figure 5.6 for layout. . . . .	147
5.8	Plot of the COOP for all occupied states as a function of eigenvalue $n$ for the overlap of the $s$ orbitals between the top adatom of the line and a second-level adatom. See Figure 5.6 for layout. . . . .	148

5.9	Plot of the COOP for all occupied states as a function of eigenvalue $n$ for the overlap of the $p_z$ orbitals between the top adatom of the line and a second-level adatom. See Figure 5.6 for layout. . . . .	148
5.10	Structure of the Si adlayer for the $(7 \times 8)$ unit cell constructed from the flat addimer case for the metastable structure. We indicate the differing bond lengths of the second-level addimers with the black arrows. The structure of the $(7 \times 8)$ unit cell is composed of two $(7 \times 4)$ unit cells. The blue ellipses indicate atoms on the surface where there is a large overlap with the HOMO state, the red ones atoms on the surface where there is a large overlap with the LUMO state. . . . .	151
5.11	Asymmetry of height for the short and long addimers of the line for the $(7 \times 8)$ unit cell. This asymmetry has been exaggerated. . . . .	151
5.12	Structure of the Si adlayer for the $(7 \times 8)$ unit cell constructed from the buckled addimer case for the metastable state. We indicate the differing bond lengths of the second-level addimers with the black arrows. The structure of the $(7 \times 8)$ unit cell is essentially composed of two $(7 \times 4)$ unit cells. See Figure 5.10 for colour coding. . . . .	152
5.13	Plot of the COOP for all occupied states as a function of eigenvalue $n$ for the overlap of the $s$ orbitals for the second-level addimers of the line for a $(7 \times 8)$ dimerised unit cell. . . . .	154
5.14	Plot of the COOP for all occupied states as a function of eigenvalue $n$ for the overlap of the $p_x$ orbitals for the second-level addimers of the line for a $(7 \times 8)$ dimerised unit cell. See Figure 5.13 for colour coding. . . . .	154
6.1	Structure of the Si adlayer for the $(7 \times 8)$ unit cell when a hole is injected into the system (top view). The light green ellipse indicates the structural defect where a polaron is formed. The red ellipse indicates where we initially inject a hole. . . . .	160
6.2	Structure of the Si adlayer for the $(7 \times 8)$ unit cell when an electron is injected into the system (top view). The light green ellipse indicates the structural defect where a polaron is formed. The red ellipse indicates where we initially inject an electron. . . . .	161

6.3	Structure of the Si adlayer for the $(7\times 8)$ unit cell when a hole is injected into the system (top view). The magenta ellipse indicates the six atoms of the unit cell where the hole is localised. . . . .	162
6.4	Band structure of the reference system (left diagram) and the hole polaron system (right diagram) along the $\Gamma - J$ (or $[110]$ ) direction. We also indicate the HOMO state. . . . .	163
6.5	Band structure of the reference system (left diagram) and the hole polaron system (right diagram) along the $\Gamma - J'$ (or $[\bar{1}10]$ ) direction. We also indicate the HOMO state. . . . .	164
6.6	Band structure of the reference system (left diagram) and the electron polaron system (right diagram) along the $\Gamma - J$ (or $[110]$ ) direction. We also indicate the LUMO state. . . . .	165
6.7	Band structure of the reference system (left diagram) and the electron polaron system (right diagram) along the $\Gamma - J'$ (or $[\bar{1}10]$ ) direction. We also indicate the LUMO state. . . . .	166
6.8	Plot of force against displacement for an equilibrium structure. The force is approximately linear for displacements within 0.01 Bohrs. . . . .	167
6.9	Comparison of harmonic (black) and deformation (red) energies for structures which are interpolations between the reference structure ( $\lambda=0$ ) and the polaron structure ( $\lambda=1$ ). The two energies converge for $\lambda \leq 0.2$ . Also shown (blue cross) is the difference in energy between the dimer structure and a structure where the atoms that we use to create the phonon modes use the hole polaron positions and all other atoms are in the reference cell positions. . . . .	170
7.1	Diagram of experimental uncertainty of indium coverage for the In-Si(111) system taken at a temperature of 700 K. This diagram is taken from Kraft <i>et al.</i> , Phys. Rev. B <b>55</b> , 5384, (1997). . . . .	180
7.2	STM image of the filled states of the $(4\times 1)$ reconstruction of the Si(111) reconstruction. An individual $(4\times 1)$ unit cell is delineated. This image is taken from H. W. Yeom <i>et al.</i> , Phys. Rev. Lett. <b>82</b> , 4898, (1998). . . . .	180

7.3	Comparison of various models that have been proposed for the (4×1) surface. Structures proposed a) Stevens <i>et al.</i> , Phys. Rev. B <b>47</b> , 1453, (1993), b) Abukawa <i>et al.</i> , J. Elec. Spec. Rel. Phen. <b>80</b> , 233, (1996), c) Bunk <i>et al.</i> , Phys. Rev. B <b>59</b> , 12228, (1999) and d) Saranin <i>et al.</i> , Phys. Rev. B <b>60</b> , 14372, (1999). Open circles are silicon atoms, light blue circles are indium adatoms. . . . .	183
7.4	Comparison of the surface structure of the two most likely models. See Figure 7.3 for colour coding. a) is the Saranin model, b) is the Bunk model.	187
7.5	Plot of corrected total energy vs bulk lattice vector for silicon in PAW. . .	187
7.6	Plot of corrected total energy vs bulk lattice vector for indium arsenide in PAW. . . . .	188
7.7	Plot of total charge density as a function of cell height for a $(\sqrt{3} \times \sqrt{3})R30^\circ$ unit cell. Space between dashed lines is the vacuum. . . . .	189
7.8	Surface structure (top two layers, several unit cells) of the relaxed $(\sqrt{3} \times \sqrt{3})R30^\circ$ with the In atom in the $T_4$ position. Yellow circles are surface silicon atoms, purple circles are indium adatoms. . . . .	189
7.9	Surface structure (top two layers, several unit cells) of the relaxed $(\sqrt{3} \times \sqrt{3})R30^\circ$ with the In atom in the $H_3$ position. See Figure 7.8 for colour coding. . . . .	190
7.10	Surface Brillouin zone of the (4×1) surface and the four $k$ -points sampled.	191
7.11	Relaxed structure of the Bunk model. Left diagram is view from above the surface, right diagram is view along the $\times 1$ direction. See Figure 7.8 for colour coding. . . . .	192
7.12	Plot of the charge density of the HOMO state as a function of cell height. Left side is bottom of the unit cell. Dashed line is position of the top of the unit cell. . . . .	193
7.13	Plot of the charge density of the second HOMO state as a function of cell height. See Figure 7.12 for layout. . . . .	194
7.14	Plot of the charge density of the third HOMO state as a function of cell height. See Figure 7.12 for layout. . . . .	194

7.15	Plot of the charge density of the HOMO state (top) and 3rd HOMO state (bottom). This is a slice parallel to the surface at a point 3 Å above the surface. . . . .	195
7.16	Relaxed structure of the Saranin model. See Figure 7.11 for layout. . . . .	196
7.17	Plot of the charge density of the HOMO state as a function of cell height. See Figure 7.12 for layout. . . . .	197
7.18	Plot of the charge density of the second HOMO state as a function of cell height. See Figure 7.12 for layout. . . . .	197
7.19	Plot of the charge density of the third HOMO state as a function of cell height. See Figure 7.12 for layout. . . . .	198
7.20	Plot of the charge density of the HOMO state (top) and 3rd HOMO state (bottom). This is a slice parallel to the surface 3 Å above the surface. . .	199
7.21	Plot comparing the grand canonical potentials $\Omega$ per (4×1) unit cell for the two (4×1) candidate models and a (4×1) component of the (7×7) surface, as a function of chemical potential per In atom $\mu_{\text{In}}$ . The zero of the grand canonical potential corresponds to the grand canonical potential of the ideal (7×7) surface. . . . .	201
B.1	How vertical flow occurs in a real system (top diagram), and how we neglect it (bottom diagram) . . . . .	221

# Bibliography

- [1] SIA, *Semiconductor Industry Association International Roadmap for Semiconductors 1999* (Sematech, Austin, TX, <http://www.semtech.org/>, 1999).
- [2] R. Feynmann, *Science* **254**, 1300 (1991).
- [3] V. Rousset *et al.*, *Nanotechnology* **7**, 144 (1996).
- [4] B. Alberts *et al.*, *Molecular Biology of the Cell and 3rd Edition* (Garland Publishing Inc., unknown, 1994).
- [5] M. P. Frank and T. F. K. Jr., *Nanotechnology* **9**, 162 (1998).
- [6] P. M. Ajayan, P. Redlich, and M. Rühle, *J. Microsc.* **185**, 275 (1997).
- [7] L. S. Schadler, S. C. Giannaris, and P. M. Ajayan, *Appl. Phys. Lett.* **73**, 3842 (1998).
- [8] O. Lourie, D. M. Cox, and H. D. Wagner, *Phys. Rev. Lett.* **81**, 1638 (1998).
- [9] R. A. Webb and S. Washburn, *Physics Today* **December**, 46 (1988).
- [10] E. G. Emberly and G. Kirczenow, *Phys. Rev. B* **58**, 10911 (1998).
- [11] E. G. Emberly and G. Kirczenow, *J. Phys. Condens. Matter* **11**, 6911 (1999).
- [12] E. G. Emberly and G. Kirczenow, *Nanotechnology* **10**, 285 (1999).
- [13] M. Magoga and C. Joachim, *Phys. Rev. B* **56**, 4722 (1997).
- [14] M. Magoga and C. Joachim, *Phys. Rev. B* **57**, 1820 (1999).
- [15] M. Magoga and C. Joachim, *Phys. Rev. B* **59**, 16011 (1999).
- [16] H. Totland, Y. M. Galperin, and V. L. Gurevich, *Phys. Rev. B* **59**, 2833 (1999).

- [17] J. Bonca and S. A. and. Trugman, *Phys. Rev. Lett.* **75**, 2566 (1995).
- [18] A. J. Heeger, S. Kivelson, J. R. Schrieffer, and W.-P. Su, *Rev. Mod. Phys.* **60**, 781 (1988).
- [19] Mikrajuddin, K. Okuyama, and F. G. Shi, *Phys. Rev. B* **61**, 8224 (2000).
- [20] H. Ness and A. J. Fisher, *Phys. Rev. Lett.* **83**, 452 (1999).
- [21] H. Ness and A. J. Fisher, *Appl. Surf. Sci.* **162-163**, 613 (2000).
- [22] M. Olson *et al.*, *J. Phys. Chem. B* **102**, 941 (1998).
- [23] H. J. Schulz, G. Cuniberti, and P. Pieri, *cond-mat/9807366v2* (1998).
- [24] R. Feynmann, *Opt. Comm.* **11**, 11 (1985).
- [25] N. W. Ashcroft and N. D. Mermin, *Solid State Physics* (Holt-Saunders International Editions, Oxford, 1976).
- [26] S. Datta, *Electronic Transport in Mesoscopic Systems* (Cambridge University Press, Cambridge, 1995).
- [27] L. D. Landau, *J. Exp. Theo. Phys.* **3**, 920 (1957).
- [28] L. D. Landau, *J. Exp. Theo. Phys.* **5**, 101 (1957).
- [29] L. D. Landau, *J. Exp. Theo. Phys.* **8**, 70 (1958).
- [30] A. Buldum, S. Ciraci, and C. Y. Fong, *J. Phys. Condens. Matter* **12**, 3349 (2000).
- [31] R. Landauer, *Philos. Mag.* **21**, 863 (1970).
- [32] R. Feynman, *Lectures on Physics and Vol. III* (Addison-Wesley, New York, 1965).
- [33] B. L. Altshuler, A. G. Aronov, and D. E. Khmelnitsky, *J. Phys. C: Solid State Phys.* **15**, 7367 (1982).
- [34] M. Sundaram, S. A. Chalmers, P. F. Hopkins, and A. C. Gossari, *Science* **254**, 1326 (1991).
- [35] D. Goldhaber-Gordon *et al.*, *Proc. IEEE* **85**, 521 (1997).
- [36] A. C. Seabaugh, J. H. Luscombe, and J. N. Randall, *Future Electron Devices* **3**, 9 (1993).

- [37] M. A. Kastner, *Rev. Mod. Phys.* **64**, 849 (1992).
- [38] R. Landauer, in *Nanostructure Physics and Fabrication*, edited by M. A. Reed and W. R. Kirk (New York: Academic, New York, 1989), p. 17.
- [39] G. M. Whitesides, J. P. Matthias, and C. T. Seto, *Science* **254**, 1312 (1991).
- [40] S. Nespurek and J. Sworakowski, *IEEE Eng. Medicine Bio.* **13**, 45 (1994).
- [41] R. A. Bissell, E. Cordova, A. E. Kaifer, and J. F. Stoddart, *Nature* **369**, 133 (1994).
- [42] Y. Wada *et al.*, *J. Appl. Phys.* **74**, 7321 (1993).
- [43] U. J. Quaade, K. Stokbro, C. Thirstrup, and F. Grey, *Surface Science* **415**, L1037 (1998).
- [44] C. Joachim, J. K. Gimzewski, and H. Tang, *Phys. Rev. B* **58**, 16407 (1998).
- [45] R. R. Birge, *Advances in Chemistry Series* (American Chemical Society, Washington, U. S. A., 1994).
- [46] M. Aiziwa, *IEEE Eng. Medicine Bio.* **13**, 94 (1994).
- [47] C. Joachim, J. K. Gimzewski, R. R. Schlittler, and C. Chavy, *Phys. Rev. Lett.* **74**, 2102 (1995).
- [48] C. Joachim and J. Gimzewski, *Chem. Phys. Lett.* **265**, 353 (1997).
- [49] E. G. Emberly and G. Kirczenow, *Phys. Rev. B* **62**, 10451 (2000).
- [50] K. Obermayer, G. Mahler, and H. Haken, *Phys. Rev. Lett.* **58**, 1792 (1987).
- [51] K. Heldmann, W. G. Teich, and G. Mahler, *Phys. Rev. B* **44**, 3829 (1991).
- [52] H. Körner and G. Mahler, *Phys. Rev. E* **47**, 3206 (1993).
- [53] P. Zanardi and F. Rossi, *Phys. Rev. Lett.* **81**, 4752 (1998).
- [54] I. Amlani *et al.*, *Science* **284**, 289 (1999).
- [55] R. P. Cowburn and M. E. Welland, *Science* **287**, 1466 (2000).
- [56] M. P. Samanta *et al.*, *Phys. Rev. B* **53**, R7626 (1996).
- [57] W. P. U. Su, J. R. Schrieffer, and A. J. Heeger, *Phys. Rev. B* **22**, 2099 (1980).

- [58] W. Tian *et al.*, J. Chem. Phys. **109**, 2874 (1998).
- [59] D. S. Wallace, Theoretical Physics Division and Harwell **DPhil thesis**, University of Oxford (1989).
- [60] A. Pinchart, C. Dallaire, and M. Gingras, Tetrahedron Letters **39**, 543 (1998).
- [61] J. R. Reimers, M. J. C. T. X. Lü, and N. S. Hush, Chem. Phys. Lett. **256**, 353 (1996).
- [62] D. A. Hutt *et al.*, Langmuir **12**, 5494 (1996).
- [63] S. J. Tans *et al.*, J. Vac. Sci. Technol. B **15**, 586 (1997).
- [64] D. L. Pearson and J. M. Tour, J. Org. Chem. **62**, 1376 (1997).
- [65] P. G. Collins, H. Bando, and A. Zettl, Nanotechnology **9**, 153 (1998).
- [66] H. Ajiki and T. Ando, Solid State Comm. **102**, 135 (1997).
- [67] J. W. Mintmire, B. I. Dunlap, and C. T. White, Phys. Rev. Lett. **68**, 631 (1992).
- [68] B. Marsen and K. Sattler, Phys. Rev. B **60**, 11593 (1999).
- [69] T. N. Todorov, G. A. D. Briggs, and A. P. Sutton, J. Phys. Condens. Matter **5**, 2389 (1993).
- [70] D. Sánchez-Portal *et al.*, Phys. Rev. Lett. **83**, 3884 (1999).
- [71] Y. Kondo and K. Takayanagi, Phys. Rev. Lett. **79**, 3455 (1997).
- [72] K. Stokbro *et al.*, Phys. Rev. Lett. **80**, 2618 (1998).
- [73] J. A. Stroscio and D. M. Eigler, Science **254**, 1319 (1991).
- [74] H. Uchida, D. Huang, J. Yoshinobu, and M. Aono, Surface Science **287**, 1036 (1993).
- [75] T. Hitosugi *et al.*, Appl. Phys. A **66**, S695 (1998).
- [76] S. Watanabe *et al.*, Phys. Rev. B **52**, 10768 (1995).
- [77] P. Doumergue *et al.*, Phys. Rev. B **59**, 15910 (1999).
- [78] P. A. Anderson *et al.*, Chem. Mater. **8**, 2114 (1996).

- [79] M. J. Kelly, *J. Phys. Condens. Matter* **7**, 5507 (1995).
- [80] H. L. Frisch and J. E. Mark, *Chem. Mater.* **8**, 1735 (1996).
- [81] Z. D. Dong *et al.*, *Jap. J. Appl. Phys.* **37**, 807 (1998).
- [82] O. Bunk *et al.*, *Phys. Rev. B* **59**, 12228 (1999).
- [83] D. M. Cornelison, M. S. Worthington, and I. S. T. Tsong, *Phys. Rev. B* **43**, 4051 (1991).
- [84] I. G. Hill and A. B. McLean, *Phys. Rev. B* **56**, 15725 (1997).
- [85] I. G. Hill and A. B. McLean, *Appl. Surf. Sci.* **123**, 371 (1998).
- [86] I. G. Hill and A. B. McLean, *Phys. Rev. B* **59**, 9791 (1999).
- [87] I. G. Hill and A. B. McLean, *Phys. Rev. Lett.* **82**, 2155 (1999).
- [88] J. Kraft, M. G. Ramsey, and F. P. Netzer, *Phys. Rev. B* **55**, 5384 (1997).
- [89] N. Nakamura, K. Anno, and S. Kono, *Surface Science* **256**, 129 (1991).
- [90] J. Nogami, S. Park, and C. F. Quate, *Phys. Rev. B* **36**, 6221 (1987).
- [91] F. Pedreschi, J. D. O'Mahoney, P. Weightman, and J. R. Power, *Appl. Phys. Lett.* **73**, 2152 (1998).
- [92] A. A. Saranin *et al.*, *Phys. Rev. B* **55**, 5353 (1997).
- [93] A. A. Saranin *et al.*, *Surface Science* **388**, 299 (1997).
- [94] A. A. Saranin *et al.*, *Phys. Rev. B* **56**, 1017 (1997).
- [95] H. W. Yeom *et al.*, *Phys. Rev. Lett.* **82**, 4898 (1999).
- [96] T. Hashizume *et al.*, *Surface Science* **386**, 161 (1997).
- [97] A. A. Baski, J. Nogami, and C. F. Quate, *Phys. Rev. B* **41**, 10247 (1990).
- [98] I. R. Collins *et al.*, *Surface Science* **325**, 45 (1995).
- [99] I. G. Hill and A. B. McLean, *Phys. Rev. B* **55**, 15664 (1997).
- [100] J. D. O'Mahoney *et al.*, *Surface Science* **365**, 801 (1996).

- [101] J. R. Power, P. Weightmann, and J. D. O'Mahoney, *Phys. Rev. B* **56**, 3587 (1997).
- [102] P. Segovia, D. Purdie, M. Hengsberger, and Y. Baer, *Nature* **402**, 504 (1999).
- [103] K. Miki *et al.*, *Phys. Rev. B* **59**, 14868 (1999).
- [104] D. R. Bowler, Wolson College **PhD Thesis**, N.A. (1997).
- [105] V. Y. Aristov, L. Douillard, and P. Soukiassian, *Surface Science* **440**, L825 (1999).
- [106] L. Douillard *et al.*, *Surface Science* **401**, L395 (1998).
- [107] F. Semond *et al.*, *Mat. Sci. Forum* **264-268**, 387 (1998).
- [108] P. Soukiassian, F. Semond, A. Mayne, and G. Dujardin, *Phys. Rev. Lett.* **79**, 2498 (1997).
- [109] P. Soukiassian and F. Semond, *J. Phys. IV France* **C6**, C6 (1997).
- [110] P. L. McEuen, *Physics World* **June**, 31 (2000).
- [111] C. Schönberger and L. Forró, *Physics World* **June**, 37 (2000).
- [112] H. Dai, *Physics World* **June**, 43 (2000).
- [113] R. E. Peierls, *Quantum Theory of Solids* (Oxford: Clarendon Press, Walton Street, Oxford, 1955).
- [114] K. Kim and D.-H. Lee, *Phys. Rev. B* **61**, 10768 (2000).
- [115] J. S. Russell, Rept. of the 14th Meeting of the BAAS 311 (1844).
- [116] C. Kittel, *Introduction to Solid State Physics and Seventh Edition* (John Wiley and Sons, New York, Chichester, Brisbane, Toronto, Singapore, 1996).
- [117] K. Huang and A. Rhys, *Proc. R. Soc. A* **204**, 406 (1950).
- [118] W. Hayes and A. M. Stoneham, *Defects and Defect Processes in Nonmetallic Solids* (John Wiley and Sons, New York, 1985).
- [119] J. C. Slater, *Phys. Rev.* **35**, 210 (1930).
- [120] R. O. Jones and O. Gunnarsson, *Rev. Mod. Phys.* **61**, 689 (1989).

- [121] E. K. U. Gross, E. Runge, and O. Heinonen, *Many-Particle Theory* (Adam Hilger, Bristol and Philadelphia and New York, 1991).
- [122] P. Fulde, *Electron Correlations in Molecules and Solids, 3rd Edition* (Springer-Verlag, Berlin, Heidelberg, New York, 1995).
- [123] H. H. Heinze, A. Gorling, and N. Rosch, *J. Chem. Phys.* **113**, 2088 (2000).
- [124] Y. Miyamoto and O. Sugino, *Phys. Rev. B* **62**, 2039 (2000).
- [125] M. Levy, *Proc. Natl. Acad. Sci. USA* **76**, 6062 (1979).
- [126] P. Hohenberg and W. Kohn, *Phys. Rev.* **136**, B864 (1964).
- [127] W. Kohn and L. J. Sham, *Phys. Rev.* **140**, A1133 (1965).
- [128] P. A. M. Dirac, *Proc. Cambridge Philos. Soc.* **26**, 376 (1930).
- [129] O. K. Andersen, *Phys. Rev. B* **12**, 3060 (1975).
- [130] J. C. Slater, *Phys. Rev.* **51**, 846 (1937).
- [131] P. M. Marcus, *Inter, J. Quan. Chem.* **1S**, 567 (1967).
- [132] D. R. Hamann, M. Schlüter, and C. Chiang, *Phys. Rev. Lett.* **43**, 1494 (1979).
- [133] V. Heine, *Solid State Phys.* **24**, 1 (1970).
- [134] D. R. Hamann, *Phys. Rev. B* **40**, 2980 (1989).
- [135] D. Vanderbilt, *Phys. Rev. B* **41**, 7892 (1990).
- [136] P. E. Blöchl, *Phys. Rev. B* **50**, 17979 (1994).
- [137] K. H. Weyrich, *Phys. Rev. B* **37**, 10269 (1988).
- [138] H. Hellmann, *Einführung in die Quantenchemie* (Franz Deuticke, unknown, 1937).
- [139] R. P. Feynmann, *Phys. Rev.* **56**, 340 (1939).
- [140] M. D. Ventura and S. T. Pantelides, *Phys. Rev. B* **61**, 16207 (2000).
- [141] C. M. Goringe, D. R. Bowler, and E. Hernández, *Rep. Prog. Phys.* **60**, 1447 (1997).
- [142] F. Bloch, *Z. Phys.* **52**, 555 (1928).

- [143] P. C. Slater and G. F. Koster, Phys. Rev. **94**, 1498 (1954).
- [144] A. P. Sutton, M. W. Finnis, D. G. Pettifor, and Y. Ohta, J. Phys. C: Solid State Phys. **21**, 35 (1988).
- [145] W. M. C. Foulkes and R. Haydock, Phys. Rev. B **39**, 12520 (1989).
- [146] J. Harris, Phys. Rev. B **31**, 1770 (1985).
- [147] W. M. C. Foulkes, University of Cambridge **PhD thesis**, N.A. (1987).
- [148] E. Londholm and S. Lundvist, Physica Scripta **32**, 220 (1985).
- [149] D. Porezag *et al.*, Phys. Rev. B **51**, 12947 (1995).
- [150] T. Frauenheim *et al.*, Phys. Rev. B **52**, 11492 (1995).
- [151] R. Gutierrez, T. Frauenheim, T. Köhler, and G. Seifert, J. Mater. Chem. **6**, 1657 (1996).
- [152] M. Elstner *et al.*, Phys. Rev. B **58**, 7260 (1998).
- [153] T. Frauenheim *et al.*, Phys. Stat. Sol. B **217**, 41 (2000).
- [154] A. P. Horsfield and A. M. Bratkovsky, J. Phys. Condens. Matter **12**, R1 (2000).
- [155] M. Büttiker, IBM J. Res. Dev. **32**, 317 (1988).
- [156] D. S. Fisher and P. A. Lee, Phys. Rev. B **23**, 6851 (1981).
- [157] H. Ness and A. J. Fisher, J. Phys. Condens. Matter **10**, 3697 (1998).
- [158] J. H. Edwards and W. J. Feast, Polymer **21**, 595 (1980).
- [159] T. Kennedy and E. H. Lieb, Phys. Rev. Lett. **59**, 1309 (1987).
- [160] J. Ashkenzi *et al.*, Phys. Rev. Lett. **62**, 2016 (1989).
- [161] P. Tavan and K. Schulten, Phys. Rev. B **36**, 4337 (1987).
- [162] S. Pleutin and J.-L. Fave, J. Phys. Condens. Matter **10**, 3941 (1998).
- [163] P. M. Grant and I. Batra, Solid State Comm. **29**, 225 (1979).
- [164] J. Ashkenzi, E. Ehrenfreund, Z. Vardeny, and A. O. Brafman, Mol. Cryst. Liq. Cryst. **117**, 193 (1985).

- [165] D. Moses *et al.*, Phys. Rev. B **26**, 3361 (1982).
- [166] Z. Vardeny, E. Ehrenfreund, O. Brafman, and B. Horovitz, Phys. Rev. Lett. **51**, 2326 (1983).
- [167] J. Orenstein and G. L. Baker, Phys. Rev. Lett. **49**, 1043 (1982).
- [168] J. Orenstein *et al.*, Phys. Rev. B **30**, 786 (1984).
- [169] B. Horovitz, Z. Vardeny, E. Ehrenfreund, and O. Brafman, Synth. Met. **9**, 215 (1984).
- [170] J. Fink and G. Leising, Phys. Rev. B **34**, 5320 (1986).
- [171] H. Ness, S. A. Shevlin, and A. J. Fisher, Phys. Rev. B **63**, 125422 (2001).
- [172] F. B. Schugerl and H. Kuzmany, J. Chem. Phys. **74**, 953 (1981).
- [173] W. H. Press, S. A. Teukolsky, W. T. Vetterling, and B. R. Flannery, *Numerical Recipes in Fortran: The Art of Scientific Computing, Second Edition* (Cambridge University Press, Cambridge, 1992).
- [174] K. A. Chao and Y. Wang, J. Phys. C: Solid State Phys. **18**, L1127 (1985).
- [175] F. Bechstedt *et al.*, in *Silicon Carbide: A Review of Fundamental Questions and Applications to Current Device Technology: Volume I*, edited by W. J. Choyke, H. Matsunami, and G. Pensl (Akademie Verlag, Mühlenstr., Berlin, Germany, 1997), p. 35.
- [176] W. J. Choyke, H. Matsunami, and G. Pensl, in *Silicon Carbide: A Review of Fundamental Questions and Applications to Current Device Technology: Volume I*, edited by W. J. Choyke, H. Matsunami, and G. Pensl (Akademie Verlag, Mühlenstr., Berlin, Germany, 1997), p. 1.
- [177] W. R. L. Lambrecht, S. Limpijumnong, S. N. Rashkeev, and B. Segall, in *Silicon Carbide: A Review of Fundamental Questions and Applications to Current Device Technology: Volume I*, edited by W. J. Choyke, H. Matsunami, and G. Pensl (Akademie Verlag, Mühlenstr., Berlin, Germany, 1997), p. 5.
- [178] K. Järrendahl and R. F. Davis, in *SiC Materials and Devices*, edited by Y. S. Park (Academic Press, Oval Road, London, U.K., 1998), p. 1.

- [179] R. S. Ramsdell, *Amer. Mineralogist* **32**, 64 (1947).
- [180] P. Käckell, J. Furthmüller, and F. Bechstedt, *Phys. Rev. B* **60**, 13261 (1999).
- [181] W. van Haeringen, P. A. Bobbert, and W. H. Backes, in *Silicon Carbide: A Review of Fundamental Questions and Applications to Current Device Technology: Volume I*, edited by W. J. Choyke, H. Matsunami, and G. Pensl (Akademie Verlag, Mühlenstr., Berlin, Germany, 1997), p. 63.
- [182] H. Nagasawa and K. Yagi, in *Silicon Carbide: A Review of Fundamental Questions and Applications to Current Device Technology: Volume I*, edited by W. J. Choyke, H. Matsunami, and G. Pensl (Akademie Verlag, Mühlenstr., Berlin, Germany, 1997), p. 335.
- [183] M. Kitabatake and J. E. Greene, *Appl. Phys. Lett.* **69**, 2048 (1996).
- [184] M. Kitabatake, in *Silicon Carbide: A Review of Fundamental Questions and Applications to Current Device Technology: Volume I*, edited by W. J. Choyke, H. Matsunami, and G. Pensl (Akademie Verlag, Mühlenstr., Berlin, Germany, 1997), p. 405.
- [185] S. Hara *et al.*, *Surface Science* **231**, L196 (1990).
- [186] S. Hara, S. Misawa, S. Yoshida, and Y. Aoyagi, *Phys. Rev. B* **50**, 4548 (1994).
- [187] S. Hara *et al.*, *Surface Science* **357-358**, 436 (1996).
- [188] F. Semond *et al.*, *Phys. Rev. Lett.* **77**, 2013 (1996).
- [189] A. Mayne, F. Semond, G. Dujardin, and P. Soukiassian, *Phys. Rev. B* **57**, R15108 (1998).
- [190] T. Fuyuki, T. Yoshinobu, and H. Matsunami, *Thin Solid Films* **225**, 225 (1991).
- [191] V. M. Bermudez, in *Silicon Carbide: A Review of Fundamental Questions and Applications to Current Device Technology: Volume I*, edited by W. J. Choyke, H. Matsunami, and G. Pensl (Akademie Verlag, Mühlenstr., Berlin, Germany, 1997), p. 447.
- [192] P. Soukiassian *et al.*, *Phys. Rev. Lett.* **78**, 907 (1997).

- [193] L. Pizzagalli *et al.*, Thin Solid Films **318**, 136 (1998).
- [194] W. Lu, P. Krüger, and J. Pollmann, Phys. Rev. Lett. **81**, 2292 (1998).
- [195] M. L. Shek, Surface Science **349**, 317 (1996).
- [196] J. M. Powers, A. Wander, M. A. van Hove, and G. A. Somorjai, Surface Science **260**, L7 (1992).
- [197] H. Hüsken, B. Schröter, and W. Richter, Surface Science **407**, 114 (1998).
- [198] J. M. Powers, A. Wander, P. J. Rous, and M. A. van Hove, Phys. Rev. B **44**, 11159 (1991).
- [199] J. P. Long, V. Bermudez, and D. Ramaker, Phys. Rev. Lett. **76**, 991 (1996).
- [200] V. M. Bermudez and J. P. Long, Appl. Phys. Lett. **66**, 475 (1995).
- [201] V. Derycke *et al.*, Phys. Rev. Lett. **81**, 5868 (1998).
- [202] L. Douillard *et al.*, Mat. Sci. Forum **264-268**, 379 (1998).
- [203] J. Kitamura *et al.*, Surface Science **433-435**, 465 (1999).
- [204] R. Kaplan, Surface Science **215**, 111 (1989).
- [205] H. Yan, X. Hu, and H. Jónsson, Surface Science **316**, 181 (1994).
- [206] H. Yan, A. P. Smith, and H. Jónsson, Surface Science **330**, 265 (1995).
- [207] M. Dayan, J. Vac. Sci. Technol. A **4**, 38 (1986).
- [208] W. Lu, P. Krüger, and J. Pollmann, Phys. Rev. B **60**, 2495 (1999).
- [209] W. Lu, P. Krüger, and J. Pollmann, Phys. Rev. B **61**, 2680 (2000).
- [210] H. W. Yeom *et al.*, Phys. Rev. B **61**, R2417 (2000).
- [211] U. Rossow *et al.*, J. Vac. Sci. Technol. B **16**, 2355 (1998).
- [212] W. Lu, W. G. Schmidt, E. L. Briggs, and J. Bernholc, Phys. Rev. Lett. **85**, 4381 (2000).
- [213] H. W. Yeom *et al.*, Phys. Rev. B **56**, R15525 (1997).
- [214] H. W. Yeom *et al.*, Phys. Rev. B **58**, 10540 (1998).

- [215] H. W. Yeom *et al.*, Surface Science **433-435**, 1999 (1999).
- [216] S. Hara *et al.*, Surface Science **421**, L143 (1999).
- [217] V. Y. Aristov, L. Douillard, O. Fauchox, and P. Soukiassian, Phys. Rev. Lett. **79**, 3700 (1997).
- [218] H. Enriquez *et al.*, Appl. Surf. Sci. **162-163**, 559 (2000).
- [219] L. Duda *et al.*, Surface Science **439**, 199 (1999).
- [220] L. Duda *et al.*, Phys. Rev. B **61**, R2460 (2000).
- [221] V. Derycke, P. Fonteneau, and P. Soukiassian, Phys. Rev. B **62**, 12660 (2000).
- [222] M. Sabisch *et al.*, Phys. Rev. B **53**, 13121 (1996).
- [223] P. Käckell, J. Furthmüller, and F. Bechstedt, Surface Science **352-354**, 55 (1996).
- [224] A. Catellani, G. Galli, and F. Gygi, Phys. Rev. Lett. **77**, 5090 (1996).
- [225] A. Catellani, G. Galli, F. Gygi, and F. Pellacini, Phys. Rev. B **57**, 12255 (1998).
- [226] V. Y. Aristov *et al.*, Phys. Rev. B **60**, 16553 (1999).
- [227] J. P. Perdew and A. Zunger, Phys. Rev. B **23**, 5048 (1981).
- [228] D. M. Ceperley and B. I. Alder, Phys. Rev. Lett. **45**, 466 (1980).
- [229] R. Car and M. Parrinello, Phys. Rev. Lett. **55**, 2471 (1985).
- [230] G. P. Francis and M. C. Payne, J. Phys. Condens. Matter **2**, 4395 (1990).
- [231] L. Pizzagalli *et al.*, Phys. Rev. B **60**, R5129 (1999).
- [232] P. Käckell *et al.*, Surface Science **391**, L1183 (1997).
- [233] R. Gutierrez *et al.*, Phys. Rev. B **60**, 1771 (1999).
- [234] M. Lübke *et al.*, J. Vac. Sci. Technol. A **16**, 3471 (1998).
- [235] G. Qian, R. M. Martin, and D. J. Chadi, Phys. Rev. B **38**, 7649 (1988).
- [236] J. E. Northup and S. Froyen, Phys. Rev. Lett. **71**, 2276 (1993).
- [237] A. Zyweitz, J. Furthmüller, and F. Bechstedt, Phys. Rev. B **59**, 15166 (1999).

- [238] O. Kubaschewski and C. Alcock, *Metallurgical Thermochemistry* (Pergamon, Oxford, 1979).
- [239] H. J. Monkhorst and J. D. Pack, *Phys. Rev. B* **13**, 5188 (1976).
- [240] V. Derycke, Private communication (1999).
- [241] A. P. Sutton, *Electronic Structure of Materials* (Clarendon Press, Oxford, 1993).
- [242] L. E. Ballentine and M. Kolár, *J. Phys. C: Solid State Phys.* **19**, 981 (1986).
- [243] R. Hoffmann, *Solids and Surfaces: A Chemist's view of Bonding in Extended Structures* (VCH, New York, 1988).
- [244] V. Eyert, B. Siberchicot, and M. Verdaguer, *Phys. Rev. B* **56**, 8959 (1997).
- [245] H. Goldstein, *Classical Mechanics: Second Edition* (Addison-Wesley, Reading, Massachusetts, 1980).
- [246] M. J. Hanjani, Third year project (2000).
- [247] A. M. Stoneham, *Theory of Defects in Solids: Electronic Structure of Defects in Insulators and Semiconductors* (Clarendon Press, Oxford University Press, Walton Street, Oxford, 1985).
- [248] W. M. Chen *et al.*, in *Silicon Carbide: A Review of Fundamental Questions and Applications to Current Device Technology: Volume II*, edited by W. J. Choyke, H. Matsunami, and G. Pensl (Akademie Verlag, Mühlenstr., Berlin, Germany, 1997), p. 79.
- [249] H. M. Rosenberg, *The Solid State, Second Edition* (Clarendon Press, Oxford University Press, Walton Street, Oxford, 1978).
- [250] C. K. Chiang *et al.*, *Phys. Rev. Lett.* **39**, 1098 (1977).
- [251] Y.-W. Park, A. J. Heeger, M. A. Druy, and A. G. MacDiarmid, *J. Chem. Phys.* **73**, 946 (1980).
- [252] J. J. Lander and J. Morrison, *Surface Science* **2**, 553 (1964).
- [253] J. E. Northrup, *Phys. Rev. Lett.* **53**, 683 (1984).
- [254] H. Nagayoshi, *Solid State Sci.* **59**, 167 (1985).

- [255] H. Öfner, S. L. Surnev, Y. Shapira, and F. P. Netzer, *Phys. Rev. B* **48**, 10940 (1993).
- [256] A. A. Saranin *et al.*, *Surface Science* **398**, 60 (1998).
- [257] J. Kraft, S. L. Surnev, and F. P. Netzer, *Surface Science* **340**, 36 (1995).
- [258] F., Owman, and P. Mårtensson, *Surface Science* **359**, 122 (1996).
- [259] Y. Tanishiro *et al.*, *Surface Science* **357-358**, 407 (1996).
- [260] S. Takeda, X. Tong, S. Ino, and S. Hasegawa, *Surface Science* **415**, 264 (1998).
- [261] J. L. Stevens, M. S. Worthington, and I. S. T. Tsong, *Phys. Rev. B* **47**, 1453 (1993).
- [262] M. S. Finney, C. Norris, P. B. Howes, and E. Vlieg, *Surface Science* **277**, 330 (1992).
- [263] H. Öfner, S. L. Surnev, Y. Shapira, and F. P. Netzer, *Surface Science* **307-309**, 315 (1994).
- [264] T. Abukawa *et al.*, *J. Elec. Spec. Rel. Phen.* **80**, 233 (1996).
- [265] T. Abukawa *et al.*, *Surface Science* **325**, 33 (1995).
- [266] K. Sakamoto, H. Ashima, H. W. Yeom, and W. Uchida, *Phys. Rev. B* **62**, 9923 (2000).
- [267] C. Kumpf *et al.*, *Phys. Rev. Lett.* **23**, 4916 (2000).
- [268] E. B. D. Grozea and L. D. Marks, *Surface Science* **461**, 23 (2000).
- [269] J. M. Nicholls, P. Mårtensson, G. V. Hansson, and J. E. Northrup, *Phys. Rev. B* **32**, 1333 (1985).
- [270] J. M. Nicholls, B. Reihl, and J. E. Northrup, *Phys. Rev. B* **35**, 4137 (1987).
- [271] J. T. Ryu *et al.*, *Surface Science* **447**, 117 (2000).
- [272] M. S. Finney *et al.*, *Physica B* **198**, 246 (1994).
- [273] S. C. Erwin, *Phys. Rev. Lett.* **75**, 1973 (1995).
- [274] A. A. Saranin *et al.*, *Phys. Rev. B* **60**, 14372 (1999).
- [275] A. B. McLean and I. G. Hill, *Appl. Surf. Sci.* **162-163**, 620 (2000).

- [276] R. H. Miwa and G. P. Srivastava, *Surface Science* **473**, 123 (2001).
- [277] J. Nakamura, S. Watanabe, and M. Aono, *Phys. Rev. B* **63**, 1993307 (2001).
- [278] D. Pettifor, *Bonding and Structure of Molecules and Solids* (Clarendon Press, Oxford University Press, Walton Street, Oxford, 1995).
- [279] F. Mandl, *Statistical Physics, Second Edition* (John Wiley and Sons, Manchester, 1988).
- [280] G. Qian and D. J. Chadi, *Phys. Rev. B* **35**, 1288 (1987).
- [281] I. Stich, M. C. Payne, R. D. King-Smith, and J. S. Lin, *Phys. Rev. Lett.* **68**, 1351 (1992).
- [282] H. Ness and A. J. Fisher, *Phys. Rev. B* **To be submitted**, N.A. (2001).
- [283] Y. Yourdshahyan, H. K. Zhang, and A. M. Rappe, *Phys. Rev. B* **63**, 081405(R) (2001).
- [284] W. Fritzsche, K. Böhm, E. Unger, and J. M. Köhler, *Nanotechnology* **9**, 177 (1998).
- [285] W. A. Reinert *et al.*, *Nanotechnology* **9**, 246 (1998).
- [286] H. W. C. Postma, M. de Jonge, Z. Yao, and C. Dekker, *Phys. Rev. B* **62**, R10653 (2000).
- [287] V. J. Langlais *et al.*, *Phys. Rev. Lett.* **83**, 2809 (1999).
- [288] G. P. Lopinski, D. D. M. Wayner, and R. A. Wolkow, *Nature* **406**, 48 (2000).
- [289] L. K. Dash and A. J. Fisher, To be published **N.A.**, N.A. (2001).
- [290] S. Kirkpatrick, C. D. Gelatt, Jr., and M. P. Vecchi, *Science* **220**, 671 (1983).